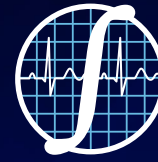


# ib



Una publicación de:  
**SOMIB**  
Sociedad Mexicana  
de Ingeniería Biomédica

## Revista Mexicana de Ingeniería Biomédica

### Modalidad de publicación

*Publicación continua:*  
una vez que se acepta y prepara un  
manuscrito, se publicará en línea

### Publication Modality

*Continuous publication:*  
once a manuscript is accepted and  
prepared, it will be released online



**SOMIB**  
Sociedad Mexicana  
de Ingeniería Biomédica

# Sociedad Mexicana de Ingeniería Biomédica

La Mesa Directiva de la Sociedad Mexicana de Ingeniería Biomédica hace una extensa invitación a las personas interesadas en participar, colaborar y pertenecer como Socio Activo de la SOMIB. La SOMIB reúne a profesionistas que se desarrollan en áreas de Ingeniería Biomédica, principalmente ingenieros biomédicos, así como otros profesionistas afines con el desarrollo de tecnología para la salud.

## Membresía Estudiante

**\$1,400.00 PESOS MXN**

15% de descuento para grupos de 5 o más personas.

## Membresía Profesionista

**\$2,400.00 PESOS MXN**

15% de descuento para grupos de 5 o más personas.

## Membresía Institucional

**\$11,600.00 PESOS MXN**

No aplica descuento.

## Membresía Empresarial

**\$20,000.00 PESOS MXN**

No aplica descuento.

EL PAGO CUBRE UN AÑO DE CUOTA. EN CASO DE REQUERIR FACTURA FAVOR DE SOLICITARLA, ADJUNTANDO COMPROBANTE DE PAGO Y ESPECIFICANDO CONCEPTO, AL CORREO ELECTRÓNICO: [gerencia@somib.org.mx](mailto:gerencia@somib.org.mx)

## Para ser socio

- › Realiza el pago de derechos, de acuerdo a la categoría que te corresponde.
- › Ingresa a [www.somib.org.mx/membresias](http://www.somib.org.mx/membresias) y elige el tipo de membresía por el cual realizaste el pago de derechos.
- › Completa el formulario correspondiente y envíalo.
- › Se emitirá carta de aceptación y número de socio por parte de la mesa directiva (aprobada la solicitud).
- › Para mayor información sobre beneficios, ingresa a [www.somib.org.mx](http://www.somib.org.mx); o escribe a [gerencia@somib.org.mx](mailto:gerencia@somib.org.mx).

**ib** Revista Mexicana de  
Ingeniería Biomédica

## AUTORES

Los trabajos a publicar en la RMIB, deben ser originales, inéditos y de excelencia. Los costos de publicación para autores son los siguientes:

**NO SOCIOS: \$5,000 PESOS MEXICANOS**

**SOCIOS: \$4,000 PESOS MEXICANOS**

## PUBLICIDAD

A las empresas e instituciones interesadas en publicitar su marca o productos en la RMIB, los costos por número son los siguientes:

**MEDIA PLANA: \$4,999.00 PESOS MXN (INCLUYE I.V.A.)**

**UNA PLANA: \$6,799.00 PESOS MXN (INCLUYE I.V.A.)**

**CONTRAPORTADA: \$7,799.00 PESOS MXN (INCLUYE I.V.A.)**

**FORROS INTERIORES: \$7,799.00 PESOS MXN (INCLUYE I.V.A.)**

DESCUENTO DEL 20% AL CONTRATAR PUBLICIDAD EN DOS O MÁS NÚMEROS.

## Datos bancarios

- › **Beneficiario:** Sociedad Mexicana de Ingeniería Biomédica A. C.
- › **Banco:** Scotiabank
- › **Referencia:** 1000000333
- › **Cuenta:** 11006665861
- › **CLABE Interbancaria:** 044770110066658614

## INFORMES

Juan Vázquez de Mella #481,  
Polanco I Sección,  
Alc. Miguel Hidalgo, C. P. 11510,  
Ciudad de México, México,  
(555) 574-4505  
[rib.somib@gmail.com](mailto:rib.somib@gmail.com)

**Fundador**  
Dr. Carlos García Moreira

## COMITÉ EDITORIAL

**Editora en Jefe**  
Dra. Dora-Luz Flores  
UNIVERSIDAD AUTÓNOMA DE BAJA CALIFORNIA

### Editores Asociados Nacionales

**Dr. Christian Chapa González**  
UNIVERSIDAD AUTÓNOMA DE CIUDAD JUÁREZ

**Dra. en C. Citlalli Jessica Trujillo Romero**  
DIVISIÓN DE INVESTIGACIÓN EN INGENIERÍA MÉDICA  
INSTITUTO NACIONAL DE REHABILITACIÓN "LUIS GUILLERMO IBARRA IBARRA"

**Dr. Rafael Eliecer González Landaeta**  
UNIVERSIDAD AUTÓNOMA DE CIUDAD JUÁREZ

**Dra. Rebeca Romo Vázquez**  
UNIVERSIDAD DE GUADALAJARA

**Dra. Isela Bonilla Gutiérrez**  
UNIVERSIDAD AUTÓNOMA DE SAN LUIS POTOSÍ

### Comité Editorial Internacional

**Dr. Leonel Sebastián Malacrida Rodríguez**  
UNIVERSIDAD DE LA REPÚBLICA, URUGUAY

**Dra. Elisa Scalco**  
INSTITUTE OF BIOMEDICAL TECHNOLOGY  
ITALIAN NATIONAL RESEARCH COUNCIL, MILAN, ITALY

**Dra. Natali Olaya Mira**  
INSTITUTO TECNOLÓGICO METROPOLITANO  
ITM, MEDELLÍN, COLOMBIA

### Índices

La Revista Mexicana de Ingeniería Biomédica aparece en los siguientes índices científicos:  
**Sistema de Clasificación de Revistas Científicas y Tecnologías del CONACYT - Q4, SCOPUS, SciELO, EBSCO, LATINDEX, Medigraphic Literatura Biomedica, Sociedad Iberoamericana de Información Científica - SIIC.**

[www.rmib.mx](http://www.rmib.mx)  
ISSN 2395-9126

**Editor técnico**  
Carla Ivonne Guerrero Robles

**Maquetadores editoriales**  
Sandra Sánchez Jáuregui  
Marco Guerrero

Se autoriza la reproducción parcial o total de cualquier artículo a condición de hacer referencia bibliográfica a la Revista Mexicana de Ingeniería Biomédica y enviar una copia a la redacción de la misma.



**Sociedad Mexicana de Ingeniería Biomédica**

Juan Vázquez de Mella #481, Polanco I Sección, Alc. Miguel Hidalgo, C. P. 11510, Ciudad de México, México, (555) 574-4505



**SOMIB**  
Sociedad Mexicana  
de Ingeniería Biomédica

**MESA DIRECTIVA**

**Dra. Norma Patricia Puente Ramírez**

PRESIDENTA

**Mtro. Edgar Del Hierro**

VICEPRESIDENTE

**Ing. Christopher Bricio**

TESORERO

**Mtro. David Palomo**

SECRETARÍA GENERAL

**Dra. Dora-Luz Flores**

EDITORA EN JEFE DE RMIB

**Afiliada a:**

International Federation of Medical and Biological Engineering (IFMB-IUPSM-ICSU)

Federación de Sociedades Científicas de México, A.C. (FESOCIME)

Consejo Regional de Ingeniería Biomédica para América Latina (CORAL)

**SOMIB**

Juan Vázquez de Mella #481, Polanco I Sección, Alc. Miguel Hidalgo, C. P. 11510, Ciudad de México, México (555) 574-4505

[www.somib.org.mx](http://www.somib.org.mx)

**REVISTA MEXICANA DE INGENIERÍA BIOMÉDICA**, Vol. 45, No. 3, Septiembre-Diciembre 2024, es una publicación cuatrimestral editada por la Sociedad Mexicana de Ingeniería Biomédica A.C., Juan Vázquez de Mella #481, Polanco I Sección, Alc. Miguel Hidalgo, C. P. 11510, Ciudad de México, México, (555) 574-4505, [www.somib.org.mx](http://www.somib.org.mx), [rib.somib@gmail.com](mailto:rib.somib@gmail.com). Editora responsable: Dra. Dora-Luz Flores. Reserva de Derechos al Uso Exclusivo No. 04-2015-041310063800-203, ISSN (impreso) 0188-9532; ISSN (electrónico) 2395-9126, ambos otorgados por el Instituto Nacional del Derecho de Autor. Responsable de la última actualización de este número: Lic. Sandra Sánchez Jáuregui, Juan Vázquez de Mella #481, Polanco I Sección, Alc. Miguel Hidalgo, C. P. 11510, Ciudad de México, México, (555) 574-4505, fecha de última modificación, 31 de agosto del 2023.

El contenido de los artículos, así como las fotografías son responsabilidad exclusiva de los autores. Las opiniones expresadas por los autores no necesariamente reflejan la postura del editor de la publicación.

Queda estrictamente prohibida la reproducción total o parcial de los contenidos e imágenes de la publicación sin previa autorización de la Sociedad Mexicana de Ingeniería Biomédica.

**Disponible en línea:**

[www.rmib.mx](http://www.rmib.mx)

**CONTENTS**  
**CONTENIDO**

|  |             |  |              |
|--|-------------|--|--------------|
| <b>Contents</b>  | <b>p 5</b>  | <b>Research Article</b>  | <b>p 68</b>  |
| <b>Research Article</b>  | <b>p 6</b>  | <b>Low-Cost Portable Pupilometer for Circadian Rhythm Studies</b>  |              |
| <b>A Real-Valued Kalman Estimation Method for Harmonic Signal Analysis in Biomedical Applications</b>  |             | <i>Pupilómetro Portátil de bajo costo para Estudios de Ritmo Circadiano</i>  |              |
| <i>Análisis de Señales Biomédicas por Medio del Método de Estimación Armónica de Kalman con un Modelo de Valores Reales</i>  |             | <b>Research Article</b>  | <b>p 80</b>  |
| <b>Research Article</b>  | <b>p 20</b> | <b>Web-based Interactive 3D Modeling and Visualization of the Human Brain towards Anatomy Education</b>  |              |
| <b>UMInSe: An Unsupervised Method for Segmentation and Detection of Surgical Instruments based on K-means</b>  |             | <i>Modelado y Visualización Interactivos en 3D del Cerebro Humano basados en la Web hacia la Educación de Anatomía</i>   |              |
| <i>UMInSe: Método no Supervisado para la Segmentación y Detección de Instrumentos Quirúrgicos Basado en K-means</i>  |             | <b>Artículo de Revisión</b>  | <b>p 99</b>  |
| <b>Review Article</b>  | <b>p 51</b> | <b>Desarrollo de Materiales Poliméricos como Hidrogeles con Curcumina para Regeneración de Tejidos de la Piel</b>  |              |
| <b>Human Mesenchymal Stem Cells Derived from Adipose Tissue and Umbilical Cord, in Combination with Acellular Human Amniotic Membranes, for Skin Healing Processes in Animal Models: a Systematic Review</b>                               |             | <i>Development of Polymeric Materials as Hydrogels with Curcumin for Skin Tissue Regeneration</i>  |              |
| <i>Células Troncales Mesenquimales Humanas Derivadas de Tejido Adiposo y Cordón Umbilical, Combinadas con Membranas Amnióticas Humanas Acelulares, para Procesos de Regeneración Cutánea en Modelos Animales: una Revisión Sistemática</i> |             | <b>Artículo de Revisión</b>  | <b>p 140</b> |
|  |             | <b>Electroquímica en Medicina: Grafeno y Electroestimulación Celular</b>   |              |
|  |             | <i>Electrochemistry in Medicine: Graphene and Celular Electrostimulation</i>   |              |
|  |             | <b>Research Article</b>  | <b>p 112</b> |
|  |             | <b>Development of a Frequent Exchange Coordinate Algorithm for Detection of Precordial Electrode Exchange during ECG based on Error and Correlation Parameters</b>                 |              |
|  |             | <i>Desarrollo de un Algoritmo de Coordenadas de Intercambio Frecuente para Detección del Intercambio de Electrodo Precordiales ECG basado en Parámetros de Error y Correlación</i> |              |

[dx.doi.org/10.17488/RMIB.45.3.1](https://doi.org/10.17488/RMIB.45.3.1)

E-LOCATION ID: 1428

## A Real-Valued Kalman Estimation Method for Harmonic Signal Analysis in Biomedical Applications

### Análisis de Señales Biomédicas por Medio del Método de Estimación Armónica de Kalman con un Modelo de Valores Reales

Johnny Rodríguez-Maldonado<sup>1</sup>  , Miguel Angel Platas-Garza<sup>1</sup> , Ernesto Zambrano-Serrano<sup>1</sup> 

<sup>1</sup>Universidad Autónoma de Nuevo León, Nuevo León - México

#### ABSTRACT

This work presents a methodology for obtaining the harmonic estimation of biomedical signals such as electrocardiogram, cardiorespiratory and blood pressure signals. The proposed methodology is achieved using polynomial approximation and the Kalman filter. As advantage, the technique includes instant estimations of signal harmonics and its derivatives using a real-valued model. Furthermore, a comparison of the results is conducted with the Savitzky-Gola, nonlinear tracking differentiator methods, extended state observer and digital differentiator base on Taylor series. The results suggest that the proposed method has the potential to enhance the quality of signal measurements, especially in the presence of noise.

**KEYWORDS:** biomedical signal analysis, harmonics estimates in ECG, derivative estimation in biomedical signals

## RESUMEN

Este trabajo presenta una metodología para obtener la estimación armónica de señales biomédicas como señales de electrocardiograma, cardiorrespiratorias y de presión arterial. La metodología propuesta utiliza la aproximación polinomial y el filtro de Kalman. Como ventaja, la técnica incluye estimaciones instantáneas de las armónicas de la señal y sus derivadas utilizando un modelo con parámetros en los reales. Además, se realiza una comparación de los resultados con los métodos de Savitzky-Golay, el diferenciador de seguimiento no lineal, observador de estados extendido y diferenciador digital basado en series de Taylor. Los resultados sugieren que el método propuesto tiene el potencial de mejorar la calidad de las mediciones de señales, especialmente en presencia de ruido.

**PALABRAS CLAVE:** análisis de señales biomédicas, estimación armónica en señales biomédicas, estimación de derivadas en señales biomédicas

### Corresponding author

TO: Johnny Rodríguez-Maldonado

INSTITUTION: Universidad Autónoma de Nuevo León,  
Nuevo León - México

ADDRESS: Pedro de Alba S/N Entre Av. Alfonso Reyes y  
Av. Fidel Velázquez, Ciudad Universitaria. San Nicolás  
de los Garza, Nuevo León, México.

EMAIL: [johnny.rodriguezml@uanl.edu.mx](mailto:johnny.rodriguezml@uanl.edu.mx)

### Received:

23 April 2024

### Accepted:

9 August 2024

## INTRODUCTION

Signal analysis is essential in many engineering fields, including power systems, vibration analysis, voice recognition, radar applications, biomedical engineering, and digital communications. Because it allows obtaining relevant features regarding system information. The human body has different systems, such as the cardiovascular, nervous, and respiratory system, among others<sup>[1]</sup>. From these systems, signals can be obtained that provide relevant information. These signals are processed for analysis<sup>[2][3]</sup>, which leads to their quantization, causing quantization error. These signals can not only be affected by quantization error but also by other errors caused by measurement instrument components or incorrect usage. One solution to this issue is the implementation of a methodology that considers noise filtering and achieves instantaneous estimates without the need for a sample window for estimation.

The measurement of biomedical signals is a cornerstone of modern healthcare, providing critical insights into physiological processes and aiding in the diagnosis and treatment of various medical conditions. Common examples of biomedical signals are electrocardiograms (ECG), electroencephalograms (EEG), and blood pressure measurements. These signals are crucial for monitoring patient health, conducting medical research, and developing new medical technologies. The precision and capabilities of biomedical signal measurement depend on sensors and signal processing techniques. Digital Signal Processing (DSP) techniques enable the extraction of meaningful information from noisy signals, improving diagnostic accuracy<sup>[4]</sup>. Therefore, the rates of change in biomedical signals are part of their analysis.

Below are some methodologies that can be implemented in signal estimation, which can also estimate the rate of change in the signal. The Savitzky-Golay (Sgolay) method includes the use of data windows<sup>[5][6]</sup>, introducing a delay in its estimates. In<sup>[7][8]</sup>, the discrete wavelet transform is implemented to cancel disturbances in ECG caused by devices or movements. However, even when the sample window size can be narrow depending on the signal resolution to be estimated, a sample window is still necessary for information estimation. On the other hand, the Nonlinear Tracking Differentiator (NTD) method<sup>[9][10]</sup> requires an adjustment parameter, which consequently implies a drawback since this parameter needs to be calibrated with respect to the signal to be estimated, leading to potentially suboptimal or highly suboptimal estimates. In response to these limitations and based on the results obtained from the methodology used in<sup>[11][12]</sup> for phasor estimation, it was proposed to employ a methodology that enables instant estimations. This methodology is grounded in the implementation of a signal model that includes its respective derivatives, all within a state transition matrix. With a zeroth-order model (approximating the signal with a zeroth-order Taylor polynomial), estimations of the electrocardiogram are obtained. By increasing the order of the Taylor polynomial, the model is modified, allowing for the estimation of signal derivatives, achieving a better response in estimation for signals corrupted by noise. This methodology surpasses the limitations of other strategies in the sense that there is no need for a sample window to perform estimations and enables a more accurate signal approximation by reducing noise. Consequently, the proposed method focuses on obtaining a more precise and comprehensive estimation in relation to the characteristics of biomedical signals. It successfully provides good estimates for signals such as electrocardiograms, cardiorespiratory signals, and blood pressure. Another method that can be implemented in the analysis of biomedical signals is the Extended State Observer (ESO), proposed for the cascade of integrator systems without measurement noise<sup>[13][14]</sup>.



In the monitoring of ECG, it is common to use modulation techniques for transmission and reception. Some techniques have been developed; for example, in<sup>[15]</sup>, a real-time algorithm for ECG-Derived Respiration is presented. In<sup>[16]</sup>, an adaptive algorithm using different modulation schemes is introduced. In<sup>[17]</sup>, a method for ECG monitoring is proposed that utilizes a transmitter-receiver system with modulation frequencies to send and receive ECG information.

Achieving a better representation of an ECG signal is another objective. For instance, in<sup>[18]</sup>, a method to obtain a better representation of blood flow signals was proposed. In<sup>[19]</sup>, a novel ECG enhancement algorithm based on sparse derivatives is introduced. In<sup>[20]</sup>, the ECG is viewed as a quasi-periodic process and employs the unbiased finite impulse response (UFIR) smoother on optimal horizons, applied to a harmonic ECG model with good results. In<sup>[21]</sup>, a new tracking differentiator is proposed, which can synchronously filter noise and estimate the derivative of the input signal. The proposed method, based on the analysis of the rate of changes in some biomedical signals such as ECG and blood pressure, involves the development of a model using a passband signal and its derivatives. By approximating the signal and its derivatives with Taylor polynomials, it is possible to develop a state transition to implement in the Kalman filter. Since the proposed method uses Taylor polynomials, the methodology is compared with a Digital Differentiator based on Taylor Series (DDTS)<sup>[21]</sup>.

The aim of this work is to present a method to estimate the derivative signal of an ECG. With the derivative, it is possible to detect high frequencies in the ECG, which are common in coronary heart disease and useful for electrocardiographic diagnosis. In<sup>[22]</sup>, the derivative of an ECG is obtained using an electronic circuit and operational amplifier. However, in this document, the derivative is obtained mathematically, and the algorithm can be implemented in any microcontroller, DSP, FPGA, or PC. Additionally, the numerical results can be obtained in real time, and the method only needs one sample to achieve the estimate of both the signal and its derivative.

## MATERIALS AND METHODS

Commonly, biological systems produce quasi-periodical signals. These signals are almost periodical signals, but with fluctuations between periods. Next, the model shown in<sup>[12][23]</sup> for a quasiperiodic signal oscillation is presented.

We start using a periodical signal  $s_p(t)$ , a fundamental approach involves to represent a periodic signal by its Fourier representation in Equation 1:

$$s_p(t) = \sum_{h=-H}^H c_h e^{jh\omega_1 t}, \quad (1)$$

where  $\omega_1$  represents the fundamental frequency in radians per second,  $H$  is the number of harmonics considered, and  $c_h$  represents the Fourier coefficient related to the  $h$ -th harmonic.

If (1) is relaxed to allow slow variations (compared with  $\omega_1$ ) in  $c_h$  in both amplitude and phase, then the expression

$$c_h(t) = a_h(t) e^{j\phi_h(t)}, \quad (2)$$

can be used to model the fluctuation through the behavior of each coefficient, where  $a_h(t)$  and  $\varphi_h(t)$  now represent the amplitude and phase variation for each harmonic. Under the assumption (Equation 2), the quasi-periodic version of  $s_p(t)$  is given by

$$s(t) = \sum_{h=-H}^H c_h(t) e^{jh\omega_1 t}, \quad (3)$$

where for a real-valued signal (Equation 3), the components should meet  $\overline{c_h(t)} = c_{-h}(t)$  for  $h \neq 0$ , with  $\overline{c_h(t)}$  representing the complex conjugate of  $c_h(t)$ . This relaxed model offers more flexibility as it allows the description of the time-varying dynamic evolution of each harmonic. The Taylor series at  $t_0$  can be used to represent each passband signal (Equation 4) by:

$$c_h(t) = \sum_{k=0}^K c_h^{(k)}(t_0) \frac{(t-t_0)^k}{k!} \varepsilon_h^{(k+1)}(t), \quad (4)$$

with  $c_h^{(k)}(t_0) = \left. \frac{d^k c_h t_0}{dt^k} \right|_{t=t_0}$  representing the  $k$ -th derivative of the  $h$ -th harmonic at  $t = t_0$ , and  $\varepsilon_h^{(k+1)}(t)$  representing the residue due to higher-order terms.

Using (Equation 4) in (Equation 3), the following ex-pressing is obtained for the quasi-periodical signal (Equation 5):

$$s(t) = \sum_{h=-H}^H r_h(t) + E(t), \quad (5)$$

where

$$r_h(t) = \sum_{k=0}^K \frac{c_h^{(k)}(t_0)}{k!} (t-t_0)^k e^{jh\omega_1 t}, \quad (6)$$

represents the  $h$ -th rotated phasor, and  $E(t)$  represents the summation over of the residues  $E(t) = \sum_{h=-H}^H \varepsilon_h^{(k+1)}(t)$ .

The relation (Equation 6) can be used to construct a transition function for the rotated phasor from time  $t_0$  to time  $t$ . We construct it by analyzing (Equation 6) per each value of  $h$ . We separate two cases,  $h = 0$  and  $h \neq 0$ .

First, for  $h = 0$ , the DC component  $r_0 = c_0$  at instant  $t$  can be related to  $t_0$  by performing the derivation of (Equation 6)  $(K-1)$  times (Equation 7):

$$\mathbf{r}_0(t) = \mathbf{\Psi}(t-t_0) \mathbf{r}_0(t_0), \quad (7)$$

where the  $i$ -th element of the vector  $\mathbf{r}_0(t) \in \mathbb{R}^{(K+1)}$  is given by the  $i$ -th **derivative** of the DC component  $c_0^{(i)}(t)$  for  $i = 1, \dots, n$ ; and the  $i$ -th element of the  $j$ -th column of the matrix  $\mathbf{\Psi}(t-t_0) \in \mathbb{R}^{(K+1) \times (K+1)}$  is given by (Equation 8):

$$\psi_{ij}(t) = \begin{cases} 0, & i > j, \\ \frac{(t-t_0)^{(j-i)}}{(j-i)!}, & i \leq j. \end{cases} \quad (8)$$

In a similar manner, for  $h \neq 0$  the  $k$ -th harmonic component  $h$  at instant  $t$  can be related to  $t_0$  by performing the derivation of (6)  $(K-1)$  times, where now, due to the complex exponential function, we have (Equation 9):

$$\mathbf{r}_h(t) = \mathbf{M}(h\omega)\Psi(t - t_0)\mathbf{M}^{-1}(h\omega)e^{jh\omega t}\mathbf{r}_h(t_0). \quad (9)$$

In this context, the  $i$ -th element of  $\mathbf{r}_h(t) \in \mathbb{C}^{(K+1)}$ , in (9) represents the  $i$ -th derivative of  $r_h^{(i)}(t)$  and  $\mathbf{M}(h\omega) \in \mathbb{C}^{(K+1) \times (K+1)}$  is a lower triangular complex matrix with elements given by (Equation 10):

$$m_{r,c} = \begin{cases} 0, & r < c, \\ 1, & r = c, \\ \frac{(r-1)!}{(c-1)!(r-c)!} (jh\omega)^{(r-c)}, & r > c. \end{cases} \quad (10)$$

A discrete representation of (Equation 10) can be obtained sampling  $s(t)$  with a uniform sampling time  $T$ , and using  $t_0 = nT$  and  $t = (n+1)T$ , it is possible to use the relations in (Equation 9) to relate the rotated phasor from sample to sample. From (Equation 9), with  $t_0 = nT$  and  $t = (n+1)T$  we have (Equation 11):

$$\mathbf{r}_h(n+1) = \Phi_h(n+1, n)\mathbf{r}_h(n), \quad h = -H, \dots, H \quad (11)$$

where  $\Phi_h(n+1, n) = \mathbf{M}(h\theta)\Psi(T)\mathbf{M}^{-1}(h\theta)e^{jnh\theta}$  works as a transition matrix from time  $nT$  to  $(n+1)T$ , and  $\theta$  represents the discrete fundamental frequency in radians.

Using (Equation 11) to represent each component in (Equation 5), a model for the signal  $s(n)$  can be constructed as follows (Equation 12):

$$\begin{aligned} \mathbf{x}(n+1) &= \mathbf{A}\mathbf{x}(n), \\ s(n) &= \mathbf{C}\mathbf{x}(n) + \mathbf{E}(n), \end{aligned} \quad (12)$$

where  $\mathbf{x} \in \mathbb{C}^{(2H+1)(K+1)}$  represents a vector formed from the union of the  $2H+1$  vectors  $\mathbf{r}_h$ , the components are ordered as follows  $\mathbf{x} = [\mathbf{r}_0 \ \mathbf{r}_1 \ \mathbf{r}_{-1} \ \mathbf{r}_2 \ \mathbf{r}_{-2} \ \dots \ \mathbf{r}_H \ \mathbf{r}_{-H}]^T$ ; thereby following (11) the matrix  $\mathbf{A} \in \mathbb{C}^{(2H+1)(K+1) \times (2H+1)(K+1)}$  is a block diagonal matrix given by (Equation 13):

$$\mathbf{A} = \begin{bmatrix} \Phi_0 & \mathbf{0} & \mathbf{0} & \dots & \mathbf{0} & \mathbf{0} \\ \mathbf{0} & \Phi_1 & \mathbf{0} & \dots & \mathbf{0} & \mathbf{0} \\ \mathbf{0} & \mathbf{0} & \Phi_{-1} & \dots & \mathbf{0} & \mathbf{0} \\ \vdots & \vdots & \vdots & \ddots & \vdots & \vdots \\ \mathbf{0} & \mathbf{0} & \mathbf{0} & \dots & \Phi_H & \mathbf{0} \\ \mathbf{0} & \mathbf{0} & \mathbf{0} & \dots & \mathbf{0} & \Phi_{-H} \end{bmatrix}, \quad (13)$$

and  $\mathbf{C} \in \mathbb{R}^{(2H+1)(K+1)}$  represents the synthesis of the signal from its harmonic components, according to (Equation 5)  $\mathbf{C}$  is given by the union of  $(2H+1)$  blocks  $\xi \in \mathbb{R}^{K+1}$ , where  $\xi = [1 \ 0 \ \dots \ 0]$ .

Only for  $h = 0$  the corresponding elements in  $\mathbf{A}$  and  $\mathbf{x}$  are real-valued. However, a real-valued version of (Equation 12) can be obtained using  $\overline{c_h(t)} = c_{-h}(t)$  for  $h \neq 0$ . We use the following linear transformation  $\tilde{\mathbf{x}} = \mathbf{P}\mathbf{x}$  where  $\tilde{\mathbf{x}} \in \mathbb{R}^{(2H+1)(K+1)}$  (Equation 14):

$$\begin{bmatrix} r_0 \\ \text{Re}(\mathbf{r}_1) \\ j\text{Im}(\mathbf{r}_1) \\ \vdots \\ \text{Re}(\mathbf{r}_h) \\ j\text{Im}(\mathbf{r}_h) \end{bmatrix} = \begin{bmatrix} \mathbf{I} & \mathbf{0} & \mathbf{0} & \dots & \mathbf{0} & \mathbf{0} \\ \mathbf{0} & \frac{1}{2}\mathbf{I} & \frac{1}{2}\mathbf{I} & \dots & \mathbf{0} & \mathbf{0} \\ \mathbf{0} & -j\frac{1}{2}\mathbf{I} & j\frac{1}{2}\mathbf{I} & \dots & \mathbf{0} & \mathbf{0} \\ \vdots & \vdots & \vdots & \ddots & \vdots & \vdots \\ \mathbf{0} & \mathbf{0} & \mathbf{0} & \dots & \frac{1}{2}\mathbf{I} & \frac{1}{2}\mathbf{I} \\ \mathbf{0} & \mathbf{0} & \mathbf{0} & \dots & -j\frac{1}{2}\mathbf{I} & j\frac{1}{2}\mathbf{I} \end{bmatrix} \begin{bmatrix} r_0 \\ \mathbf{r}_1 \\ \mathbf{r}_{-1} \\ \vdots \\ \mathbf{r}_H \\ \mathbf{r}_{-H} \end{bmatrix}, \quad (14)$$

Using the lineal transformation (Equation 14), a real-valued representation of (Equation 12) is (Equation 15):

$$\begin{aligned} \tilde{\mathbf{x}}(n+1) &= \tilde{\mathbf{A}}\tilde{\mathbf{x}}(n), \\ s(n) &= \tilde{\mathbf{C}}\tilde{\mathbf{x}}(n) + E(n), \end{aligned} \quad (15)$$

where  $\tilde{\mathbf{A}} = \mathbf{PAP}^{-1}$  and  $\tilde{\mathbf{C}} = \mathbf{CP}^{-1}$  are real-valued matrices and  $\tilde{\mathbf{x}} = [r_0 \text{Re}(\mathbf{r}_1) j\text{Im}(\mathbf{r}_1) \dots \text{Re}(\mathbf{r}_h) j\text{Im}(\mathbf{r}_h)]$ .

### Application of the Kalman Filter and Coefficient Estimation

The standard discrete Kalman filter<sup>[24][25]</sup> can be applied to obtain the estimate of the harmonic components using the model (Equation 12). The Kalman filter implementation is shown in Algorithm 1. After the filtering process. The amplitudes and phases of each component  $c_h(t)$ , as well as its derivatives, can be derived from the estimates of  $\tilde{\mathbf{x}}$ .

#### ALGORITHM 1. Pseudocode of the Kalman Filter

- 
- 1: **procedure**
  - 2: **Initialize parameters.**
  - 3: **for** each sample  $n$
  - 4: Predict state:
 
$$\tilde{\mathbf{x}}^-(n) = \tilde{\mathbf{A}}\tilde{\mathbf{x}}^-(n-1)$$
  - 5: Predict covariance:
 
$$\mathbf{P}^-(n) = \tilde{\mathbf{A}}\mathbf{P}(n-1)\mathbf{A}'$$
  - 6: Update Kalman gain:
 
$$\mathbf{K}(n) = \mathbf{P}^-(n)\tilde{\mathbf{C}}'(\tilde{\mathbf{C}}\mathbf{P}^-(n)\tilde{\mathbf{C}}' + \sigma_e^2)^{-1}$$
  - 7: Update state.
 
$$\tilde{\mathbf{x}}(n) = \tilde{\mathbf{x}}^-(n) + \mathbf{K}(n)(s(n) - \tilde{\mathbf{C}}\tilde{\mathbf{x}}^-(n))$$
  - 8: Update covariance.
 
$$\mathbf{P}(n) = (\mathbf{I} - \mathbf{K}(n))\tilde{\mathbf{C}}\mathbf{P}^-(n)$$
  - 9: **end for**
  - 10: **end procedure**
- 

## RESULTS AND DISCUSSION

In this section, the estimates of the TKA filter are illustrated and compared with the Sgolay, NTD, ESO, and DDTS methods. The test signals are ECG, RAW (data corresponding to heart R-wave to R-wave

intervals), and blood pressure. As the first test signal, a synthetic ECG is developed with mathematical functions to obtain its derivative, using the set of derivatives of each of its functions. Hence, the estimation error in the signal and its derivative can be obtained. However, since the derivative in the measurement signals is not known, the error is only calculated with respect to the measurement signal.

### Performance Results of the TKA Filter

The performance of the algorithm is showcased in this section, utilizing a polynomial approximation of  $K = 2$  and  $H = 64$  harmonics as detailed in Equation 4. In what follow we evaluate the capacity to reconstruct the input signal after applying the analysis and synthesis stages for the proposed real-valued TKA (Taylor-Kalman Algorithm). For the TKA, the analysis stage includes the state estimation using the Kalman algorithm, and then the synthesis stage computes a reconstruction of the input signal from the filter estimates. We also evaluate the performance of the TKA as a derivative are also computed. The proposed TKA Filter was implemented on a computer with Matlab 2016b, Intel Core i5 @ 2.6 GHz, 8.00 GB RAM, and operative system Mojave for MacOS is used.

As the PhysioNet signals<sup>[26]</sup> have not information about the derivative of the measurement signal. There is a problem when the performance of the derivative estimation is evaluated. To solve this situation, a math model of ECG is used to create synthetic ECG signals with known derivatives, obtained with each function of (Equation 16). The used model was proposed in<sup>[27]</sup>, the synthetic ECG signal is defined as follows (Equation 16):

$$f_0(t) = 0, \quad 0 \leq t \leq 200 \quad (16.a)$$

$$f_1(t) = a - \frac{a}{15} \left( \frac{8}{b} \left( t - \left( 200 + \frac{b}{2} \right) \right) \right)^2, \quad 200 \leq t \leq 200 + b \quad (16.b)$$

$$f_2(t) = 0, \quad 200 + b \leq t \leq 440 \quad (16.c)$$

$$f_3(t) = \left[ \frac{140-d}{100} g + 1 \right] c \left[ \frac{-1.1*0.3(t-440)}{20} \right], \quad 440 \leq t \leq 440 + \frac{d}{7} \quad (16.d)$$

$$f_4(t) = \left[ \frac{140-d}{100} g + 1 \right] c \left[ \frac{-1.1*0.6(t-[400+1.5\frac{d}{7}])}{20} \right], \quad 440 + \frac{d}{7} \leq t \leq 440 + 3\frac{d}{7} \quad (16.e)$$

$$f_5(t) = \left[ \frac{140-d}{100} g + 1 \right] c \left[ \frac{-1.1*0.5(t-[400+5\frac{d}{7}])}{20} \right], \quad 440 + 3\frac{d}{7} \leq t \leq 440 + 6\frac{d}{7} \quad (16.f)$$

$$f_6(t) = \left[ \frac{140-d}{100} g + 1 \right] c \left[ \frac{-1.1*0.5(t+440)}{20} \right], \quad 440 + 6\frac{d}{7} \leq t \leq 440 + d \quad (16.g)$$

$$f_7(t) = 0, \quad 440 + d \leq t \leq 440 + d + 680 \quad (16.h)$$

$$f_8(t) = a - \frac{a}{15} \left( \frac{80}{f} \left( t - \left( 680 + \frac{f}{2} \right) \right) \right)^2, \quad 440 + d \leq t \leq 440 + d + f. \quad (16.i)$$

The range for each one of the variables  $a \cdots g$  used in the definition of the synthetic ECG is show in the Table 1.

TABLE 1. Parameters of the synthetic ECG signal.

| Variable | Function in synthetic ECG signal | Physiological interval |
|----------|----------------------------------|------------------------|
| a        | Amplitude of P wave              | 0-0.3 mV               |
| b        | Length of P wave                 | 0-160 ms               |
| c        | Amplitude of the QRS complex     | 0-0.5 mV               |
| d        | Length or QRS complex            | 50-120 ms              |
| e        | Amplitude of T wave              | 0-0.8 mV               |
| f        | Length of T wave                 | 0-300 ms               |
| g        | Amplitude of the QRS complex     | 0-50 mV                |

In Figure 1. The signal estimates are illustrated in top of the graph, while the derivative estimates are illustrated in bottom of the graph, the parameters used to generate the synthetic signal for this example are  $a = 0.1$ ,  $b = 160$ ,  $c = 0.096$ ,  $d = 120$ ,  $e = 0.2$ ,  $f = 300$ ,  $g = 50$ .

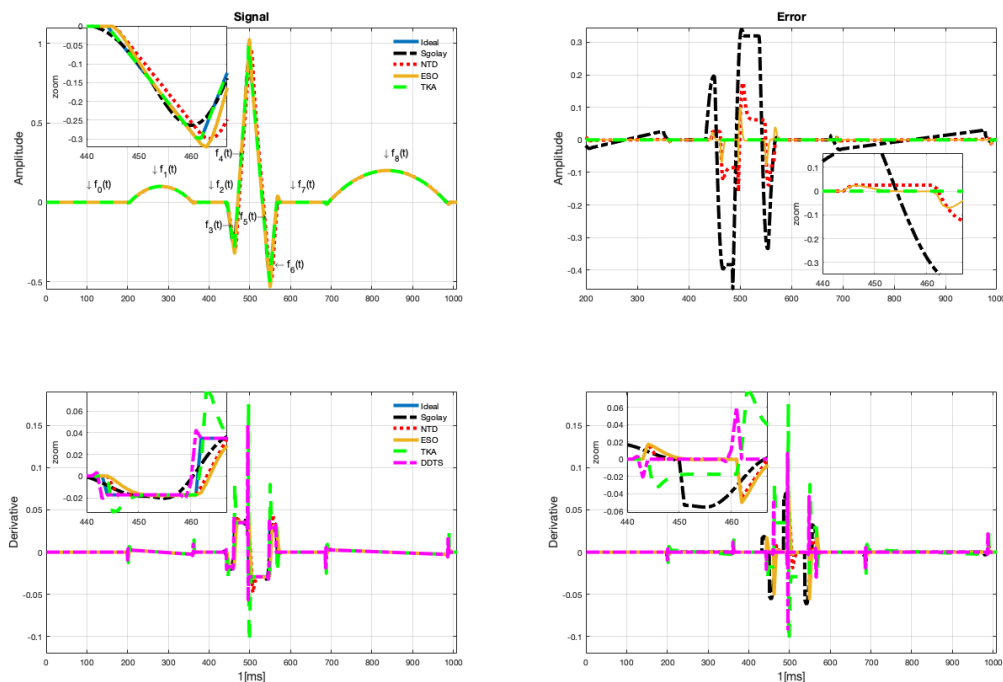
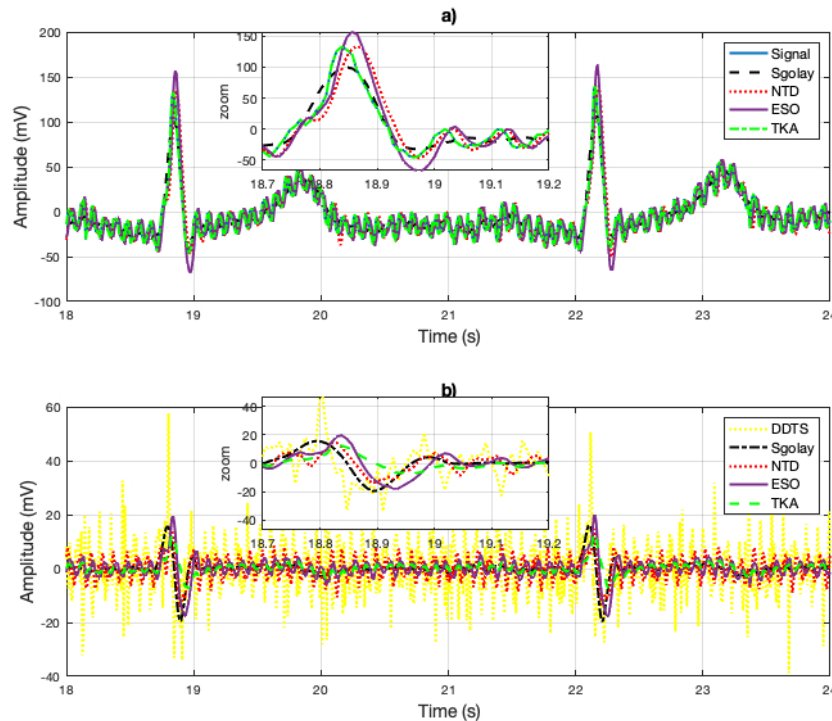


FIGURE 1. Synthetic ECG signal and derivative estimates with Sgolay, NTD, ESO, DDTS, and TKA.

The input signal, as well as the estimates from the four algorithms, are displayed in Figure 1, (the measurement is illustrated in left top graph, and the error estimate in the right top graph). Furthermore, a zoomed-in view is offered to facilitate a closer examination of the estimation details. As it can be seen, the Sgolay estimation smooths (filters out high-frequency signals), which can lead to estimation errors in some cases or segments of the signal. On the other hand, NTD estimation provides errors in sections with abrupt changes in amplitude. And the ESO estimates have a similar behavior to the NTD but with greater amplitude. It can be observed that signal estimates provided by the proposed TKA method have the best performance. In

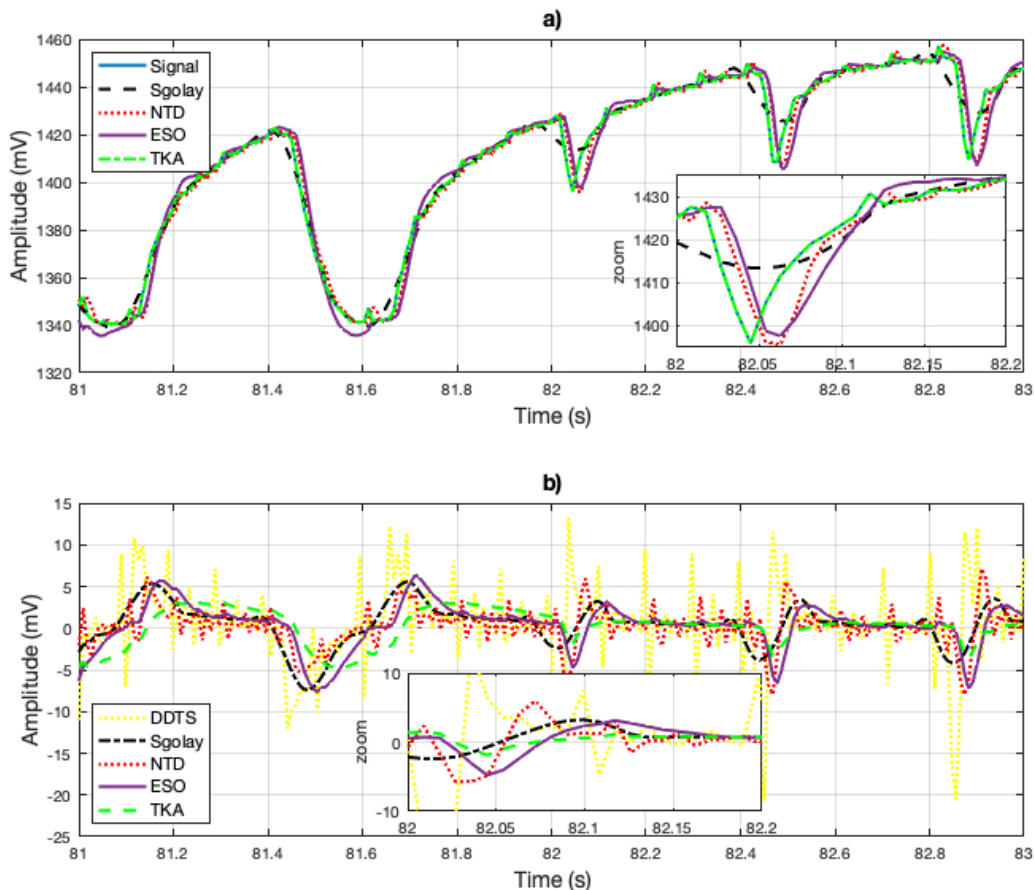
Figure 1, left of bottom graph, the estimation of the derivative of the signal is shown, which corresponds to the same zoomed-in section of the signal. Similarly, in the derivative estimation, the Sgolay method tends to smooth the signal, NTD method provides a significant number of errors when the signal exhibits rapid changes in amplitude. It is important to remark that no additional differentiator algorithms are needed to compute the estimation of the derivative when the proposed Kalman algorithm is used. Also, the error in derivative estimation is shown in the bottom right graph in Figure 1. When an abrupt change in the signal occurs, the estimations have considerable errors, with better estimates obtained using the ESO and DDTS methods. However, the measurement signals are smoother than the synthetic signal.

Signal under estimation is an Electrocardiogram (ECG) signal sourced from the PhysioNet database<sup>[26]</sup>, (Signals recorded in labor, between 38 and 41 weeks of gestation; four signals acquired from maternal abdomen; direct electrocardiogram recorded simultaneously from fetal head; positioning of electrodes was constant during all recordings; Ag-AgCl electrodes (3M Red Dot 2271) and abrasive material to improve skin conductance (3M Red Dot Trace Prep 2236); bandwidth: 1Hz - 150Hz (synchronous sampling of all signals); additional digital filtering for removal of power-line interference (50Hz) and baseline drift, Sampling rate: 1 kHz; resolution: 16 bits; input ranges are included in the records in EDF format). On the other hand, the results are depicted in Figure 2, where the estimation is compared with the Sgolay, NTD, ESO and TKA, The DDTS cannot estimate the signal; it can only estimate the derivative of the signal. As can be seen in the zoomed area, better estimates of the signal are obtained with TKA. The Sgolay filter smooths the changes, while NTD and ESO provide similar estimates. However, the ESO method yields larger estimates in amplitude. The derivative estimate is shown in the graph in Figure 2. Unlike the synthetic signal, DDTS provided the worst case in the estimates and is illustrated in yellow to distinguish it from the other signal estimates. The derivative estimates with TKA improve, with regard to the synthetic signal due to the smooth changes in the amplitude of the derivative.



**FIGURE 2.** a) Signal reconstruction with the Sgolay, NTD, ESO and TKA methods. And Zoomed-in view of the reconstructed (estimated) signal. In b) the derivative estimates are illustrated and zoomed-in view of the derivative estimation of the signal.

As a third example, a cardiorespiratory signal RAW (data corresponding to heart R-wave to R-wave intervals). Data correspond to heart R-wave to R-wave intervals, Oxygen consumption, and mechanical power output on a beat-to-beat basis recorded all along the graded exercise test sessions. Participants are 18 teenagers athletes ( $15.2 \pm 2$  years) from the Regional Physical and Sports Education Centre (CREPS) of French West Indies (Guadeloupe, France)<sup>[26]</sup>. The results obtained using the Sgolay, NTD, ESO and TKA methods illustrated in Figure 3.a). In figure, a zoomed-in view of the signal is shown. Similarly to Figure 2, the estimates for rapid changes in the signal are deficient with the Sgolay and NTD methods. The DDTS method produced large errors when the signal had abrupt changes. In Figure 2 b), a close-up of the derivative estimation is presented, and the results show a behavior very similar to the derivative signal estimates in the electrocardiogram.



**FIGURE 3. a) Signal reconstruction using the Sgolay, NTD, ESO and TKA methods. b) Zoomed-in view of the estimation. c) Estimation of the derivative of the estimated signal and include the derivative estimation with DDTS.**

In Table 2, the RMSE error (17) estimates in signal and derivative estimate are show, as can be seen, TKA provided the better signal reconstruction. The best derivative estimates of the synthetic signal were obtained by NTD, the estimates in TKA are degraded by the transients, however they are closer to the NTD estimates and can be obtained without an additional derivative stage. The derivative of the synthetic signal is provided by the derivative of each function ( $f_0(t), f_1(t), \dots, f_8(t)$ ). However, since the measurement signal does not provide a known derivative, the error is not calculated. To obtain the derivative of the measurement signal, it would need to be processed by another method. Hence, in Table 2, only the error of the signal is calculated.



TABLE 2. RMSE in signal and derivative estimates.

| Signal    |            | RMSE                    |         |         |                |                          |
|-----------|------------|-------------------------|---------|---------|----------------|--------------------------|
|           |            | METHOD                  |         |         |                |                          |
|           |            | Sgolay                  | NTD     | ESO     | DDTS           | TKA                      |
| Synthetic | Signal     | 0.0059                  | 0.0311  | 0.0102  | Not applicable | $7.2722 \times 10^{-5}$  |
|           | Derivative | 0.1821                  | 0.006   | 0.0059  | 0.0061         | 0.0089                   |
| ECG       | Signal     | 12.0219                 | 12.9263 | 13.7664 | Not applicable | $7.7915 \times 10^{-5}$  |
| RAW       | Signal     | 4.4964                  | 5.6750  | 7.4522  | Not applicable | $1.1348 \times 10^{-5}$  |
| Blood     | Signal     | $1.5211 \times 10^{-4}$ | 0.2916  | 0.0577  | Not applicable | $4.1782 \times 10^{-15}$ |
| RAW 2     | Signal     | 0.0475                  | 0.0525  | 0.0656  | Not applicable | $1.4625 \times 10^{-15}$ |

As a reference for the accuracy of the estimations, the root mean square error (RMSE) is calculated, which is defined as (Equation 17):

$$\text{RMSE} = \sqrt{\frac{\sum (s(n) - \hat{s}(t))^2}{N}} \quad (17)$$

where  $s(n)$  represents the input signal and the signal estimation is defined as  $\hat{s}(t)$  and  $N$  is the ample size.

## CONCLUSIONS

The objective of this work is to verify the efficiency of TKA for the estimation of biomedical signals; three types of biomedical signals (ECG, synthetic ECG, cardiorespiratory and blood pressure) were analyzed. The capacity for signal reconstruction and derivative estimation were compared with the Sgolay, NTD, ESO and DDTS methods. Also, the estimation of the input signal is not obtained by the DDTS method, because it can only estimate the derivative of the signal. The results obtained for signal estimation show an advantage over the Sgolay, NTD and ESO methods, as well as a superiority in the estimation of its first derivative compared to the ESO method. On the other hand, note that the estimation is with respect to the synthetic derivative of the ECG signal, which has large discontinuities. Hence, in measurement signals that are smoother, it could be expected that the estimates in the derivative would have more precision. Looking ahead, to enhance the generalizability of our findings, we plan to extend our testing to include a wider array of real physiological signals like EMG and EEG.

## ACKNOWLEDGEMENT

All the authors acknowledge the research grant CF-2023-I-1110 from CONAHCYT (Mexico) and the support from the “Departamento de Electrónica y Automatización” at the Facultad de Ingeniería Mecánica y Eléctrica, UANL.

All the authors acknowledge to PhysioNet,<sup>[15]</sup> a public collection of biomedical signals.

## AUTHOR CONTRIBUTIONS

J. R. M. data curation, investigation, methodology, project administration, software, visualization, and writing original draft; E. Z. S. conceptualization, formal analysis, funding acquisition, and resources; M. A. P. G. supervision, validation, and writing review and editing.

## REFERENCES

- [1] W. Bouaziz, E. Schmitt, G. Kaltenbach, B. Geny and T. Vogel, “Health benefits of cycle ergometer training for older adults over 70: a review,” *Eur. Rev. Aging. Phys. Act.*, vol. 12, Nov. 2015, Art. no. 8, doi: <https://doi.org/10.1186/s11556-015-0152-9>
- [2] R. M. Rangayyan, *Biomedical Signal Analysis*, 2nd ed. Wiley-IEEE Press, 2015.
- [3] K. Najarian and R. Splinter, *Biomedical Signal and Image Processing*, 2nd ed. Boca Raton, FL, United State: CRC Press, 2012, doi: <https://doi.org/10.1201/b11978>
- [4] R. M Rangayyan, *Biomedical Signal Analysis: A Case-Study Approach*, Wiley-IEEE Press, 2002.
- [5] T. U. Zaman, D. Hossain, T. Arefin, A. Rahman, S. N. Islam, F. Haque, “Comparative analysis of de-noising on ECG signal,” *Int. J. Emerging Technol. Adv. Eng.*, vol. 2, no. 11, pp. 479-486, 2012.
- [6] N. Pombo, B. M. C. Silva, A. M. Pinho, and N. Garcia, “Classifier Precision Analysis for Sleep Apnea Detection Using ECG Signals,” *IEEE Access*, vol. 8, pp. 200477-200485, 2020, doi: <https://doi.org/10.1109/ACCESS.2020.3036024>
- [7] L. R. Castro and S. M. Castro, “Wavelets y sus aplicaciones,” in *I Congreso Argentino de Ciencias de la Computación*, Argentina, Oct. 1995. [Online]. Available: <http://sedici.unlp.edu.ar/handle/10915/24289>
- [8] G. Saripalli, P. H. Prajapati, and A. D. Darji, “CSD Optimized DWT Filter for ECG Denoising,” in *2020 24th International Symposium on VLSI Design and Test (VDATE)*, Bhubaneswar, India, 2020, pp. 1-6, doi: <https://doi.org/10.1109/VDATE50263.2020.9190624>
- [9] J. Feng, G. Li, W. Wang, and X. Liang, “The Application of Improved Tracking-differentiator Filter in ECG Data,” *DEStech*, Apr. 2018, doi: <https://doi.org/10.12783/dtcse/mso2018/20519>
- [10] Y. Tang, Y. Wu, M. Wu, X. Hu, and L. Shen, “Nonlinear Tracking-Differentiator for Velocity Determination Using Carrier Phase Measurements,” *IEEE J. Sel. Top. Signal Process.*, vol. 3, no. 4, pp. 716-725, Aug. 2009, doi: <https://doi.org/10.1109/JSTSP.2009.2024591>
- [11] J. Rodríguez-Maldonado, C. Posadas-Castillo, and E. Zambrano-Serrano, “Alternative Method to Estimate the Fourier Expansions and Its Rate of Change,” *Mathematics*, vol. 10, no. 20, Jan. 2022, Art. no. 20, doi: <https://doi.org/10.3390/math10203832>
- [12] J. Rodriguez Maldonado, “Total Harmonic Distortion Estimation, Minimization Inter Harmonic Amplitude and Expanding Bands Rejection in TKF filters,” *IEEE Lat. Am. Trans.*, vol. 14, no. 2, pp. 652-656, Feb. 2016, doi: <https://doi.org/10.1109/TLA.2016.7437206>
- [13] J. Han, “A Class of Extended State Observers for Uncertain Systems,” *Control Dec.*, vol. 10, no. 1, pp. 85-88, 1995.
- [14] B.-Z. Guo, Z.-L. Zhao, “Extended state observer for nonlinear systems with uncertainty,” *IFAC Proc. Vol.*, vol. 44, no. 1, pp. 1855-1860, 2011, doi: <https://doi.org/10.3182/20110828-6-IT-1002.00399>
- [15] J. L. Vargas-Luna, W. Mayr, and J. A. Cortés-Ramírez, “Amplitude Modulation Approach for Real-Time Algorithms of ECG-Derived Respiration,” *Rev. Mex. Ing. Biomed.*, vol. 35, no. 1, pp. 53-69, 2014.

- [16] J. R. Cárdenas-Valdez, F. Ramírez-Arzate, Á. H. Corral-Domínguez, C. Hurtado-Sánchez, A. Calvillo-Téllez, and E. E. García-Guerrero, "Development of an Adaptive Acquisition and Transmission System for Digital Processing of ECG Signals under Variable n-QAM Schemes," *Rev. Mex. Ing. Biomed.*, vol. 44, no. 4, pp. 117-127, 2023, doi: <https://doi.org/10.17488/RMIB.44.4.8>
- [17] M. E. Cano, R. A. Jaso, M. E. Tavares, J. C. Estrada, et al., "A simple alternative for modulating and recording the PQRST complex," *Rev. Mex. Ing. Biomed.*, vol. 32, no. 2, pp. 100-108, Dec. 2011.
- [18] D. Torres Guzmán and C. S. Carbajal Fernández, "Mejora de la Señal de Flujo Sanguíneo en Implantes Coronarios Mediante la Detección de Distorsiones Eventuales," *Rev. Mex. Ing. Biomed.*, vol. 36, no. 1, pp. 33-53, 2015.
- [19] X. Ning and I. W. Selesnick, "ECG Enhancement and QRS Detection Based on Sparse Derivatives," *Biomed. Signal Process. Control*, vol. 8, no. 6, pp. 713-723, Nov. 2013, doi: <https://doi.org/10.1016/j.bspc.2013.06.005>
- [20] C. Lastre-Domínguez, O. Ibarra-Manzano, J. A. Andrade-Lucio, and Y. S. Shmaliy, "Denoising ECG Signals Using Unbiased FIR Smoother and Harmonic State-Space Model," 2020 28th European Signal Processing Conference (EUSIPCO), Amsterdam, Netherlands, 2021, pp. 1279-1283, doi: <https://doi.org/10.23919/Eusipco47968.2020.9287522>
- [21] I.R. Khan, R. Ohba, "New design of full band differentiators based on taylor series," *IEE Proc. - Vis. Image Signal Process.*, vol. 146, no. 4, pp. 185-189, 1999, doi: <https://doi.org/10.1049/ip-vis:19990380>
- [22] P. H. Langner and D. B. Geselowitz, "First Derivative of the Electrocardiogram," *Circ. Res.*, vol. 10, pp. 220-226, Feb. 1962, doi: <https://doi.org/10.1161/01.res.10.2.220>
- [23] J. Rodríguez Maldonado and M. A. Platas Garza, "Comparative Load Reduction and Analysis of Taylor Kalman Fourier Filters in Synchrophasor Measurement," *IEEE Lat. Am. Trans.*, vol. 16, no. 8, pp. 2153-2160, Aug. 2018, doi: <https://doi.org/10.1109/TLA.2018.8528229>
- [24] D. G. Manolakis, V. K. Ingle, and S. M. Kogon, *Statistical and Adaptive Signal Processing: Spectral Estimation, Signal Modeling, Adaptive Filtering and Array Processing*. Boston, United State: Artech House Publishers, 2005.
- [25] D. Simon, *Optimal State Estimation: Kalman, H Infinity, and Nonlinear Approaches*. Hoboken, JN, United State: John Wiley & Sons, 2006, doi: <https://doi.org/10.1002/0470045345>
- [26] C. Chabert, D. Mongin, E. Hermand, A. Collado, and O. Hue, "Cardiorespiratory measurement from graded cycloergometer exercise testing (version 1.0.0)," *PhysioNet*, doi: <https://doi.org/10.13026/2qs3-kh43>
- [27] J. Kubicek, M. Penhaker, and R. Kahankova, "Design of a synthetic ECG signal based on the Fourier series," 2014 International Conference on Advances in Computing, Communications and Informatics (ICACCI), Delhi, India, 2014, pp. 1881-1885, doi: <https://doi.org/10.1109/ICACCI.2014.6968312>

[dx.doi.org/10.17488/RMIB.45.3.2](https://dx.doi.org/10.17488/RMIB.45.3.2)

E-LOCATION ID: 1434

# UMInSe: An Unsupervised Method for Segmentation and Detection of Surgical Instruments based on K-means

## UMInSe: Método no Supervisado para la Segmentación y Detección de Instrumentos Quirúrgicos Basado en K-means

Rodrigo Eduardo Arevalo-Ancona<sup>1</sup> , Daniel Haro-Mendoza<sup>2</sup>  , Manuel Cedillo-Hernandez<sup>1</sup> , Victor J. Gonzalez-Villela<sup>2</sup> 

<sup>1</sup>Instituto Politécnico Nacional, Ciudad de México - México

<sup>2</sup>Universidad Nacional Autónoma de México, Ciudad de México - México

### ABSTRACT

Surgical instrument segmentation in images is crucial for improving precision and efficiency in surgery, but it currently relies on costly and labor-intensive manual annotations. An unsupervised approach is a promising solution to this challenge. This paper introduces a surgical instrument segmentation method using unsupervised machine learning, based on the K-means algorithm, to identify Regions of Interest (ROI) in images and create the image ground truth for neural network training. The Gamma correction adjusts image brightness and enhances the identification of areas containing surgical instruments. The K-means algorithm clusters similar pixels and detects ROIs despite changes in illumination, yielding an efficient segmentation despite variations in image illumination and obstructing objects. Therefore, the neural network generalizes the image features learning for instrument segmentation in different tasks. Experimental results using the JIGSAWS and EndoVis databases demonstrate the method's effectiveness and robustness, with a minimal error (0.0297) and high accuracy (0.9602). These results underscore the precision of surgical instrument detection and segmentation, which is crucial for automating instrument detection in surgical procedures without pre-labeled datasets. Furthermore, this technique could be applied in surgical applications such as surgeon skills assessment and robot motion planning, where precise instrument detection is indispensable.

**KEYWORDS:** JIGSAWS database, K-means, surgical instruments segmentation, unsupervised segmentation

## RESUMEN

La segmentación de instrumentos quirúrgicos en imágenes es crucial para mejorar la precisión y eficiencia en cirugía, pero actualmente depende de anotaciones manuales costosas y laboriosas. Un enfoque no supervisado es una solución prometedora para este desafío. Este artículo introduce un método de segmentación de instrumentos quirúrgicos utilizando aprendizaje automático no supervisado, basado en el algoritmo K-means, para identificar Regiones de Interés (ROI) en imágenes y crear el *ground truth* de las imágenes para el entrenamiento de redes neuronales. La corrección Gamma ajusta el brillo de la imagen y mejora la identificación de áreas que contienen instrumentos quirúrgicos. El algoritmo K-means agrupa píxeles similares y detecta las ROI a pesar de los cambios en la iluminación, logrando una segmentación eficiente a pesar de las variaciones en la iluminación de la imagen y los objetos obstructores. Por lo tanto, la red neuronal generaliza el aprendizaje de las características de la imagen para la segmentación de instrumentos en diferentes tareas. Los resultados experimentales utilizando las bases de datos JIGSAWS y EndoVis demuestran la efectividad y robustez del método, con un error mínimo (0.0297) y alta precisión (0.9602). Estos resultados subrayan la precisión en la detección y segmentación de instrumentos quirúrgicos, lo cual es crucial para automatizar la detección de instrumentos en procedimientos quirúrgicos sin conjuntos de datos pre-etiquetados. Además, esta técnica podría aplicarse en aplicaciones quirúrgicas como la evaluación de habilidades del cirujano y la planificación de movimientos de robots, donde la detección precisa de instrumentos es indispensable.

**PALABRAS CLAVE:** base de datos JIGSAWS, K-means, segmentación instrumentos quirúrgicos, segmentación no supervisada

### Corresponding author

TO: Daniel Haro-Mendoza

INSTITUTION: Universidad Nacional Autónoma de México

ADDRESS: Centro de Ingeniería Avanzada,  
Departamento de Mecatrónica, Facultad de Ingeniería,  
Universidad Nacional Autónoma de México, Coyoacán,  
04510, Ciudad de México, México

EMAIL: [danielharo@comunidad.unam.mx](mailto:danielharo@comunidad.unam.mx)

**Received:**

7 May 2024

**Accepted:**

22 August 2024

## INTRODUCTION

Minimally invasive surgery (MIS) represents a significant advancement in surgical procedures by reducing the complexity and enhancing the success rate of surgeries. These procedures improve surgeons' control over their instruments, leading to more precise operations. Additionally, MIS techniques significantly decrease patient recovery time and infection risks. The use of small incisions minimizes patient discomfort and faster healing. These advantages reduce wound exposure and its possible adverse effects, such as infections, and result in shorter hospital stays and quicker recoveries<sup>[1]</sup>.

A critical and indispensable requirement of MIS is the accurate detection and segmentation of surgical instruments. This process provides essential information about the location of the instruments, allowing for better planning of subsequent movements and reducing the chances of harming the patient. Detecting surgical instruments in images during surgery is crucial, as these procedures rely on real-time video data captured during the operation. Furthermore, the detection of surgical instruments has applications beyond the operating room. It can be used to practice surgical techniques, evaluate surgeons' skills, and perform detailed analyses for improved surgery planning. This approach enhances the precision and safety of surgical procedures and contributes to surgeons' ongoing education and training, ultimately leading to better patient outcomes.

The detection and segmentation of surgical instruments during MIS present several significant challenges. These challenges are related to different factors, including noise or image distortions caused by interference and fluctuations in illumination. Such issues produce low contrast between the surgical instruments and the surrounding tissues or background within the acquired images. These complexities highlight the necessity for advanced technological solutions to ensure accurate and reliable instrument detection.

Effective segmentation of surgical instruments is crucial for several reasons<sup>[2][3]</sup>. Firstly, it produces a precise visualization of the tools used during surgery, essential for enhancing the safety, precision, and efficiency of the procedures<sup>[4][5]</sup>. In addition, accurate visualization aids in surgical planning and execution, benefiting doctors and patients. Automating the segmentation process can simplify surgical workflows, enabling more focused surgical research and the development of advanced systems for skill evaluation and training. Automated segmentation systems play a pivotal role in improving the overall surgical process. This technique developed a sophisticated training and simulation environments where surgeons can improve their skills in a controlled, virtual setting before applying them in real-life situations. These systems enhance a surgeon's abilities, dexterity, and precision, contributing to better surgical outcomes<sup>[6][7]</sup>. Moreover, integrating computer vision systems into surgical practices and training can significantly advance the field. These technologies enable the development of new, surgery-focused innovations that improve surgical techniques and patient care. Implementing these technologies in the medical field enhances the capabilities of surgical procedures, leading to more effective treatments and better patient outcomes<sup>[8][9]</sup>.

In summary, the detection and segmentation of surgical instruments in minimally invasive surgeries are critical components that face several technical challenges. Addressing these challenges with advanced technological solutions can significantly improve surgical procedures' safety, precision, and efficiency. Automated segmentation and computer vision systems aid in real-time surgery and provide valuable tools for surgical training and skill development, paving the way for future advancements in medical technology and patient care.

This paper introduces a novel approach for the image segmentation of surgical instruments by implementing an unsupervised image segmentation algorithm. The primary objective of the proposed method is to accurately detect and segment suturing surgical instruments to determine their spatial location within an image. This method automates the generation of labels necessary for training a neural network, thereby addressing two critical challenges in the field. Firstly, the proposed approach eliminates the need for manual label generation. Instead, it utilizes the K-means algorithm to segment the image, identifying regions of interest (ROIs) where the suturing instruments are located. This automated label generation facilitates the training process for the neural network. Secondly, employing a neural network for image segmentation allows for the generalization of suturing instrument detection. This capability enables the trained model to identify and segment suturing instruments across various tasks and scenarios, not limited to a specific context. This versatility is demonstrated using different scenarios from the JIGSAW and EndoVis datasets. The proposed method offers an efficient and effective solution for the segmentation of surgical instruments in images. By automating label generation and leveraging the power of neural networks, this approach enhances the accuracy and applicability of surgical instrument detection and segmentation across diverse surgical scenarios. The main contributions of this approach are:

1. The K-means application for the detection of surgical instruments to create image labeling for the neural network training. This algorithm reduces errors by determining the similarity between pixels despite illumination changes, image distortions, noise adding, or video brightness changes.
2. The K-means algorithm, known for its efficiency, swiftly identifies patterns and segments images into homogeneous regions, providing a streamlined and effective image labeling process.
3. Automatically generated labels facilitate the neural network training process, improving the efficiency and effectiveness of the segmentation process.
4. Implementing a neural network-based segmentation approach that generalizes the detection of suturing instruments across various tasks and scenarios demonstrates versatility and robustness.
5. The proposed method is validated using different scenarios from the JIGSAW, Endoscape and EndoVis datasets, showcasing its applicability and effectiveness in multiple contexts.
6. Offering an efficient and effective solution for surgical instrument segmentation that enhances the accuracy and broad applicability of surgical instrument detection and segmentation across diverse surgical scenarios.

The rest of the paper is divided into sections: Section 2 describes a literature review of surgical instrument segmentation techniques to provide a better understanding. Section 3 describes materials and the proposed method. Section 4 presents the experimental results. Section 5 discusses the results obtained and analyzes why the proposed method outperforms other approaches. Finally, Section 6 concludes this paper.

### **Literature review**

This section describes some techniques employed for surgical instrument segmentation, providing context for this paper's proposed method. Most recent and representative works for image surgical instrument segmentation reported in the scientific literature are depicted in Table 1. This literature review provides a better understanding of the current methods for segmenting surgical instruments into different tasks, which is the basis for this work.

TABLE 1. Literature review. (Continue in the next page).

| Author                                  | Description   | Application   | Efficiency   | Database   |
|---|---|---|--|--|
| Attia, <i>et al.</i> <sup>[10]</sup>    | It utilizes recurrent neural networks and long short-term memory networks to determine relationships and learn dependencies between neighboring pixels.   | Endoscopic images   | Accuracy = 93.3 %<br>IoU = 82.7 %                    | MICCAI 2016  |
| Papp, <i>et al.</i> <sup>[11]</sup>     | In this approach, different neural networks (UNet, TerausNet-11, TerausNet-16, Linknet-34) were used to create a general method for tool segmentation. The trained models were compared with their pre-trained counterparts, and the results show that the pre-trained models have lower accuracy than the trained ones.                                    | Trained with endoscopic images and tested with suturing surgical instruments. | Accuracy = 97.3 %<br>IoU = 70.96 %<br>Dice = 79.91 % | Trained with MICCAI 2016 and tested with JIGSAW database.  |
| Rahbar, <i>et al.</i> <sup>[12]</sup>   | This approach employed an enhanced U-Net with the GridMask (EUGNet) data augmentation technique, designed to improve the performance of the proposed deep learning model.   | Endoscopic images   | Accuracy = 86.3 %<br>IoU=80.6 %<br>Dice = 89.5 %     | da Vinci Research Kit (dVRK) open-source platform.<br>Videos for testing our algorithm from open sources on the Internet, including the U.S. National Library of Medicine. The binary segmentation EndoVis 17 dataset. |
| Colleoni, <i>et al.</i> <sup>[13]</sup> | This approach combines robotic instrument simulation with artificial surgical images generated by a Cycle-GAN to train a U-Net model for surgical instrument segmentation.  | Suturing surgical instruments   | IoU = 86.3%  | UCL Dataset, MICCAI '17 Dataset. Robot Assisted Radical Prostatectomy (RARP45) Dataset.  |
| Deepika, <i>et al.</i> <sup>[14]</sup>  | A pretrained region-based convolutional neural network (R-CNN) model was used. The original classification head was replaced with a new layer consisting of 6 outputs. This modified network was subsequently fine-tuned using our annotated neurosurgical video dataset to enhance its performance for the specific task of surgical instrument detection. | Neurosurgery  | IoU = 96%<br>Precision = 96.7%                       | The dataset consists primarily of 5 instruments which are commonly used in neurosurgery such as Suction, Bipolar Forceps, Straight Needle Holder, Straight Micro Scissor and Dural Tooth Forceps.                      |
| Leifman, <i>et al.</i> <sup>[15]</sup>  | Integrate synthetic images into the training workflow with the help of a CycleGAN. Using a dataset of laparoscopic images paired with their bounding box annotations, we automatically produce pixel-perfect segmentations through the application of DeepMAC. This technique enhances instance segmentation by leveraging CenterNet.                       | Laparoscopic instruments  | Dice = 89%<br>Accuracy = 93%                         | Endoscopic Vision 2015 Instrument Segmentation and Tracking Dataset. EndoVis2019.  |



TABLE 1. Literature review. (Continue in the next page).

| Author                                | Description  | Application            | Efficiency   | Database                                   |
|---------------------------------------|--|------------------------|--|--|
| Mishra, <i>et al.</i> <sup>[16]</sup> | A transfer learning is used in the neural network to extract the background and foreground of the image for endoscopic instruments segmentation.   | Endoscopic instruments | Accuracy = 89%   | Not mentioned.                             |
| Lou, <i>et al.</i> <sup>[17]</sup>    | A Min-Max Similarity (MMS) approach utilizes a contrastive learning framework for dual-view training by employing classifiers and projectors.  | Endoscopic instruments | Dice = 93%<br>IoU = 89%  | EndoVis 17.<br>ART-NET.<br>RoboTool.       |
| Colleoni and Stoyanov <sup>[18]</sup> | Used train deep learning models cycle-GAN and MUNIT frameworks using image-to-image translation techniques.  | Endoscopic images      | IoU = 96%  | MICCAI 2015 EndoVis                        |
| Jha, <i>et al.</i> <sup>[19]</sup>    | A Dual decoder attention network (DDANet) is implemented.  | Laparoscopic surgeries | Dice = 87%<br>IoU = 81%<br>Recall = 87%<br>Precision = 93 %<br>Accuracy = 98 % | Robust Medical Instrument Segmentation     |
| Allan, <i>et al.</i> <sup>[20]</sup>  | Perform a position estimation of surgical instruments. Surgical instruments are segmented them to identify their location using silhouette detection and optical flow.   | Laparoscopic surgeries | Precision = 87 %<br>Recall = 93 %<br>F1 score = 90 %                           | Da Vinci LND dataset                       |
| Wang, <i>et al.</i> <sup>[21]</sup>   | Clustering similar pixels using the random forest algorithm. Subsequently, they perform the 3D position estimation of the surgical instruments by calculating their kinematics.  | Endoscopic images      | IoU = 82 %   | Not mentioned                              |
| Yu, <i>et al.</i> <sup>[22]</sup>     | Segment the surgical instruments using convolutional neural networks. The neural network used for the segmentation task is based on the U-Net model, which they modified to obtain a feature map that eliminates the need to crop the image, focusing on the specific area where the surgical instruments are located. | Endoscopic images      | Accuracy = 91 %<br>IoU = 86 %<br>Dice = 92 %                                   | Robotic Instrument Segmentation Challenge. |

TABLE 1. Literature review. (Continue from previous page).

| Author                                   | Description   | Application        | Efficiency   | Database   |
|--|---|--------------------|--|--|
| Xue and Gu <sup>[23]</sup>               | Implemented a surgical instrument segmentation method based on the MobileNetV2 neural network model, in which they added the Atrous Spatial Pyramid Pooling layer to focus on spatial features of the image using the Convolutional Block Attention Module CBAM to improve the efficiency of the neural model.                          | Common instruments | IoU = 86 %<br>Accuracy = 88 %                                      | No public dataset, the dataset consists in 7 common surgical instruments with a data augmentation. |
| Baby, <i>et al.</i> <sup>[24]</sup>      | MaskRCNN model for surgical instrument segmentation. In addition, they added a layer for their classification (bipolar forceps, prograsp forceps, large needle driver, vessel sealer/suction Instrument, grasping retractor/ clip applicator, monopolar curved scissors, ultrasound probe).   | Endoscopic images  | IoU = 72 %   | Robotic Instrument Segmentation Challenge.   |
| Streckert, <i>et al.</i> <sup>[25]</sup> | The images were created by placing surgical instruments on a green screen where surgical procedures replaced the background. Additionally, to increase the dataset size, they used a GAN to generate more images of surgical procedures. Subsequently, two neural models based on the SegNet network were trained for feature learning. | Endoscopic images  | Dataset Endovio:<br>IoU = 91 %<br>Synthetic dataset:<br>IoU = 89 % | Robotic Instrument Segmentation Challenge. <sup>[28]</sup>   |
| Yamada, <i>et al.</i> <sup>[26]</sup>    | Employs hierarchical clustering to automatically detect key events and changes in the surgical workflow.  | Surgeons practice  | Accuracy = 88 %  | Not mentioned  |
| Zhang, <i>et al.</i> <sup>[27]</sup>     | Employment of surgical tools with detailed textures as annotation samples and a WGAN-GP.  | Endoscopic surgery | IoU = 92 %   | Dataset 1 and 2 are recorded using the STRAS robot   |
| Qayyum, <i>et al.</i> <sup>[28]</sup>    | The region of interest is cropped to reduce processing time and the U-Net model is applied for image segmentation.  | Endoscopic         | Accuracy = 95 %<br>F1 score = 95 %                                 | MICCAI 2022  |

## MATERIALS AND METHODS

In this chapter, we outline the datasets, tools, and methodologies employed in the development and validation of our proposed algorithm for the segmentation of surgical instruments. The approach combines advanced image processing techniques, unsupervised learning algorithms, and neural network training to achieve accurate and efficient segmentation. We first describe the datasets used in the experiments, including the JIGSAWS, MICCAI 2015 EndoVis and Endoscope databases, which provide the necessary data for training and testing. Next, we detail the preprocessing steps applied to the images, including brightness adjustment and binarization, which are crucial for enhancing the visibility and differentiation of surgical instruments. Finally, we present the segmentation method, focusing on the stages of approximate detection, region of interest identification, and neural network training.

### Description of the databases used

In this section, we provide an overview of the databases utilized for developing and validating our segmentation algorithm. We discuss the JIGSAWS database and the MICCAI 2015 EndoVis database, highlighting their relevance and features.

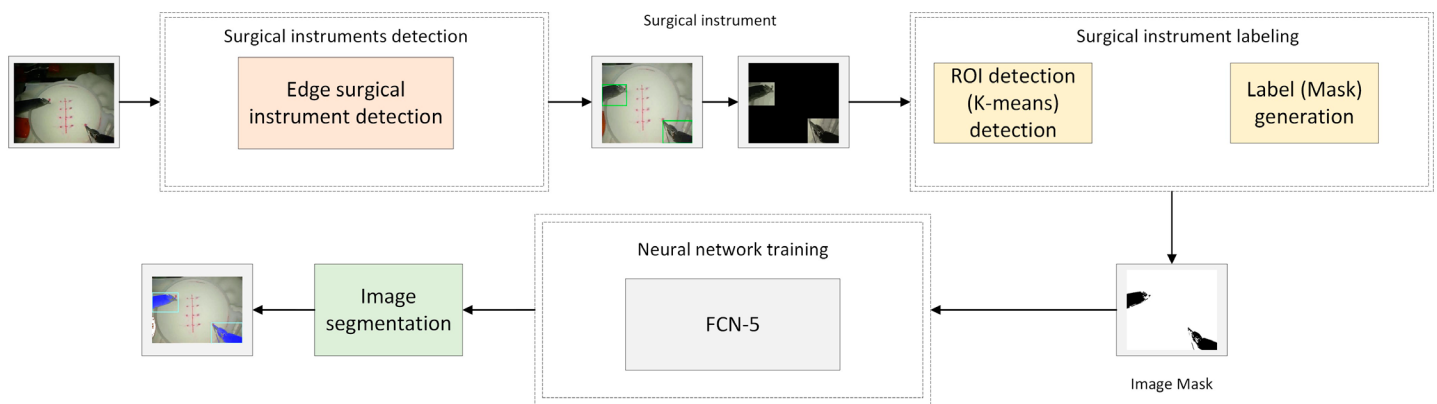
The **JIGSAWS (JHU-ISI Gesture and Skill Assessment Working Set) database**<sup>[29]</sup> evaluates surgical skills in minimally invasive surgery procedures at Johns Hopkins University. The presented algorithm training and validation used the experimental data from the freely available JIGSAWS database, which contains stereoscopic video data and kinematic data of the position and orientation of the tips of the da Vinci system forceps. Both data sets were captured by the da Vinci™ Robot API with a sampling rate of 30Hz. The test subjects included eight surgeons with different skill levels in robotic teleoperation: two expert surgeons with over 100 hours of experience, two intermediate surgeons with 10-100 hours of experience, and four novice surgeons with less than 10 hours of experience. The experiments requested from the surgeons involved performing surgical tasks such as suturing, needle passing, and knot tying. The videos are annotated with specific gestures, skill assessments, and sensor data from the da Vinci robotic system, providing detailed analysis of movements and techniques. Used to develop machine learning algorithms, this database facilitates automated skill assessment, surgical training with real-time feedback, and research to improve surgical techniques. Each video contains a total of 1794 frames, with a frame width of 640 pixels and a frame height of 480 pixels.

The **MICCAI 2015 EndoVis database**<sup>[30]</sup> is a set of high-resolution videos recorded during endoscopic surgical procedures. It was created to drive the development of advanced algorithms for detecting, segmenting, and tracking surgical instruments. Each video is annotated with precise labels, segmentation masks, and instrument motion trajectories, facilitating research in computer vision applied to surgery. This database is an essential tool for improving the precision and effectiveness of surgical procedures. This database contains 160 images with a size of 640x480.

The **Endoscape 2023 database**<sup>[31]</sup> This dataset presents laparoscopic videos designed for surgical anatomy and tool segmentation, object detection, and the assessment of the Critical View of Safety during procedures. The dataset offers a comprehensive collection of annotated videos, providing a robust foundation for research and development in surgical image analysis.

## Description of the proposed method

This section outlines our segmentation method for surgical instruments. Figure 1 illustrates the comprehensive workflow of our proposed method, offering a detailed visual representation of the segmentation process. This process employs the K-means algorithm for the masks or labels generation by clustering pixels. This precise segmentation of surgical instruments enables their subsequent detection and localization. The real potential lies in the neural network. The neural network is trained to generalize the learning of the surgical instrument's features. The trained model identifies the surgical instruments in videos related to different tasks, providing new possibilities in surgical technology, inspiring a future where surgical procedures are more accurate and efficient. This approach leverages advanced self-learning algorithms, ensuring accurate segmentation of surgical instruments for developing surgical guidance and automation systems. These advancements aim to improve surgical outcomes and patient safety by providing greater accuracy and efficiency in identifying and manipulating surgical instruments during procedures.



**FIGURE 1. Unsupervised surgical instruments segmentation general diagram.**

The proposed method for the segmentation of surgical instruments consists of three detailed stages:

1. **Approximate Detection of Surgical Instruments:** This initial stage aims to reduce computational costs by focusing on specific image areas. This task is achieved through edge detection techniques, which identify and outline the boundaries of potential surgical instruments. Concentrating computational resources on these edges effectively narrows down the regions of interest, streamlining the subsequent segmentation process.
2. **Identification of Regions of Interest for image labeling:** In this stage, the focus is on the areas identified in the previous step. The K-means clustering algorithm segments the image by grouping similar pixels. This segmentation process identifies specific areas where the surgical instruments are located. Once these regions are located, the image is binarized to create clear distinctions between the instruments and the background. This binarized image generates masks or labels essential for training the neural network.
3. **Neural Network Training:** The final stage involves training a neural network using the masks automatically generated in the previous step. These masks serve as labels, providing the neural network with accurate examples of surgical instruments. The training focuses on generalizing feature learning, enabling the neural network to detect and segment surgical instruments across various tasks and scenarios. This generalization ensures the neural network can perform robustly in different surgical environments, enhancing its applicability and reliability.

This method ensures efficient, accurate, and adaptable segmentation of surgical instruments through edge detection for initial focus, K-means clustering for precise segmentation, and neural network training for generalized detection. This comprehensive approach lays the groundwork for advanced surgical guidance systems, improving surgical outcomes and patient safety through enhanced instrument detection and segmentation capabilities.

### Approximate detection of surgical instruments

In this section, we describe the initial stage of our segmentation method for surgical instruments, focusing on reducing computational costs by narrowing down the areas of interest within the image. Figure 2 illustrates this stage, where edge detection techniques are employed to identify and outline the boundaries of potential surgical instruments. By concentrating computational resources on these edges, we streamline the segmentation process.

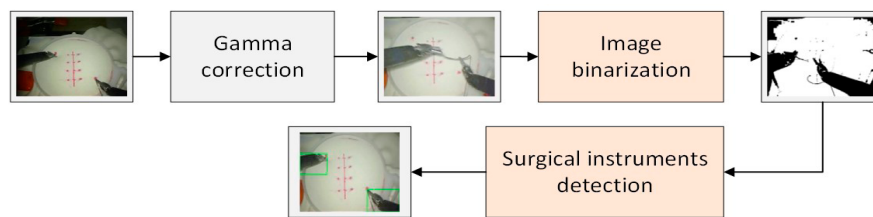


FIGURE 2. Image frame preprocessing diagram.

The image quality is modified by increasing the brightness to enhance surgical instrument detection using the Gamma correction<sup>[32][33]</sup>. This adjustment is crucial for improving the precision in identifying preliminary Regions of Interest where surgical instruments are located. By brightening the image, the contrast between the surgical instruments and the surrounding tissues is increased, making the instruments more distinguishable. This step is essential for accurately focusing the detection process on the relevant areas of the image. Figure 3 illustrates this image preprocessing step, showing the difference in clarity and instrument visibility before and after the brightness adjustment.

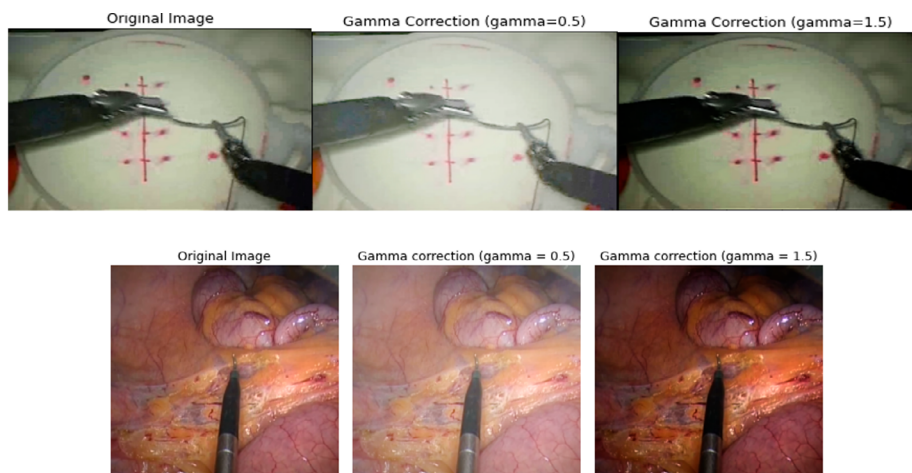
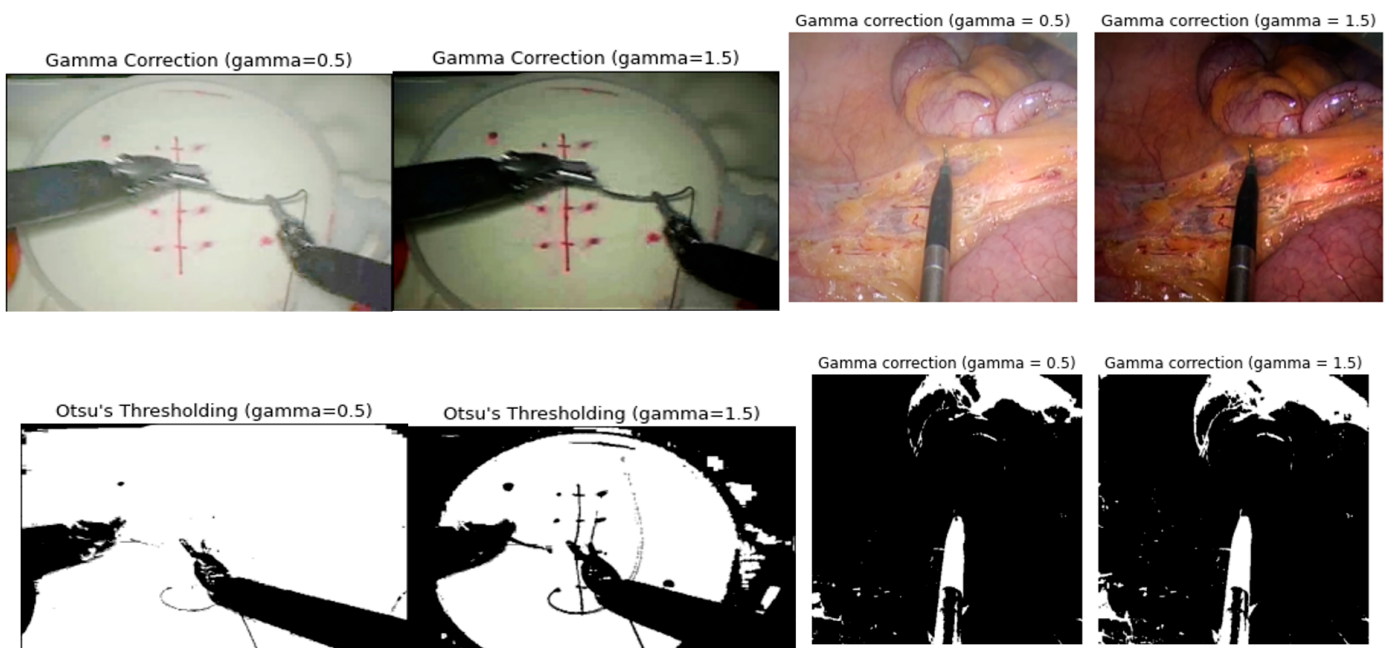


FIGURE 3. Image bright adjusts with different gamma values.

Figure 3 demonstrates the effects of with different  $\gamma$  values on image brightness. When  $\gamma$  is less than one, the image becomes brighter, enhancing the visibility of surgical instruments. Conversely, a  $\gamma$  value greater than one darkens the

image, which can be useful in different lighting conditions. This technique provides precise control over image luminosity, allowing for tailored adjustments that enhance the detection process. After gamma correction, the image is binarized to approximate the location of surgical instruments. Binarization converts the processed image into a binary format (black and white), simplifying the detection process. To automate the binarization step, the Otsu algorithm is employed<sup>[34]</sup>. This algorithm analyzes the grayscale histogram of the image to determine the optimal threshold value that maximizes the variance between the foreground (surgical instruments) and the background. By doing so, it enhances the separation of the instruments from the surrounding tissues, ensuring accurate detection. Figure 4 showcases how different  $\gamma$  values affect image brightness and the subsequent steps of binarization and thresholding, culminating in a more efficient and precise detection of surgical instruments. This method leverages the combined power of gamma correction and optimal thresholding to improve the overall effectiveness of the surgical instrument detection process.



**FIGURE 4. Image binarization with different image gamma correction.**

Figure 4 illustrates the approximate location of surgical instruments under different brightness adjustments achieved through gamma correction. A gamma value less than one has been found to significantly enhance the algorithm's performance, leading to more efficient and accurate localization of surgical instruments.

### Identification of regions of interest for image labeling

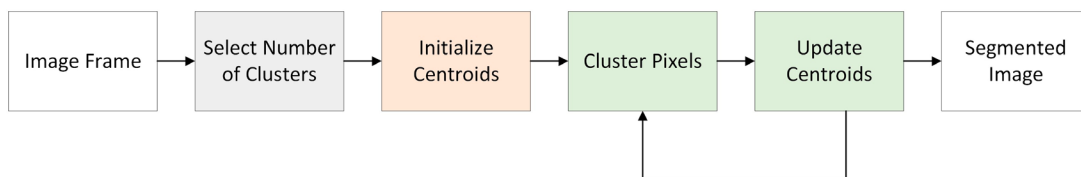
This section describes the use of unsupervised learning techniques for image segmentation, focusing on the identification of Regions of Interest (ROIs) in surgical images. It explains how the K-means algorithm is applied to cluster pixels with similar characteristics, such as color, texture, or intensity, enabling the precise detection and segmentation of surgical instruments within the images. This approach enhances segmentation accuracy, reducing errors and optimizing the generation of image labels for subsequent neural network training.

Machine learning algorithms are crucial in data analysis by constructing models that discern patterns and aid in decision-making processes<sup>[35]</sup>. These algorithms are categorized into supervised, semi-supervised, and unsupervised learning

methods. Supervised learning utilizes labeled data to identify pattern-related features, while semi-supervised learning augments training efficiency by generating new data based on existing labels. In contrast, unsupervised learning, such as data clustering techniques, identifies patterns in data without relying on predefined labels. By analyzing and clustering data based on similarities or differences, these methods unveil diverse patterns within datasets, offering insights and uncovering hidden relationships crucial for tasks like image segmentation<sup>[36]</sup>.

Unsupervised image segmentation identifies and analyzes patterns and features within image regions<sup>[37]</sup>. On the one hand, unsupervised methods do not require any label for pattern recognition, such as, autosupervised neural network models, which used the labels that are automatically generated by an algorithm like in this proposal. On the other hand, some algorithms cluster similar pixels together based on shared characteristics like color, texture, or intensity, enabling the identification of areas requiring detailed scrutiny due to their significance within the image. In surgical instrument segmentation, Regions of Interest contain information regarding the precise locations of instruments. Utilizing unsupervised learning techniques facilitates the detection of features and patterns autonomously, enhancing the accuracy of image analysis.

This paper used the K-means (Figure 5, Figure 6) algorithm to identify ROIs and segment surgical instruments effectively within images to generate image labels for the neural network training. By iteratively clustering similar pixels, K-means optimizes the detection of specific image areas, thereby reducing false positive errors in segmentation. Each pixel is assigned to a class based on its proximity to centroids, which represent characteristic points in the feature space of each class. This assignment is determined by minimizing the Euclidean distance between pixels and centroids, iteratively adjusted until convergence<sup>[38][39][40]</sup>. The utilization of K-means enhances the precision of surgical instrument detection and segmentation (Table 2), demonstrating its efficacy in improving image analysis methodologies for surgical tasks.




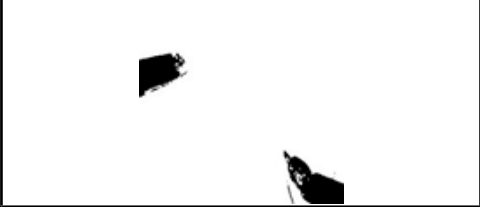

**FIGURE 5. K-means flowchart.**

Algorithm of image labeling generation:

1. Frame extraction ( $I(x,y)$ )
2. Gamma correction ( $I'(x,y)$ )
3. Aproximate surgical instrument detection
  - 3.1. Otsu thresholding
    - If  $I'(x,y) < 0$   
 $I_b(x,y) = 0$
    - Else  
 $I_b(x,y) = 255$
4. Contour detection for surgical instrument detection
5. K-means segmentation
  - Number of cluster selection
  - Pixel clustering
6. Ground truth selection

**FIGURE 6. Algorithm description for image labeling generation.**

TABLE 2. Image ground truth generation.

| Image Frame   | Generated Segmentation Mask  | Ground Truth  |
|---|--|---|
|  |  |  |

In conclusion, the precise identification of Regions of Interest through unsupervised learning techniques, such as the K-means algorithm, lays a solid foundation for effective surgical instrument segmentation. This step is crucial in generating accurate labels that are then used to train neural networks, ensuring that the system can generalize and reliably identify surgical instruments across a variety of scenarios.

### Neural network training for surgical instrument generalize segmentation

In this section, we delve into the process of training a neural network to achieve generalized segmentation of surgical instruments across various datasets. The objective is to develop a robust model that, once trained on a specific dataset like JIGSAWS, can accurately segment surgical instruments in different datasets without the need for retraining. Utilizing a Fully Convolutional Network (FCN-5) architecture, this approach leverages automatically generated training labels and optimized hyperparameters to enhance segmentation accuracy. The following text will explore the details of the training process, the effectiveness of the chosen architecture, and the overall impact on the efficiency and reliability of surgical instrument segmentation.

The neural network is used to segment surgical instruments in images. The primary goal is to achieve effective generalization, meaning that once trained on the JIGSAWS dataset, the neural network can accurately segment surgical instruments in other data sets, regardless of variations in the specific instruments present in those data sets. For this purpose, a neural network architecture based on Fully Convolutional Networks, such as the FCN-5 model is used (Figure 7).

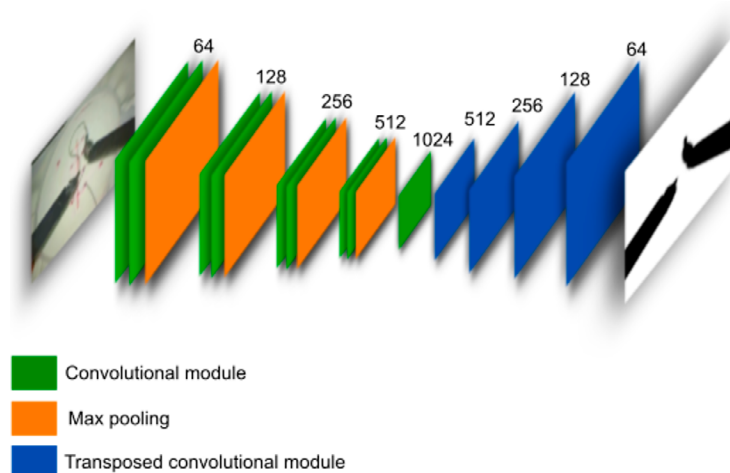


FIGURE 7. Fully Convolutional Networks (FCN-5) architecture.



TABLE 3. Training hyperparameters

| Hyperparameters |         |
|-----------------|---------|
| Optimizer       | Adam    |
| Learning Rate   | 0.00009 |
| Epochs          | 30      |

The FCN-5 architecture is used for these types of applications since this neural network learns specific image features for surgical instrument segmentation. Table 3 describes the neural network's training hyperparameters, including details such as learning rate, number of training epochs, and other specific settings that influence the network's performance and generalization ability. These hyperparameters are essential to optimizing the training process and ensuring that the network can effectively handle the diversity of surgical instrument images. The training process involves using the JIGSAWS dataset to train the neural network. The proposed method automatically generates the necessary labels for training, eliminating the need for manual labeling. This is achieved through the use of the K-means algorithm and image binarization. The loss function used in this method is the Jaccard index, also known as Intersection over Union (IoU) (Equation 1). This metric evaluates the overlap between the model prediction and the ground truth. The IoU is calculated by dividing the intersection area between the prediction and the ground truth by the area of their union. A higher IoU value indicates higher segmentation accuracy, meaning the model prediction matches the ground truth better.

$$\text{IoU} = \frac{\text{Area of Intersection}}{\text{Area of Union}} \quad (1)$$

The Intersection Area is the number of pixels that match the prediction and the ground truth. The Union Area, another important factor in the Jaccard index calculation, is the total number of pixels present in both the model prediction and the ground truth. It counts shared pixels only once, which is a key aspect in the accuracy evaluation of the segmentation.

After training, the neural network can generalize, applying the acquired knowledge to segment surgical instruments across different datasets accurately. This capability is achieved without retraining the neural network for each new dataset, showcasing the method's effectiveness and efficiency in diverse conditions.

A key contribution of this method is its ability to automatically generate labels for training the neural network. This automation reduces the time of image labeling. Additionally, the training process significantly enhances segmentation accuracy. This approach reduces the time required by eliminating the labor-intensive task of creating manual labels.

Moreover, the automated label generation process ensures that the neural network is exposed to various training examples, further improving its ability to generalize across different datasets. This robustness allows the network to effectively handle variations in surgical images, such as differences in light-

ing, instrument types, and surgical environments. The primary advantages of this method include:

1. The trained neural network can effectively segment surgical instruments in new datasets without retraining.
2. This approach reduces the need for manual intervention, accelerates the training process, and enhances accuracy, making it a time-saving boon for busy professionals in the field.
3. The approach ensures consistent and reliable results across different conditions and datasets

## RESULTS AND DISCUSSION

In this section, we present a detailed evaluation of a surgical instrument segmentation algorithm, implemented using Python and tested on diverse datasets, including JIGSAWS and EndoVis. We delve into the algorithm's performance by comparing the generated segmentation masks with manually created ground truth, utilizing key metrics such as the Jaccard index, accuracy, precision, recall, F1 score, and Mean Squared Error (MSE). The impact of varying gamma values and cluster numbers on segmentation efficiency is analyzed, and the proposed method is contrasted with existing segmentation techniques in the literature. Furthermore, we assess the performance of different neural networks for surgical instrument segmentation, balancing precision and processing time to determine the most effective approach for surgical applications.


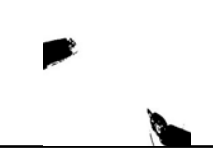
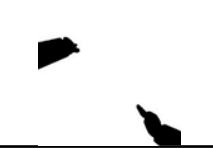
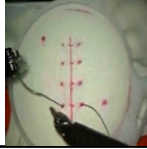

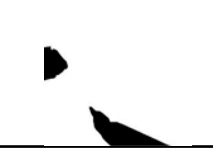


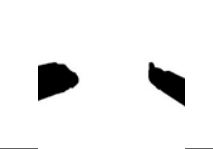
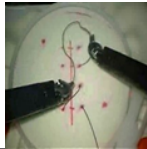
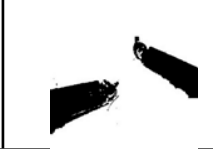
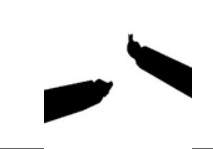

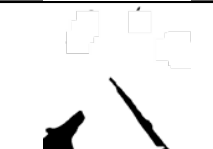
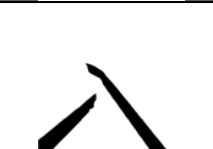
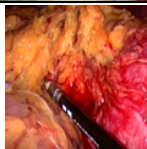
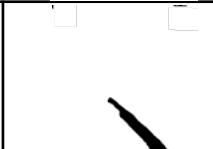
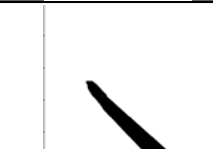



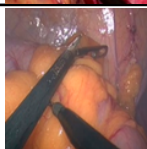


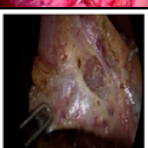





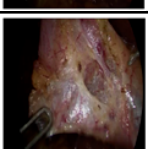


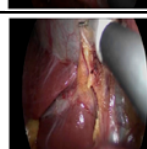


The algorithm outlined in this paper is implemented using the Python framework and executed on hardware equipped with an Intel(R) Core (TM) i7-6700 CPU @ 3.40GHz, 8 GB of RAM, and an NVIDIA GeForce GTX 960 GPU. The experiments were conducted using the Suring videos from the JIGSAWS dataset, Endoscopy 2023 dataset and the **MICCAI 2015 EndoVis database**, which contained different videos and image frames.

The proposed system was assessed by comparing the generated mask in the surgical instrument segmentation and manually generated ground truth. This process involved detecting and segmenting surgical instruments to analyze their accuracy and effectiveness in image localization. This assessment validated the system's performance for surgical instrument segmentation.

Table 4 compares the generated mask through the segmentation proposed method to the created ground truth. The mask derived from unsupervised segmentation demonstrates a high similarity to the ground truth, providing precise surgical instrument image localization through the segmentation and detection process. The applications of the proposed algorithm encompass different tasks, such as assessing surgeons' skills by estimating instrument positions, establishing parameters to alert surgeons of potential instrument-organ proximity or collision risks, exploring novel surgical techniques, predicting trajectories, and enhancing risk mitigation during surgical procedures.

In order to determine the optimal value of gamma and optimize the number of clusters for efficient segmentation, a quantitative set of metrics to evaluate the system's performance are employed. These metrics include the Jaccard index (Intersection over Union), accuracy, precision, F1 score, Mean Squared Error (MSE), and Recall.

TABLE 4. Comparison among original JIGSAWS's image frame, generated segmentation mask and ground truth.

| Image Frame   | Generated Segmentation Mask   | Ground Truth  | Image Frame  | Generated Segmentation Mask   | Ground Truth  |
|---|---|---|--|---|---|
|    |    |    |    |    |    |
|    |    |    |    |    |    |
|    |    |    |    |    |    |
|    |    |    |    |    |    |
|   |   |   |   |   |   |
|  |  |  |  |  |  |

The Jaccard index (Equation 1) is a widely used metric for evaluating the performance of image segmentation and object detection algorithms. It quantifies the overlap detected pixels between the predicted segmentation and the ground truth, with values ranging from 0 to 1. A Jaccard index of 0 indicates no overlap between the regions, while a value of 1 signifies complete overlap. Thus, a higher Jaccard index indicates a better alignment between the predicted and ground truth regions. This metric is particularly valuable in image segmentation tasks, where the primary objective is to assess the accuracy of the predicted regions relative to the actual regions.

The Accuracy is used in classification problems to evaluate the performance of a model. It is defined as the proportion of correct predictions about the total predictions made by the model (Equation 2). Accuracy measures how well a model correctly classifies instances.

$$acc = \frac{\text{Correct pixels prediction}}{\text{Total predictions}} \quad (2)$$

Precision evaluates the pixels segmentation related to the ROI and it is compared to the ground truth. The image segmentation precision can be defined as the proportion of pixels correctly classified as part of the region of interest (true positives) relative to the total pixels classified as part of that region (true positives plus false positives) Equation 3.

$$precision = \frac{Tp}{Tp + Fp} \quad (3)$$

where true positives (TP) are the pixels correctly classified and false positives (FP) are pixels incorrectly classified. Recall measures the correct pixels of the class of interest concerning the total pixels of that class (Equation 4).

$$recall = \frac{Tp}{Tp + Fn} \quad (4)$$

where false negatives (FN) are the relevant pixels, the model has not identified as part of the region of interest. A high recall indicates that the model can effectively identify the most relevant pixels. The F1 Score evaluates the segmentation performance (Equation 5). It provides a balance between precision and recall.

$$F1 = \frac{2(Precision \times Recall)}{Precision + Recall} \quad (5)$$

The Mean Squared Error (MSE) compares the ground truth with the values obtained by segmentation and measures the errors (Equation 6).

$$MSE = \frac{1}{n} \sum (y_i - \hat{y}_i)^2 \quad (6)$$

where  $y_i$  is the ground truth pixel value and  $\hat{y}_i$  is the predicted value.

**TABLE 5. Surgical instrument segmentation efficiency applying different  $\gamma$  and clusters values.**

|                        | $\gamma = 0.5$ |        |        |        |         | $\gamma = 1.5$         |       |        |        |        |         |
|------------------------|----------------|--------|--------|--------|---------|------------------------|-------|--------|--------|--------|---------|
|                        | N = 5          | N = 15 | N = 25 | N = 50 | N = 150 |                        | N = 5 | N = 15 | N = 25 | N = 50 | N = 150 |
| <b>IoU</b>             | 0.964          | 0.965  | 0.965  | 0.910  | 0.910   | <b>IoU</b>             | 0.962 | 0.795  | 0.798  | 0.943  | 0.943   |
| <b>Acc</b>             | 0.968          | 0.970  | 0.970  | 0.915  | 0.915   | <b>Acc</b>             | 0.794 | 0.824  | 0.824  | 0.950  | 0.951   |
| <b>MSE</b>             | 0.031          | 0.002  | 0.029  | 0.084  | 0.084   | <b>MSE</b>             | 0.205 | 0.178  | 0.175  | 0.049  | 0.048   |
| <b>F1 score</b>        | 0.933          | 0.935  | 0.935  | 0.746  | 0.746   | <b>F1 score</b>        | 0.721 | 0.749  | 0.751  | 0.902  | 0.902   |
| <b>Preci-<br/>sion</b> | 0.937          | 0.939  | 0.939  | 0.909  | 0.909   | <b>Preci-<br/>sion</b> | 0.710 | 0.730  | 0.731  | 0.886  | 0.887   |
| <b>Recall</b>          | 0.935          | 0.936  | 0.936  | 0.706  | 0.706   | <b>Recall</b>          | 0.869 | 0.886  | 0.887  | 0.924  | 0.925   |

Table 5 and Figure 8 presents the system's surgical instruments segmentation performance with different gamma values, which adjust the image brightness. These experiments indicate that increasing image brightness improves the efficiency of segmentation and detection of surgical instruments. Furthermore, the image segmentation with different number of clusters is presented where the segmentation process is improved; however, this increase in efficiency comes with an increase in processing time. It is important to note that if the value of  $\gamma$  exceeds 1, the efficiency of image segmentation decreases. This effect is because a gamma value greater than one makes the image darker, making accurate identification of surgical instruments complex due to lower visibility and contrast in the resulting images.

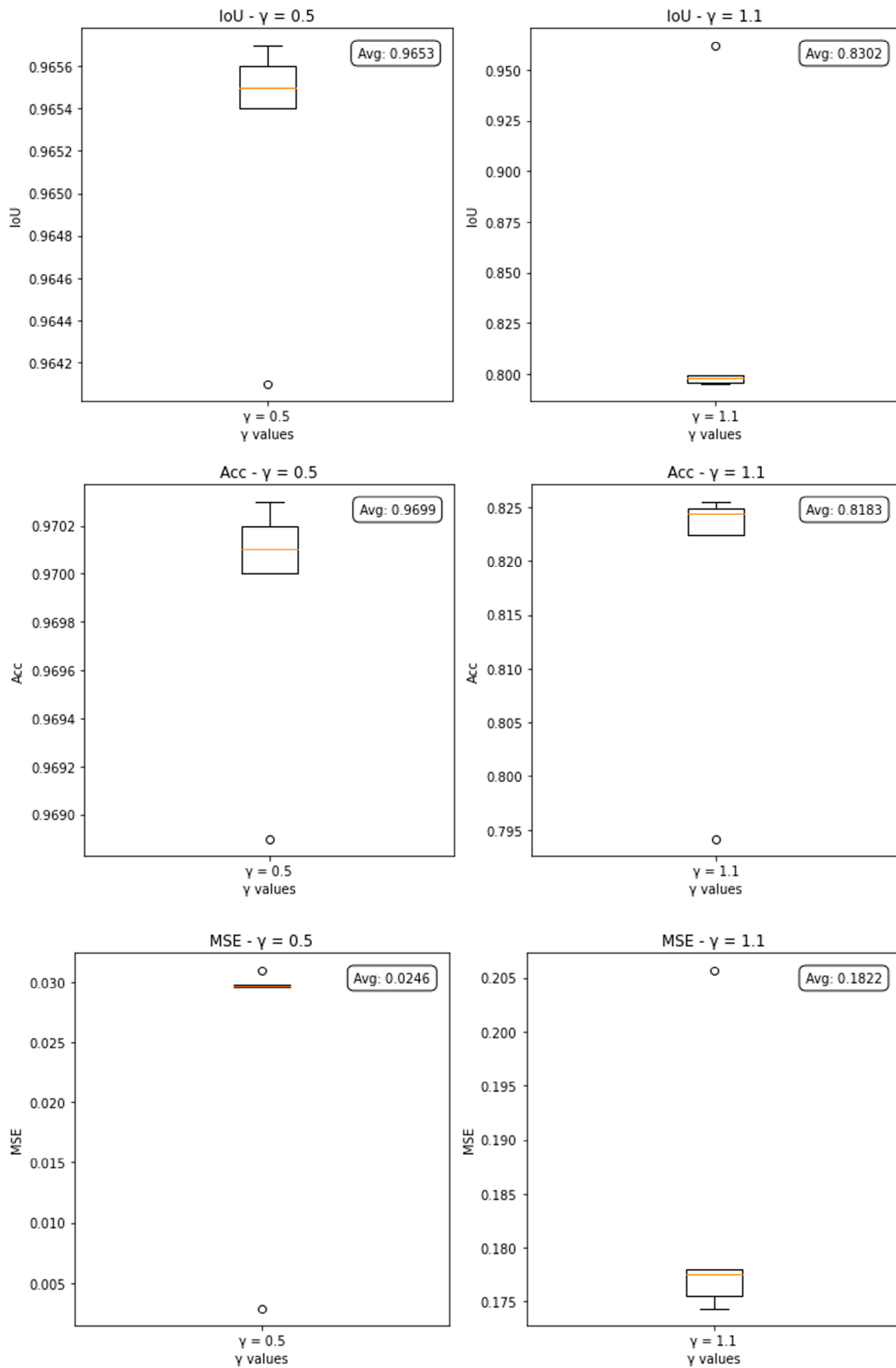


FIGURE 8. Surgical instruments segmentation efficiency. (Continue in the next page).

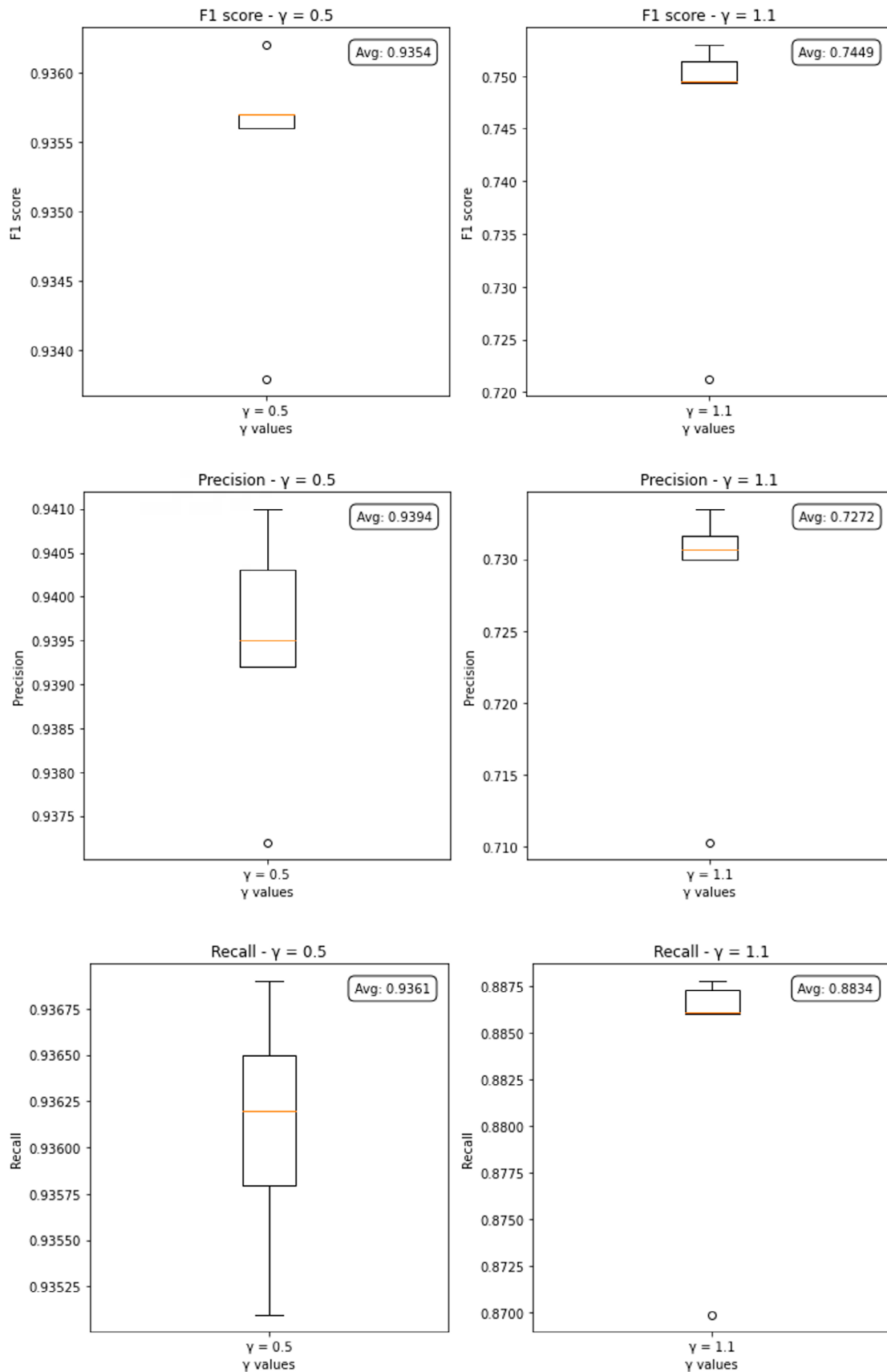


FIGURE 8. Surgical instruments segmentation efficiency. (Continue from previous page).

The results indicate that brightness is a key factor in image segmentation. A lower  $\gamma$ , more robust and accurate segmentation is achieved when a moderate number of clusters is used ( $N \leq 25$ ). Specifically, the IoU and accuracy remain high up to several clusters of  $N = 25$ , decreasing from  $N = 50$ . The decrease in efficiency is because several regions of interest are generated, generating errors when binarizing the image and leading to the segmentation of surgical instruments where the error increases and the processing time increases. On the other hand, with a higher  $\gamma$ , a different behavior is observed. The initial precision is low with a small number of clusters ( $N \leq 25$ ), but it improves significantly as the number of clusters increases, reaching optimal values from  $N = 50$  because the algorithm allows for better detection of image details by dividing it into regions of interest.

Figure 9 demonstrates a correlation between the processing time and the number of clusters employed. The processing time increases if the number of clusters for image segmentation increases. Hence, it is necessary to balance processing time and desired efficiency. By optimizing this balance, we can ensure the system's efficient performance, delivering accurate results without sacrificing time efficiency. Upon analyzing the results with different gamma values and the number of clusters from extracted frames, we determined that the optimal gamma value is 0.5, coupled with a cluster count of 5 for pixel clusters. This configuration effectively provides a balance between precise surgical instrument identification, processing time, and segmentation efficiency, ensuring optimal system performance.

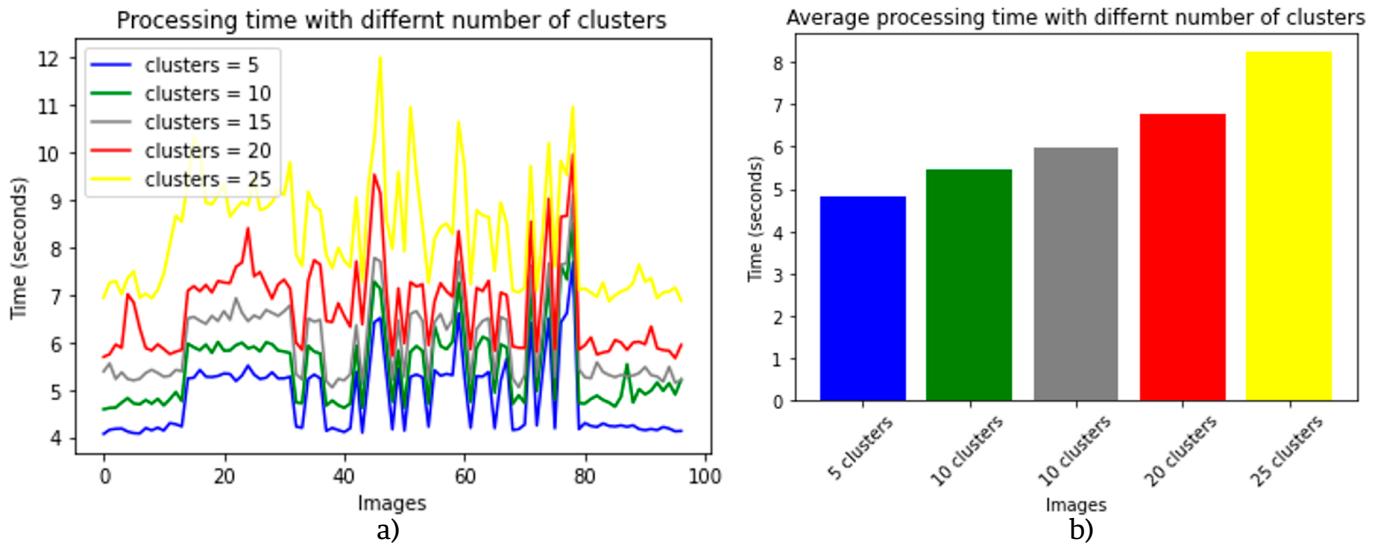


FIGURE 9. Processing time with different number of clusters.

TABLE 6. JIGSAWS instrument segmentation for tampered images.

| Dataset | Attack                               | IoU    | Attack                               | IoU    | Attack                               | IoU    |
|---------|--------------------------------------|--------|--------------------------------------|--------|--------------------------------------|--------|
| JIGSAWS | Salt and pepper noise adding 0.001   | 0.8570 | Salt and pepper noise adding 0.005   | 0.8550 | Salt and pepper noise adding 0.05    | 0.7963 |
|         | JPEG compression quality factor = 90 | 0.8528 | JPEG compression quality factor = 70 | 0.7792 | JPEG compression quality factor = 50 | 0.7524 |
|         | Median filter kernel = 3 x 3         | 0.9592 | Gaussian filter kernel = 3 x 3       | 0.9581 | Blurring kernel = 3 x 3              | 0.9593 |
|         | Median filter kernel = 7 x 7         | 0.9435 | Gaussian filter kernel = 7 x 7       | 0.9546 | Blurring kernel = 7 x 7              | 0.9498 |

TABLE 7. Endovis dataset instrument segmentation for tampered images.

| Dataset         | Attack                               | IoU    | Attack                               | IoU    | Attack                               | IoU    |
|-----------------|--------------------------------------|--------|--------------------------------------|--------|--------------------------------------|--------|
| Endovis dataset | Salt and pepper noise adding 0.001   | 0.8537 | Salt and pepper noise adding 0.005   | 0.8535 | Salt and pepper noise adding 0.05    | 0.8403 |
|                 | JPEG compression quality factor = 90 | 0.7898 | JPEG compression quality factor = 70 | 0.7772 | JPEG compression quality factor = 50 | 0.7504 |
|                 | Median filter kernel = 3 x 3         | 0.7532 | Gaussian filter kernel = 3 x 3       | 0.8062 | Blurring kernel = 3 x 3              | 0.8021 |
|                 | Median filter kernel = 7 x 7         | 0.7435 | Gaussian filter kernel = 7 x 7       | 0.8007 | Blurring kernel = 7 x 7              | 0.7954 |

TABLE 8. Endoscape dataset instrument segmentation for tampered images.

| Dataset        | Attack                               | IoU    | Attack                               | IoU    | Attack                               | IoU    |
|----------------|--------------------------------------|--------|--------------------------------------|--------|--------------------------------------|--------|
| Endoscape 2023 | Salt and pepper noise adding 0.001   | 0.8510 | Salt and pepper noise adding 0.005   | 0.8657 | Salt and pepper noise adding 0.05    | 0.8653 |
|                | JPEG compression quality factor = 90 | 0.8718 | JPEG compression quality factor = 70 | 0.8185 | JPEG compression quality factor = 50 | 0.7653 |
|                | Median filter kernel = 3 x 3         | 0.8658 | Gaussian filter kernel = 3 x 3       | 0.8399 | Blurring kernel = 3 x 3              | 0.8531 |
|                | Median filter kernel = 7 x 7         | 0.8518 | Gaussian filter kernel = 7 x 7       | 0.8309 | Blurring kernel = 7 x 7              | 0.8520 |

Tables 6-8 present the results of surgical instrument segmentation under various image processing distortions using three different datasets: JIGSAWS, Endovis, and Endoscape 2023. The segmentation's performance is evaluated using the Intersection over Union (IoU) metric, which measures the overlap between the predicted and ground-truth segmentation masks. Table 6 shows the segmentation performance on the JIGSAWS dataset under different types of image processing attacks where adding different levels of salt and pepper noise slightly decreases the IoU as the noise level increases, with the highest IoU (0.8570) at 0.001 and the lowest (0.7963) at 0.05. On the other hand, the IoU decreases when the image is distorted with JPEG compression. For instance, the IoU drops from 0.8528 at a quality factor of 90 to 0.7524 at a quality factor of 50, indicating that higher compression significantly degrades segmentation performance. Also, the application of different filters (median, Gaussian, and blurring) with different kernel sizes (3x3 and 7x7) shows that the segmentation is quite robust to these distortions, maintaining high IoU values, particularly with a 3x3 kernel size where the IoU remains above 0.9580.

Table 7 presents the results for the Endovis dataset. Like the JIGSAWS dataset, segmentation performance slightly decreases with increased noise levels. The performance against JPEG compression shows a noticeable drop in IoU with higher compression (lower quality factors), from 0.7898 with a quality factor of 90 down to 0.7504 at 50. The results against image filtering indicate that the IoU values are lower than the JIGSAWS dataset.

Finally, Table 8 shows the performance of the Endoscope 2023 dataset; the IoU slightly improves against salt and pepper noise adding, reaching the highest IoU of 0.8657. However, at the highest noise level (0.05), the IoU slightly decreases to 0.8653. Like the other datasets, the IoU decreases as the JPEG compression quality factor is reduced.



The IoU values are generally robust across different filters, with slight variations. The median filter (3x3 kernel) has the best performance at an IoU of 0.8658, while the Gaussian filter (7x7 kernel) has the lowest at an IoU of 0.8309.

Across all datasets, segmentation performance degrades as the salt and pepper noise level increases or as JPEG compression quality decreases, which is expected due to the increased image distortion. The segmentation algorithms are robust to filtering distortions, particularly with smaller kernel sizes. This suggests the model can handle slight smoothing or blurring without significantly compromising accuracy. The JIGSAWS dataset generally shows higher IoU values under distortion than Endovis and Endoscape, indicating that the segmentation model might be better suited or trained for this specific dataset.

These tables and their corresponding analysis highlight the robustness and limitations of the surgical instrument segmentation model when subjected to various common image processing distortions. Understanding these effects is critical for improving the reliability of segmentation algorithms in practical, real-world scenarios where images may undergo different types of preprocessing.

### Algorithm comparison

In this section, the proposed surgical instruments segmentation and detection approach is compared with 7 different methods presented in the literature. Which a resume of this comparison is showcase in Table 5.

Table 9 showcases the efficacy of the proposed method for surgical instrument segmentation, offering an efficient and effective solution. Unlike methods reliant on neural networks, the K-means algorithm can discern image patterns and structures autonomously, eliminating the need for pre-labeled data and making it ideal for medical environments requiring surgical instrument detection. Furthermore, the K-means algorithm demonstrates its adaptability by effectively handling changes in camera positioning and environmental illumination, thereby reducing segmentation errors. This robustness sets it apart from other methods that may require more complex supervised information or parameter adjustments, making it a practical and reliable system. The effectiveness of our proposed method is underscored by its comparison with existing research, affirming that the unsupervised approach based on K-means not only simplifies segmentation but also delivers superior efficiency and accuracy in identifying surgical instruments within medical images.

The Table 9 compares different surgical instrument segmentation methods assessed using metrics such as IoU, precision, recall, and F1 Score. Although comparisons have been made with existing methods, it is crucial to highlight that the proposed method outperforms other approaches, especially regarding clinical applicability and computational efficiency.

Unlike complex methods such as supervised deep neural networks, the proposed method uses an auto-supervised segmentation techniques such as K-means and Otsu image binarization for image ground truth generation and a neural network for the generalization of the image segmentation. It is significantly less intensive regarding the requirements for human time to create each image's ground truth. This stage demonstrates a high accuracy for image ground truth creation. Subsequently, it generates efficient neural network training to generalize characteristics and reduce processing time to segment surgical instruments in different scenarios, as in the case of the three datasets. This characteristic makes it a viable option for applications or in resource-constrained environments.

TABLE 9. Literature algorithms comparison with the proposed segmentation and detection approach.

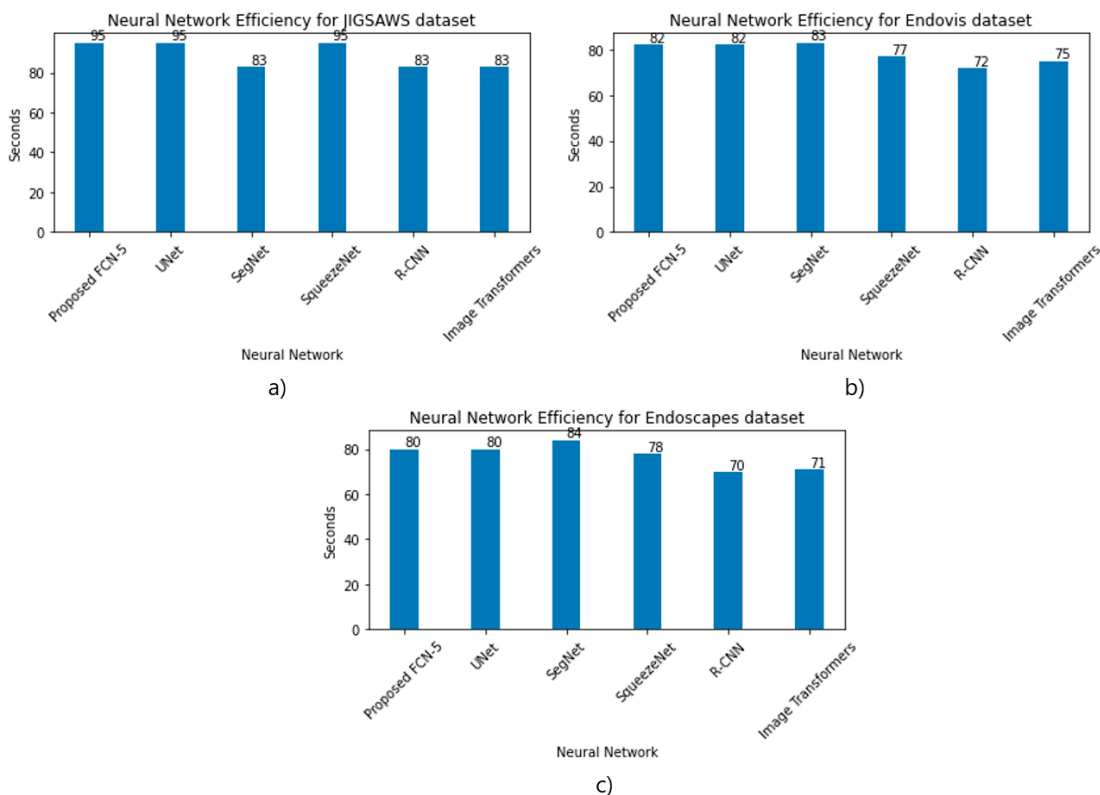
| Method                                   | Technique   | Metric   | Dataset   |
|--|---|--|---|
| Allan, <i>et al.</i> <sup>[20]</sup>     | Optical flow  | Precision = 0.874<br>Recall = 0.93<br>F1 Score = 0.898   | Ex vivo study from da Vinci Research Kit robotic system <sup>[10]</sup> .   |
| Yu, <i>et al.</i> <sup>[22]</sup>        | Neural network: Hollistic Unet  | Accuracy = 0.9156<br>IoU = 0.8645<br>Dice = 0.9220   | Robotic Instrument Segmentation Challenge <sup>[28]</sup> .   |
| Jha, <i>et al.</i> <sup>[19]</sup>       | Neural network: DDANet  | Recall = 0.8703<br>Precision = 0.9348<br>F2 score = 0.8613<br>Accuracy = 0.9897<br>Dice = 0.8739<br>IoU = 0.8739 | Robotic Instrument Segmentation Challenge <sup>[28]</sup> .   |
| Xue, <i>et al.</i> <sup>[23]</sup>       | Atrous Spatial Pyramid Pooling layer and Convolutional Block Attention Module CBAM  | IoU = 0.861<br>Accuracy = 0.885  | No public dataset, the dataset consists in 7 common surgical instruments with a data augmentation.  |
| Wang, <i>et al.</i> <sup>[21]</sup>      | Random forest   | IoU = 0.9481   | Not mention.  |
| Baby, <i>et al.</i> <sup>[24]</sup>      | MaskRCNN  | IoU = 72.54  | Robotic Instrument Segmentation Challenge <sup>[28]</sup> .   |
| Streckert, <i>et al.</i> <sup>[25]</sup> | GAN, SegNet   | Dataset Endovio:<br>IoU = 91.21<br>Synthetic dataset:<br>IoU = 89.55   | Robotic Instrument Segmentation Challenge <sup>[28]</sup> .   |
| Proposed Method                          | Unsupervised segmentation: Machine learning K-means and Otsu image binarization for ground truth creation and FCN model for the generalization of the instrument segmentation | IoU = 0.9641<br>Acc = 0.9689<br>Precision = 0.9372<br>Recall = 0.358<br>F1 Score = 0.9338<br>MSE = .0310         | Trained with and tested with JHU-ISI Gesture and Skill Assessment Working Set (JIGSAWS), in addition it is tested with Endovis and Endoscape datasets <sup>[29]</sup> |

In clinical applicability, the proposed method offers a high accuracy of 0.9372 and an IoU of 0.9641, placing it above several methods using advanced neural networks or optical flow techniques. For example, Allan *et al.* report an F1 Score of 0.898 using optical flow in an ex vivo study, while our method achieves an F1 Score of 0.9338 in the primary dataset on the JIGSAWS dataset, which includes surgical tasks in more diverse and challenging environments.

On the other hand, while methods such as the one proposed by Yu *et al.*, with a holistic Unet network, present good precision (0.9220) and an acceptable IoU (0.8645), the proposed method achieves a better balance between precision and recall. Although the proposed method's recall could be higher, this approach could be improved with additional adjustments or combinations with other techniques, but it already demonstrates superiority in terms of overall accuracy. Another aspect to highlight is the proposed method's simplicity compared to approaches such as GAN or SegNet, which require extensive training and the use of synthetic data sets. The proposed method uses a

more direct approach and is less prone to overfitting, maintaining robustness critical in segmenting surgical instruments in various conditions.

Despite being an auto-supervised technique, the proposed approach has a higher generalization ability on different datasets without the need for retraining. The proposed method improves performance metrics and offers clear advantages in practical applicability and computational efficiency. This makes it ideal for implementation in surgical support systems, where speed, precision, and simplicity are essential for clinical adoption.

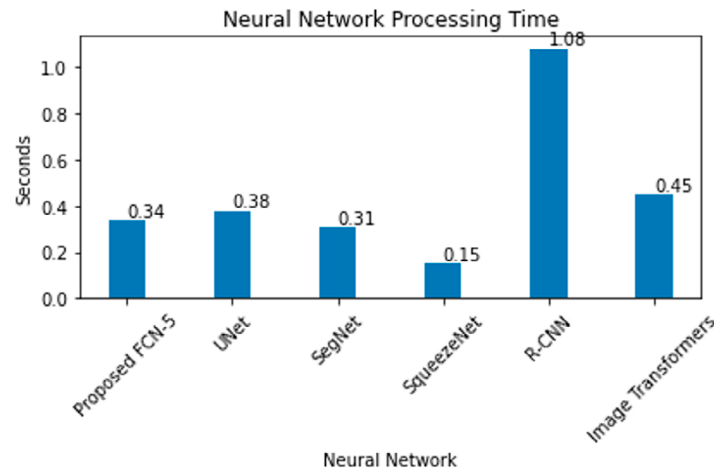


**FIGURE 10.** Neural networks efficiency for different dataset using JIGSAWS surgical instruments training.

Figure 10 illustrates the efficiency of surgical instrument segmentation using the JIGSAWS database to train different neural networks. Among the models evaluated, UNet and FCN-5 perform better in segmenting these instruments, especially in the Knot-Tying and Needle-Passing tasks. The IoU index measures high efficiency. This algorithm ensures that the surgical instrument's segmentation in the images leads to accurate segmentation without significant errors. This finding underscores the K-means algorithm's effectiveness in image labeling, which contributes to the development of precise segmentation systems. Moreover, the practical application of pre-training with the JIGSAWS database generalizes the surgical instrument segmentation with the neural network training for other tasks. This approach was applied to the EndoVis database; it achieved an 82 % efficiency in recognizing specific surgical instruments used in endoscopies. This adaptability generates an accurate segmentation in diverse contexts, showcasing the robustness of the method.

Combining the neural network with automatic label generation and pre-training with JIGSAWS has proven to be an effective strategy for accurately and efficiently segmenting surgical instruments, both in specific tasks

and broader applications like endoscopies. In addition, the results in the Figure 10 demonstrate that the proposed neural network outperforms other existing models in efficiency, including those based on Image Transformers. This superiority is observed in the segmentation capacity of surgical instruments, especially under controlled conditions. However, to maximize their applicability, the Image Transformers must be adjusted and manipulated to improve their efficiency in complex surgical scenarios. Future research should focus on optimizing these models, seeking a balance between accuracy and efficiency so that they can adapt to a wider variety of imaging conditions and clinical scenarios.



**FIGURE 11.** Neural networks efficiency for different dataset using JIGSAWS surgical instruments training.

Figure 11 shows the processing time of five different neural networks used for the segmentation of surgical instruments, where SqueezeNet has the fastest processing time with 0.15 seconds, indicating that it is the most efficient network in terms of speed, while SegNet (0.31 seconds), FCN-5 (0.34 seconds), and UNet (0.38 seconds) have moderate processing times, with SegNet being slightly faster than FCN-5 and UNet; On the other hand, RCNN has the longest processing time with 1.08 seconds, which could be a disadvantage in applications where speed is crucial, although SqueezeNet is the fastest network, since UNet and FCN-5 have a higher efficiency in terms of precision in the segmentation of surgical instruments, demonstrating that, despite not being the fastest, they offer a more precise and reliable segmentation, essential in surgical applications. Figure 11 highlights the importance of considering computational cost and accuracy when selecting a neural network for surgical instrument segmentation.

To reduce the computational time without decreasing the accuracy of the proposed system, an adaptive image resolution processing could be implemented, which begins with lower resolution analysis, increases detail only where needed, and can balance speed and accuracy, such as the Unit model. This technique can be used on the ground truth generation using some image descriptors for image region of interest detection where the surgical instrument is located. Multi-scale analysis is another approach that processes images at multiple resolutions simultaneously, allowing for quicker feature identification. Additionally, developing a hybrid model, where a lightweight model performs initial segmentation and is combined with a neural network, such as a GAN model, to refine critical regions, reducing the processing time while maintaining high accuracy.

## Discussion

Our research focuses on developing a method for image segmentation of surgical instruments using the unsupervised K-means algorithm to automatically generate the ground truth for training neural networks. The results demonstrate high precision and accuracy in the detection and segmentation of surgical instruments, with a minimum error of 0.0297 and a precision of 0.9702 when evaluating the labels generated for training the neural networks. This approach accurately identifies patterns for detecting surgical instruments despite image shape, size, and texture changes.

The adaptability of the K-means algorithm to changes in lighting and camera position is a key advantage, allowing this algorithm to be used in different surgical environments. The results automate the detection and segmentation of instruments for the generation of ground truth. The proposed method demonstrates superior accuracy, efficiency, and adaptability compared with other existing approaches. Unlike other methods, the presented algorithm in this paper reduces human-machine work to generate training ground truth for systems based on neural networks; the proposed self-supervised approach eliminates the need to create the ground truth of surgical instruments manually. This unique feature makes it ideal for medical environments requiring the detection of surgical instruments.

Table 6 highlights the effectiveness of the proposed method for the segmentation of surgical instruments, offering an efficient solution. Unlike the techniques presented in the literature, the proposed method has the advantage of automatically generating the ground truth for the training of neural networks, which allows generalizing the learning of characteristics of surgical instruments to use them in databases other than those trained to segment surgical instruments precisely. This robustness distinguishes it from other methods that may require more complex monitoring or parameter adjustments, making it a practical and reliable system.

The number of clusters used in the k-means algorithm to detect regions of interest impacts the quality of the segmentation and the processing time. As the clusters increase, more detailed segmentation is allowed as more regions of interest are generated. However, this also increases processing time exponentially due to the computational complexity of the number of clusters. This balance between segmentation quality and processing time is essential in optimizing the segmentation process.

A number of clusters between  $N = 5$  and  $N = 10$  are ideal, providing high performance (IoU and accuracy) without significantly increasing processing time. The choice of the number of clusters must consider a compromise between the quality of the segmentation and the processing time. The segmentation quality affects the neural network's training, which increases the error when applying the system in a different environment. Some aspects to consider would be the type of system where it is implemented since if it has few processing resources, the processing time would increase even more. Additionally, if the system is implemented in applications different from the evaluation or training of surgeons, environmental changes must be considered when training the neural network. The system is designed to evaluate the surgeon's ability to perform surgery since, generally, even if they are experts, surgeons adjust the environment to the patient's characteristics to increase the surgical procedure's success. Finally, while more clusters can improve segmentation accuracy, especially in images with significant brightness correction, it also significantly increases processing time.

Combining the neural network with the automatic generation of labels generated by the K-means algorithm and pre-training with JIGSAWS has proven to be an effective strategy for accurately and efficiently segmenting surgical instruments in specific tasks and broader applications, such as endoscopies. However, our method has some limitations that will be addressed in future research to improve the segmentation of surgical instruments when using the pretrained neural network. On the other hand, methods should be explored to enhance the precision of segmenting the parts related to the surgical instrument. Implementing our algorithm in current robotic surgery systems could benefit patients and surgeons, automating the detection of surgical instruments and reducing human errors, for example, by detecting and correcting possible collisions between surgical instruments by surgeons.

Based on the results presented in the previous tables, a more developed section on the limitations of the proposed method could include the following points: the proposed method demonstrates strong performance in surgical instrument segmentation under various image distortions, certain limitations should be noted regarding its applicability in different surgical scenarios and imaging conditions. The results from the JIGSAWS, Endovis, and Endoscape datasets indicate that the segmentation performance declines as the salt and pepper noise level increases. The method's performance deteriorates with lower JPEG compression quality factors, with IoU values falling as compression increases (quality factor = 50). In clinical environments where images might be compressed for storage or transmission, this could reduce segmentation accuracy. The method exhibits robustness to filtering techniques such as median, Gaussian, and blurring, the results show variability across different kernel sizes and filter types. For instance, the Endovis dataset displayed lower IoU values under filtering distortions than the JIGSAWS dataset. This inconsistency suggests that the method's robustness might vary depending on the specific characteristics of the dataset or the surgical context, such as the type of instruments or the nature of the surgery. The method performs differently across the JIGSAWS, Endovis, and Endoscape datasets, with the JIGSAWS dataset generally yielding higher IoU values. This disparity indicates that the process may be more finely tuned or optimized for specific datasets. Therefore, its generalizability may be limited across different surgical scenarios, instruments, or imaging devices. This raises concerns about the method's applicability in diverse clinical settings where different datasets with varying characteristics are encountered.

## CONCLUSIONS

This paper presents a method for surgical instrument segmentation using the unsupervised K-means algorithm to generate the ground truth necessary to train neural networks automatically. The results demonstrate high precision and accuracy, validating the effectiveness of the auto supervised approach in identifying patterns despite variations in the shape, size, and texture of the images. Combining the K-means algorithm with pretrained neural networks in JIGSAWS has proven an effective strategy, allowing accurate and efficient segmentation in various applications, including endoscopies. Unlike other methods, the algorithm presented in this paper reduces the human effort required to generate training ground truth for neural network-based systems. The proposed self-supervised approach eliminates the need for manual creation of ground truth for surgical instruments. This unique feature makes it ideal for medical environments requiring the detection of surgical instruments. Although some limitations will be addressed in future research, implementing our method in robotic surgery systems promises to improve surgical efficiency and reduce human errors by automating the detection of surgical instruments.

The proposed method shows promise in surgical instrument segmentation, especially under controlled conditions. However, its sensitivity to certain image distortions, variability across datasets, and potential challenges in complex scenarios highlight areas where further refinement and validation are urgently needed. Addressing these limitations will be crucial for enhancing the method's applicability and reliability across a wider range of surgical scenarios and imaging conditions. Training the neural network used in segmentation with images from diverse scenarios and environments, including distorted images, is essential to improve the system image generalization and surgical instrument segmentation. This approach will enhance the model's ability to generalize segmentation tasks and improve efficiency under varying conditions. We can create a more robust and versatile segmentation system by developing an adaptive algorithm capable of adjusting to different environmental factors. Furthermore, continuing the investigation with a more robust neural model is planned as a future research. Combined with the current system, this advanced model will overcome existing limitations and enhance the method's performance, ensuring accurate and reliable surgical instrument segmentation across a broader spectrum of clinical applications.

### **ACKNOWLEDGEMENT**

The authors would like to thank DGAPA for the support provided to carry out this work, through both the UNAM-DGAPA-PAPIIT IT102321 project: "Development of task planning and coordination algorithms for hybrid robots, redundant robots and mobile robots, which interact with each other within a context of an intelligent environment and a cyber-physical system", and the UNAM-DGAPA-PAPIME PE110923 project: "Development of a remote robotics laboratory to implement programming practices of planning and navigation algorithms in physical test benches". D.H-M acknowledges the financial support from CONAHCyT -Mexico through the doctoral scholarship granted ID 857876. R.E.A-A acknowledges the financial support from CONAHCyT -Mexico through the postdoctoral scholarship granted ID 744415. All authors acknowledge the IPN, UNAM and CONAHCyT for the support provided in this research.

### **ETHICAL APPROVAL**

This article does not contain any studies with human participants or animals performed by any of the authors.

### **DECLARATION OF COMPETING INTEREST**

The authors declare that they have no known competing financial interests or personal relationships that could have appeared to influence the work reported in this paper.

### **DATA AVAILABILITY**

The algorithm, the ground truth, and the resulting segmentation images of this paper are in: <https://github.com/mrg-mex/UMInSe-Unsupervised-surgical-instrument-segmentation>

### **AUTHOR CONTRIBUTIONS**

R. E. A. A. conceptualization, methodology, validation, investigation, and writing original draft; D. H. M. conceptualization, methodology, software, validation, investigation, and writing original draft; M. C. H.

methodology, formal analysis, data curation, writing review and editing, visualization, supervision, project administration and funding acquisition; V. J. G. V. methodology, formal analysis, data curation, writing review and editing, visualization, supervision, project administration and funding acquisition.

## REFERENCES

- [1] X. Wang, L. Wang, X. Zhong, C. Bai, X. Huang, R. Zhao, and M. Xia, "Pal-Net: A modified U-Net of reducing semantic gap for surgical instrument segmentation," *IET Image Process.*, vol. 15, no. 12, pp. 2959-2969, 2021, doi: <https://doi.org/10.1049/ipr2.12283>
- [2] S. Nema and L. Vachhani, "Unpaired deep adversarial learning for multi-class segmentation of instruments in robot-assisted surgical videos," *Int. J. Med. Robot.*, vol. 19, no. 4, 2023, no. art. e2514, doi: <https://doi.org/10.1002/rcs.2514>
- [3] E.-J. Lee, W. Plishker, X. Liu, S. S. Bhattacharyya, and R. Shekhar, "Weakly supervised segmentation for real-time surgical tool tracking," *Healthc. Technol. Lett.*, vol. 6, no. 6, pp. 231-236, 2019, doi: <https://doi.org/10.1049/htl.2019.0083>
- [4] N. Ahmidi, L. Tao, S. Sefati, Y. Gao, et al., "A Dataset and Benchmarks for Segmentation and Recognition of Gestures in Robotic Surgery," *IEEE Trans. Biomed. Eng.*, vol. 64, no. 9, pp. 2025-2041, 2017, doi: <https://doi.org/10.1109/TBME.2016.2647680>
- [5] F. Chadebecq, F. Vasconcelos, E. Mazomenos and D. Stoyanov, "Computer Vision in the Surgical Operating Room," *Visc. Med.*, vol. 36, no. 6, pp. 456-462, 2020, doi: <https://doi.org/10.1159/000511934>
- [6] D. Psychogyios, E. Mazomenos, F. Vasconcelos, and D. Stoyanov, "MSDESIS: Multitask Stereo Disparity Estimation and Surgical Instrument Segmentation," *IEEE Trans. Med. Imaging*, vol. 41, no. 11, pp. 3218-3230, 2022 doi: <https://doi.org/10.1109/tmi.2022.3181229>
- [7] C. González, L. Bravo-Sanchéz, and P. Arbeláez, "Surgical instrument grounding for robot-assisted interventions," *Comput. Methods Biomech. Biomed. Eng.: Imaging Vis.*, vol. 10, no. 3, pp. 299-307, 2022, doi: <https://doi.org/10.1080/21681163.2021.2002725>
- [8] W. Burton, C. Myers, M. Rutherford, and P. Rullkoetter, "Evaluation of single-stage vision models for pose estimation of surgical instruments," *Int. J. Comput. Assist. Radiol. Surg.*, vol. 18, no. 12, pp. 2125-2142, 2023, doi: <https://doi.org/10.1007/s11548-023-02890-6>
- [9] Y. Jin, Y. Yu, C. Chen, Z. Zhao, P.-A. Heng, and D. Stoyanov, "Exploring Intra- and Inter-Video Relation for Surgical Semantic Scene Segmentation," *IEEE Tran. Med. Imaging*, vol. 41, no. 11, pp. 2991-3002, 2022, doi: <https://doi.org/10.1109/TMI.2022.3177077>
- [10] M. Attia, M. Hossny, S. Nahavandi, and H. Asadi, "Surgical tool segmentation using a hybrid deep CNN-RNN auto encoder-decoder," 2017 IEEE International Conference on Systems, Man, and Cybernetics (SMC), Banff, AB, Canada, 2017, pp. 3373-3378, doi: <https://doi.org/10.1109/SMC.2017.8123151>
- [11] D. Papp, R. N. Elek, and T. Haidegger, "Surgical Tool Segmentation on the JIGSAWS Dataset for Autonomous Image-based Skill Assessment," 2022 IEEE 10th Jubilee International Conference on Computational Cybernetics and Cyber-Medical Systems (ICCC), Reykjavík, Iceland, 2022, doi: <https://doi.org/10.1109/ICCC202255925.2022.9922713>
- [12] M. Daneshgar Rahbar and S. Z. Mousavi Mojab, "Enhanced U-Net with GridMask (EUGNet): A Novel Approach for Robotic Surgical Tool Segmentation," *J. Imaging*, vol. 9, no. 12, 2023, no art. 282, doi: <https://doi.org/10.3390/jimaging9120282>
- [13] E. Colleoni, D. Psychogyios, B. Van Amsterdam, F. Vasconcelos, and D. Stoyanov, "SSIS-Seg: Simulation-Supervised Image Synthesis for Surgical Instrument Segmentation," *IEEE Trans. Med. Imaging*, vol. 41, no. 11, pp. 3074-3086, 2022, doi: <https://doi.org/10.1109/tmi.2022.3178549>
- [14] P. Deepika, K. Udupa, M. Beniwal, A. M. Uppar, V. Vikas, and M. Rao, "Automated Microsurgical Tool Segmentation and Characterization in Intra-Operative Neurosurgical Videos," 2022 44th Annual International Conference of the IEEE Engineering in Medicine & Biology Society, Glasgow, Scotland, United Kingdom, 2022, pp. 2110-2114, doi: <https://doi.org/10.1109/EMBC48229.2022.9871838>
- [15] G. Leifman, A. Aides, T. Golany, D. Freedman, and E. Rivlin, "Pixel-accurate Segmentation of Surgical Tools based on Bounding Box Annotations," 2022 26th International Conference on Pattern Recognition (ICPR), Montreal, QC, Canada, 2022, pp. 5096-5103, doi: <https://doi.org/10.1109/ICPR56361.2022.9956530>
- [16] R. Mishra, A. Thangamani, K. Palle, P. V. Prasad, B. Mallala, and T.R. V. Lakshmi, "Adversarial Transfer Learning for Surgical Instrument Segmentation in Endoscopic Images," 2023 IEEE International Conference on Paradigm Shift in Information Technologies with Innovative Applications in Global Scenario (ICPSITIAGS), Indore, India, 2023, pp. 28-34, doi: <https://doi.org/10.1109/ICPSITIAGS59213.2023.10527520>
- [17] A. Lou, K. Tawfik, X. Yao, Z. Liu, and J. Noble, "Min-Max Similarity: A Contrastive Semi-Supervised Deep Learning Network for Surgical Tools Segmentation," *IEEE Trans. Med. Imaging*, vol 42, no. 10, pp. 2023, doi: <https://doi.org/10.1109/TMI.2023.3266137>



- [18] E. Colleoni and D. Stoyanov, "Robotic Instrument Segmentation With Image-to-Image Translation," *IEEE Robot. Autom. Lett.*, vol. 6, no. 2, pp. 935-942, 2021, doi: <https://doi.org/10.1109/LRA.2021.3056354>
- [19] D. Jha, S. Ali, N. K. Tomar, M. A. Riegler, and D. Johansen, "Exploring Deep Learning Methods for Real-Time Surgical Instrument Segmentation in Laparoscopy," 2021 IEEE EMBS International Conference on Biomedical and Health Informatics (BHI), Athens, Greece, 2021, doi: <https://doi.org/10.1109/BHI50953.2021.9508610>
- [20] M. Allan, S. Ourselin, D. J. Hawkes, J. D. Kelly and D. Stoyanov, "3-D Pose Estimation of Articulated Instruments in Robotic Minimally Invasive Surgery," *IEEE Trans. Med. Imaging*, vol. 37, no. 5, pp. 1204-1213, pp. 1204-1213, 2018, doi: <https://doi.org/10.1109/tmi.2018.2794439>
- [21] L. Wang, C. Zhou, Y. Cao, R. Zhao, and K. Xu, "Vision-Based Markerless Tracking for Continuum Surgical Instruments in Robot-Assisted Minimally Invasive Surgery," *IEEE Robot. Autom. Lett.*, vol. 8, no. 11, pp. 7202-7209, 2023, doi: <https://doi.org/10.1109/LRA.2023.3315229>
- [22] L. Yu, P. Wang, X. Yu, Y. Yan, and Y. Xia, "A Holistically-Nested U-Net: Surgical Instrument Segmentation Based," *J. Digit. Imaging*, vol. 33, no. 2, pp. 341-347, 2020, doi: <https://doi.org/10.1007%2Fs10278-019-00277-1>
- [23] M. Xue and L. Gu, "Surgical instrument segmentation method based on improved MobileNetV2 network," 2021 6th International Symposium on Computer and Information Processing Technology (ISCIPIT), Changsha, China, 2021, pp. 744-747, doi: <https://doi.org/10.1109/ISCIPIT53667.2021.00157>
- [24] B. Baby, D. Thapar, M. Chasmai, T. Banerjee, et al., "From Forks to Forceps: A New Framework for Instance Segmentation of Surgical Instruments," 2023 IEEE/CVF Winter Conference on Applications of Computer Vision (WACV), Waikoloa, HI, USA, 2023, doi: <https://doi.org/10.1109/WACV56688.2023.00613>
- [25] T. Streckert, D. Fromme, M. Kaupenjohann and J. Thiem, "Using Synthetic Data to Increase the Generalization of a CNN for Surgical Instrument Segmentation," 2023 IEEE 12th International Conference on Intelligent Data Acquisition and Advanced Computing Systems: Technology and Applications (IDAACS), Dortmund, Germany, 2023, pp. 336-340, doi: <https://doi.org/10.1109/IDAACS58523.2023.10348781>
- [26] Y. Yamada, J. Colan, A. Davila, and Yasuhisa Hasegawa, "Task Segmentation Based on Transition State Clustering for Surgical Robot Assistance," 2023 8th International Conference on Control and Robotics Engineering (ICCRE), Niigata, Japan, 2023, pp. 260-264, doi: <https://doi.org/10.1109/ICCRE57112.2023.10155581>
- [27] Z. Zhang, B. Rosa, and F. Nageotte, "Surgical Tool Segmentation Using Generative Adversarial Networks With Unpaired Training Data," *IEEE Robot. Autom. Lett.*, vol 6, no. 4, pp. 6266-6273, 2021, doi: <https://doi.org/10.1109/LRA.2021.3092302>
- [28] A. Qayyum, M. Bilal, J. Qadir, M. Caputo, et al., "SegCrop: Segmentation-based Dynamic Cropping of Endoscopic Videos to Address Label Leakage in Surgical Tool Detection," 2023 IEEE 20th International Symposium on Biomedical Imaging (ISBI), Cartagena, Colombia, 2023, doi: <https://doi.org/10.1109/ISBI53787.2023.10230822>
- [29] Y. Gao, S. Vedula, C. E. Reiley, N. Ahmidi, et al., "JHU-ISI Gesture and Skill Assessment Working Set (JIGSAWS): A Surgical Activity Dataset for Human Motion Modeling," *Modeling and Monitoring of Computer Assisted Interventions (M2CAI)*, Boston, United State, 2014.
- [30] L. Maier-Hein, S. Mersmann, D. Kondermann, S. Bodenstedt, et al., "Can Masses of Non-Experts Train Highly Accurate Image Classifiers? A crowdsourcing approach to instrument segmentation in laparoscopic images," *Med. Image Comput. Comput. Assist. Interv.*, vol. 17, pp. 438-445, 2014, doi: [https://doi.org/10.1007/978-3-319-10470-6\\_55](https://doi.org/10.1007/978-3-319-10470-6_55)
- [31] A. Murali, D. Alapatt, P. Mascagni, A. Vardazaryan, et al., "The Endoscapes Dataset for Surgical Scene Segmentation, Object Detection, and Critical View of Safety Assessment: Official Splits and Benchmark," 2023, arXiv:2312.12429, doi: <https://doi.org/10.48550/arXiv.2312.12429>
- [32] M. Ju, D. Zhang, and Y. J. Guo, "Gamma-Correction-Based Visibility Restoration for Single Hazy Images," *IEEE Signal Process. Lett.*, vol. 25, no. 7, pp. 1084-1088, 2018, doi: <https://doi.org/10.1109/LSP.2018.2839580>
- [33] R. Silpasai, H. Singh, A. Kumarl and L. Balyan, "Homomorphically Rectified Tile-wise Equalized Adaptive Gamma Correction for Histopathological Color Image Enhancement," 2018 Conference on Information and Communication Technology (CICT), Jabalpur, India, 2018, doi: <https://doi.org/10.1109/INFOCOMTECH.2018.8722364>
- [34] H. Ye, S. Yan and P. Huang, "2D Otsu image segmentation based on cellular genetic algorithm," 9th International Conference on Communication Software and Networks (ICCSN), Guangzhou, China, 2017, pp. 1313-1316, doi: <https://doi.org/10.1109/ICCSN.2017.8230322>
- [35] P. Flach, *Machine Learning: The Art and Science of Algorithms that Make Sense of Data*, 1st Ed. Edinburgh, United Kingdom: Cambridge University Press, 2012.
- [36] A. C. Müller and S. Guido, *Introduction to Machine Learning with Python*, United States of America: O`Reilly, 2017.
- [37] P. Yin, R. Yuan, Y. Cheng and Q. Wu, "Deep Guidance Network for Biomedical," *IEEE Access*, vol. 8, pp. 116106-116116, 2020, doi: <https://doi.org/10.1109/ACCESS.2020.3002835>

- [38] I. El rube', "Image Color Reduction Using Progressive Histogram Quantization and K-means Clustering," 2019 International Conference on Mechatronics, Remote Sensing, Information Systems and Industrial Information Technologies (ICMRSISIT), Ghana, 2020, doi: <https://doi.org/10.1109/ICMRSISIT46373.2020.9405957>
- [39] R. E. Arevalo-Ancona and M. Cedillo-Hernandez, "Zero-Watermarking for Medical Images Based on Regions of Interest Detection using K-Means Clustering and Discrete Fourier Transform," Int. J. Adv. Comput. Sci. Appl., vol. 14, no. 6, 2023, doi: <https://dx.doi.org/10.14569/IJACSA.2023.0140662>
- [40] P. Sharma, "Advanced Image Segmentation Technique using Improved K Means Clustering Algorithm with Pixel Potential," 2020 Sixth International Conference on Parallel, Distributed and Grid Computing (PDGC), Wanknaghat, India, 2020, pp. 561-565, doi: <https://doi.org/10.1109/PDGC50313.2020.9315743>

[dx.doi.org/10.17488/RMIB.45.3.3](https://dx.doi.org/10.17488/RMIB.45.3.3)

E-LOCATION ID: 1435

# Human Mesenchymal Stem Cells Derived from Adipose Tissue and Umbilical Cord, in Combination with Acellular Human Amniotic Membranes, for Skin Healing Processes in Animal Models: a Systematic Review

## Células Troncales Mesenquimales Humanas Derivadas de Tejido Adiposo y Cordón Umbilical, Combinadas con Membranas Amnióticas Humanas Acelulares, para Procesos de Regeneración Cutánea en Modelos Animales: una Revisión Sistemática

Valentina Giraldo<sup>1</sup> , Guillermo Mayorga<sup>1</sup> , Karen Saavedra<sup>1</sup> , Diana Esquivel<sup>2</sup> , Selem Torres<sup>2</sup> , Lina Andrea Gómez<sup>1,3</sup>  

<sup>1</sup>Universidad de La Sabana, Facultad de Medicina, Chía - Colombia

<sup>2</sup>Instituto de Terapia Celular, Jalisco - México

<sup>3</sup>Universidad de La Sabana, Biomedical Research Center (CIBUS), Chía - Colombia.

### ABSTRACT

This systematic review aims to document the available research evidence regarding using mesenchymal stem cells (MSCs) and acellular amniotic membranes (AAM) as scaffolds in the murine model for tissue regeneration. This research was developed by analyzing available information on databases like Google Scholar, Pubmed, Scopus, and Web of Science, using the following key terms "Human Stem Cells", "Amniotic membrane", "Wound healing" and "Animal model". A total of 519 articles published from January 2013 to March 2024 were found, but only 8 studies were included in this review, the inclusion criteria were as follows the use of human-derived stem cells (UCMSCs and ADMSCs) seeded in decellularized hAM, in murine models with induced wounds (incisions or burns); exclusion criteria: stem cells obtained from non-human origin, combination of human stem cells from different tissues, use of a different biological scaffold, and studies that not assess efficacy in skin regeneration. The main outcomes were decreased wound closure time, increased angiogenesis, remodeling and increase in extracellular matrix deposition, increased synthesis of growth factors and anti-inflammatory cytokines, and optimization of biomechanical properties. Moreover, one of the main findings was that combining these methods can improve the healing process in chronic wounds. The main bias was related to the inclusion of more studies that used ADMSC (5 of 8); additionally, there were differences in the animal model used, the induced wound, and the comparison of different variables between the studies. In conclusion, we found that the combination of MSCs and AAM as a bio-scaffold improves general tissue healing and regeneration.

**KEYWORDS:** adipose-derived MSCs, biological scaffold, human amniotic membrane, mesenchymal stem cells, umbilical cord MSCs, wound healing

## RESUMEN

Esta revisión sistemática tiene como objetivo documentar la evidencia disponible sobre el uso de células madre mesenquimales (MSC) y membranas amnióticas acelulares (AAM) como andamios biológicos en modelos murinos para la regeneración de tejidos. Esta investigación se desarrolló buscando información disponible en bases de datos como *Google Scholar*, *Pubmed*, *Scopus* y *Web of Science*, utilizando los siguientes términos clave "Células madre humanas", "Membrana amniótica", "Curación de heridas" y "Modelo animal". Fueron encontrados un total de 519 artículos publicados desde enero de 2013 hasta marzo de 2024, pero solo se incluyeron 8 estudios en esta revisión. El criterio de inclusión: uso de células madre derivadas de humanos (UCMSC y ADMSC) sembradas en hAM descelularizadas en modelos murinos con heridas inducidas (incisiones o quemaduras). Los criterios de exclusión fueron: células madre obtenidas de origen no humano, combinación de células madre humanas de diferentes tejidos, uso de un andamio biológico diferente y estudios que no evalúen la eficacia en la regeneración de la piel. Los principales resultados fueron una disminución del tiempo de cierre de la herida, aumento de la angiogénesis, remodelación, aumento del depósito de matriz extracelular, síntesis de factores de crecimiento y citocinas antiinflamatorias junto con la optimización de las propiedades biomecánicas, que en conjunto pueden mejorar el proceso de curación en heridas crónicas. El sesgo principal se relaciona con la inclusión de más estudios que emplearon ADMSC (5 de 8), adicionalmente hubo diferencias entre el modelo animal empleado, la herida inducida y la comparación de diferentes variables entre los estudios. En conclusión, encontramos que la combinación de MSC y AAM como bioestructura mejora la curación y regeneración general del tejido.

**PALABRAS CLAVE:** andamio biológico, cicatrización de heridas, células madre mesenquimales, CMM derivadas de tejido adiposo, CMM del cordón umbilical, membranas amnióticas humanas

### Corresponding author

TO: Lina Andrea Gómez

INSTITUTION: Faculty of Medicine, Universidad de La Sabana.

ADDRESS: Puente del Común, Km. 7, Autopista Norte de Bogotá, Chía, Cundinamarca, Colombia.

EMAIL: [lina.gomez3@unisabana.edu.co](mailto:lina.gomez3@unisabana.edu.co)

### Received:

10 May 2024

### Accepted:

8 September 2024

## INTRODUCTION

Given the complexity of its treatment, skin lesions represent a great challenge nowadays, in the United States alone, wound care costs reached \$126.864 billion in 2019<sup>[1]</sup>. A huge portion of the investment is destined for chronic wounds, characterized by not following a normal healing course and failing to restore functional or anatomical integrity after 3 months<sup>[2]</sup>. Additionally, its prevalence is estimated to affect around 40 million people worldwide<sup>[3]</sup>. Similarly, other types of wounds, such as burns, have a worldwide incidence of 11 million cases per year<sup>[4]</sup>, and depending on the depth and extension, they can progress towards chronic non-healing wounds.

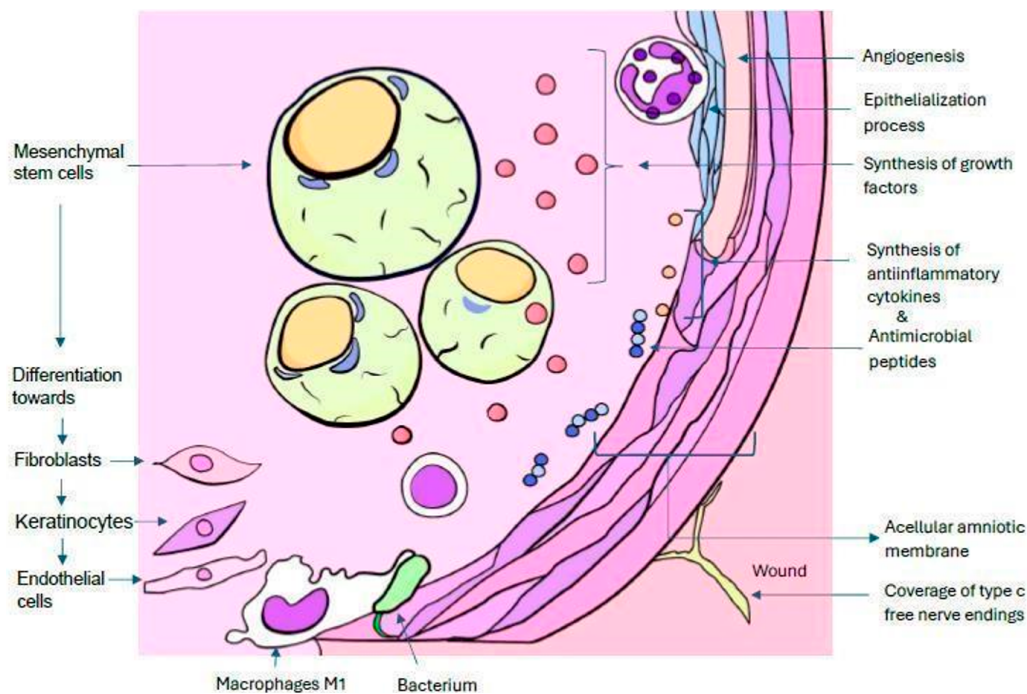
Under normal circumstances, the healing process consists of 4 phases. Phase I: Hemostasis occurs immediately after the injury, aiming to restore the normal barrier function of the skin. It begins with vasoconstriction, finishing with the formation of a clot that covers the wound, acting as a provisional scaffold for cell migration<sup>[3]</sup>. The platelets within this clot produce a variety of pro-inflammatory agents, including thrombin, fibrinogen, angiogenic factors, growth factors, cytokines, and chemokines, which in conjunction promote migration of fibroblasts, monocytes, neutrophils, endothelial cells, along with bone marrow-derived mesenchymal stem cells (BMSCs). Phase 2: Inflammation begins with neutrophils producing bacterial lysis and removal of cellular debris. Likewise, monocytes help by differentiating into M1 macrophages aiming to amplify the inflammatory response. At the end of this stage, M2 macrophages and BMSCs initiate the healing process through their anti-inflammatory properties. Phase 3: Proliferation occurs when granulation tissue is formed by the action of fibroblasts, while the migration of keratinocytes initiates the re-epithelialization process<sup>[3]</sup>. Phase 4: Remodeling, a progressive decrease of cellularity and blood vessels occurs. In this transition process from granulation tissue to scar formation, metalloproteinases (MMPS) degrade collagen type III fibers previously arranged as temporary scaffolds. At the same time, fibroblasts increase the amount of collagen type I fibers to complete the healing and regeneration process<sup>[3]</sup>.

On the contrary, the healing process in chronic wounds has been altered by the increase of IL-1, IL-6, TNF $\alpha$ , and the permanence of MMPS; along with a rise in the macrophages differentiation to M1 pro-inflammatory subtype, causing Fibroblasts to decrease their proliferation, with a consequent reduction in the synthesis of extracellular matrix and the making of granulation tissue<sup>[4]</sup>. Similarly, the formation of new blood vessels decreases, resulting in a pro-inflammatory, hypoxic, and ischemic environment<sup>[5]</sup>. Together, these conditions lead to the chronification of many diseases, such as diabetes, peripheral arterial disease, venous insufficiency, or ulcers derived from localized pressure. Consequently, this propitiates the development and progression of non-healing chronic wounds<sup>[6]</sup>.

In addition to the complex phases of the healing process, the often-observed imbalance in diverse ailments further complicates the course of chronic wounds and their treatment when co-morbidity is observed. Therefore, therapeutic alternatives have been developed to optimize the outcomes of treating skin lesions, while decreasing the burden imposed on the health system. Among these therapeutic options, stem cell therapy has been widely studied for its role in the tissue regeneration process. It is currently a topic of ongoing research and evolution.

Regarding wound regeneration, the most analyzed human mesenchymal stem cell populations have been adipose tissue and umbilical cord-derived MSCs. Advantages of using human umbilical cord-derived mesenchymal stem cells (UCMSCs) include their accessibility, as they are obtained from waste tissue at the time of delivery; low immunogenicity due to the low expression of HLA-1 as well as greater potential for proliferation, compared to other sources of stem cells<sup>[7]</sup>. Similarly, adipose tissue-derived stem cells (ADMSCs) have demonstrated great abil-

ity to modulate the inflammatory response of dendritic cells and T lymphocytes; as well an important cellular plasticity, which gives them the ability to differentiate into various cell lineages such as fibroblasts, keratinocytes, endothelial and epithelial cells<sup>[8]</sup>. Furthermore, ADMSCs present multiple autocrine and paracrine effects, which promote tissue repair; and are easily obtained through minimally invasive liposuction procedures<sup>[8][9]</sup>. Remarkably, studies have been carried out utilizing exosomes derived from ADMSCs, which have shown similar effects, by decreasing the synthesis of proinflammatory cytokines, such as IL-1 $\beta$  and TNF $\alpha$ <sup>[10]</sup>, (Figure 1).



**FIGURE 1. Synergistic effects between stem cells and amniotic membrane in wound healing. Courtesy of Guillermo Mayorga. Elaborated using Adobe illustrator.**

Although subcutaneous local infiltration of stem cells has been tested in non-healing chronic wounds, the main drawbacks are the increased apoptosis susceptibility; secondary to the shear stress caused at the time of infiltration, accompanied by an excessive inflammatory process at the wound site, which perpetuates the non-optimal environment for cell survival<sup>[11]</sup>. Consequently, different research has been done using stem cells in association with biological scaffolds, many of them developed with tissue engineering, while others performed with natural human amniotic membranes (hAM). Overall, results evidence improvement in cell survival rate, overcoming the limitations of using MSCs applied directly into the wound without a scaffold, and exhibiting significant synergistic effects on tissue regeneration.

Biological polymer scaffolds can be used in the tissue regeneration process, these can be naturally based on proteins (collagen, fibrin) or polysaccharides (cellulose, hyaluronic acid). Likewise, synthetic polymers (polyethylene, polystyrene) have been developed, which are distinguished mainly by their mechanical properties<sup>[12]</sup>.

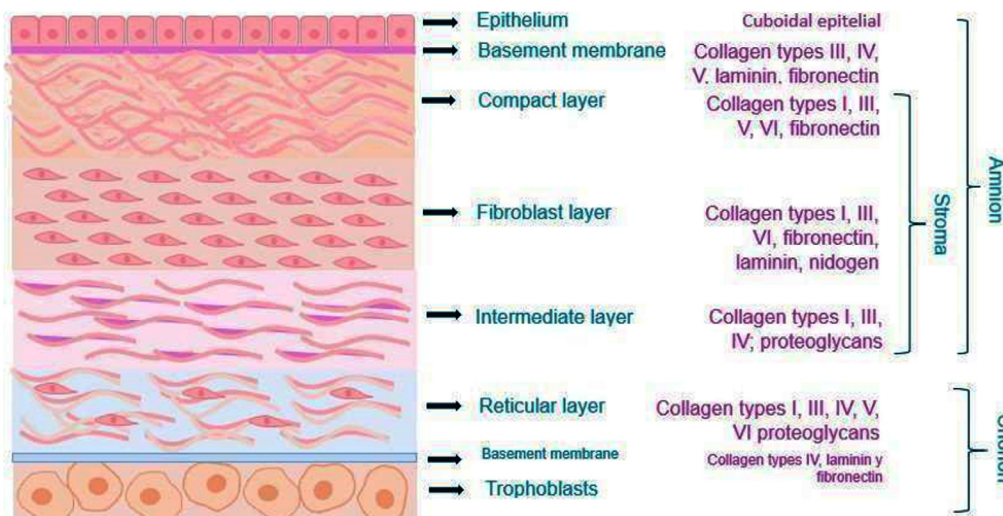
In this case, hAM was chosen due to its numerous advantages, such as its easy procurement, good aesthetic results in the healing process, and its ability to synthesize a wide variety of molecules that promote tissue regen-

eration. Its use avoids resorting to the exploitation of natural resources, its cost is significantly lower compared to polymers, laborious manufacturing processes are avoided, and rejection by the recipient is an adverse reaction that occurs in few cases<sup>[13]</sup>.

One of the most fascinating properties of hAM described in the literature is the ability to regulate the production of proinflammatory cytokines, while promoting the release of IL-4, IL-10, TGF- $\beta$ , hepatocyte growth factor (HGF), prostaglandin E2 (PGE-2), histocompatibility antigen HLA- G and indoleamine 2,3- dioxygenase (IDO), all of them exhibiting anti-inflammatory properties<sup>[14]</sup>.

Additionally, hAM displays antimicrobial functions through the release of elafin and beta-defensins, both of which are antimicrobial peptides. Moreover, it can contribute to analgesia acting as a physical barrier when used to cover the wound and nerves, while stimulating angiogenesis via the release of vascular endothelial growth factor (VEGF-A), angiopoietin 1, and fibroblast growth factor (FGF-2). Studies have also reported that the use of hAM promotes cell differentiation and adhesion through structural proteins such as type I collagen, laminin, and fibronectin, which also support epithelialization. Finally, this biocompatible scaffold can be easily obtained and exhibits outstanding regenerative properties, making it a feasible option for treating non-healing chronic wounds<sup>[15]</sup>.

To optimize the use of hAM, several research has been developed to decellularized the membrane scaffold and colonize it with stem cells. Aiming to prevent graft rejection, thus allowing a more synergic treatment of non-healing chronic wounds. This decellularization process removes the epithelium while preserving the stroma of the hAM (Figure 2), maintaining the components of the extracellular matrix, and the presence of tissue regenerating-associated growth factors. These associated biomolecules include nerve growth factor (NGF), epidermal growth factor EGF, Keratinocyte Growth Factor KGF, Basic fibroblast growth factor bFGF, and Transforming growth factor beta  $\alpha$  and  $\beta$  (TGF $\alpha$  and  $\beta$ )<sup>[16]</sup>, resulting in the AAM. Human amniotic membranes offer a combination of biological and structural benefits that make them ideal for applications in regenerative medicine, especially for skin regeneration.



**FIGURE 2. Structure of the amniotic membrane, prepared using Microsoft Word, adapted from<sup>[14]</sup>.**

Interestingly, available evidence regarding the use of stem cells in combination with human amniotic membranes has been documented with great outcomes, in in vivo experiments carried out in mice and rat models. Hence, this systematic review aimed to analyze the studies using human stem cells derived from adipose tissue and/or umbilical cord in combination with acellular human amniotic membrane in the healing process of skin wounds in murine models and provide solid bases for defining the type of stem cells to be used in future human trials.

## **MATERIALS AND METHODS**

### **Literature research**

Between May 8 and 12 2024, an electronic search was carried out in the Google Scholar, Pubmed, Scopus, and Web of Science databases, grouping the terms that constituted the PICO question: "Human Stem Cells", "Amniotic mechanisms", "Wound healing", and "Animal model", articulated to fulfill the objective stated in the previous section. The final structure of each search strategy was adjusted based on the thesaurus vocabulary and the Boolean operators specific to each database.

### **Inclusion and exclusion criteria**

Studies published from January 2013 to March 2024 were considered eligible, in which the effects on skin regeneration were evaluated, using human mesenchymal stem cells (UCMSC and ADMSC) seeded in decellularized hAM, in murine models with induced incisions or burns, with prior approval from the associated animal care and use committees. The reason for only considering murine models is that a gap and discrepancy were identified in the literature regarding the most studied stem cell (ADMSCs) and the stem cell used in the few studies identified in humans (UC-MSCs), thus, this systematic review arises to provide solid bases for future trials in humans. Exclusion criteria were considered as follows: non-primary studies, obtaining stem cells of non-human origin, a combination of human stem cells from different tissues, use of a biological scaffold different from the one stated, studies not designed to assess efficacy in skin regeneration, and articles written in languages other than English or Spanish. These exclusion criteria were considered to enable a comparison with the studies finally selected.

### **Study selection**

Just the authors VG and GM participated in the selection of potentially relevant studies to reduce the risk of selection bias and this process was carried out in three stages. The first stage focused on eliminating duplicate records. The second stage centered on exclusion of articles according to their title and abstract. In these two stages, the collaborative web application named Rayyan was used. Finally, the third stage consisted of a full-text analysis. The last two stages were guided by inclusion and exclusion criteria. This process was based on the statements established in the PRISMA 2020 protocol.

### **Data extraction**

The studies were required to contain this information: population sample, type of injury, methodology in terms of origin and processing of stem cells and amniotic membranes, information on the interventions, and outcome measures. Data were independently extracted and organized in a detailed manner on a worksheet for further analysis.



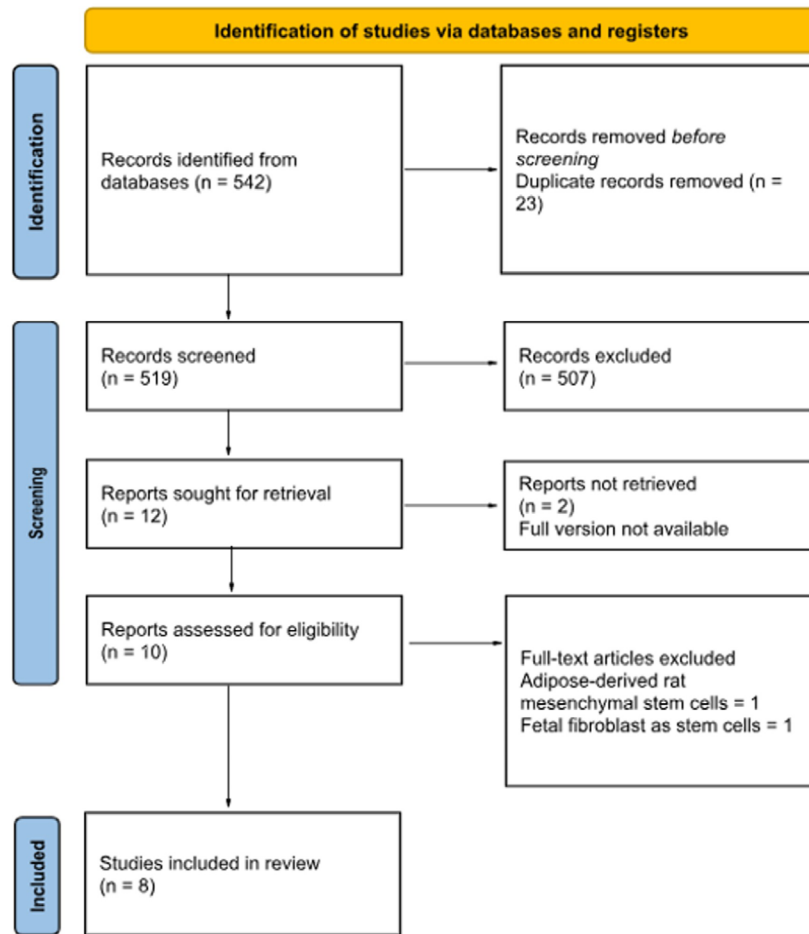


FIGURE 3. Prisma flowchart.

## RESULTS AND DISCUSSION

### Search results

After removing duplicated studies, according to the PRISMA 2020 flowchart, the search performed yielded a total of 519 studies (Figure 3). Considering the information found on the titles and abstracts, 12 studies were fully assessed, out of which 4 studies were excluded. Finally, 8 primary studies were included.

### Characteristics of the studies

The main findings of the analyzed studies are presented in Table 1. All studies used murine models, with the most used species being BALB/c mice and Wistar rats. All studies included signed informed consent for aesthetic liposuction procedures and elective cesarean sections to obtain ADMSCs, UCMSCs, and hAMs.

Isolation and culture procedures for human mesenchymal stem cells were similar, along with their characterization to meet the criteria established by the International Society of Cellular Therapy (ISCT) for MSCs. As per the de-epithelization of the human amniotic membrane, the methods used were mechanical and enzymatic. Of the included studies, 6 described macroscopic characteristics, 8 referred histological features, 4 made immunohistochemical analyses, 2 presented biomechanical characteristics, and 1 performed molecular biology studies.

TABLE 1. Analysis of the characteristics of the studies included in the systematic review. (Continue in the next page).

|  | Animal model                  | Type of induced wound   | Methodology  | Analysis/studies carried out   | Outcomes   |
|--|-------------------------------|---|--|--|--|
| Khalatbary, <i>et al.</i> , (2023) <sup>[10]</sup> | 60 experimental Wistar rats   | Excisional wound on the back and two sagittal incisions on the sides of the wound | <p>Stem cell process: human origin, obtained by liposuction, subsequently washed, isolated, centrifuged, seeded, incubated and finally characterized</p> <p>AAM process: human origin, obtained during cesarean sections, subsequently washed, decellularized with trypsin solution, triton, sodium deoxycholic acid, washed again, and lyophilized. Decellularization was confirmed by H&amp;E</p> <p>Diabetes mellitus was induced in all rats by intraperitoneal injection of streptozotocin</p> <p>They were divided into four groups: control, injection of ADMSCs-derived exosomes, AMS, AMS + ADMSCs-derived exosomes</p> | <p>Samples were taken from five mice from each subgroup at the end of the 1, 2, 3 weeks for analysis:</p> <ul style="list-style-type: none"> <li>-Histological</li> <li>-H&amp;E: nuclei and cytoplasm</li> <li>-Toluidine blue: mast cells</li> <li>-Masson's trichrome: collagen</li> <li>-Immunohistochemical</li> <li>-Anti-ki67 antibodies: cell proliferation</li> <li>-Anti-CD86 antibodies: M1 macrophages</li> <li>-Molecular: TGF-<math>\beta</math>, bFGF, VEGF, TNF-<math>\alpha</math> and IL-1<math>\beta</math> by qRT-PCR</li> <li>-Tensiometric: maximum force and energy absorption were determined by a material testing machine</li> </ul> | <ul style="list-style-type: none"> <li>-Wound area Wound closure rate</li> <li>-Total volumes of the new epidermis and dermis</li> <li>-Numerical density of fibroblasts, neutrophils, mast cells, blood vessels in the dermis</li> <li>-Cell proliferation and macrophages M1</li> <li>-Collagen deposit Levels of TGF-<math>\beta</math>, bFGF, -VEGF, TNF-<math>\alpha</math>, IL-<math>\beta</math> Tensile strength test</li> </ul> |
| Zhou, <i>et al.</i> , (2023) <sup>[13]</sup>       | 48 experimental C57BL/6J mice | Second- degree burns of 1 cm in diameter at dorsal level                          | <p>Stem cell process: obtained from healthy donors by cesarean section, subsequently washed and incubated</p> <p>AAM process: obtained from healthy donors by cesarean section, stored, frozen, thawed, decellularized by enzymatic digestion and confirmed by DAPI</p> <p>They were divided into four groups: control, mAM + UC-MSCs, UC-MSCs, sham</p>   | <p>Five mice from each subgroup were sacrificed on days 7 and 11 for analysis:</p> <ul style="list-style-type: none"> <li>-RNA</li> <li>-Seq transcriptomic analysis to compare the gene expression profile</li> <li>-Biological effects of mAM</li> <li>-MSC on HUVECs using transwell cell migration and tube formation assays</li> <li>-Survival of mAM-MSC using bioluminescence imaging</li> <li>-Histological: H&amp;E</li> <li>-Immunohistochemical: anti-CD31, antibodies, angiogenesis</li> </ul>   | <ul style="list-style-type: none"> <li>-Effects of mAM on MSC</li> <li>-Survival of mAM-MSC</li> <li>-Wound area</li> <li>-Wound closure rate</li> <li>-Vascularization</li> </ul>   |
| Moghim, <i>et al.</i> , (2023) <sup>[17]</sup>     | 60 experimental Wistar rats   | Two excisional wounds of total thickness of 1 cm in diameter at the dorsal level  | <p>Stem cell process: obtained from liposuction material from healthy patients undergoing cosmetic surgery, washed, isolated, centrifuged, incubated and characterized</p> <p>AAM process: obtained after cesarean deliveries of healthy women, washed, frozen, thawed, decellularized by swabbing with NaOH and washed</p> <p>They were divided into three groups: control, dAM + ADMSCs, sAM + ADMSCs</p>  | <p>The rats were sacrificed on days 3,7,16,21 for analysis:</p> <ul style="list-style-type: none"> <li>-Molecular: VEGF and Col-I by qRT-PCR</li> <li>-Histological</li> <li>-H&amp;E</li> <li>-Masson's trichrome</li> </ul>  | <ul style="list-style-type: none"> <li>-Real-Time PCR results</li> <li>-Wound area</li> <li>-Vascularization</li> <li>-Collagen deposit</li> </ul>   |

**TABLE 1. Analysis of the characteristics of the studies included in the systematic review. (Continue in the next page).**

|   | <b>Animal model</b>         | <b>Type of induced wound</b>                                | <b>Methodology</b>   | <b>Analysis/studies carried out</b>   | <b>Outcomes</b>   |
|---|-----------------------------|---|--|---|---|
| Aghayan, <i>et al.</i> , (2022) <sup>[18]</sup> | 24 experimental Wistar rats | Excisional wound of total thickness of 1 cm at dorsal level | <p>Stem cell process: obtained from liposuction surgery waste (&lt;40 years) and from full-term cesarean births (&gt;38 weeks), washed, isolated, centrifuged, incubated and characterized</p> <p>AAM process: obtained from full-term cesarean deliveries, washed, frozen, thawed, decellularized by cell scraper and multiple washing and incubated. Decellularization was confirmed by H&amp;E</p> <p>They were divided into four groups: control, AAM, ADMSCs + AAM, PLMSCs + AAM</p>  | <p>Three rats from each subgroup were sacrificed on days 7 and 14 for analysis:</p> <ul style="list-style-type: none"> <li>-Histological</li> <li>-H&amp;E</li> <li>-Masson's trichrome</li> </ul>  | <ul style="list-style-type: none"> <li>-Wound closure rate</li> <li>-Epithelialization</li> <li>-Angiogenesis</li> <li>-Collagen deposit</li> <li>-Epidermal and dermal thickness</li> <li>-Number of inflammatory cells</li> <li>-Cutaneous annexes</li> </ul>   |
| Xiao, <i>et al.</i> , (2021) <sup>[19]</sup>    | 40 experimental BABL/C mice | Total thickness defect of 1 cm in diameter at dorsal level  | <p>Stem cell process: obtained during liposuction procedures, isolated, centrifuged, incubated and characterized</p> <p>AAM process: obtained from healthy women undergoing cesarean section, frozen, thawed, washed, incubated, decellularized by cell scraping and multiple washing, confirmed by H&amp;E. Finally lyophilized</p> <p>Diabetes mellitus was induced in all mice by intraperitoneal injection of streptozotocin. They were divided into four groups: control, ADMSCs-derived exosomes, hAAM, hAAM + ADMSCs-derived exosomes</p> | <p>The healing of the wounds was evaluated by macroscopic observation on days 1,3,7 and 14. Three analyses were performed:</p> <ul style="list-style-type: none"> <li>-Biological effects ADMSC-exos on HDFs and HUVECs using tube formation assays and scratch assay</li> <li>-Histological: <ul style="list-style-type: none"> <li>-H&amp;E</li> <li>-Masson's trichrome</li> </ul> </li> <li>-Immunohistochemical <ul style="list-style-type: none"> <li>-Anti-CD206 antibodies: M2 macrophages</li> <li>-Anti-collagen III antibodies: extracellular matrix</li> <li>-Anti-CD31 antibodies</li> </ul> </li> </ul> | <ul style="list-style-type: none"> <li>-Effects ADMSC-exos on HDFs and HUVECs</li> <li>-Appearance and rate of closure of the wound</li> <li>Infiltration of inflammatory cells</li> <li>-Macrophage M2</li> <li>-Vascularization</li> <li>-Extracellular matrix reservoir</li> <li>-Type III collagen</li> <li>-Cutaneous annexes</li> </ul> |
| Hashemi, <i>et al.</i> , (2020) <sup>[20]</sup> | 32 experimental albino mice | Third-degree burns (20% SCT) in the cervical region         | <p>Stem cell process: obtained from mothers who are candidates for cesarean section, washed, incubated and characterized</p> <p>AAM process: obtained from mothers who are candidates for cesarean section, decellularized using a mechanical method and cold peeling</p> <p>They were divided into four groups: DHAM + HWJMSCs, HWJMSCs injection, HWJMSCs application and DHAM. The corresponding treatment was administered 24 hours of the burn</p>  | <p>Half of the rats in each subgroup (4) were sacrificed on the 7th and 14th for analysis:</p> <ul style="list-style-type: none"> <li>-Molecular: gene cGFP and MTT assay</li> <li>-Histological: H&amp;E</li> </ul>  | <ul style="list-style-type: none"> <li>-Effects of HWJMSCs on acellular hAM, the viability of cells after labeling and perching on DHAM</li> <li>-Histological findings: re-epithelialization, granulation tissue, hemorrhage and inflammation</li> </ul>   |

TABLE 1. Analysis of the characteristics of the studies included in the systematic review. (Continue from previous page).

|  | Animal model                | Type of induced wound  | Methodology  | Analysis/studies carried out  | Outcomes  |
|--|-----------------------------|--|--|---|---|
| Wu, <i>et al.</i> , (2016) <sup>[21]</sup>       | 32 experimental albino mice | Defects of total thickness of 0.8 x 0.8 cm on the back         | <p>Stem cell process: not specified</p> <p>AAM process: obtaining not specified, decellularized with sodium dodecyl sulfate, hypotonic tris buffer and treatment with protease and nuclease inhibitors. Confirmation by H&amp;E</p> <p>They were divided into four groups: hAM, AAM, ADMSC + AAM</p>   | <p>The wound healing rate at 7.14 and 28 days and two analysis at 28 days:</p> <ul style="list-style-type: none"> <li>-Immunohistochemical</li> <li>-Anti-CK19 and human derived mitochondria antibodies</li> <li>-Histological: H&amp;E</li> </ul>   | <ul style="list-style-type: none"> <li>-Wound healing rate</li> <li>-Histological characteristics: epidermal layers, cutaneous annexes</li> </ul>   |
| Sabapathy, <i>et al.</i> , (2014) <sup>[7]</sup> | 9 SCID experimental mice    | Excisional wound with an area of 1 cm <sup>2</sup> on the back | <p>Stem cell process: obtained from patients undergoing elective cesarean section with full-term pregnancy, washed, isolated, incubated and characterized</p> <p>AAM process: obtained from patients undergoing elective cesarean section with full-term pregnancy, washed, decellularized with Tris buffer and sodium dodecyl sulfate, washed, immersed in a buffer reaction and sterilized</p> <p>They were divided into three groups: HWJMSCs injection, AAM + HWJMSCs, control</p> | <p>The analyses were carried out after 14 days:</p> <ul style="list-style-type: none"> <li>-Multilineage differentiation analysis by stains and flow cytometry</li> <li>-Establishing the safety of isolated and expanded MSCs by flow cytometry and qRT-PCR</li> <li>-Histological: Masson's trichrome</li> <li>-Tracking the transplanted cells in vivo by ICG and using IVIS imaging system</li> <li>-Tensiometric: characterize the mechanical properties by a tensile testing machine</li> </ul> | <ul style="list-style-type: none"> <li>-Differentiation Plasticity</li> <li>-Safety</li> <li>-Singer classification</li> <li>-Cell survival</li> <li>-Biomechanical properties</li> </ul> |

AAM, acellular amniotic membrane; H&E, hematoxylin and eosin; ADMSCs, adipose tissue-derived stem cells; AMS, bioengineered three-dimensional microporous amniotic membrane scaffold; qRT-PCR, quantitative Real Time-Polymerase Chain Reaction; mAM, micronized amniotic membrane; UC-MSCs, umbilical cord-derived mesenchymal stem cells; HUVECs, Human Umbilical Vein Endothelial Cells; dAM, decellularized amniotic membrane; sAM, stromal amniotic membrane; PLMSCs, placenta-derived mesenchymal stem cells; hAAM, human acellular amniotic membrane; HDFs, primary human dermal fibroblasts; DHAM, decellularized human amniotic membrane; HWJMSCs, Wharton's jelly-derived mesenchymal stem cells; hAM; human amniotic membrane, ICG, Indocyanine green; IVIS, In Vivo Imaging System.

## **Results found in the analyzed studies**

### *Macroscopic characteristics*

Macroscopic observation through photographic recording of the wound area at transverse moments showed that the intervention groups (AMS + ADSCs-derived exosomes, mAM + UC-MSCs, dAM + ADMSCs, hAAM + ADSCs-derived exosomes and ADMSCs + AAM) had a greater and faster effect in reducing the wound area, compared to other interventions, including the control group<sup>[10][13][17][19][21]</sup>.

### *Immunological and immunohistochemical characteristics*

In one study, a mathematical equation was used to calculate the newly formed epidermal and dermal volumes in the treated groups. Interestingly, the AMS + ADSCs-derived exosome groups showed greater volumes compared to the other groups on days 7, 14, and 21<sup>[10]</sup>. Additionally, via the histological study, authors reported that the AMS + ADSCs-derived exosomes group had, comparatively, higher vascular density on days 7, 14, and 21<sup>[10]</sup>. Although several studies compare AAM + HWJMSCs to other intervention groups, one of them evaluated hyperkeratosis and epidermal hyperplasia, finding higher values in comparison<sup>[7]</sup>. Similarly, in two studies staining with CD31 was performed and a greater pro-angiogenic effect was observed in the intervention groups (mAM + UC-MSCs and hAAM + ADSCs-derived exosomes), compared to the other groups<sup>[13]</sup>.

Regarding collagen deposition, Masson's trichrome staining was used to stain collagen fibers, revealing that in the AMS + ADSCs-derived exosomes and dAM + ADMSCs groups, the wound bed had a greater amount of collagen with a better arrangement of fibers; therefore, constituting a more organized regenerated structure<sup>[10][17]</sup>. In another study, collagen expression was determined by immunohistochemical staining of collagen III and it was evident that the hAAM + ADSCs-derived exosomes group showed the highest expression compared to the other groups<sup>[19]</sup>. Likewise, the group HWJMSCs + AAM was evaluated through the orientation of collagen fibers, which was superior to the other intervention groups<sup>[7]</sup>.

In terms of cell proliferation, immunohistochemical staining of ki67 and CD86 demonstrated that cell proliferation in the AMS + ADSCs-derived exosomes group was significantly higher compared to the other groups on days 7, 14 and 21; while the density of M1 macrophages was considerably lower in this group<sup>[10]</sup>. Immunohistochemical staining of CD206 demonstrated increased recruitment of M2 macrophages to the wound bed<sup>[19]</sup>. Furthermore, three of the studies performing immunohistochemical analyses evaluated the regeneration of skin annexes. One of the studies performed immunohistochemical staining of cytokeratin 19 and mitochondria and reported the observation of hair follicle structure on day 28 (ADMSCs + AAM group). Though a second study aiming to improve wound healing in diabetic mice by applying hAAM + ADSCs-derived exosomes, hair follicles and sebaceous glands

failed to regenerate<sup>[19]</sup>, the third experiment used the Singer classification to quantify the regeneration of skin wounds via Masson's trichrome staining, with great outcomes. Authors report the presence of hair follicles and apocrine glands in the AAM + HWJMSCs group<sup>[7]</sup>.

*Biomechanical characteristics.* Two of the studies included tensile strength tests. In the first one, the AMS + ADSCs-derived exosomes group exhibited greater maximum strength and energy absorption on day 21, compared to the other groups<sup>[10]</sup>. While on the second study, the analysis of all biomechanical parameters (stress, strain, Young's modulus, stiffness, tenacity modulus and tensile strength) indicated that the AAM + HWJMSCs group had better scores when compared to other groups (HWJMSCs and control)<sup>[7]</sup>.

*Molecular biology studies.* In one interesting study, the level of gene transcription of various representative factors was evaluated through real-time polymerase chain reaction. Factors included in this study were associated with proliferation and regeneration (TGF- $\beta$  and bFGF), angiogenesis (VEGF), and inflammation (TNF $\alpha$  and IL-1 $\beta$ ) on day 7. In comparison to other groups, the AMS + ADSCs-derived exosomes group had greater expression of the factors associated with proliferation, regeneration, and angiogenesis and lower expression of proinflammatory factors<sup>[10]</sup>.

## Discussion

The function of the human amniotic membrane as an acellular scaffold for mesenchymal stem cells derived from different tissues and its role in tissue regeneration has been extensively studied over time<sup>[22][23]</sup>, this systematic review aims to consolidate the available evidence on the combined use of human stem cells derived from adipose tissue and umbilical cord seeded in acellular human amniotic membranes and their role in the skin wound healing process in mice and rats.

It is important to highlight that MSCs are easily obtained and have been successfully isolated from various human tissues<sup>[24]</sup>. When using stem cells to accelerate the skin regeneration process, it is evident that the viability of this type of cells is low, due to different friction forces generated during processing and application, ultimately compromising the survival of the stem cells<sup>[11]</sup>. Likewise, it has been shown that not all stem cells have the same capacity to migrate towards the site of injury, which prevents the recruitment of an adequate number of MSCs<sup>[25]</sup>.

Various biological and synthetic scaffolds provide a favorable environment for growth, proliferation, and maintenance of stem cells destined for a specific tissue space<sup>[26]</sup>. AAM is a biological scaffold with excellent results in skin healing, and the evidence analyzed in this manuscript supports a synergistic effect with stem cells. Both present anti-inflammatory effects, through the release of growth factors and similar properties<sup>[27]</sup>. Of special interest in hAM, is the mechanical characteristics of the basement membrane conferred by its proteins<sup>[28]</sup>.

This systematic review allowed the comparison and analysis of a variety of studies regarding the use of bioscaffolds (MSCs + dHAM) in skin wounds. Eight (8) articles were reviewed, and all of them evaluated one or more of the following criteria: macroscopic, histological, and immunohistochemical characteristics, collagen deposits, cell proliferation, and biomechanical properties.

This confirms that both ADMSCs and UC-MSCs, seeded in dHAM, show positive outcomes in terms of wound area reduction compared to the control groups<sup>[10][13][17][19][21]</sup>. Regarding immunohistochemical characteristics, it was determined that on days 7, 14, and 21, the epidermal volume and the rate of angiogenesis and cellular proliferation were

higher in the dHAM + ADSCs- derived exosomes group<sup>[10]</sup>, suggesting a favorable and less inflammatory environment conducive to healing. Only one study measured the rate of hyperkeratosis and epidermal hyperplasia, which was higher in the dHAM + HWJMSCs group<sup>[7]</sup>. On the other hand, an important factor to consider in the skin healing process is the accumulation of collagen deposits and the organization of its fibers, exposing that in the dHAM + ADSCs-derived exosomes, dHAM + ADMSCs, and HWJMSCs + dHAM groups, better collagen fiber organization was observed<sup>[7][10][17]</sup>. Additionally, the dHAM + ADSCs-derived exosomes group reported a higher concentration of type III collagen<sup>[19]</sup>. It should be noted that only two studies evaluated the regeneration of skin appendages; of these, only two studies successfully regenerated skin appendages such as hair follicles by day 28<sup>[7][19]</sup> and apocrine glands<sup>[7]</sup>. The variability in these results may be due to the differences in the animal models used, the application methodology, or the source of the cells provided. When evaluating biomechanical properties, the study groups were subjected to traction, tension, deformation, and stiffness tests, where the dHAM + HWJMSCs group had the best outcomes<sup>[7]</sup>. This aspect is crucial to ensure not only rapid healing but also the provision of functional and resilient tissue. At the molecular level, the dHAM + ADSCs-derived exosomes group showed greater expression of factors associated with cellular proliferation and lower expression of pro-inflammatory factors<sup>[10]</sup>. This suggests that these combinations not only accelerate the healing process but also favorably modulate the cellular environment to promote more efficient healing with fewer inflammatory complications. Nevertheless, the use of human amniotic membranes combined with mesenchymal stem cells (MSCs) could have several limitations that are important to consider:

**Immunological Rejection:** Although hAM has immunomodulatory properties, there is a risk of immunological rejection when combined with MSCs. **Quality Variability:** The quality of amniotic membranes can vary depending on the source and processing method, which can affect the efficacy of the treatment. **Risk of Infection:** Being a biological tissue, there is a risk of transmission of infections if not handled properly<sup>[29]</sup>. **Costs and Availability:** Obtaining and processing amniotic membranes and MSCs can be expensive and are not always available in all regions. **Limited Efficacy:** In some cases, the observed benefits cannot be fully attributed to the cellular plasticity of MSCs, as the number of grafted cells may be low.

Overcoming the limitations of using human amniotic membranes combined with mesenchymal stem cells (MSCs) requires a multifaceted approach:

**Improving Immunological Compatibility:** Genetic engineering techniques can be used to modify MSCs and reduce the risk of immunological rejection. **Process Standardization:** Developing standardized protocols for obtaining and processing amniotic membranes can help reduce variability in quality. **Quality Control and Safety:** Implement strict quality control and safety testing to minimize the risk of infections. **Research and Development:** Invest in research to improve the efficacy of combination therapies and better understand the mechanisms of action of MSCs. **Cost Reduction:** Encourage mass production and process optimization to reduce costs and improve availability. **Education and Training:** Train healthcare professionals in the proper management of these therapies to maximize their benefits and minimize risks<sup>[30]</sup>.

It is important to mention that the information obtained from ADMSCs exceeds that found about HWJMSCs, which explains the inequality when presenting the results found in the PRISMA search, since we found differences regarding the animal model and wound etiology. Additionally, it should be considered that not all articles compare the same parameters, which generates a bias when objectively evaluating the results. We consider that the fundamental parameters to evaluate similar investigations should be related to the effects on the wound area, the capacity for angiogenesis and collagen synthesis, the biomechanical properties, and the induction of molecular factors that favor cell proliferation.

Specifically in future clinical trials in humans, parameters such as improvement in pain and systemic effects of the use of this method for tissue regeneration should also be reported.

Moreover, some studies evaluated experimental results in up to four-time intervals, while other authors considered a two-time interval. Although evaluation periods may vary depending on the researchers' projections, resources, materials, and the disposition of the experimental and control groups, these determinants must be methodically evaluated before initiating the experiment to obtain reproducible results.

Another relevant consideration is that experimental studies carried out in humans are scarce and only studies of UC-MSCs + dHAM in skin regeneration were found. Hashemi and collaborators described the use of stem cells derived from the umbilical cord seeded in acellular human amniotic membrane, obtaining positive outcomes in terms of reducing wound size and healing time<sup>[31]</sup>. Overall, the analysis presented throughout this systematic review indicates that stem cells derived from adipose tissue and umbilical cord seeded in decellularized human amniotic membranes show positive results in clinical trials with murine animals. It is expected that in the future, these studies will pave the way for clinical trials in humans to be able to carry out evidence-based guided tissue regeneration therapies.

## CONCLUSIONS

This systematic review of the literature evidence the synergy reported in the use of stem cells from adipose tissue and umbilical cord tissue of human origin in combination with the acellular human amniotic membrane for the treatment of skin lesions, such as ulcers and burns in rodents, promises great outcomes. Groups treated with MSCs reported better outcomes in terms of the reduction of the wounded area, better healing time, greater vascular density, and collagen formation. Interestingly, when evaluating biomechanical characteristics, better results were found when stem cells were combined with amniotic membranes. Based on these, we infer that stem cells derived from adipose and umbilical cord tissues of human origin, combined with acellular amniotic membranes, are a promising option in the treatment of wounds and burns. Although further clinical trials are needed, these investigations showed promising results that may promote the use of these biological scaffolds in humans, as part of a regenerative therapy.

## ACKNOWLEDGEMENT

The authors thank the University of La Sabana, for facilitating access to content in databases; the financial support through the project MED-291-2020.

## AUTHOR CONTRIBUTIONS

V. G. conceptualization, data curation, formal analysis, investigation, methodology, project administration, and writing original draft; G. M. data curation, formal analysis, investigation, software, visualization, and writing original draft; K. S. data curation, formal analysis, investigation, and writing original draft; D. E. funding data curation, supervision, validation, and writing-review and editing; S. T. funding data curation, supervision, validation, and writing-review and editing; L. A. G. conceptualization, funding data curation, resources, supervision, validation, and writing-review and editing.



## REFERENCES

- [1] D. Queen and K. Harding, "What's the true costs of wounds faced by different healthcare systems around the world?," *Int. Wound J.*, vol. 20, no. 10, pp. 3935-3938, 2023, doi: <https://doi.org/10.1111/iwj.14491>
- [2] S. Bowers and E. Franco, "Chronic Wounds: Evaluation and Management," *Am. Fam. Physician*, vol. 101, no. 3, pp. 159-166, 2020. [Online]. Available: <https://www.aafp.org/pubs/afp/issues/2020/0201/p159.html>
- [3] K. Las Heras, M. Igartua, E. Santos-Vizcaino, and R. M. Hernandez, "Chronic wounds: Current status, available strategies and emerging therapeutic solutions," *J. Control. Release*, vol. 328, pp. 532-550, 2020. doi: <https://doi.org/10.1016/j.jconrel.2020.09.039>
- [4] A. M. Jorgensen, M. Varkey, A. Gorkun, C. Clouse, et al., "Bioprinted Skin Recapitulates Normal Collagen Remodeling in Full-Thickness Wounds," *Tissue Eng. Part A*, vol. 26, no. 9-10, pp. 512-526, 2020, doi: <https://doi.org/10.1089/ten.tea.2019.0319>
- [5] R. D. Galiano, O. M. Tepper, C. R. Pelo, K. A. Bhatt, et al., "Topical vascular endothelial growth factor accelerates diabetic wound healing through increased angiogenesis and by mobilizing and recruiting bone marrow-derived cells," *Am. J. Pathol.*, vol. 164, no. 6, pp. 1935-1947, 2004, doi: [https://doi.org/10.1016/s0002-9440\(10\)63754-6](https://doi.org/10.1016/s0002-9440(10)63754-6)
- [6] C. K. Sen, "Human Wound and Its Burden: Updated 2020 Compendium of Estimates," *Adv. Wound Care*, vol. 10, no. 5., pp. 281-292, 2021. doi: <https://doi.org/10.1089/wound.2021.0026>
- [7] V. Sabapathy, B. Sundaram, S. V. M., P. Mankuzhy, and S. Kumar, "Human wharton's jelly mesenchymal stem cells plasticity augments scar-free skin wound healing with hair growth," *PLoS One*, vol. 9, no. 4, 2014, art. no. e93726, doi: <https://doi.org/10.1371/journal.pone.0093726>
- [8] A. Hassanshahi, M. Hassanshahi, S. Khabbazi, Z. Hosseini-Khah, et al., "Adipose-derived stem cells for wound healing," *J. Cell. Physiol.*, vol. 234, no. 6, pp. 7903-7914, 2019, doi: <https://doi.org/10.1002/jcp.27922>
- [9] L. Mazini, L. Rochette, B. Admou, S. Amal, and G. Malka, "Hopes and limits of adipose-derived stem cells (ADSCs) and mesenchymal stem cells (MSCs) in wound healing," *Int. J. Mol. Sci.*, vol. 21, no. 4, 2020, art. no. 1306, doi: <https://doi.org/10.3390/ijms21041306>
- [10] A. R. Khalatbary, M. Omraninava, D. Nasiry, M. Akbari, et al., "Exosomes derived from human adipose mesenchymal stem cells loaded bioengineered three-dimensional amniotic membrane-scaffold-accelerated diabetic wound healing," *Arch. Dermatol. Res.*, vol. 315, no. 10, pp. 2853-2870, 2023, doi: <https://doi.org/10.1007/s00403-023-02709-z>
- [11] B. A. Aguado, W. Mulyasmita, J. Su, K. J. Lampe, and S. C. Heilshorn, "Improving viability of stem cells during syringe needle flow through the design of hydrogel cell carriers," *Tissue Eng. Part A*, vol. 18, no. 7-8, pp. 806-815, 2012, doi: <https://doi.org/10.1089/ten.tea.2011.0391>
- [12] J. Elango, C. Zamora-Ledezma, and J. E. Maté-Sánchez de Val, "Natural vs Synthetic Polymers: How Do They Communicate with Cells for Skin Regeneration—A Review," *J. Compos. Sci.*, vol. 7, no. 9, 2023, art. no. 385, doi: <https://doi.org/10.3390/jcs7090385>
- [13] G. Satchanska, S. Davidova, and P. D. Petrov, "Natural and Synthetic Polymers for Biomedical and Environmental Applications," *Polymers*, vol. 16, no. 8, 2024, art. no. 1159, doi: <https://doi.org/10.3390/polym16081159>
- [14] A. L. Ingraldi, R. G. Audet, and A. J. Tabor, "The Preparation and Clinical Efficacy of Amnion-Derived Membranes: A Review," *J. Funct. Biomateri.*, vol. 14, no. 10, 2023, art. no. 531, doi: <https://doi.org/10.3390/jfb14100531>
- [15] Z. Zhou, J. Xun, C. Wu, C. Ji, et al., "Acceleration of burn wound healing by micronized amniotic membrane seeded with umbilical cord-derived mesenchymal stem cells," *Mater. Today Bio.*, vol. 20, 2023, art. no. 100686, doi: <https://doi.org/10.1016/j.mtbio.2023.100686>
- [16] S. Doudi, M. Barzegar, E. A. Taghavi, A. Ehterami, et al., "Applications of acellular human amniotic membrane in regenerative medicine," *Life Sci.*, vol. 310, 2022, art. no. 121032, doi: <https://doi.org/10.1016/j.lfs.2022.121032>
- [17] V. Moghimi, J. Rahvarian, Z. Esmaeilzadeh, N. Mohammad-Pour, et al., "Adipose-derived human mesenchymal stem cells seeded on denuded or stromal sides of the amniotic membrane improve angiogenesis and collagen remodeling and accelerate healing of the full-thickness wound," *Acta Histochem.*, vol. 125, no. 3, 2023, art. no. 152027, doi: <https://doi.org/10.1016/j.acthis.2023.152027>
- [18] H. R. Aghayan, M. S. Hosseini, M. Gholami, F. Mohamadi-Jahani, et al., "Mesenchymal stem cells' seeded amniotic membrane as a tissue- engineered dressing for wound healing," *Drug Deliv. Transl. Res.*, vol. 12, no. 3, pp. 538-549, 2022, doi: <https://doi.org/10.1007/s13346-021-00952-3>
- [19] S. Xiao, C. Xiao, Y. Miao, J. Wang, R. Chen, Z. Fan, Z. Hu, "Human acellular amniotic membrane incorporating exosomes from adipose-derived mesenchymal stem cells promotes diabetic wound healing," *Stem Cell Res. Ther.*, vol. 12, no. 1, 2021, art. no. 255, doi: <https://doi.org/10.1186/s13287-021-02333-6>
- [20] S. S. Hashemi, M. R. Pourfath, A. Derakhshanfar, A. Behzad-Behbahani, and J. Moayedi, "The role of labeled cell therapy with and without scaffold in early excision burn wounds in a rat animal model," *Iran J. Basic Med. Sci.*, vol. 23, no. 5, pp. 673-679, 2020, doi: <https://doi.org/10.22038/ijbms.2020.34324.8156>

- [21] W. Minjuan, X. Jun, S. Shiyun, N. Haitao, et al., "Hair Follicle Morphogenesis in the Treatment of Mouse Full- Thickness Skin Defects Using Composite Human Acellular Amniotic Membrane and Adipose Derived Mesenchymal Stem Cells," *Stem Cells Int.*, vol. 2016, 2016, art. no. 8281235, doi: <https://doi.org/10.1155/2016/8281235>
- [22] P. Chen, M. Lu, T. Wang, D. Dian, Y. Zhong, and M. Aleahmad, "Human amniotic membrane as a delivery vehicle for stem cell-based therapies," vol. 272, 2021, art. no. 119157, doi: <https://doi.org/10.1016/j.lfs.2021.119157>
- [23] M. Fénelon, S. Catros, C. Meyer, J.-C. Fricain, et al., "Applications of human amniotic membrane for tissue engineering," *Membranes*, vol. 11, no. 6, 2021, art. no. 387, doi: <https://doi.org/10.3390/membranes11060387>
- [24] A. Trounson and C. McDonald, "Stem Cell Therapies in Clinical Trials: Progress and Challenges," *Cell Stem Cell.*, vol. 17, no. 1. pp. 11-22, 2015, doi: <https://doi.org/10.1016/j.stem.2015.06.007>
- [25] E. Mirzadegan, H. Golshahi, and S. Kazemnejad, "Current evidence on immunological and regenerative effects of menstrual blood stem cells seeded on scaffold consisting of amniotic membrane and silk fibroin in chronic wound," *Int. Immunopharmacol.*, vol. 85, 2020, art. no. 106595, doi: <https://doi.org/10.1016/j.intimp.2020.106595>
- [26] A. M. Murthi and M. Lankachandra, "Technologies to Augment Rotator Cuff Repair," *Orthop. Clin. North Am.*, vol. 50, no. 1, pp. 103-108, 2019, doi: <https://doi.org/10.1016/j.oct.2018.08.005>
- [27] A. L. Takejima, J. C. Francisco, R. B. Simeoni, L. Noronha, et al., "Role of mononuclear stem cells and decellularized amniotic membrane in the treatment of skin wounds in rats," *Tissue Barriers*, vol. 10, no. 2, 2022, art. no. 1982364, doi: <https://doi.org/10.1080/21688370.2021.1982364>
- [28] S. Iranpour, N. Mahdavi-Shahri, R. Miri, H. Hasanzadeh, et al., "Supportive properties of basement membrane layer of human amniotic membrane enable development of tissue engineering applications," *Cell Tissue Bank*, vol. 19, no. 3, pp. 357-371, 2018, doi: <https://doi.org/10.1007/s10561-017-9680-z>
- [29] M. Salazar Dobrosky, "Utilización de membrana amniótica como apósito biológico en quemaduras y heridas cutáneas," *Rev. Med. Sinerg.*, vol. 7, no. 11, 2022, art. no. e912, doi: <https://doi.org/10.31434/rms.v7i11.912>
- [30] C. L. Insausti, M. Rodríguez, G. Castellanos, and J. M. Moraleda, "Amniotic membrane-derived stem cells: immunomodulatory properties and potential clinical application," *Rev. Hematol. Mex.*, vol. 15, no. 1, pp. 11-20, 2014. [Online]. Available: <https://revistadehematologia.org.mx/article/propiedades-inmunomoduladoras-de-las-celulas-madre-de-la-membrana-amniotica-nuevas-perspectivas/>
- [31] R. Saleh and H. M. Reza, "Short review on human umbilical cord lining epithelial cells and their potential clinical applications," *Stem Cell Res. Ther.*, vol. 8, no. 1, 2017, art. no. 222 doi: <https://doi.org/10.1186/s13287-017-0679-y>

## ANNEXE



### PRISMA 2020 for Abstracts Checklist

| Section and Topic       | Item # | Checklist item  | Reported (Yes/No) |
|-------------------------|--------|---|-------------------|
| <b>TITLE</b>            |        |   |                   |
| Title                   | 1      | Identify the report as a systematic review.   | Yes               |
| <b>BACKGROUND</b>       |        |   |                   |
| Objectives              | 2      | Provide an explicit statement of the main objective(s) or question(s) the review addresses.   | Yes               |
| <b>METHODS</b>          |        |   |                   |
| Eligibility criteria    | 3      | Specify the inclusion and exclusion criteria for the review.  | Yes               |
| Information sources     | 4      | Specify the information sources (e.g. databases, registers) used to identify studies and the date when each was last searched.  | Yes               |
| Risk of bias            | 5      | Specify the methods used to assess risk of bias in the included studies.  | No                |
| Synthesis of results    | 6      | Specify the methods used to present and synthesise results.   | Yes               |
| <b>RESULTS</b>          |        |   |                   |
| Included studies        | 7      | Give the total number of included studies and participants and summarise relevant characteristics of studies.   | Yes               |
| Synthesis of results    | 8      | Present results for main outcomes, preferably indicating the number of included studies and participants for each. If meta-analysis was done, report the summary estimate and confidence/credible interval. If comparing groups, indicate the direction of the effect (i.e. which group is favoured). | Yes               |
| <b>DISCUSSION</b>       |        |   |                   |
| Limitations of evidence | 9      | Provide a brief summary of the limitations of the evidence included in the review (e.g. study risk of bias, inconsistency and imprecision).   | Yes               |
| Interpretation          | 10     | Provide a general interpretation of the results and important implications.   | Yes               |
| <b>OTHER</b>            |        |   |                   |
| Funding                 | 11     | Specify the primary source of funding for the review.   | Yes               |
| Registration            | 12     | Provide the register name and registration number.  | No                |



**PRISMA 2020 Checklist**

| Section and Topic             | Item # | Checklist item   | Location where item is reported |
|-------------------------------|--------|--|---------------------------------|
| <b>TITLE</b>                  |        |  |                                 |
| Title                         | 1      | Identify the report as a systematic review.  | Page 1                          |
| <b>ABSTRACT</b>               |        |  |                                 |
| Abstract                      | 2      | See the PRISMA 2020 for Abstracts checklist.   | Page 12                         |
| <b>INTRODUCTION</b>           |        |  |                                 |
| Rationale                     | 3      | Describe the rationale for the review in the context of existing knowledge.  | Page 2                          |
| Objectives                    | 4      | Provide an explicit statement of the objective(s) or question(s) the review addresses.   | Page 4                          |
| <b>METHODS</b>                |        |  |                                 |
| Eligibility criteria          | 5      | Specify the inclusion and exclusion criteria for the review and how studies were grouped for the syntheses.  | Page 5                          |
| Information sources           | 6      | Specify all databases, registers, websites, organisations, reference lists and other sources searched or consulted to identify studies. Specify the date when each source was last searched or consulted.  | Page 5                          |
| Search strategy               | 7      | Present the full search strategies for all databases, registers and websites, including any filters and limits used.   | Pages 5                         |
| Selection process             | 8      | Specify the methods used to decide whether a study met the inclusion criteria of the review, including how many reviewers screened each record and each report retrieved, whether they worked independently, and if applicable, details of automation tools used in the process.                     | Page 5                          |
| Data collection process       | 9      | Specify the methods used to collect data from reports, including how many reviewers collected data from each report, whether they worked independently, any processes for obtaining or confirming data from study investigators, and if applicable, details of automation tools used in the process. | Page 5                          |
| Data items                    | 10a    | List and define all outcomes for which data were sought. Specify whether all results that were compatible with each outcome domain in each study were sought (e.g. for all measures, time points, analyses), and if not, the methods used to decide which results to collect.                        | Page 5                          |
|                               | 10b    | List and define all other variables for which data were sought (e.g. participant and intervention characteristics, funding sources). Describe any assumptions made about any missing or unclear information.   | Page 5                          |
| Study risk of bias assessment | 11     | Specify the methods used to assess risk of bias in the included studies, including details of the tool(s) used, how many reviewers assessed each study and whether they worked independently, and if applicable, details of automation tools used in the process.                                    | Page 5                          |
| Effect measures               | 12     | Specify for each outcome the effect measure(s) (e.g. risk ratio, mean difference) used in the synthesis or presentation of results.  | NA                              |
| Synthesis methods             | 13a    | Describe the processes used to decide which studies were eligible for each synthesis (e.g. tabulating the study intervention characteristics and comparing against the planned groups for each synthesis (item #5)).   | Pages 5                         |
|                               | 13b    | Describe any methods required to prepare the data for presentation or synthesis, such as handling of missing summary statistics, or data conversions.  | Page 5                          |
|                               | 13c    | Describe any methods used to tabulate or visually display results of individual studies and syntheses.   | Pages 5                         |
|                               | 13d    | Describe any methods used to synthesize results and provide a rationale for the choice(s). If meta-analysis was performed, describe the model(s), method(s) to identify the presence and extent of statistical heterogeneity, and software package(s) used.  | NA                              |
|                               | 13e    | Describe any methods used to explore possible causes of heterogeneity among study results (e.g. subgroup analysis, meta-regression).   | NA                              |
|                               | 13f    | Describe any sensitivity analyses conducted to assess robustness of the synthesized results.   | NA                              |
| Reporting bias assessment     | 14     | Describe any methods used to assess risk of bias due to missing results in a synthesis (arising from reporting biases).  | NA                              |
| Certainty assessment          | 15     | Describe any methods used to assess certainty (or confidence) in the body of evidence for an outcome.  | NA                              |



**PRISMA 2020 Checklist**

| Section and Topic                              | Item # | Checklist item   | Location where item is reported |
|--|--------|--|---------------------------------|
| <b>RESULTS</b>                                 |        |  |                                 |
| Study selection                                | 16a    | Describe the results of the search and selection process, from the number of records identified in the search to the number of studies included in the review, ideally using a flow diagram.   | Pages 5-6                       |
|  | 16b    | Cite studies that might appear to meet the inclusion criteria, but which were excluded, and explain why they were excluded.  | Pages 5-6                       |
| Study characteristics                          | 17     | Cite each included study and present its characteristics.  | Pages 7-10                      |
| Risk of bias in studies                        | 18     | Present assessments of risk of bias for each included study.   | -                               |
| Results of individual studies                  | 19     | For all outcomes, present, for each study: (a) summary statistics for each group (where appropriate) and (b) an effect estimate and its precision (e.g. confidence/credible interval), ideally using structured tables or plots.   | NA                              |
| Results of syntheses                           | 20a    | For each synthesis, briefly summarise the characteristics and risk of bias among contributing studies.   | NA                              |
|  | 20b    | Present results of all statistical syntheses conducted. If meta-analysis was done, present for each the summary estimate and its precision (e.g. confidence/credible interval) and measures of statistical heterogeneity. If comparing groups, describe the direction of the effect. | NA                              |
|  | 20c    | Present results of all investigations of possible causes of heterogeneity among study results.   | NA                              |
|  | 20d    | Present results of all sensitivity analyses conducted to assess the robustness of the synthesized results.   | NA                              |
| Reporting biases                               | 21     | Present assessments of risk of bias due to missing results (arising from reporting biases) for each synthesis assessed.  | NA                              |
| Certainty of evidence                          | 22     | Present assessments of certainty (or confidence) in the body of evidence for each outcome assessed.  | NA                              |
| <b>DISCUSSION</b>                              |        |  |                                 |
| Discussion                                     | 23a    | Provide a general interpretation of the results in the context of other evidence.  | Pages 10-11                     |
|  | 23b    | Discuss any limitations of the evidence included in the review.  | Pages 10-11                     |
|  | 23c    | Discuss any limitations of the review processes used.  | Pages 10-11                     |
|  | 23d    | Discuss implications of the results for practice, policy, and future research.   | Page 11                         |
| <b>OTHER INFORMATION</b>                       |        |  |                                 |
| Registration and protocol                      | 24a    | Provide registration information for the review, including register name and registration number, or state that the review was not registered.   |                                 |
|  | 24b    | Indicate where the review protocol can be accessed, or state that a protocol was not prepared.   |                                 |
|  | 24c    | Describe and explain any amendments to information provided at registration or in the protocol.  |                                 |
| Support  | 25     | Describe sources of financial or non-financial support for the review, and the role of the funders or sponsors in the review.  | Page 12                         |
| Competing interests                            | 26     | Declare any competing interests of review authors.   | Page 12                         |
| Availability of data, code and other materials | 27     | Report which of the following are publicly available and where they can be found: template data collection forms; data extracted from included studies; data used for all analyses; analytic code; any other materials used in the review.   | Pages 14-17                     |

<https://dx.doi.org/10.17488/RMIB.45.3.4>

E-LOCATION ID: 1442

## Low-Cost Portable Pupilometer for Circadian Rhythm Studies

### Pupilómetro Portátil de bajo costo para Estudios de Ritmo Circadiano

Ingrid Ameyalli Hernández-Barríos<sup>1</sup> , Edgar Guevara<sup>2</sup>  

<sup>1</sup>Universidad Autónoma de San Luis Potosí, Instituto de Investigación en Comunicación Óptica, San Luis Potosí - México

<sup>2</sup>Consejo Nacional de Humanidades, Ciencias y Tecnologías / Universidad Autónoma de San Luis Potosí, San Luis Potosí - México

#### ABSTRACT

Given the price tag of commercially available devices, developing a low-cost, portable pupilometer based on the Raspberry Pi platform is significant for advancing clinical and research applications in neurology and circadian rhythm studies. This study aimed to design and characterize a pupilometer capable of assessing pupillary light response (PLR) to different wavelengths and its relationship with circadian cycles. Using a Raspberry Pi, a no-infrared filter (NoIR) camera, and custom software, the device was tested on a healthy 24-year-old female subject over 20 days, measuring responses to 635 nm (red) and 463 nm (blue) light stimuli at two daily intervals (8:00 AM and 8:00 PM) in both eyes. Results showed that blue light induced greater pupillary constriction than red light ( $F(1)=284.37$ ,  $p=6.9e-27$ ), with more pronounced responses in the morning ( $F(1)=12.02$ ,  $p=0.001$ ), likely due to higher parasympathetic activity. Significant lateral asymmetry ( $F(1)=12.36$ ,  $p=0.0008$ ) was also observed in the pupillary response to blue light, suggesting potential intracranial factors. These findings demonstrate the pupilometer's efficacy in capturing detailed pupillary dynamics, proposing its utility to evaluate pupillary light response in connection with circadian rhythms and lateral asymmetry, providing an affordable solution.

**KEYWORDS:** biomedical instrumentation, circadian rhythms, pupillometry

## RESUMEN

Dado el precio de los dispositivos disponibles en el mercado, el desarrollo de un pupilómetro portátil de bajo coste basado en la plataforma Raspberry Pi es importante para avanzar en las aplicaciones clínicas y de investigación en neurología y estudios del ritmo circadiano. Este estudio tuvo como objetivo diseñar y caracterizar un pupilómetro capaz de evaluar la respuesta pupilar a la luz (PLR) a diferentes longitudes de onda y su relación con los ciclos circadianos. Utilizando una Raspberry Pi, una cámara sin filtro infrarrojo (NoIR) y software personalizado, el dispositivo se probó en una mujer sana de 24 años durante 20 días, midiendo las respuestas a estímulos de luz de 635 nm (rojo) y 463 nm (azul) en dos intervalos diarios (8:00 AM y 8:00 PM) en ambos ojos. Los resultados mostraron que la luz azul inducía una mayor constricción pupilar que la luz roja ( $F(1)=284.37$ ,  $p=6.9e-27$ ), con respuestas más pronunciadas por la mañana ( $F(1)=12.02$ ,  $p=0.001$ ), probablemente debido a una mayor actividad parasimpática. También se observó una asimetría lateral significativa ( $F(1)=12.36$ ,  $p=0.0008$ ) en la respuesta pupilar a la luz azul, lo que sugiere posibles factores intracraneales. Estos hallazgos demuestran la eficacia del pupilómetro para captar la dinámica pupilar detallada, proponiendo su utilidad para evaluar la respuesta pupilar a la luz en relación con los ritmos circadianos y la asimetría lateral, proporcionando una solución asequible.

**PALABRAS CLAVE:** instrumentación biomédica, pupilometría, ritmo circadiano

### Corresponding author

TO: Edgar Guevara

INSTITUTION: Universidad Autónoma de San Luis Potosí

ADDRESS: SIERRA LEONA 550, LOMAS 2ª SECC., CP 78210, SAN LUIS POTOSÍ, SLP, MEXICO.

EMAIL: edgar.guevara@uaslp.mx

**Received:**

06 June 2024

**Accepted:**

26 September 2024

## INTRODUCTION

The measurement of pupillary light response (PLR) is crucial in clinical and research settings for evaluating neurological functions and circadian rhythms. Pupillometry, the study of pupil dynamics, has been widely used to assess autonomic nervous system activity, diagnose various neurological disorders, and understand sleep-wake cycles <sup>[1]</sup>. However, current pupilometers, often used in clinical and research environments, are expensive and not easily accessible for all institutions or researchers <sup>[2]</sup>. This gap highlights the need for developing cost-effective, portable devices that can provide reliable data on pupillary responses.

Despite the advancements in pupillometry, there remains a significant disparity between the available high-cost, high-precision instruments and the need for affordable alternatives that maintain accuracy and usability <sup>[3]</sup>. The scientific community has expressed a strong desire for more accessible tools to facilitate broader research and clinical applications <sup>[4]</sup>. This need is particularly pressing in low-resource settings and for small-scale studies where budget constraints limit the use of sophisticated equipment <sup>[3][5][6]</sup>.

Results from Lobato-Rincón *et al.* <sup>[7]</sup> indicated that the pupillary response amplitude was highest and latency shortest under white and green light for all subjects. Age significantly influenced PLR, with older adults exhibiting increased latency for white light and reduced constriction velocity for green light. Additionally, red light produced the smallest amplitude responses and most prolonged latencies, suggesting lower sensitivity to this wavelength. These findings underscore the age-related variations in PLR and highlight the necessity of incorporating different wavelengths in pupillometric studies to enhance understanding of autonomic nervous system integrity and its diagnostic potential. Moreover, Privitera *et al.* <sup>[8]</sup> emphasized the importance of pupillary response differentials in serving as a critical prognostic indicator and incorporating them into routine assessments of neurologically injured patients. The presence of a differential is associated with worse outcomes, highlighting the need for clinicians to monitor both eyes' pupillary response values to predict patient recovery trajectories better. Bonmati-Carrion *et al.* <sup>[9]</sup> explored the relationship between the human PLR and circadian system status, highlighting the importance of lateralization in pupil response. Intrinsically photosensitive retinal ganglion cells (ipRGCs), which contain the photopigment melanopsin, play a crucial role in both the regulation of PLR and the entrainment of circadian rhythms through their connections to the olivary pretectal nucleus (OPN) and the suprachiasmatic nuclei (SCN). The study demonstrated that a robust circadian system, characterized by high stability and low internal desynchronization, correlates with a reduced PLR to blue light (460-490 nm). This correlation suggests that pupillometry can be a non-invasive tool to assess circadian system integrity and function, providing valuable insights into the interplay between light exposure, pupillary response, and circadian health. Furthermore, Münch *et al.* <sup>[10]</sup> investigated how the PLR varies with circadian phases and levels of wakefulness. The study highlighted the role of ipRGCs in circadian regulation and PLR. Their findings indicated that the pupil's response to blue light, which primarily stimulates ipRGCs, showed significant circadian modulation. This modulation was evident through a stronger post-stimulus pupil constriction during the night, correlating with higher melatonin levels, and a reduced response closer to wake times. In contrast, responses to red light were more influenced by subjective sleepiness rather than circadian rhythms.

These findings underscore the importance of considering circadian and wake-dependent factors when evaluating PLR, particularly in clinical settings where accurate autonomic and circadian function assessment is critical. The

study demonstrates that the PLR, especially in response to blue light, can serve as a valuable non-invasive marker for circadian rhythm and overall neurological health.

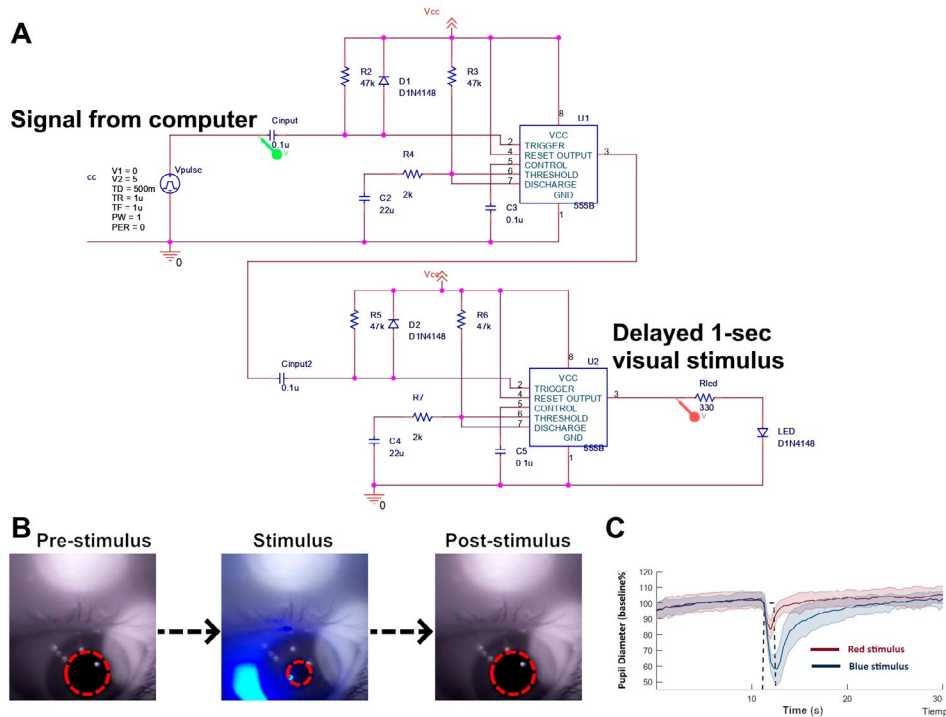
We developed a low-cost, portable pupilometer using the Raspberry Pi platform in response to this need. This device is designed to measure pupillary responses to different light wavelengths and evaluate their relationship with circadian rhythms and lateral asymmetry. By leveraging affordable technology and open-source software, our pupilometer offers a practical solution for researchers and clinicians who require reliable pupillometric data without the financial burden of high-end equipment.

The remainder of this paper is structured as follows: first, we provide a detailed overview of the materials and methods used to develop and characterize the pupilometer. Next, we present the results of our validation study, including the pupillary response data collected from our test subject. At the same time, we discuss the implications of our findings, potential applications of the device, and the limitations of our study. Finally, we conclude with suggestions for future research directions and potential improvements to the device.

## **MATERIALS AND METHODS**

### **Development of the instrument and data acquisition**

This low-cost portable pupilometer was based on the Raspberry Pi3 with a NoIR V2 camera with a Sony IMX219PQ back-illumination CMOS sensor, operating in the visible (400-700 nm) and near-infrared (800-2500 nm) spectral range. The Raspberry Pi 3 and NoIR V2 camera were chosen for this study due to their combination of affordability, availability, and technical capabilities. The Raspberry Pi 3, a widely available single-board computer, was selected for its ability to handle real-time image acquisition while maintaining a low cost, which is critical for developing accessible biomedical instruments. The NoIR V2 camera, compatible with the Raspberry Pi, was chosen for its capacity to capture high-quality images across the visible and near-infrared spectrum, essential for accurately measuring pupillary light response, as our previous work reported its sensor noise, linearity and spatial resolution <sup>[11]</sup>. These components were determined to be the most suitable options that meet the project's requirements for cost-effectiveness, availability, and functionality. While these components effectively fulfilled the needs of this study, future iterations of the device may consider integrating higher-resolution cameras or more powerful processing units to enhance performance further. The camera was software controlled from the Python programming language using the PiCamara API application programming interface. An external timer electronic circuit was added to provide a delayed visual stimulus while recording video (Figure 1A). Since microprocessor-based systems are not inherently capable of performing parallel tasks, this circuit was used to add a delay and duration to the stimulus, ensuring that the pupilometer was recording before the stimulus was presented, thereby allowing the complete time course of the pupillary response to be captured. Images in raw data format were preprocessed (contrast-adjusted and format-converted) on the Raspberry Pi with Python and then handled in MATLAB R2017b and ImageJ 1.52p for further analysis.



**FIGURE 1. Experimental setup: (A) Electronic circuit for delayed stimulus; (B) Example of stimulation sequence and typical pupillary responses; (C) Corresponding time course of pupillary response to different stimuli wavelengths.**

## Experimental protocol

The study was conducted with a 24-year-old female participant in good ocular and general health according to her routine medical checkup. Measurements were carried out over a period of 20 days, which were chosen according to a sample size computation. Two measurement sessions were performed each day, one in the morning (8:00 AM) and one in the evening (8:00 PM), to evaluate pupillary responses at different times of the circadian cycle. This 12 hour difference between sessions was chosen per the work of Münch *et al.* [10]. According to Tekin *et al.* [12], each light stimulus lasted 200 milliseconds and was provided at random to prevent biases in the pupillary response; an example of pupillary response can be seen in panel B of Figure 1. Ambient lighting conditions were kept constant throughout the experiment to ensure uniformity of measurements, by turning all artificial light off and shutting the door of the room where the experiments were carried out. Two types of light stimuli were used: red light (635 nm) and blue light (463 nm), as depicted in Figure 1C. These stimuli were selected because of their differential influence on retinal photopigments and their relevance to circadian modulation and because it has been found that both stimuli produced reliable and repeatable pupillary responses, with no significant difference in repeated measures [13][14]. Each measurement session included multiple repetitions for each stimulus type, with 10 repetitions per stimulus in each session, resulting in a total of 800 measurements. This allowed averaging and reduced intraindividual variability in pupillary responses. Before each measurement session, the participant underwent a 10-minute dark adaptation period. During this time, the participant remained in a room with controlled lighting to stabilize the pupillary diameter before exposure to stimuli. Our dynamic pupillometer was used to record pupillary diameter before, during, and after the presentation of the light stimuli, as illustrated in Figure 2. Measurements were taken at a rate of 25 frames per second, allowing rapid changes in pupillary diameter to be captured.



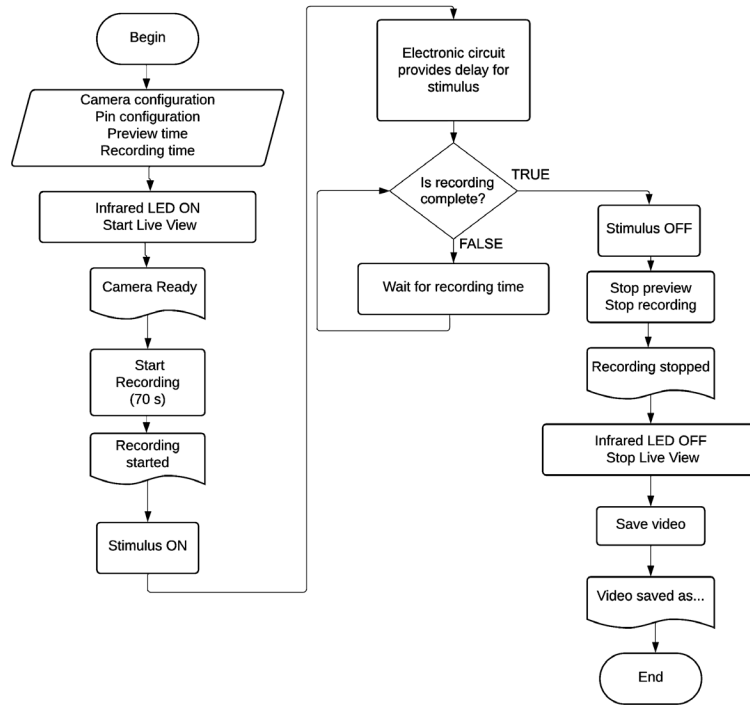


FIGURE 2. Flow chart showing the operation of the pupillometer.

## Image processing and statistical Analysis

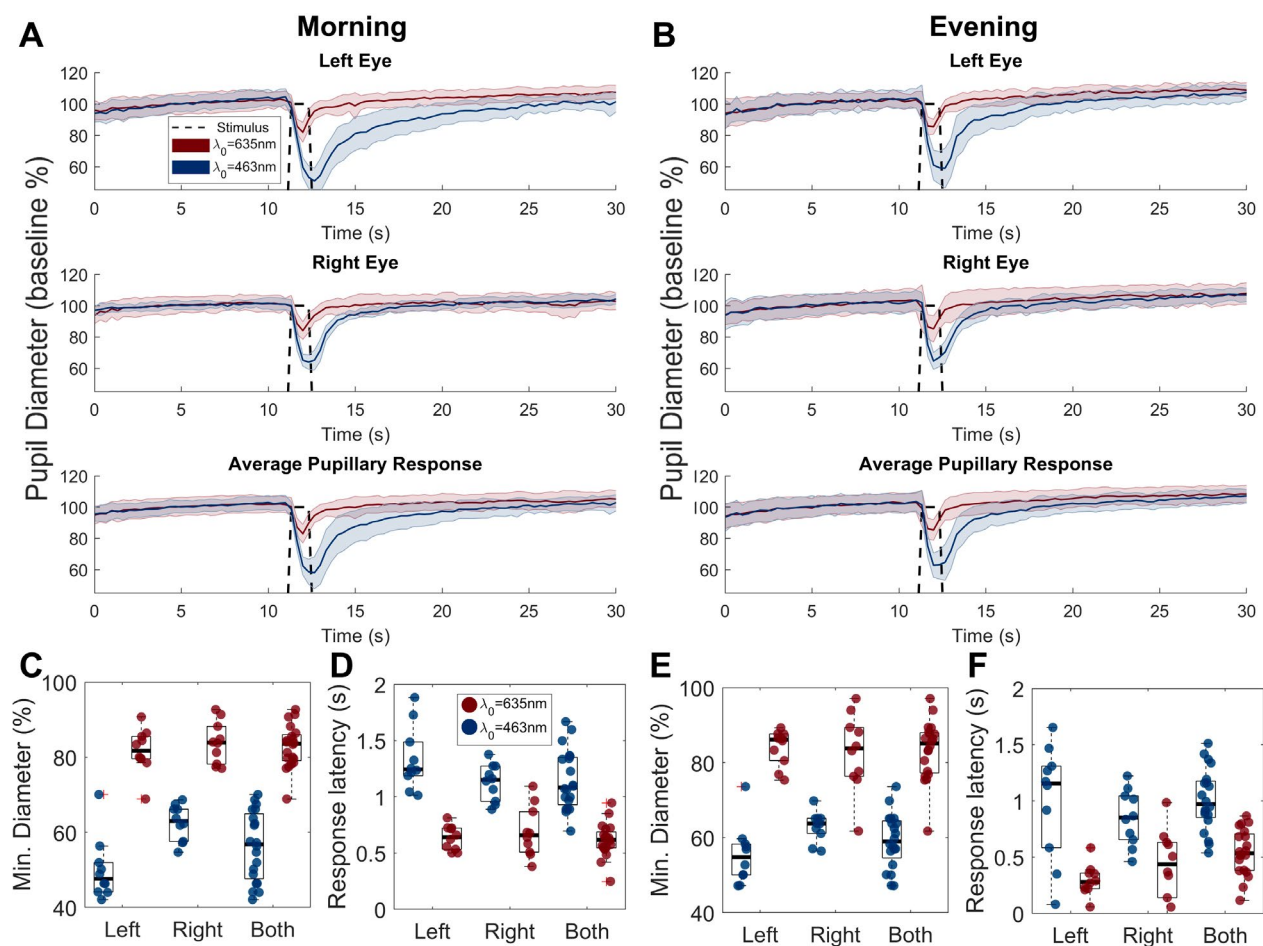
Pupil diameter was manually obtained from the image series in ImageJ software v1.52p, with the ellipse selection tool as depicted with a dotted red line in Figure 1B, and then all subsequent analyses were carried out in MATLAB R2017b (Mathworks Inc., Natick, MA). Pupillary response measurements were analyzed to determine minimal pupillary contraction amplitude and response latency [9]. Results were compared between morning and afternoon sessions to identify possible circadian variations.

The Shapiro-Wilk test was used to assess the normality of our data, as it is the method that has demonstrated the greatest statistical power [15][16]. Simultaneously, Q-Q plots were produced to appreciate the distribution of our data visually. For data that do not show a normal distribution, quantile normalization was performed before comparison between groups, which involves first ranking the pupillary response time of each sample by magnitude, calculating the average value of pupillary response times occupying the same range, and then replacing the values of all response times occupying that range with this average value. The next step is to rearrange these response times of each sample in their original arrangement [17]. To compare the time and minimum diameter (maximum constriction) of the pupillary response between groups, a 3-way analysis of variance (ANOVA) was performed with the factors: time of acquisition, wavelength, and eye laterality. Tukey-Kramer-type corrections were then performed for multiple comparisons [18].

## RESULTS AND DISCUSSION

The average pupillary responses are shown in Figure 3; panel A contains the results from the 8:00 AM (morning) experiment, and panel B contains the results from the 8:00 PM (evening experiments). The red curve depicts the average response to the stimulus at 635 nm and the blue curve shows the average response to the stimulus at 463

nm. Standard deviation is denoted by the shading around the average responses. The black dotted line marks stimulus duration and onset. It can be appreciated from the graphs that the 635nm stimulus elicits a reduced and earlier response than the 463nm stimulus, regardless of the time of the experiment and lateralization (left or right eye). Two features were extracted from these curves: the minimum diameter of the pupillary response and the time at which this minimum diameter was achieved, i.e., the response latency. Figures 3C and E show the minimum diameter during the morning and evening experiments. Despite the different times, the minimum diameter is always smaller for the 463nm stimulus, i.e., a greater constriction is reached with blue light stimuli. These results are supported by the work of Kardon *et al.* [14] where they compared chromatic pupil responses and found that blue light stimuli preferentially activate melanopsin-mediated responses, leading to greater pupil constriction than red light stimuli, especially at lower intensities. This is significant for understanding the distinct roles of different photoreceptors. Figures 3D and F show the response latency during the morning and evening experiments. It can be observed that the response latency is always greater for blue light stimuli than for red light stimuli. Furthermore, this response latency is greater during the morning experiments for both stimuli, suggesting a circadian effect in the pupillary response.



**FIGURE 3.** Pupillometry results. (A) Pupillary response for the morning experiment (8:00 AM) for the left eye, right eye and their average; (B) same as A but for the evening experiment (8:00 PM); (C) Minimum diameter for both wavelengths during the morning experiment; (D) Response latency for both wavelengths for the morning experiment; (E) same as C but for the evening experiment and (F) same as D, but for the evening experiment.

Table 1 shows the results from the 3-way ANOVA based on maximum constriction (minimum diameter) data. There was no significant difference ( $F(1, 73) = 1.29, p = 0.2597$ ) in the pupillary response based on the time of the experiment (8:00 AM vs. 8:00 PM). There was a highly substantial difference ( $F(1, 73) = 284.37, p = 6.9e-27$ ) in the pupillary response between red (635 nm) and blue (463 nm) light stimuli, with blue eliciting a significantly greater constriction than red. Our results indicated a significant difference in the pupillary response between the left and right eyes ( $F(1, 73) = 12.36, p = 0.0008$ ), where the left eye consistently showed greater constriction than the right eye. Finally, the effect of color on the pupillary response differs significantly between the left and right eyes ( $F(1, 73) = 10.24, p = 0.0020$ ). Table 2 presents the results of a post-hoc Tukey-Kramer test for repeated measures, analyzing the differences in the minimum diameter of the pupillary response between various combinations of Color and Side (left or right eye). The pupillary response was generally smaller for blue light than red light in both eyes, with significant differences observed. Also, there is a significant lateral difference in the pupillary response to blue light, with the right eye showing a larger response (lesser constriction) than the left eye. Finally, no significant lateral difference is observed in the response to red light between the right and left eyes.

**TABLE 1. Analysis of variance for the minimum diameter data as the dependent variable. Statistical significance is denoted with bold figures.**

| Source     | Constrained Type III sum of squares | d.f. | Mean Square | F      | Prob>F         |
|------------|-------------------------------------|------|-------------|--------|----------------|
| Time       | 58.24                               | 1    | 58.24       | 1.29   | 0.2597         |
| Color      | 12837.09                            | 1    | 12837.09    | 284.37 | <b>6.9e-27</b> |
| Side       | 558.15                              | 1    | 558.15      | 12.36  | <b>0.0008</b>  |
| Time*Color | 26.66                               | 1    | 26.66       | 0.59   | 0.4447         |
| Time*Side  | 85.14                               | 1    | 85.14       | 1.89   | 0.1739         |
| Color*Side | 462.38                              | 1    | 462.38      | 10.24  | <b>0.0020</b>  |
| Error      | 3295.33                             | 73   | 45.14       |        |                |
| Total      | 17322.98                            | 79   |             |        |                |

**TABLE 2. Post-hoc Tukey-Kramer test for repeated measures of minimum diameter. Statistical significance is denoted with bold figures.**

| Group A                | Group B               | Lower Limit | A - B  | Upper Limit | corrected Prob. |
|------------------------|-----------------------|-------------|--------|-------------|-----------------|
| Color=Blue,Side=Right' | Color=Red,Side=Right' | -26.11      | -20.53 | -14.94      | <b>6.23E-14</b> |
| Color=Blue,Side=Right' | Color=Blue,Side=Left' | 4.50        | 10.09  | 15.68       | <b>5.79E-05</b> |
| Color=Blue,Side=Right' | Color=Red,Side=Left'  | -25.64      | -20.05 | -14.47      | <b>1.63E-13</b> |
| Color=Red,Side=Right'  | Color=Blue,Side=Left' | 25.03       | 30.62  | 36.20       | <b>2.19E-22</b> |
| Color=Red,Side=Right'  | Color=Red,Side=Left'  | -5.11       | 0.47   | 6.06        | 0.9960          |
| Color=Blue,Side=Left'  | Color=Red,Side=Left'  | -35.73      | -30.14 | -24.56      | <b>5.23E-22</b> |

Table 3 shows the results from the 3-way ANOVA based on response latency data. Contrary to the minimum diameter data, there was a significant difference ( $F(1, 73) = 12.02, p = 0.001$ ) in the pupillary response latency based on the experiment's time (8:00 AM vs. 8:00 PM). Also, a highly significant difference ( $F(1, 73) = 81.98, p = 1.4e-13$ ) was found in the latency of the pupillary response between red (635 nm) and blue (463 nm) light stimuli. Furthermore, the main effect of 'side' on the pupillary response latency is significant ( $F(1, 73) = 4.25, p = 0.043$ ), thus indicating

a substantial distinction in the pupillary response latency between the left and right eyes. Finally, the interaction between ‘color’ and ‘side’ is significant ( $F(1, 73) = 4.25, p = 0.043$ ), suggesting that the difference in latency due to color varies between the left and right eyes. Table 4 explores the interaction between the side and color variables through a post-hoc Tukey-Kramer test to correct for multiple pairwise comparisons. The analysis revealed that the response latency is generally shorter for red light than blue light, with significant differences observed in both eyes. Moreover, a notable lateral difference exists in the response latency for both colors, with the right eye exhibiting a shorter latency than the left eye. Furthermore, a significant difference in response latency is observed between red and blue light in the left eye. Münch *et al.* [10] found that the post-stimulus pupil response to blue light, indicative of intrinsic melanopsin activity, shows a circadian pattern, peaking after nocturnal melatonin secretion. This aligns with our findings that blue light elicits greater pupil constriction and that the response latency is longer in the morning, suggesting a circadian influence. Münch *et al.* [10] also reported that red light responses correlate more with subjective sleepiness than the circadian phase, which might explain our observation of lesser and earlier constriction with red light stimuli, independent of the experiment time. Our study adds to this by highlighting lateral differences in pupillary responses, with the left eye showing more significant constriction and longer latency, particularly to blue light. In general, lateralization is not examined explicitly in pupillometry. However, some individual differences in neural responsivity (including locus coeruleus-norepinephrine activity) suggest that lateral differences in autonomic responses could be an area for further research [19].

Overall, these results highlight the importance of considering both the stimulus's color and the eye being measured when analyzing pupillary responses. The findings align with current scientific literature, such as studies by Herbst *et al.* [13], Kawasaki *et al.* [14], and Rukmini *et al.* [20], which also emphasize the differential effects of blue and red light on pupillary response and the potential circadian influences on these responses.

**TABLE 3. Analysis of variance for the response latency data as the dependent variable. Statistical significance is denoted with bold figures.**

| Source     | Constrained Type III sum of squares | d.f. | Mean Square | F     | Prob>F         |
|------------|-------------------------------------|------|-------------|-------|----------------|
| Time       | 0.78                                | 1    | 0.78        | 12.02 | <b>0.001</b>   |
| Color      | 5.31                                | 1    | 5.31        | 81.98 | <b>1.4e-13</b> |
| Side       | 0.28                                | 1    | 0.28        | 4.25  | <b>0.043</b>   |
| Time*Color | 0.09                                | 1    | 0.09        | 1.40  | 0.240          |
| Time*Side  | 0.00                                | 1    | 0.00        | 0.00  | 0.988          |
| Color*Side | 0.28                                | 1    | 0.28        | 4.25  | <b>0.043</b>   |
| Error      | 4.73                                | 73   | 0.06        |       |                |
| Total      | 11.46                               | 79   |             |       |                |

A comparison of commercially available pupillometers used in scientific studies and the prototype here developed is included in Table 5 [21][22][23]. The authors acknowledge that this comparison accounts solely for the material costs of the prototype and excludes additional expenses common to commercial devices, such as labor, scaling, and other overheads.

**TABLE 4. Post-hoc Tukey-Kramer test for repeated measures of response latency. Statistical significance is denoted with bold figures.**

| Group A                 | Group B                | Lower Limit | A - B | Upper Limit | corrected Prob. |
|-------------------------|------------------------|-------------|-------|-------------|-----------------|
| 'Color=Blue,Side=Right' | 'Color=Red,Side=Right' | 0.05        | 0.26  | 0.48        | <b>8.25E-03</b> |
| 'Color=Blue,Side=Right' | 'Color=Blue,Side=Left' | 0.37        | 0.58  | 0.79        | <b>2.22E-09</b> |
| 'Color=Blue,Side=Right' | 'Color=Red,Side=Left'  | 0.50        | 0.71  | 0.92        | <b>2.05E-12</b> |
| 'Color=Red,Side=Right'  | 'Color=Blue,Side=Left' | 0.11        | 0.32  | 0.53        | <b>1.00E-03</b> |
| 'Color=Red,Side=Right'  | 'Color=Red,Side=Left'  | 0.24        | 0.45  | 0.66        | <b>2.43E-06</b> |
| 'Color=Blue,Side=Left'  | 'Color=Red,Side=Left'  | -0.08       | 0.13  | 0.34        | <b>3.77E-01</b> |

**TABLE 5. Post-hoc Tukey-Kramer test for repeated measures of response latency. Statistical significance is denoted with bold figures.**

| Feature            | NeurOptics NPi-300                     | NeuroLight Algiscan                    | This work   |
|--------------------|--|--|---|
| Type               | Handheld, Infrared Pupillometer        | Handheld, Infrared Pupillometer        | Portable, Infrared Pupillometer   |
| Spatial resolution | ±0.03 mm                               | ±0.1 mm                                | ±0.33mm   |
| Measurement Time   | 2 seconds for single measurement       | 1 second for single measurement        | Single frame: 40ms, needs at least 2 seconds to record pupil constriction |
| Data Storage       | Internal storage, data can be exported | Internal storage, data can be exported | Internal storage, data can be manually exported                           |
| Weight             | 344g, portable                         | Lightweight, portable                  | 150g, portable  |
| Price              | Approximately \$3,350 USD              | Approximately \$3,015 USD              | Approximately \$85 USD  |

## CONCLUSION

This study successfully demonstrated the development and characterization of a low-cost, portable pupillometer based on the Raspberry Pi platform. This device can effectively measure pupillary responses to different light wavelengths and evaluate their relationship with circadian rhythms and lateral asymmetry. However, our study has several limitations. Firstly, the sample size was limited to a single participant, which may not comprehensively represent the population. Additionally, the study did not account for potential inter-individual variability in pupillary responses, which could influence the generalizability of the findings.

Future research should include a more extensive and more diverse sample to validate the results and enhance the robustness of the conclusions. It would also be beneficial to investigate the impact of different environmental factors, such as light exposure history and sleep patterns, on pupillary responses. Furthermore, integrating additional sensors to monitor physiological parameters like heart rate and skin conductance could provide a more holistic understanding of the autonomic nervous system's role in pupillary dynamics.

Potential improvements to the device could involve enhancing the camera resolution and sensitivity to capture more precise measurements and incorporating real-time data processing capabilities to facilitate immediate analysis. Expanding the device's functionality to include various light intensities and durations could offer more compre-

hensive insights into the mechanisms underlying pupillary light reflexes. These advancements would significantly contribute to the utility of the pupilometer in clinical diagnostics and therapeutic monitoring, particularly for circadian rhythm disorders and phototherapy applications..

## ETHICAL STATEMENT

Written informed consent was obtained from the participant of the study. The current study is part of a broader project that was approved by the IRB and registered under the number CEI-UASLP/04-2023.

## COMPETING INTERESTS STATEMENT

The authors declare that they have no known competing financial interests or personal relationships that could have appeared to influence the work reported in this paper.

## AUTHOR CONTRIBUTIONS

I. A. H. B. methodology, software, formal analysis, investigation, resources, data curation, writing - original draft, and visualization; E. G. conceptualization, methodology, software, validation, formal analysis, resources, writing - review & editing, visualization, supervision, project administration, and funding acquisition.

## REFERENCES

- [1] S. Mathôt, "Pupillometry: Psychology, Physiology, and Function," *J. Cogn.*, vol. 1, no. 1, 2018, art. no. 16, doi: <https://doi.org/10.5334/joc.18>
- [2] D. F. Ferreira, S. Ferreira, C. Mateus, N. Barbosa-Rocha, L. Coelho, and M. A. Rodrigues, "Advancing the understanding of pupil size variation in occupational safety and health: A systematic review and evaluation of open-source methodologies," *Saf. Sci.*, vol. 175, 2024, art. no. 106490, doi: <https://doi.org/10.1016/j.ssci.2024.106490>
- [3] H. M. Pinheiro and R. M. da Costa, "Pupillary Light Reflex as a Diagnostic Aid from Computational Viewpoint: A Systematic Literature Review," *J. Biomed. Inform.*, vol. 117, 2021, art. no. 103757, doi: <https://doi.org/10.1016/j.jbi.2021.103757>
- [4] M. Okubo, K. Ishikawa, T. Oyama, and Y. Tanaka, "The look in your eyes: The role of pupil dilation in disguising the perception of trustworthiness," *J. Trust Res.*, vol. 13, no. 1, pp. 87–97, 2023, doi: <https://doi.org/10.1080/21515581.2023.2165090>
- [5] J. G. Cárdenas-Solís, D. A. Gutiérrez Hernández, E. Guevara, R. Santiago-Montero, et al., "Polynomial Approximation of Time Series of Pupil Response to Controlled Light Stimuli," *J. Adv. Comput.*, vol. 7, no. 1, pp. 1–10, 2017, doi: <https://doi.org/10.5923/j.ac.20170701.01>
- [6] M. T. Galván-González, V. Zamudio, C. Lino, J. G. Cárdenas Solís, et al., "Analysis of pupillary response after a stimulus of light to generate characteristic groups," in 2017 International Conference on Electronics, Communications and Computers (CONIELECOMP), Cholula, Mexico, 2017, pp. 1–6, doi: <https://doi.org/10.1109/CONIELECOMP.2017.7891817>
- [7] L.-L. Lobato-Rincón, M. del C. Cabanillas-Campos, C. Bonnin-Arias, E. Chamorro-Gutiérrez, A. Murciano-Cespedosa, and C. Sánchez-Ramos Roda, "Pupillary behavior in relation to wavelength and age," *Front. Hum. Neurosci.*, vol. 8, 2014, art. no. 221, doi: [doi.org/10.1109/CONIELECOMP.2017.7891817](https://doi.org/10.1109/CONIELECOMP.2017.7891817)
- [8] C. M. Privitera, S. V. Neerukonda, V. Yokobori, A. M. Puccio, et al., "A differential of the left eye and right eye neurological pupil index is associated with discharge modified Rankin scores in neurologically injured patients," *BMC Neurol.*, vol. 22, no. 1, 2022, art. no. 273, doi: <https://doi.org/10.1186/s12883-022-02801-3>
- [9] M. A. Bonmati-Carrion, K. Hild, C. Isherwood, S. J. Sweeney, et al., "Relationship between Human Pupillary Light Reflex and Circadian System Status," *PLoS One*, vol. 11, no. 9, 2016, art. no. e0162476, doi: <https://doi.org/10.1371/journal.pone.0162476>
- [10] S. Sondhi, M. Khan, R. Vijay, A. K. Salhan, and S. Chouhan, "Acoustic analysis of speech under stress," *Int. J. Bioinform. Res. Appl.*, vol. 11, no. 5, pp. 417–432, 2015, doi: <https://doi.org/10.1504/ijbra.2015.071942>
- [11] E. Guevara, M. Miranda-Morales, K. Hernández-Vidales, M. Atzori, and F. J. González, "Low-cost embedded system for optical imaging of intrinsic signals," *Rev. Mex. Fis.*, vol. 65, no. 6, pp. 651–657, 2019, doi: <https://doi.org/10.31349/RevMexFis.65.651>
- [12] K. Tekin, M. A. Sekeroglu, H. Kiziltoprak, S. Doguizi, M. Inanc, and P. Yilmazbas, "Static and dynamic pupillometry data of healthy individuals," *Clin. Exp. Optom.*, vol. 101, no. 5, pp. 659–665, 2018, doi: <https://doi.org/10.1111/cxo.12659>








- [13] K. Herbst, B. Sander, D. Milea, H. Lund-Andersen, and A. Kawasaki, "Test-Retest Repeatability of the Pupil Light Response to Blue and Red Light Stimuli in Normal Human Eyes Using a Novel Pupillometer," *Front. Neurol.*, vol. 2, 2011, art. no. 10, doi: <https://doi.org/10.3389/fneur.2011.00010>
- [14] R. Kardouk, S. C. Anderson, T. G. Damarjian, E. M. Grace, E. Stone, and A. Kawasaki, "Chromatic pupil responses: preferential activation of the melanopsin-mediated versus outer photoreceptor-mediated pupil light reflex," *Ophthalmology*, vol. 116, no. 8, pp. 1564-1573, 2009, doi: <https://doi.org/10.1016/j.ophtha.2009.02.007>
- [15] N. M. Razali and Y. B. Wah, "Power comparisons of shapiro-wilk, kolmogorov-smirnov, lilliefors and anderson-darling tests," *JOSMA*, vol. 2, no. 1, pp. 21-33, 2011.
- [16] D. J. Steinskog, D. B. Tjøstheim, and N. G. Kvamstø, "A Cautionary Note on the Use of the Kolmogorov-Smirnov Test for Normality," *Mon. Wea. Rev.*, vol. 135, no. 3, pp. 1151-1157, 2007, doi: <https://doi.org/10.1175/MWR3326.1>
- [17] Y. Zhao, L. Wong, and W. W. B. Goh, "How to do quantile normalization correctly for gene expression data analyses," *Sci Rep*, vol. 10, 2020, art. no. 15534, doi: <https://doi.org/10.1038/s41598-020-72664-6>
- [18] S. Lee and D. K. Lee, "What is the proper way to apply the multiple comparison test?," *Korean J. Anesthesiol.*, vol. 71, no. 5, pp. 353-360, 2018, doi: <https://doi.org/10.4097/kja.d18.00242>
- [19] M. Grueschow, N. Stenz, H. Thörn, U. Ehlert, et al., "Real-world stress resilience is associated with the responsivity of the locus coeruleus," *Nat. Commun.*, vol. 12, no. 1, 2021, art. no. 2275, doi: <https://doi.org/10.1038/s41467-021-22509-1>
- [20] A. V. Rukmini, D. Milea, M. Baskaran, A. C. How, et al., "Pupillary Responses to High-Irradiance Blue Light Correlate with Glaucoma Severity," *Ophthalmology*, vol. 122, no. 9, pp. 1777-1785, 2015, doi: <https://doi.org/10.1016/j.ophtha.2015.06.002>
- [21] M. H. Lee, B. Mitra, J. K. Pui, and M. Fitzgerald, "The use and uptake of pupillometers in the Intensive Care Unit," *Aust. Crit. Care*, vol. 31, no. 4, pp. 199-203, 2018, doi: <https://doi.org/10.1016/j.aucc.2017.06.003>
- [22] IDEMD. "Pupillometry - NeuroLight." IDEMD Accessed: Aug. 18, 2024. [Online]. Available: <https://www.idmed.fr/en/pupillometry/>
- [23] NEUROPTICS. "Measure Pupil Size with NPi-300 Pupillometer," NeuroOptics. Accessed: Aug. 18, 2024. [Online]. Available: <https://neuroptics.com/npi-300-pupillometer/>

<https://dx.doi.org/10.17488/RMIB.45.3.5>

E-LOCATION ID: 1448

## Web-based Interactive 3D Modeling and Visualization of the Human Brain towards Anatomy Education

### Modelado y Visualización Interactivos en 3D del Cerebro Humano basados en la Web hacia la Educación de Anatomía

Ma. De Jesus Gutierrez-Sanchez<sup>1</sup> , Juan-Carlos Gonzalez-Islas<sup>1</sup>  , Anilu Franco-Arcega<sup>1</sup> ,  
Alberto Suarez-Navarrete<sup>1</sup> , Jose Gregorio Robles-Guzman<sup>1</sup> , Gonzalo Alberto Torres-Samperio<sup>1</sup> 

<sup>1</sup>Universidad Autónoma del Estado de Hidalgo - México

#### ABSTRACT

Today, visualization of 3D medical images is an essential tool for medical education. Web-based 3D tools for the teaching-learning process have turned out to be an efficient alternative to conventional systems. In this work, we aim the modeling process and 3D web-based interactive visualization of the human brain using 3D web technologies and an improvement of the Methodology for the Development of Virtual Reality Educational Environments (MEDEERV, for its acronym in Spanish). 20 undergraduate medicine, dentistry, gerontology, and computer science students performed a brain model usability test (9 women; 11 men, mean age = 22.1 years, SD = 0.70). To this end, we used a post-test questionnaire with Likert scale answers whose alpha of Cronbach was 0.93.

The proof of concept of the brain model that we have developed in this work provides evidence of the viability of the system to be used as a web tool for basic neuroanatomy learning. The main contribution of this work focuses on the implementation of MEDEERV to model the 3D human brain, plus the usability testing for reengineering feedback. This approach to modeling, visualizing, and evaluating could be used in other areas of human anatomical teaching. Although the experimental results show a good user experience, functionality and usability, it is necessary to generate a new version and carry out a study with a larger and more specific population with knowledge of brain anatomy.

**KEYWORDS:** 3D human brain, Web-based 3D brain, 3D medical imaging, web-based anatomy learning, 3D modeling and visualization



## RESUMEN

Hoy en día, la visualización de imágenes médicas en 3D es una herramienta esencial para la enseñanza de la medicina. Las herramientas 3D basadas en web para el proceso de enseñanza-aprendizaje han resultado ser una alternativa eficaz a los sistemas convencionales. En este trabajo, nos centramos en el proceso de modelado y visualización interactiva en 3D del cerebro humano basado en la web utilizando tecnologías 3D y una mejora de la Metodología para el Desarrollo de Entornos Educativos de Realidad Virtual (MEDEERV). 20 estudiantes universitarios de medicina, odontología, gerontología y ciencias computacionales realizaron una prueba de usabilidad del modelo cerebral (9 mujeres; 11 hombres, edad media = 22,1 años, DE = 0,70). Para ello, utilizamos un cuestionario pos-test con respuestas en escala Likert y cuyo alfa de Cronbach fue de 0,93.

La prueba de concepto del modelo cerebral que hemos desarrollado en este trabajo aporta evidencias de la viabilidad del sistema para ser utilizado como herramienta web para el aprendizaje de neuroanatomía básica. La principal contribución de este trabajo se centra en la implementación de MEDEERV para modelar el cerebro humano en 3D, además de las pruebas de usabilidad para la retroalimentación de la reingeniería. Este enfoque para modelar, visualizar y evaluar otras áreas anatómicas humanas. Aunque los resultados experimentales muestran una buena experiencia de usuario, funcionalidad y usabilidad, es necesario generar una nueva versión y realizar un estudio con una población más amplia y específica con conocimientos de anatomía cerebral.

**PALABRAS CLAVE:** cerebro humano 3D, cerebro humano basado en la web, imagenología médica 3D, aprendizaje de anatomía basado en la web, modelado y visualización 3D

### Corresponding author

TO: Juan-Carlos Gonzalez-Islas

INSTITUTION: UNIVERSIDAD AUTÓNOMA DEL ESTADO DE HIDALGO.

ADDRESS: CARRETERA PACHUCA-TULANCINGO KM. 4.5, COL. CARBONERAS, 42184 MINERAL DE LA REFORMA, HIDALGO MEXICO.

EMAIL: [juan\\_gonzalez7024@uaeh.edu.mx](mailto:juan_gonzalez7024@uaeh.edu.mx)

### Received:

03 July 2024

### Accepted:

11 October 2024

## INTRODUCTION

In recent years, technological advances have prompted a change in anatomy education from the traditional way of the last century. Due to the increase in the number of students in medical schools and changes in the anatomy curriculum, the time devoted to this subject has decreased. This situation has led to a lack of anatomy knowledge among new doctors<sup>[1]</sup>. Anatomy is the basis for clinical examinations, surgery and radiology, so medical and health-care students must understand the key concepts, structures and their relationships<sup>[2]</sup>.

The human brain is one of the most complex organs in human anatomy, so the subject of neuroanatomy is one of the most difficult and can sometimes discourage students<sup>[3]</sup>. Traditionally, the study of neuroanatomy is based on 2D images, however, this often does not adequately reflect the complex geometry and spatial arrangement of anatomical structures<sup>[4]</sup>. On the other hand, neuroanatomical examination using cadaveric dissection or fixed anatomical pieces is another method, and although the experience and realism provided by this option are unquestionable, it is an expensive resource with low availability, accessibility, and high costs for laboratory maintenance<sup>[5]</sup>. In this way, using neuroanatomical artificial physical models is another traditional study tool, but often with limited accuracy.

Recently, the advent of 3D technologies has improved the way of learning the structural and functional connectivity of the brain for neuroscience applications<sup>[6]</sup>. Nowadays, there are several virtual modeling tools able to reproduce realistic and easily explorable objects. Many works in literature confirm the evolution of study techniques from traditional resources to digital and 3D<sup>[7]</sup>. There is evidence that understanding of anatomy can be improved by using visual table images, virtual reality (VR) and augmented reality (AR)<sup>[8]</sup>. However, medical experts are still unaware of the many advanced 3D-MI visualization techniques that could enhance their ability to analyze data and help them make decisions about specific medical problems<sup>[9]</sup>.

In neuroscience, one of the common challenges is to understand how the brain works and how to study brain disorders. To this end, Virtual Brain (TVB) is a neuroinformatics platform with a brain simulator that incorporates a range of neuronal models and dynamics<sup>[10]</sup>. In this sense,<sup>[11]</sup> a realistic virtual model of the human brain is proposed, which could be used in a neurosurgical simulation for both educational and preoperative planning purposes. To address the advantages of visualizing complex 3D anatomies for neuroscience educational and surgical purposes, several virtual reality (VR) and augmented reality (AR) solutions have been proposed<sup>[6][12][13][14][15][16][17][18]</sup>. However, although there are notable results with AR and VR systems, they have some limitations to overcome due to problems caused by VR headsets and motion sickness.

Although there is significant progress in neuroanatomy 3D visualization, the limitation in using commercially available 3D models remains their absence of a systematic approach to achieving scientific accuracy. In addition, complexity in the creation and interpretation of realistic models is another important element; not only technical skills are required, but also artistic creativity and expert mastery of medical knowledge and teaching<sup>[19]</sup>. On the other hand, traditional neuroanatomy curricula offer a limited approach to educating a variety of learning styles. Similarly, the fact that visualization technologies exist is not a sufficient consideration to use these resources in teaching, as a focused approach to educational intervention is required<sup>[8]</sup>. In addition to the previous challenges, in this work, scalability, reproducibility, and usability assessment issues are addressed<sup>[20]</sup>.



The methodology consists of seven main stages, the systematic design, the functional design, the virtual world modeling, the environmental effects, the implementation, the user-virtual environment, and the usability testing; as well as other secondary blocks. Each of these stages contains a series of phases that must be broken down to create an optimal virtual environment. These stages are described below.

### Systematic instructional design

Instructional design is the process of creating effective, interactive and engaging learning plans focused on how people learn. In this stage, the competencies and skills that the student should develop depending on the learning area and the target population are identified. In this case, the expected result that undergraduate health science students will have to acquire through interaction with a 3D virtual model of the brain, is learning the basic neuro-anatomical structures.

### Functional design

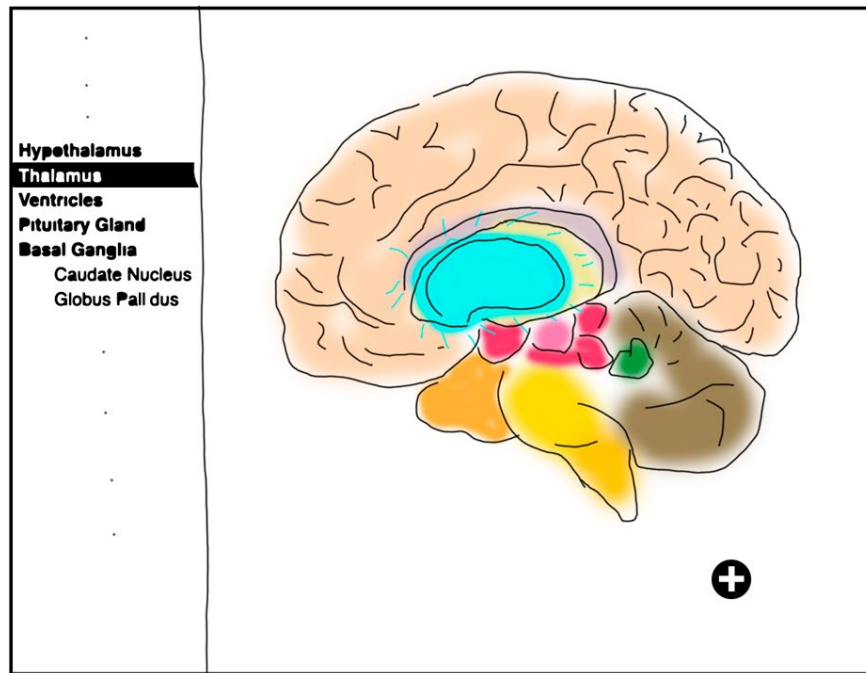
In this phase, the requirements and actions that the system will take for its proper functioning are indicated, with the aim of making it intuitive and dynamic with a gamified approach. The aim is that the user can develop skills such as spatial visualization, memory and deductive reasoning by manipulating objects within the 3D brain virtual environment. To create the virtual scenario, the learning objectives that the students are intended to develop when browsing the application must be established. Two objectives that have been proposed with the subordinate skill are presented in Table 1.

**TABLE 1. Objectives and design of functional skill.**

| Design of functional skill  |  |
|---|--|
| Learning Objectives   | Subordinate Skill  |
| Learn the main structures of the human brain in a detailed and free form.         | The user will develop memory to identify the composition of the organic groups of the complete brain system. |
|   | The user will be able to identify the position occupied by an element within the 3D complex system.          |
| Reinforce the general information of each element that makes up the brain system. | The user will logically and deductively identify the possible structures of the brain.                       |

### Virtual world modelling

The process of 3D brain modeling through scripting and artistic design represents the first step of the third phase in MEDEERV. In this process, it is necessary to have a script of the system where the actions that the user can perform in it are described step by step. This script identifies the modeling techniques that will be implemented for the creation of the brain. Next, the artistic design is established, where the main models of the virtual world will be identified. The 3D block of the brain that should be embedded in the web page will be managed from a main menu. For example, Figure 2, illustrates an animation perspective of a selected part that is highlighted during the interaction through the artistic design.



**FIGURE 2. Artistic design of the brain with highlighted selected part.**

The process of creating the 3D models is a time-consuming activity. Table 2, presents the position in which each element is located, to prioritize the order in which the elements that are part of the brain will be modeled.

**TABLE 2. Names of the brain parts in blueprints.**

| Right hemisphere  | Middle brain      |
|-------------------|-------------------|
| Left hemisphere   | Hindbrain         |
| Frontal lobe      | Pons              |
| Parietal lobe     | Cerebellum        |
| Temporal lobe     | Oblongata Medulla |
| Occipital lobe    |                   |
| Hard body         |                   |
| Limbic system     | Diencephalon      |
| Cingulate Gyrus   | Thalamus          |
| Hippocampus       | Hypothalamus      |
| Griseum Indusium  | Pineal Gland      |
| Septal Nucleus    | Optic chiasma     |
| Toothed twist     | Pituitary gland   |
| Fornix            |                   |
| Amygdala          |                   |
| Mammillary Body   |                   |
| Basal ganglia     | Ventricles        |
| Putamen           | Lateral ventricle |
| Caudate Nucleus   | Third Ventricle   |
| Side Pale Globe   | Fourth ventricle  |
| Medium Pale Globe |                   |

For the creation of each of the brain elements, reference images that allow copying or tracing the geometric shape of the figure to be modeled are necessary. To this end, there are blueprint images, which show orthogonal views of different sides of the object and are based on figures presented in neuroanatomy literature (Figure 3).

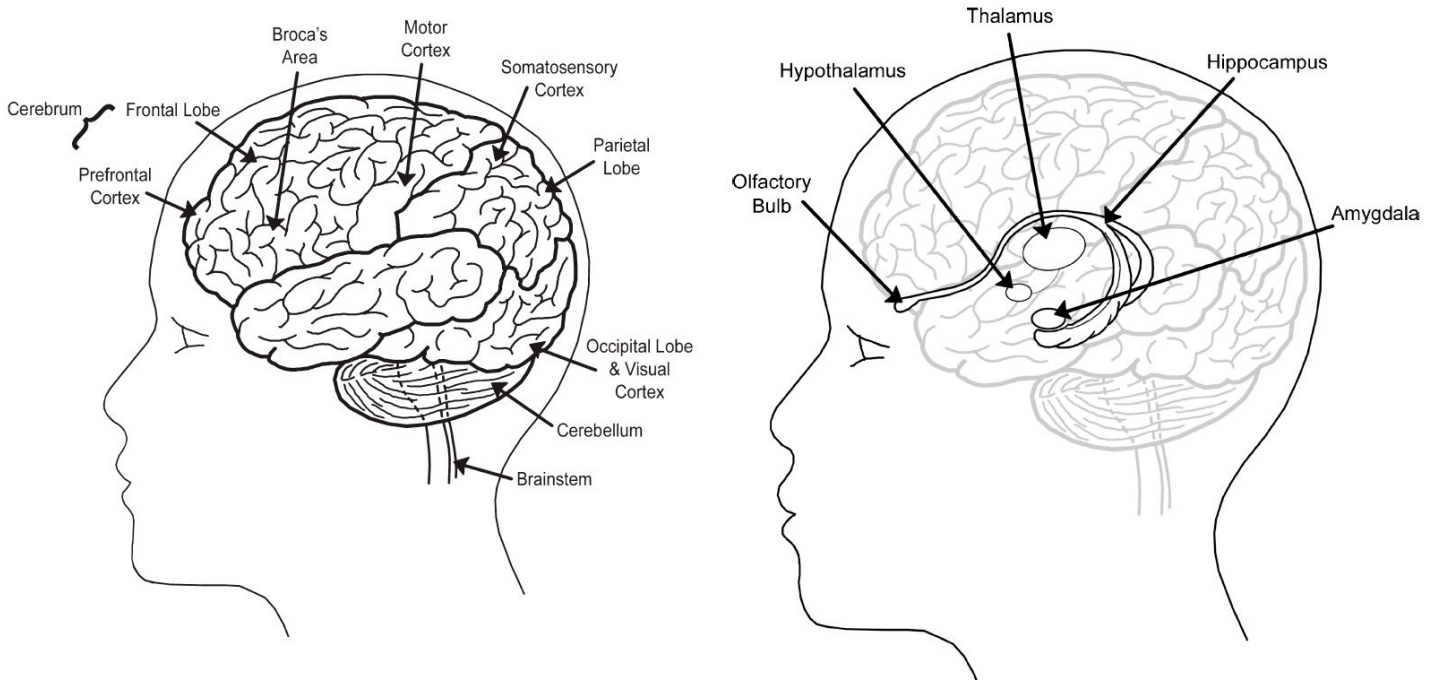


FIGURE 3. Labeled areas of the human brain. Image taken from "Human brain anatomy" by Burger [24].

Then, these blueprints are posed in each orthogonal view of the Blender scene, to give a shape from initial single primitive (Figure 4).

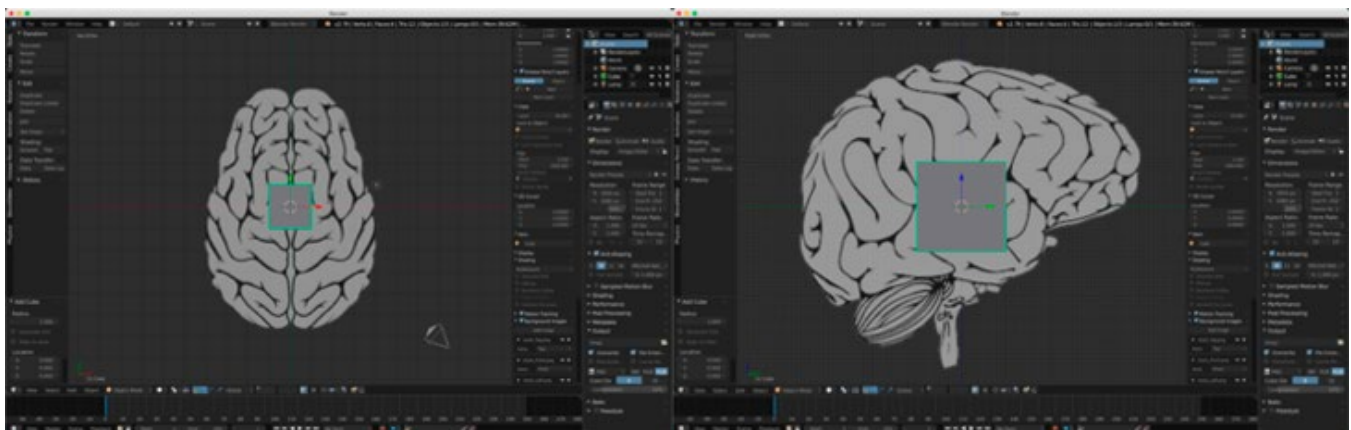
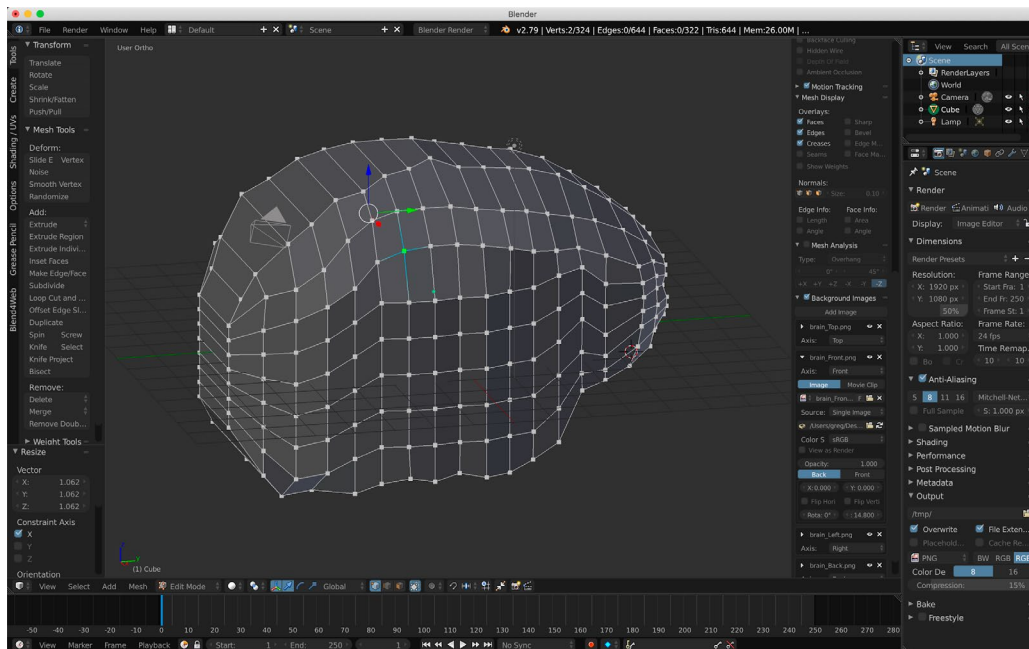


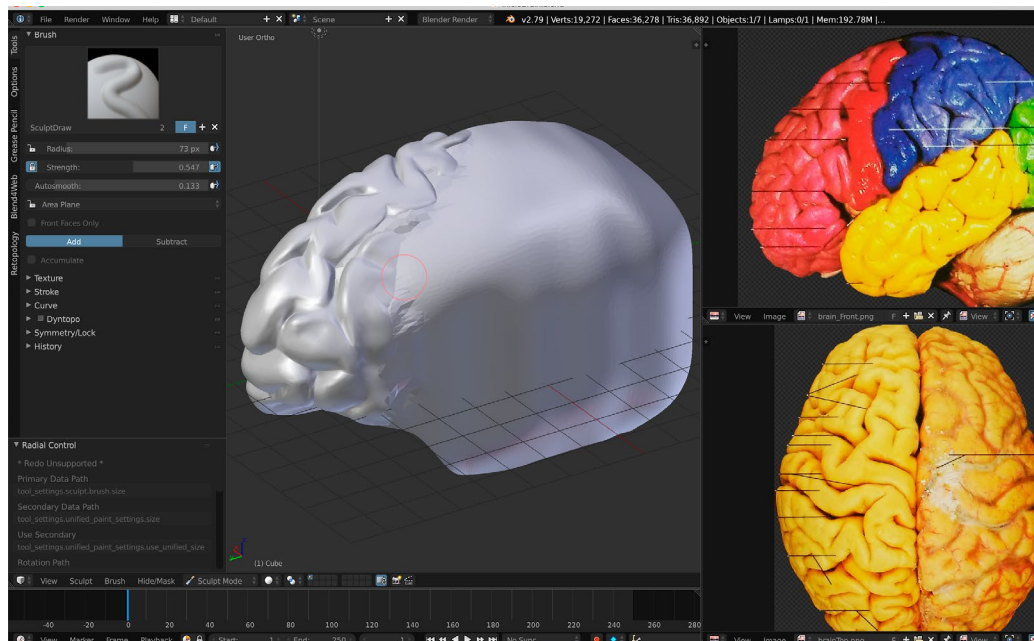
FIGURE 4. Top view (left) and side view (right) of the brain model in blueprint imported in Blender.

Subsequently, using the box modeling technique to model anything from a simple primitive, we get a model volumetrically resembling the cerebral hemispheres as shown in Figure 5.



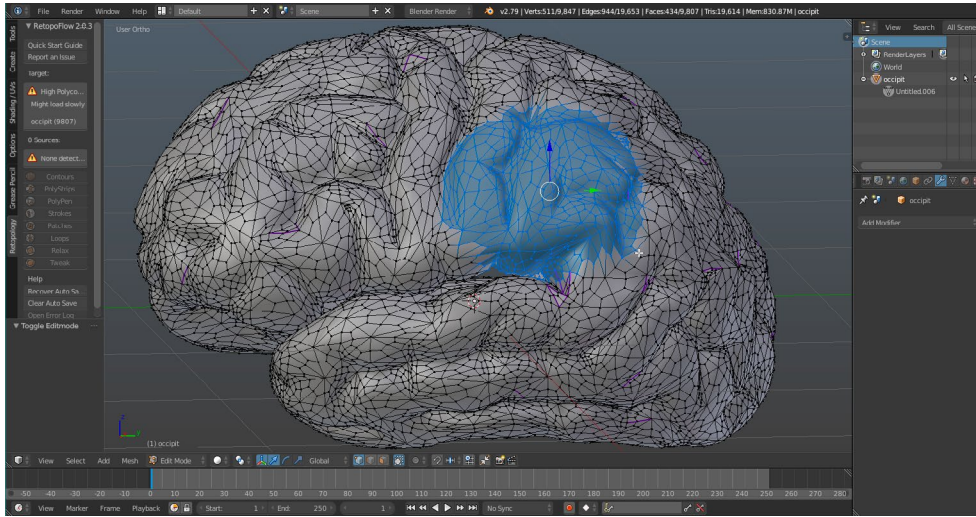
**FIGURE 5.** Perspective view of the final brain model using the box modeling technique.

To obtain a smoothed surface model, the model is modified by subdivision of surfaces. Then, the sculptural modeling technique is used to deform the surface. Figure 6 presents the model obtained up to this stage of the process.



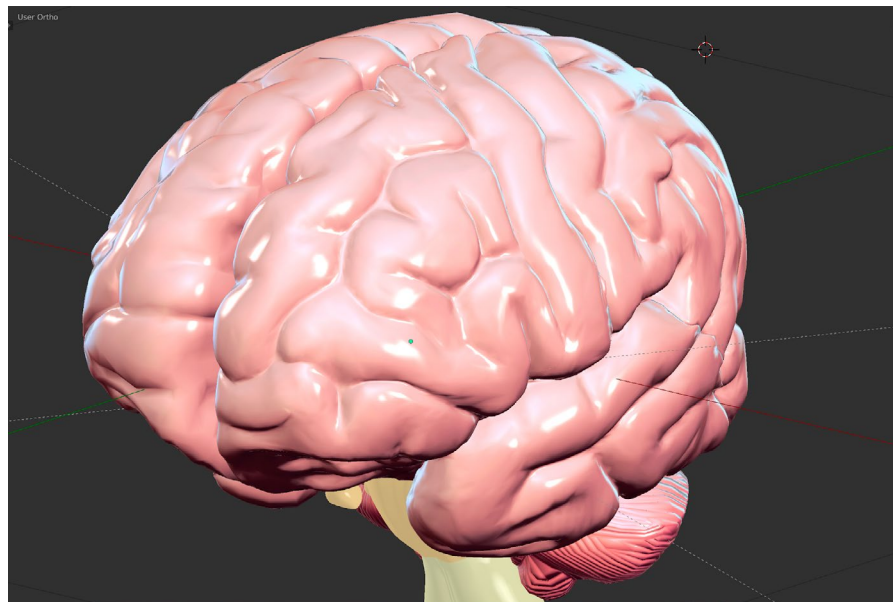
**FIGURE 6.** Perspective view of the model resulting from the sculpting process with photographic references.

The previous model involves computationally expensive rendering work. Since there are more than twenty parts that compose the complete model of the human brain, it cannot be considered to have detailed models, so it is required to perform retopology of the most complex parts in the mesh. The same process is replicated for each organ to be modeled, some of them are simpler shapes compared to the level of detail of the cerebral hemispheres, therefore, retopology is not necessary. The final result of the retopology process is a less dense mesh as shown in Figure 7.



**FIGURE 7.** Perspective view of the lower density mesh using vertex selection.

The materials, colors and textures section, to simulate a more realistic appearance, is based on traditional neuro-anatomy teaching and achieved by implementing Oren-Nayar shadows and Toon type reflection. These tools are applied to each component of the brain displaying the complete organ in greater detail. Figure 8 and Figure 9 show the cerebellum and cerebral hemispheres after having assigned Matcap-type material and colors, respectively.

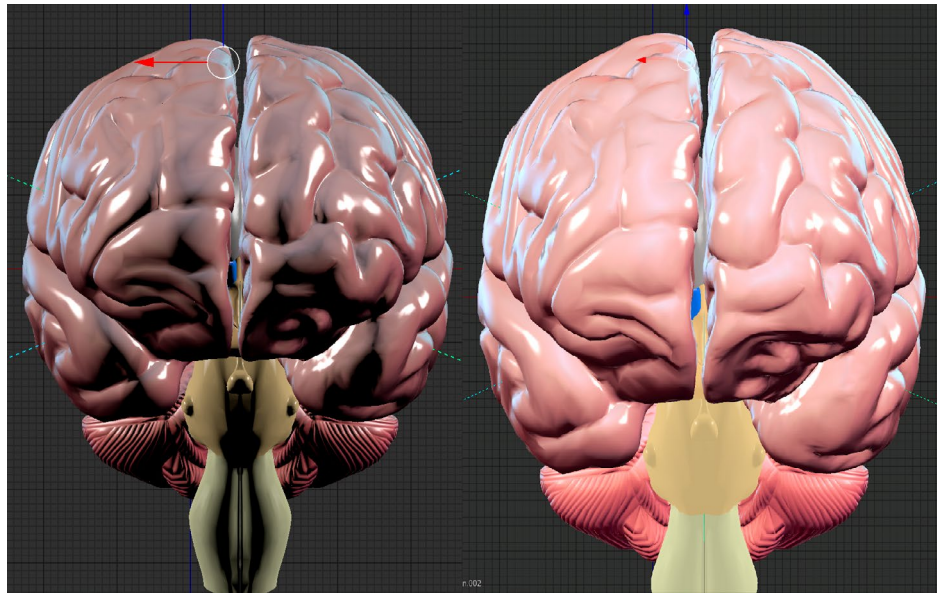


**FIGURE 8.** Perspective view of the cerebellum with assigned material and texture.

### Environmental effects

Once the models are finished, we proceed to animate the objects with which users will interact in the virtual world. In the same form, the special effects such as particles, fire, among others are included. To complement the stage, depending on the purpose the lighting scene is setup. Lighting settings offer a more realistic experience, taking into account the angle of the objects with the aim of reducing shadows. A scene without lighting results in a lack of depth and 3D appearance. Figure 9, shows a perspective view of two kinds of lighting, sun and ambient.

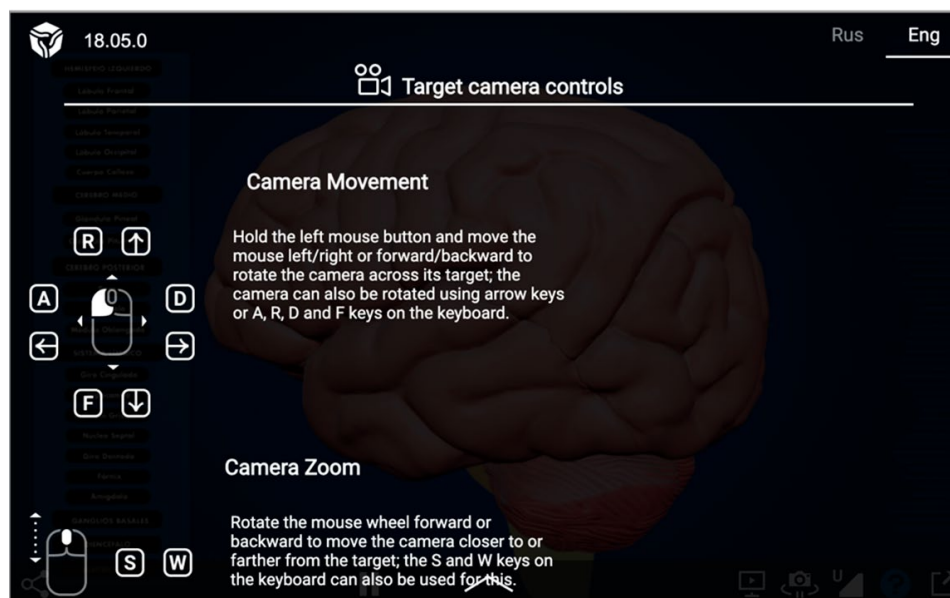




**FIGURE 9.** Perspective view of illuminated model with two suns (left) and perspective view of illuminated model with ambient lights (right).

### Implementation

In this stage, the goal is to animate the 3D model by creating the physical behaviors to show, hide or highlight the model elements, when an organ is selected. The animation process is performed by programming parameters in a timeline, using nodes to create a logical tree of decisions. This process is done with the Blend4Web tool, added as a plugin in Blender, useful for creating the logical animation of the scene elements and uploading the model to a web page. Navigation mechanisms are those tools that will be provided to the user to navigate the virtual world. Twenty-four buttons have been added to the scene to access navigation to both organ sets and individual organs. Figure 10, shows the navigation mechanism of 3D brain web-based model.



**FIGURE 10.** Navigation mechanisms of the 3D brain web-based model.

Finally, in this stage, multimedia objects, for better interaction with the virtual world, videos, audios, music or text can be implemented. There are multimedia objects with information cards so the user can have greater knowledge of the brain, as well as the different organs that make it up. The implementation of the human brain as a completely independent 3D element is a reference as the first step in the process of creating completely 3D-based web pages.

## Support

To visualize the 3D brain on the web, the Blender scenario was exported to an HTML file using Blend4Web, which allows navigation in different browsers. The technical requirements to run the model are: latest browser version of Google Chrome, Firefox, Safari or Opera; any 64-bit CPU, graphics card compatible with OpenGL 4.3 or higher and a minimum of 2 GB RAM.

## Usability testing

In this section, we just describe some of the essentials to conduct usability testing. Usability testing is the process of learning about users by observing them using a product to accomplish the specific goals of interest. It is crucial to focus on the user and not the product, because you know what works for your users<sup>[25]</sup>. In that sense, in this work usability is the extent to which the 3D brain can be used by undergraduate students to achieve specific objectives effectively, efficiently and with satisfaction in a neuroanatomy education context.

Among the essential planning steps, after having established the test objectives, it is determined how the product will be tested and how the user groups will be established. On the other hand, there has been a debate about how many participants are needed in a reliable usability test to identify usability issues<sup>[26][27]</sup> and<sup>[28]</sup> consider that a majority or about 80 % (given a 30 probability of detection) of usability issues will be observed with the first five participants<sup>[29]</sup>. In fact, a study can be conducted with 5 users and get excellent results as long as the users are all from the same subgroup. If there is time and budget to test with 10 participants, two or even three subgroups can be identified<sup>[25]</sup>. In<sup>[30]</sup> a study was conducted with 12 participants to assess the user experience in virtual upper limb rehabilitation environments. While in<sup>[13]</sup> SONIA: an immersive customizable virtual reality system for the education and exploration of brain networks was evaluated by 11 subjects, showing attractive visual design and good educational value. Regarding the usability evaluation of Web-Based 3D Medical Image Visualization of the brain, 12 participants evaluated the system, the experimental results show the 3D visualization method improves the educational performance of students<sup>[31][32]</sup>. Subsequently, we have organized the 3D brain model test using a navigation test and created a post-test questionnaire to get immediate feedback from participants after the virtual trip, whose opinion response options were based on the Likert scale<sup>[33]</sup>. Table 3 shows a real response sample of the post-test usability questionnaire provided by an undergraduate medicine participant.

**TABLE 3. Real response sample of the post-test usability questionnaire provided by an undergraduate medicine participant.**

| Post-test usability questionnaire                                 |                        |               |              |            |                     |
|---|------------------------|---------------|--------------|------------|---------------------|
| Question  | Possible answers       |               |              |            |                     |
|   | Strongly disagree<br>1 | Disagree<br>2 | Neutral<br>3 | Agree<br>4 | Strongly agree<br>5 |
| 1. Is the app intuitive?  |                        |               |              | ✓          |                     |
| 2. Is the application easy to use?                                |                        |               |              | ✓          |                     |
| 3. Does the application give freedom of navigation?               |                        |               | ✓            |            |                     |
| 4. Did the application present any errors?                        |                        |               |              | ✓          |                     |
| 5. Does the application meet the teaching objective?              |                        | ✓             |              |            |                     |
| 6. Are the elements of the application model easy to understand?  |                        |               |              |            | ✓                   |
| 7. Did you find the content of the application structured?        |                        |               |              | ✓          |                     |
| 8. Is the information displayed in a structured and concrete way? |                        |               |              | ✓          |                     |
| 9. Did you find the interface attractive?                         |                        |               |              | ✓          |                     |
| 10. Did the app help reinforce your knowledge?                    |                        |               | ✓            |            |                     |

### Experimental setting

Following the guidelines to develop the usability test of our early version, the experimental sample was divided into four subgroups of five participants each. The characteristics of each subgroup were defined depending on the domain knowledge as it relates to the brain neuroanatomy (medicine, dentistry, and gerontology) and the technical skills with 3D computing modelling (computer science). All participants in each stratum were randomly selected among undergraduate students of the final semesters. Before performing the usability test, an informed consent form will be given to users to read and approve, if applicable. The study was developed according to the ethical principles of medical research involving human subjects established in the Declaration of Helsinki.

The technical test consists of using the 3D model brain in the web. The model was run in the browser using WebGL, the library that enhances the graphical capabilities of HTML5 web browsers using JavaScript and OpenGL. EWebGL is included in the Google Chrome, Firefox, and Safari web browsers and specifically in any updated browser. The virtual brain was presented in the Firefox and Google Chrome browsers, since they are the most used by average users. The computers where the test was run were Intel Core i5-4590 CPU @ 3.30 GHz, memory (RAM) 4.0 GB. The 3D web-based human brain based on the 3D web is shown in Figure 11.

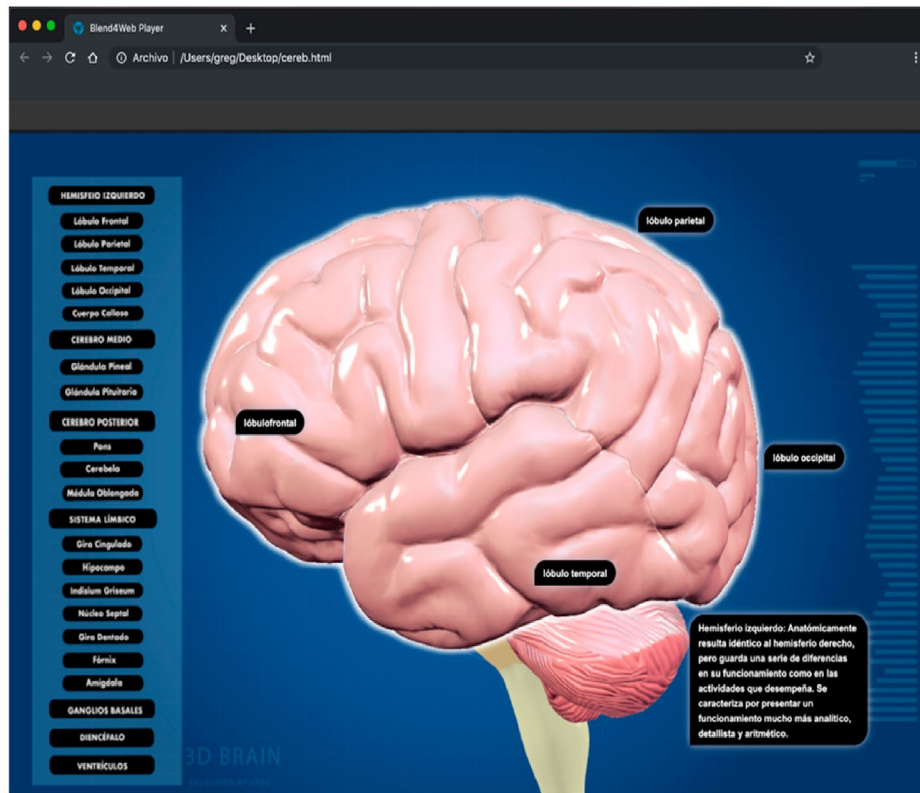


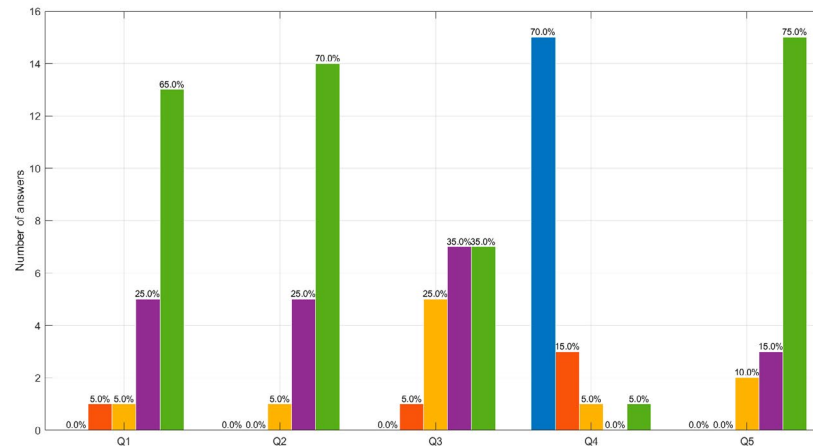
FIGURE 11. Web browser view of the human 3D interactive web-based human brain.

After the test, users will answer the usability post-test questionnaire on the Google Forms platform, through the corresponding link and QR code.

## RESULTS AND DISCUSSION

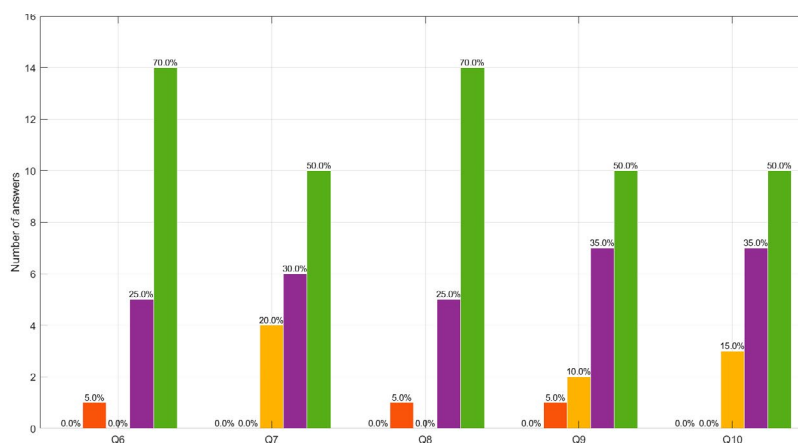
The most significant visualization and usability results of the 3D interactive web-based human brain proposed in this research are described below. In 2024, a usability study was conducted on the use of a 3D interactive web-based human brain for the teaching of basic neuroanatomy. The purpose of the study was to determine whether users could easily learn the basis of neuroanatomy using a web-based platform. The web-based 3D interactive human brain was tested by 20 participants (9 women; 11 men, mean age = 22.1 years, SD = 0.70). Each participant spent an average time of 10 minutes to complete the exploration of all modules and then answered the post-test questionnaire described in the previous section. The questions 5, 6, 8 and 10 were oriented to assess the functionality of neuroanatomy learning purpose, while questions 3, 4 and 7 were for operability; and usability was assessed with the questions 1, 2 and 9.

Firstly, to estimate the internal consistency reliability of the post-test questionnaire scores, we calculate the alpha of Cronbach ( $\alpha$ )<sup>[34]</sup>. Where for this case,  $\alpha=0.93$ , so it is considered that the set of items is consistent to applied research. Figure 12, shows a bar chart to summarize the answers of the users for the first five questions.



**FIGURE 12.** Number of answers to questions 1 to 5 of the acceptance and usability test. Strongly disagree (Pos 1- blue), disagree (Pos 2-orange), neutral (Pos 3-yellow), agree (Pos 4-purple) and strongly agree (Pos 5-green), where position (Pos) is sorted from left to right.

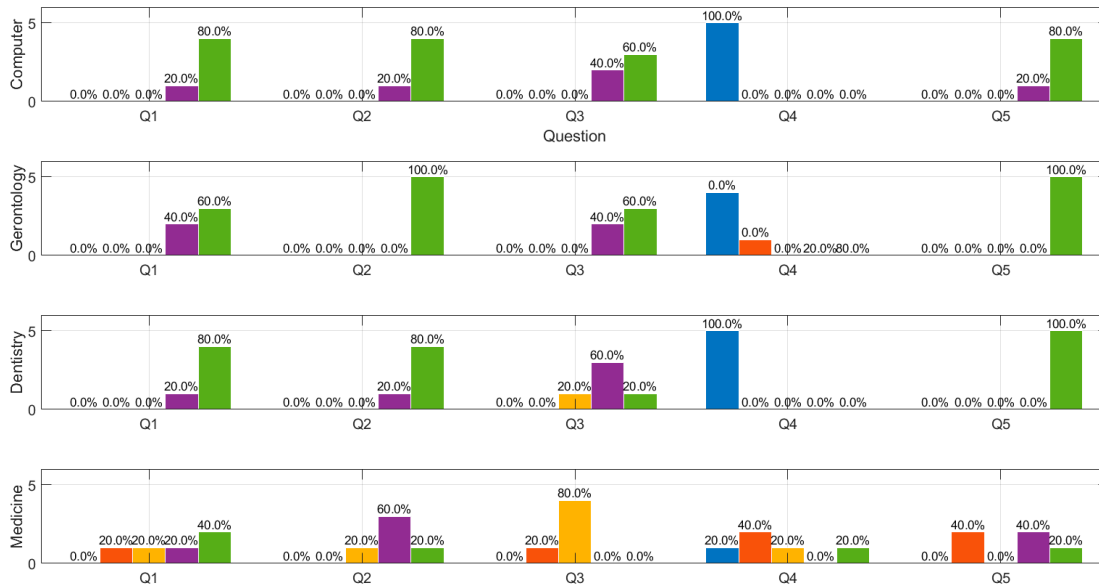
The first question about intuition is related to user interaction with the app without information about its use. 65 % of users totally agree and 25 % agree that the app is intuitive. Question 2 aims to determine the ease of handling the app, for which 70 % completely agree on the ease of handling and 25 % agree. Regarding freedom of navigation in the web environment, an equal amount of 25 % of users totally agreed. Although, in terms of execution errors in the web environment 15 users commented that there were none, some errors were found during the test that required attention. One of the most important objectives of this project is the teaching-learning purpose of neuroanatomy. In that sense, 75 % of the responses lead to the fact that the 3D model and the visualization of the human brain totally agree with this objective. Figure 13, shows the results for questions 6 to 10.



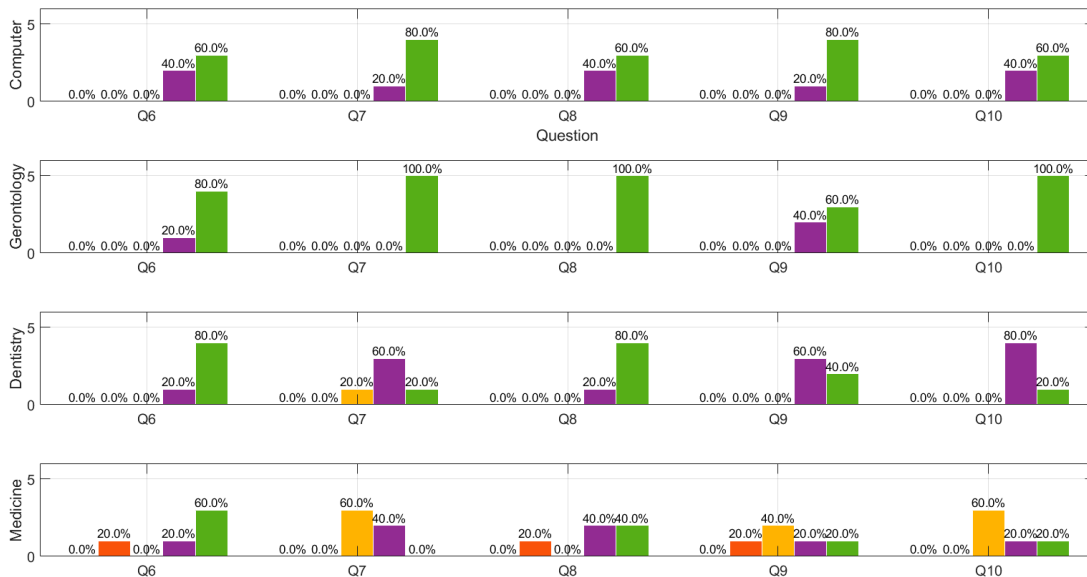
**FIGURE 13.** Number of answers to questions 6 to 10 of the acceptance and usability test. Strongly disagree (Pos 1- blue), disagree (Pos 2-orange), neutral (Pos 3-yellow), agree (Pos 4-purple) and strongly agree (Pos 5-green), where position (Pos) is sorted from left to right.

Question 6 refers to an easy understanding of the elements of neuroanatomy in the 3D model, for which 70 % of the users totally agreed and 25 % agreed. 16 participants positively answered about the organization in a logical and coherent way, which is proof that the users had no difficulty identifying the usefulness of each content. Regarding measurement, if the learning elements are excessive or too technical, 70 % of the responses focused on the total agreement of the concrete nature of the information, which implies that the material is accessible to a wider group

of users who are not experts in the subject. 50 % respondents totally agree that the app is attractive with respect to colors, text size, and gadgets; and 35 % agree respecting the same aspect. Finally, 17 users answered that the model helped reinforce their knowledge, even when there are health sciences and computer users among them. With the objective of developing a general usability analysis for each subgroup by testing each of the questions, Figure 14 and Figure 15 present the responses to the post-test questionnaire for each subgroup.



**FIGURE 14.** Number of answers to questions 1 to 5 related to acceptance and usability test by stratum. Strongly disagree (Pos 1- blue), disagree (Pos 2-orange), neutral (Pos 3-yellow), agree (Pos 4-purple) and strongly agree (Pos 5-green), where position (Pos) is sorted from left to right.



**FIGURE 15.** Number of answers to questions 1 to 5 related to the acceptance and usability test by stratum. Strongly disagree (Pos 1- blue), disagree (Pos 2-orange), neutral (Pos 3-yellow), agree (Pos 4-purple) and strongly agree (Pos 5-green), where position (Pos) is sorted from left to right.

Questions 1, 2, and 9, are related to the usability of the web-based system. In this sense, students of computer science, dentistry, and gerontology, reflected to be in agreement or total agreement in this section, however, students of medicine, who are the most knowledgeable ones in neuroanatomy, had the least favorable responses. With respect to the operability of the system (Q3, Q4), the perception is generally the same among groups as in the case of usability, while in question 7 referring to the structure of the application content, the 4 subgroups have a similar perception tending to be favorable. Finally, regarding the neuroanatomy learning proposal, the computer science, gerontology, and dentistry students (Q5, Q6 and Q8) reported equal favorable perception, while medical students commented that they disagreed or were neutral with the learning objective, ease of understanding and structure of the application content. Regarding whether the app helped to reinforce their knowledge (Q10), gerontology students agreed positively, while medical students were 60 % neutral.

On the other hand, to get a general performance over the usability test, the most frequent response was strongly agreed with 33 apparitions. The mean of the responses was 4.4 and the standard deviation was 0.83. This implies that overall, users responded positively to the evaluation of the brain model. An overview of the results of the usability study appears below, with recommended changes for areas where users found disadvantages and difficulties.

#### *Favorable findings*

- The users liked the brain model and the fact that it is available on the web.
- They all found the drop-down menus and multimedia objects attractive.
- Six users annotated the simplicity and clarity of the 3D models as pleasing
- Most of the users commented that the neuroanatomy information was easy to find and very informative.

#### *Recommendations*

The following is a list of the top user recommendations, some of them were considered to reengineer the early version.

- Enlarging the catalog, since when selecting the group of diencephalon organs, it only shows general information of the group and the information pertaining to this group is missing (was considered).
  - Increasing zoom speed.
  - Reducing camera speed (was considered), and
  - Improving the artistic design of the background.

Although we do not use the system usability scale as a measure of usability, there are some works such as the one presented in <sup>[14]</sup>, where they have used the SUS score of the user study with a value  $79.8 \pm 11.6$ , which means a positive user-interaction, as presented in this work. While our system in its early version as a proof of concept has interesting results and represents a novel contribution to the teaching of neuroanatomy using web-based 3D technology, it has some limitations. Our small sample may help explain the lack of significant group differences on some question perceptions. On the other hand, the study was developed only among students, so it is necessary to get teachers and professionals of neuroanatomy to participate. In addition, a long-term comparative study of the findings between traditional neuroanatomy teaching methods and the proposed system is also needed.

## CONCLUSIONS

In this study, we have presented a 3D interactive web-based human brain modeling process and visualization approach for neuroanatomy education settings, using 3D web technologies and the improved MEDEERV. This methodology allows creating significant learning and establishing best practices to industry standards for generating a more cooperative environment among professionals. The usability capabilities of the web model were evaluated using a post-test questionnaire. The early version as a proof-of-concept of the brain model provides preliminary evidence that the brain model is user-friendly, has an effective user interaction, and is useful to learn about basic neuroanatomy. Then, it is possible to implement the proposed methodology to model and visualize 3D anatomy models in a scalable, reproducible, and standardized way.

The 3D web-based brain visualization provides an advantage towards the learning process in neuroanatomy education settings, which could be expanded to other areas of health and anatomy. The work represents an advance in the integration of interactive 3D technologies in medical education, particularly in the field of neuroanatomy. The web implementation facilitates access and use of this tool, which could positively impact the training of future health professionals and the understanding of brain anatomy by a broader audience. The advantage of interactive visualization of 3D medical objects is focused on improving diagnosis and decision-making in neurological clinical environments. This technology can be used to complement traditional cadaver approaches to better understand complex anatomy such as the brain.

Finally, in this work, the participants who conducted the usability test were undergraduate students in the final semesters of health and computing sciences, as future work we proposed including practicing health professionals and medical educators would provide a broader perspective. Likewise, a simultaneous comparative study with traditional neuroanatomy learning methods is also proposed to determine the success and motivation of medical school students in neuroanatomy courses.

## ETHICAL STATEMENT

The authors declare that they have no potential conflicts of interest regarding the research, authorship and / or publication of the article. Images that were taken from other works were licensed under the Creative Commons Zero (CC0) license (“CC0 Content”), which allows the content to be used for all personal and commercial purposes without attribution to the author/owner of the CC0 content.

## AUTHOR CONTRIBUTIONS

Conceptualization, J-C.G-I., M-J.G-S. and J-G.R-G.; methodology, J.-C.G.-I., M.-J.G.-S. and G-A.T-S.; software, J-G.R-G. and A.S-N.; validation, A.S-N. and A.F-A.; formal analysis, J-C.G-I. and G-A.T-S.; investigation, J-C.G-I. and M-J.G-S.; resources, M-J.G-S. and A.S-N; data curation, J-C.G-I. A.F-A. and J-G.R-G; writing—original draft preparation, J-C.G-I., M-J.G-S. and J-G.R-G.; writing—review and editing, A.S.-N. and G-A.T-S.; visualization, M-J.G-S. and J-G.R-G.; supervision, J.-C.G.-I.; project administration, M.-J.G.-S.; funding acquisition, A.S.-N



## REFERENCES

- [1] E. Alim, Ö. Coskun and T. V. Peker, "Comparison and Evaluation of the Effectiveness of Traditional Neuroanatomy Teaching in Medical Education with Virtual-Reality Application Based On 3D Virtual," *Gazi Med. J.*, vol. 35, no. 4, pp. 407-415, 2024, doi: <https://doi.org/10.12996/gmj.2024.4191>
- [2] I. D. Keenan and A. Ben Awadh, "Integrating 3D visualisation technologies in undergraduate anatomy education," *Adv. Exp. Med. Biol.*, no. 1120, pp. 39-53, 2019, doi: [https://doi.org/10.1007/978-3-030-06070-1\\_4](https://doi.org/10.1007/978-3-030-06070-1_4)
- [3] M. A. Javaid, S. Chakraborty, J. Cryan, H. Schellekens and A. Toulouse, "Understanding neurophobia: Reasons behind impaired understanding and learning of neuroanatomy in cross-disciplinary healthcare students," *Anat. Sci. Educ.*, no. 11, pp. 81-93, 2028, doi: <https://doi.org/10.1002/ase.1711>
- [4] C. Ekstrand, A. Jamal, R. Nguyen, A. Kudryk, J. Mann and I. Mendez, "Immersive and interactive virtual reality to improve learning and retention of neuroanatomy in medical students: a randomized controlled study," *CMAJ Open*, vol. 6, no. 1, pp. 103-109, 2018, doi: <https://doi.org/10.9778/cmajo.20170110>
- [5] F. Nicolosi, F. Pessina, C. A. Gelmi, F. Belotti, D. E. Mahoney, E. Agosti and G. Spena, "New neuroanatomy learning paradigms for the next generation of trainees: a novel literature-based 3D methodology," *Clin. Neurol. Neurosurg.*, vol. 210, 2021, art. no. 106948, doi: <https://doi.org/10.1016/j.clin-neuro.2021.106948>
- [6] M. V. Petersen, J. Mlakar, S. Haber, M. Parent, Y. Smith, P. L. Strick and M. A. Griswold, "Holographic reconstruction of axonal pathways in the human brain," *Neuron*, vol. 104, no. 6, pp. 1056-1064, 2019, doi: <https://doi.org/10.1016/j.neuron.2019.09.030>
- [7] S. B. Tomlinson, B. k. Hendricks and A. Cohen-Gadol, "Immersive three-dimensional modeling and virtual reality for enhanced visualization of operative neurosurgical anatomy," *World Neurosurg.*, vol. 131, pp. 313-320, 2019, doi: <https://doi.org/10.1016/j.wneu.2019.06.081>
- [8] I. D. Keenan and A. Ben Awadh, "Biomedical Visualisation . Advances in Experimental Medicine and Biology," in *Integrating 3D Visualisation Technologies in Undergraduate Anatomy Education*, P. M. Rea, Ed., vol. 1120, Cham, Switzerland: Springer, 2019, ch. 4, pp. 39-53, doi: [https://doi.org/10.1007/978-3-030-06070-1\\_4](https://doi.org/10.1007/978-3-030-06070-1_4)
- [9] L. Zhou, M. Fan, C. Hansen, C. Johnson and D. Weiskopf, "A Review of Three-Dimensional Medical Image Visualization," *Health Data Sci.*, vol. 2022, 2022, art. no. 9840519, doi: <https://doi.org/10.34133/2022/9840519>
- [10] H. Aerts, M. Schirner, T. Dholander, B. Jeurissen, *et al.*, "Modeling brain dynamics after tumor resection using The Virtual Brain," *NeuroImage*, vol. 213, 2020, art. no. 116738, doi: <https://doi.org/10.1016/j.neuroimage.2020.116738>
- [11] L. T. De Paolis, A. De Mauro, J. Raczowsky and G. Aloisio, "Virtual Model of the Human Brain for Neurosurgical Simulation," *Stud. Health Technol. Inform.*, vol. 150, pp. 811-815, 2009, doi: <https://doi.org/10.3233/978-1-60750-044-5-811>
- [12] B. Fiani, F. De Stefano, A. Kondilis, C. Covarrubias, L. Reier and K. Sarhadi, "Virtual reality in neurosurgery: "can you see it?"-A review of the current applications and future potential," *World Neurosurg.*, vol. 141, pp. 291-298, 2020, doi: <https://doi.org/10.1016/j.wneu.2020.06.066>
- [13] O. Hellum, Y. Mu, M. Kersten-Oertel and Y. Xiao, "A novel prototype for virtual-reality-based deep brain stimulation trajectory planning using voodoo doll annotation and eye-tracking," *Comput. Methods Biomech. Biomed. Eng. Imaging Vis.*, vol. 10, no. 4, pp. 418-424, 2022, doi: <https://doi.org/10.1080/21681163.2021.1997645>
- [14] O. Hellum, C. Steele and Y. Xiao, "SONIA: an immersive customizable virtual reality system for the education and exploration of brain networks," *Front. Virtual Real.*, vol. 4, 2024, art. no. 2023, doi: <https://doi.org/10.3389/frvir.2023.1244096>
- [15] K. B. Schloss, M. A. Schoenlein, R. Tredinnick, S. Smith, *et al.*, "The UW virtual brain project: an immersive approach to teaching functional neuroanatomy," *Transl. Issues Psychol. Sci.*, vol. 7, no. 3, pp. 297-314, 2021, doi: <https://psycnet.apa.org/doi/10.1037/tps0000281>
- [16] S. K. Taswell, T. Veeramacheneni and C. Taswell, "BrainWatch software for interactive exploration of brain scans in 3D virtual reality systems," in 2017 39th Annual International Conference of the IEEE Engineering in Medicine and Biology Society, Jeju, Korea (South), 2017, pp. 3704-3707, doi: <https://doi.org/10.1109/EMBC.2017.8037662>
- [17] J. J. G. Keiriz, L. Zhan, O. Ajilore, A. D. Leow and A. G. Forbes, "NuroCave: A web-based immersive visualization platform for exploring connectome datasets," *Netw. Neurosci.*, vol. 2, no. 3, pp. 344-361, 2018, doi: [https://doi.org/10.1162%2Fnetn\\_a\\_00044](https://doi.org/10.1162%2Fnetn_a_00044)
- [18] D. J. Henssen, L. van den Heuvel, G. V. De Jong, M. A. Vorstenbosch, A. M. van Cappellen van Walsum, M. M. Van den Hurk and R. H. Bartels, "Neuroanatomy learning: Augmented reality vs. cross-sections," *Anat. Sci. Educ.*, vol. 13, no. 3, pp. 353-365, 2020, doi: <https://doi.org/10.1002/ase.1912>
- [19] Q. Yuan, X. Chen, J. Zhai, Y. Chen, *et al.* "Application of 3D modeling and fusion technology of medical image data in image teaching," *BMC Med. Educ.*, vol. 21, no. 1, 2021, art. no. 194, doi: <https://doi.org/10.1186/s12909-021-02620-z>
- [20] O. Hellum, M. Kersten-Oertel and Y. M. Xiao, "Assessment of user interaction strategies for neurosurgical data navigation and annotation in virtual reality," *Virtual Real.*, vol. 27, no. 2, pp. 1345-1355, 2022, doi: <https://doi.org/10.1007/s10055-022-00740-5>
- [21] S. Soobia , N. Jhanjhi, N. Mehmod and H. Mamoon, "Analysis of Software Development Methodologies," *Int. J. Comput. Dig. Syst.*, vol. 8, no. 5, pp. 446-460, 2019, doi: <http://dx.doi.org/10.12785/ijcds/080502>
- [22] J. Polcar, M. Gregor, P. Horejsi, and P. Kopecek, "Methodology for designing virtual reality applications," in 26th International DAAAM Symposium, Zadar, Croatia, 2016.
- [23] G. A. Torres-Samperio, A. Franco-Arcega, M. J. Gutiérrez-Sánchez and A. Suárez-Navarrete, "Metodología para el modelado de sistemas de realidad virtual para el aprendizaje en dispositivos móviles," *Pistas Edu.*, vol. 39, no. 127, pp. 518-534, 2018. [Online]. Available: <https://pistaseducativas.celaya.tecnm.mx/index.php/pistas/article/view/1054>

- [24] J. R. Burger, "Human Brain anatomy," in Human Memory Modeled with Standard Analog and Digital Circuits: Inspiration for Man-made Computers, USA: Wiley & Sons, Inc., 2009, pp. 301-308.
- [25] C. M. Barnum, Usability testing essentials: Ready, set... test!, 2nd ed., Cambridge, MA, USA: Elsevier, 2020, pp. 197-246.
- [26] J. Lewis, "Sample sizes for usability studies: Additional considerations," Hum. Factors, vol. 36, no. 2, p. 368-378, 1994, doi: <https://doi.org/10.1177/001872089403600215>
- [27] J. Nielsen and T. Landauer, "A mathematical model of the finding of usability problems," in CHI '93: Proceedings of the INTERACT '93 and CHI '93 Conference on Human Factors in Computing Systems, Amsterdam, 1993, pp. 206-213, doi: <https://doi.org/10.1145/169059.169166>
- [28] R. A. Virzi, "Refining the test phase of the usability evaluation: How many subjects is enough?," Hum. Factors, vol. 34, no. 4, pp. 457-468, 1992, doi: <https://doi.org/10.1177/001872089203400407>
- [29] B. Albert and T. S. Tullis, Measuring the user experience: Collecting, analyzing, and presenting UX metrics, Cambridge, MA, USA: Elsevier, 2022.
- [30] V. Herrera-Tirado, J. Albusac-Jimenez, C. Gonzalez-Morcillo, R. Perales-Gomez, L. Blanco-Coloma, S. Ceruelo-Abajo and A. D. Reyes Guzman, "Valoración de la Experiencia del Usuario en Entornos Virtuales de Rehabilitación de Miembros Superiores," in XLI Congreso Anual de la Sociedad Española de Ingeniería Biomedica, Cartagena, Colombia, 2023, pp. 157-160.
- [31] S. Settapat, T. Achalakul and M. Ohkura, "The usability evaluation of web-based 3D medical image visualization. In Design, User Experience, and Usability. Theory, Methods, Tools and Practice," in First International Conference, DUXU 2011, Held as Part of HCI International 2011, Orlando, FL, USA, 2011, pp. 507-516, doi: [https://doi.org/10.1007/978-3-642-21708-1\\_57](https://doi.org/10.1007/978-3-642-21708-1_57)
- [32] S. Settapat, T. Achalakul and M. Ohkura, "Web-based 3D medical image visualization framework for biomedical engineering education," Comput. Appl. Eng. Educ., vol. 22, no. 2, pp. 216-226, 2014, doi: <https://doi.org/10.1002/cae.20548>
- [33] A. Joshi, S. Kale, S. Chandel and D. K. Pal, "Likert Scale: Explored and Explained," Br. J. Appl. Sci. Technol., vol. 7, no. 4, pp. 396-403, 2015. [Online]. Available: <https://eclass.aspete.gr/modules/document/file.php/EPPAIK269/5a7cc366dd963113c6923ac4a73c3286ab22.pdf>
- [34] Universidad de Valencia. (2022). Apuntes de estimación de la fiabilidad de consistencia interna de los ítems de un instrumento de medida. [Online]. Available: <https://www.uv.es/~fríasnav/AlfaCronbach.pdf>

<https://dx.doi.org/10.17488/RMIB.45.3.6>

E-LOCATION ID: 1470

# Desarrollo de Materiales Poliméricos como Hidrogeles con Curcumina para Regeneración de Tejidos de la Piel

## Development of Polymeric Materials as Hydrogels with Curcumin for Skin Tissue Regeneration

Mateo Pérez Ruiz<sup>1,2</sup> , Miriam Veronica Flores Merino<sup>2</sup>  , Abraham Gonzalez Ruiz<sup>3</sup> 

<sup>1</sup>Universidad Tecnológica de San Juan del Río - México

<sup>2</sup>Universidad Autónoma del Estado de México, Facultad de Química - México

<sup>3</sup>Instituto Nacional de Investigaciones Nucleares - México

### RESUMEN

El objetivo de esta revisión es destacar los avances en el desarrollo de hidrogeles y el uso de curcumina en el tratamiento de heridas crónicas. Las heridas crónicas, como úlceras por presión, vasculares, neuropáticas y neoplásicas, representan un significativo problema de salud global, siendo entre el 1-2 % de todas las heridas que existen, y tan solo en México el 9.4 % de la población adulta padece de heridas crónicas, exacerbadas por complicaciones de la diabetes mellitus. Esta revisión sistemática utilizó la biblioteca virtual *OMICsearch* y el gestor de búsqueda Mendeley, considerando investigaciones que incluyeran alguna de las palabras clave como biopolímeros, curcumina, heridas crónicas e hidrogeles., por lo que se descartó cualquiera que no se relacionara con estas y que no estuviera comprendida en el periodo de búsqueda entre 2006 y 2024. Se encontró a partir de 50 artículos seleccionados que la curcumina, un fitofármaco con propiedades antioxidantes, antiinflamatorias y proangiogénicas, ha demostrado ser eficaz en la cicatrización. Por otra parte, los hidrogeles ofrecen ventajas significativas en el tratamiento de heridas debido a su capacidad para proporcionar control espaciotemporal en las etapas de curación, regular los microambientes de las heridas y liberar moléculas activas de manera controlada. En conclusión, aunque la piel es el órgano más extenso del cuerpo y comúnmente afectado por heridas, estas también pueden ocurrir en otras áreas debido a cirugías, tumores cancerígenos y úlceras de diversas etiologías. El desarrollo de hidrogeles con curcumina no solo se enfoca en heridas cutáneas, sino que también aborda enfermedades inflamatorias, tumores, enfermedades hepáticas, asma y osteoartritis, con aplicaciones farmacéuticas y cosméticas.

**PALABRAS CLAVE:** biopolímeros, curcumina, heridas crónicas, hidrogeles

### ABSTRACT

The aim of this review is to highlight advances in the development of hydrogels and the use of curcumin in the treatment of chronic wounds. Chronic wounds, such as pressure, vascular, neuropathic and neoplastic ulcers, represent a significant global health problem, accounting for 1-2 % of all existing wounds, and in Mexico alone, 9.4 % of the adult population suffers from chronic wounds, exacerbated by complications of diabetes mellitus. This systematic review used the virtual library OMCsearch and the search engine Mendeley, considering research that included some of the keywords such as biopolymers, curcumin, chronic wounds and hydrogels, so any that were not related to these and that did not fall within the search period between 2006 and 2024 were discarded. We found from 50 selected articles that curcumin, a phytopharmaceutical with antioxidant, anti-inflammatory and proangiogenic properties, has been shown to be effective in wound healing. Moreover, hydrogels offer significant advantages in wound treatment due to their ability to provide spatiotemporal control in the healing stages, regulate wound microenvironments and release active molecules in a controlled manner. In conclusion, although the skin is the largest organ of the body and commonly affected by wounds, wounds can also occur in other areas due to surgery, cancerous tumors and ulcers of various etiologies. The development of curcumin hydrogels not only focuses on skin wounds, but also addresses inflammatory diseases, tumors, liver diseases, asthma and osteoarthritis, with pharmaceutical and cosmetic applications.

**KEYWORDS:** biopolymers, curcumin, chronic wounds, hydrogels

#### Autor de correspondencia

DESTINATARIO: Miriam Verónica Flores Merino

INSTITUCIÓN: UNIVERSIDAD AUTÓNOMA DEL ESTADO DE  
MÉXICO

DOMICILIO: P.º COLÓN S/N, RESIDENCIAL COLÓN Y COL CIPRÉS,  
C.P. 50120, TOLUCA DE LERDO, MÉXICO.

CORREO ELECTRÓNICO: mvfloresm@uaemex.mx

#### Recibido:

26 Septiembre 2024

#### Aceptado:

18 Noviembre 2024

## INTRODUCCIÓN

La piel es el órgano más extenso del cuerpo humano, desempeñando un papel crucial en la homeostasis del organismo. Está compuesta por tres capas fundamentales: epidermis, dermis e hipodermis, que trabajan en constante interacción para garantizar su funcionamiento óptimo. La epidermis es la capa más externa, cuya principal función es proteger contra patógenos y la pérdida de agua. La dermis es la capa intermedia compuesta por vasos sanguíneos, nervios y folículos pilosos. Dicha composición permite brindar termorregulación y percepciones sensoriales al organismo humano. Finalmente, la hipodermis es la capa más profunda, compuesta principalmente de tejido adiposo y tejido conectivo; actuando como aislante térmico y amortiguador. La piel puede verse afectada por diversas lesiones, como heridas, que comprometen su capacidad para realizar sus funciones. Algunas heridas, a pesar de iniciar como un proceso agudo, pueden desarrollar un curso clínico impredecible, caracterizado por una curación desordenada y prolongada en el tiempo, lo que las convierte en heridas crónicas<sup>[1]</sup>.

Las heridas presentan diferentes fases de curación como la *fase inflamatoria* que se caracteriza por la necrosis y que requiere limpieza de la herida, seguida de la *fase de proliferación* donde se forma nuevo tejido de granulación y se sintetiza la matriz extracelular para la nueva piel y finalmente la *fase de remodelación* donde culmina con el cierre completo de la herida y la formación de una cicatriz. En esencia las heridas crónicas parecen estar estancadas en una fase inflamatoria ya que su proceso de curación rebasa el plazo de hasta los 6 meses<sup>[1][2]</sup>. Cabe resaltar que las causas más frecuentes de las heridas crónicas son las úlceras por presión, las úlceras vasculares (arteriales y venosas), las úlceras neuropáticas (pie diabético) y las úlceras neoplásicas<sup>[3]</sup>. En general a pesar de representar solo un 1-2 % de las lesiones a nivel mundial, las heridas crónicas generan una carga socioeconómica y psicosocial significativa para la población y los sistemas de salud. En este contexto, las personas con este tipo de heridas pueden sufrir de baja autoestima, aislamiento social, depresión y ansiedad<sup>[4]</sup>.

En México se estima que el 9.4 % de los adultos presentan algún tipo de herida crónica. Por otra parte, la población mexicana tiene un alto riesgo de desarrollar este tipo de heridas derivado de las complicaciones de la diabetes mellitus. En las estadísticas se reporta que cada año se registran 368,069 casos nuevos de diabetes mellitus, y se identifica como la causa número cuatro de morbilidad entre las enfermedades no transmisibles<sup>[5]</sup>. En este sentido los biopolímeros apoyados de moléculas con actividades terapéuticas son una alternativa importante para el tratamiento de heridas. Destacándose a los hidrogeles, como biopolímeros dentro del campo de la regeneración de tejidos, ya que cuenta con adecuadas propiedades de biocompatibilidad, promoción de cicatrización y biodegradabilidad para el tratamiento de heridas crónicas. Los hidrogeles han servido ampliamente como vehículos de principios activos que presentan baja solubilidad o necesitan ser administrados de forma controlada (ejemplo: liberación modificada)<sup>[6]</sup>.

Por otro lado, los productos para el tratamiento de heridas crónicas basados en plantas medicinales han demostrado ser alternativas a las terapias convencionales, debido a su gran accesibilidad, bajo costo y con escasos efectos secundarios significativos<sup>[7]</sup>. Dentro de los tratamientos con principios activos obtenidos de plantas, destaca la curcumina como un activo natural con efectos positivos para la curación del pie diabético, catalogado como una herida crónica. La curcumina es la sustancia más abundante en los curcuminoides extraídos de la cúrcuma (*Curcuma longa* L.). A pesar de que diversos estudios han confirmado y evaluando la actividad química, física y biológica que tiene la curcumina para la promoción de la cicatrización de las heridas<sup>[7]</sup>, todavía existen algunas lagunas respecto a su eficacia, ya que no todos los estudios han obtenido resultados concluyentes y no existe un

consenso claro acerca de sus bondades para el tratamiento de heridas. Por estas razones, la presente revisión busca denotar los avances actuales acerca del desarrollo de los hidrogeles y el uso de curcumina como una opción en el tratamiento de heridas crónicas, siendo un punto de referencia sobre investigaciones relevantes en este tema, ya que ofrece un análisis crítico de las investigaciones recientes, proporcionando una guía clara sobre el estado actual del conocimiento.

## MATERIALES Y MÉTODOS

La presente investigación de revisión se basó principalmente en el uso de la biblioteca virtual *OMICsearch* de Instituto Nacional de Medicina Genómica (INMEGEN) y se complementó con el gestor de búsqueda Mendeley, los cuales brindan herramientas para filtrar por palabras de interés. En esta búsqueda se utilizaron las siguiente palabras clave: biopolímeros, curcumina, heridas crónicas, hidrogeles con la intención de identificar las diferentes investigaciones en este contexto acerca de materiales poliméricos utilizados para la síntesis de hidrogeles como soporte de curcumina para la regeneración tisular, realizándose la conceptualización de la piel como un órgano complejo, heridas crónicas como un problema de salud que requiere diferentes etapas para su recuperación, identificar polímeros usados en el tratamiento de heridas, así como reconocer los beneficios terapéuticos de la curcumina en este contexto y finalmente identificar los hidrogeles con o sin curcumina desarrollados a la fecha para este fin. Los artículos seleccionados se filtraron de entre más de 500 artículos que contenían las palabras clave, en dos idiomas principalmente español e inglés, se descartaron los que estuvieran fuera del periodo tiempo del 2006 al 2024, al final fueron considerandos un total de 50 artículos seleccionados.

## RESULTADOS Y DISCUSIÓN

Esta revisión permitió comprender la complejidad de las heridas que puede presentar la piel. Se identificaron las heridas crónicas como un problema de salud particular, que requiere tratamientos específicos más avanzados y disponibles a la población. Los hidrogeles como materiales poliméricos y la curcumina surgen como opciones terapéuticas prometedoras para la regeneración tisular.

### Piel

La piel es un órgano complejo, con múltiples funciones fundamentales para mantener la homeostasis de nuestro organismo. También se le llama cutis, y forma un órgano protector externo del cuerpo poseedor de una excelente flexibilidad. La piel está constituida por dos capas externas: 1) la epidermis que es el tejido más superficial de la piel, y actúa como una barrera protectora contra agentes externos nocivos, como toxinas, bacterias y deshidratación. Este tejido está compuesto por cinco capas de células epiteliales diferenciadas, denominadas queratinocitos, que se originan en la capa basal y se desplazan hacia la superficie, donde se descaman; y 2) la dermis que es el tejido conectivo que constituye la capa intermedia de la piel, con un grosor, elasticidad y firmeza variables según la región corporal. La dermis tiene una función esencial en la defensa del organismo contra las agresiones externas, como el calor, la radiación ultravioleta, los microorganismos y las sustancias tóxicas<sup>[7][8]</sup>. Por último, la capa más profunda de la piel es la hipodermis, formada por tejido adiposo. La hipodermis tiene varias funciones, entre las que se encuentran el almacenamiento de energía, la amortiguación de impactos y el aislamiento térmico del organismo<sup>[9]</sup>.

En este sentido la piel es uno de los órganos de mayor interés para la ingeniería de tejidos, si bien ha habido gran-

des avances en este campo, aún existen desafíos. La ingeniería de tejidos consiste en el empleo de células y biomateriales sintéticos o naturales, capaces de generar una estructura tisular con propiedades funcionales. Esta estructura tisular se basa en la comunicación e interacción entre las células y la matriz extracelular, que actúa como un andamio que provee soporte y señalización al tejido. Los soportes celulares empleados en ingeniería de tejidos deben reunir una serie de requisitos, tales como: una porosidad óptima que permita la incorporación y la vascularización del tejido, una biodegradabilidad ajustable al ritmo de regeneración tisular, una compatibilidad con el medio biológico, una estabilidad estructural y funcional a lo largo del tiempo, una ausencia de efectos adversos sobre el sistema inmune y las células, y una disponibilidad y manipulación sencillas<sup>[10]</sup>.

### **Heridas crónicas**

En términos generales una herida es una lesión que afecta a los tejidos blandos, causada por factores exógenos, como un arma blanca, o por factores endógenos, como una fractura ósea. La ruptura de la barrera cutánea expone el interior del organismo a la contaminación por microorganismos patógenos, lo que puede provocar una infección <sup>[4]</sup> y por lo tanto complicar el proceso de curación de la herida. Hay que destacar que la recuperación de las heridas es un proceso multifactorial y dinámico que implica diferentes procesos: 1) inflamación, 2) proliferación y 3) remodelación del tejido lesionado. Dependiendo del tiempo en que tarde en curarse una herida, pueden ser clasificadas en agudas o crónicas<sup>[1][2]</sup>.

Las heridas normalmente tienen un periodo muy corto de curación mientras que las heridas crónicas se definen como una lesión cutánea que persiste más de 3 meses o que no progresa adecuadamente en el proceso de reparación tisular, sin alcanzar un resultado anatómico o funcional óptimo. Este término se utiliza frecuentemente en el ámbito médico para referirse a un tipo de úlcera que afecta a la piel y los tejidos subyacentes<sup>[4]</sup>. También se puede conceptualizar como una patología de creciente prevalencia a nivel global, vinculada al aumento de enfermedades crónicas y metabólicas, como la diabetes, la obesidad y las enfermedades cardiovasculares. Estos factores, junto con el envejecimiento y la inmunosupresión, favorecen la aparición de úlceras crónicas, destacando las úlceras del pie diabético, que se relacionan con la hiperglucemia, la neuropatía periférica, la enfermedad vascular y la neuroartropatía<sup>[4]</sup>.

### **Tratamiento de heridas mediante el uso de biopolímeros**

La recuperación en heridas depende de las condiciones de vida del paciente y el tipo de fármaco y el tratamiento que se recibe. El tratamiento de heridas a través de biopolímeros busca, entre otras bondades, brindar un mecanismo de liberación de sustancias permitiendo dosificaciones modificadas que garanticen su efectividad terapéutica. Los biopolímeros se consideran todos aquellos polímeros que provienen de fuentes naturales, a pesar de que pueden ser modificados en el laboratorio para cumplir ciertas características en la aplicación deseada (ejemplo: regeneración de tejidos blandos)<sup>[11]</sup>.

Considerando que varios factores retrasan la recuperación de las heridas (infecciones microbianas, desnutrición, condiciones fisiológicas subyacentes entre otras), se busca que la mayoría de los biopolímeros que se utilizan como apósitos tengan propiedades antimicrobianas, alta biodegradabilidad, biocompatibilidad adecuada, y un buen rendimiento mecánico; lo cual contrasta con lo reportado por Alven S.<sup>[12]</sup>, al mencionar que la mayoría de estos mate-

riales carecen de estas características. En la Tabla 1 se muestran diversos materiales con activos diferentes a la curcumina, que pueden ser aplicados para el tratamiento de heridas. Dentro de las principales funciones de los biopolímeros como apósitos destacan la 1) migración epidérmica mejorada la 2) promoción de la síntesis de colágeno y angiogénesis y 3) protección contra la contaminación. Motivo por el que biomateriales para apósitos desarrollados en el campo de regeneración de tejidos deben ser delgados, pero con una resistencia mecánica adecuada para mantener la estructura con alta capacidad de absorber grandes exudados y con facilidad de remoción<sup>[2]</sup>, dentro este polímero se puede encontrar la celulosa de la cual hay diversas aplicaciones tanto en el ámbito de ingeniería de tejidos como en áreas de desarrollo de membranas de separación de compuestos<sup>[13]</sup>, lo que nos permite asumir que es una gran opción en el campo de materiales para la recuperación de heridas.

**TABLA 1. Biopolímeros y su aplicación en tratamientos de heridas y otros padecimientos relacionados.**

| Base polimérica                                   | Descripción  | Aplicación   | Ref. |
|---|--|--|------|
| Tela de algodón, Hidrogeles y esponjas compuestas | Apósitos de tela de algodón, almohadillas de nanofibras biocompuesto cargados con <i>Aloe vera</i> .   | Tratamiento de heridas, por las propiedades analgésica, antibacteriana, antioxidante, antifúngico, antiviral, cicatrizante, antiinflamatorio, limpiador, antiséptico del <i>Aloe vera</i> .  | [12] |
| Colágeno y gelatina                               | Polímero con estabilidad química y térmica, permeable al O <sub>2</sub> .  | Para heridas por quemaduras y úlceras. Resistente al ataque bacteriano, así como a otros traumatismos mecánicos.   | [14] |
| Quitosano   | Red de polímero 3D, con fuerte absorción de agua, excelente compatibilidad, no adhesivo, degradable y rentable.  | Heridas agudas a crónicas, exudativas, heridas contaminadas, úlceras venosas de las piernas, diabetes y quemaduras de primer y segundo grado.  | [15] |
| Alginato  | Material Fibroso, altamente absorbente, requiere doble aplicación para evitar el secado.   | Adecuados para todo tipo de heridas a excepción de heridas secas.  | [1]  |
| Ácido hialuronico                                 | Posee una rápida degradación, presenta buena absorción de agua.  | Tratamiento de quemaduras, heridas quirúrgicas epiteliales y crónicas. Modula la herida a través de receptores HA específicos, inflamación, migración celular y angiogénesis.  | [16] |
| Celulosa bacteriana-curcumina                     | Celulosa polimérica de origen bacteriana combinada con curcumina.  | Presenta buenos resultados en heridas crónicas infectadas  | [4]  |
| Heparina  | Matriz extracelular Sulfato de heparán/heparina. Con cadenas de polisacáridos lineales compuestas de ácido piro-sulfúrico unido repetidamente (1→4) y residuos de 2-amino-2-desoxiglucopiranososa (glucosamina). | HS/HP juegan un papel clave en la señalización química entre las células a través de la unión y regulación de las actividades de los factores de crecimiento que se unen a la heparina, las enzimas proteolíticas y los inhibidores de la proteasa leucocitaria y procesos de carcinogénesis | [17] |
| Celulosa  | Red 3D, ayuda a la retención de agua, permeable a fluidos.   | Aplicable en úlceras cutáneas, favoreciendo la formación del tejido de granulación y la restauración de la epidermis.  | [18] |

La Tabla 1 nos muestra como dentro del grupo de biopolímero encontrados en esta revisión 7 de cada 8 desarrollos están relacionados con aplicaciones en el tratamiento de heridas aprovechando las características de estos materiales como el *Aloe vera*, colágeno, quitosano, alginato, ácido hialuronico, celulosa bacteriana, celulosa para formar estructuras compatibles con activos y capaces de ser usados para la regeneración tisular en general pero principalmente en daños de tejido por quemaduras, úlceras cutáneas, heridas quirúrgicas, pie diabético, entre otras. La tabla muestra que la mayoría de los estudios se centran en biopolímeros para promover la cicatrización. Sin embargo, solo



un par de investigaciones exploraron sinergias al incorporar compuestos naturales como el *Aloe vera* y la curcumina.

### Curcumina

En su composición la cúrcuma (*Curcuma longa L.*) presenta un polifenol denominado curcumina, la cúrcuma es una especia dietética de la India que ha mostrado muchos beneficios relacionados con la salud y efectos farmacológicos<sup>[19]</sup>, se ha utilizado ampliamente como remedio a base de hierbas y durante siglos en la medicina indígena para tratar una variedad de afecciones inflamatorias<sup>[18][19][20]</sup> y otras enfermedades. Es considerado como un nutraceutico con amplio espectro protector contra diferentes enfermedades, por ejemplo, la fibrosis, los trastornos neurológicos, las enfermedades hepáticas, la diabetes y el asma<sup>[21]</sup>. El ingrediente medicinal activo de la cúrcuma se ha identificado como curcuminoides, que incluye un componente activo curcumina (diferuloilmetano) - (1,7-bis (4-hidroxi-3-metoxifenil) -1,6-hepadieno-3,5-diona) y resulta beneficioso en el tratamiento de diversos trastornos, incluidas las enfermedades de la piel. La curcumina posee propiedades antiinflamatorias, antioxidantes y antiproliferativas que están mediadas por la regulación de varias citocinas inflamatorias, factores de crecimiento, proteína quinasas, factores de transcripción y otras enzimas<sup>[22]</sup>. Además, se ha demostrado que la curcumina también induce la apoptosis a través de vías mitocondriales y mediadas por receptores, así como a través de la activación de cascadas de caspasas<sup>[22]</sup>, que en distintas variedades de cáncer ha demostrado resultados excelentes en su tratamiento<sup>[23]</sup> y con respecto a su toxicidad se ha reportado un bajo nivel y bajos efectos adversos durante su uso con intenciones farmacológicas<sup>[24]</sup>. En la Tabla 2 se describen diversas presentaciones farmacéuticas que incluyen en su formulación a la curcumina como activo terapéutico principal en el tratamiento de diversos padecimientos, demostrando que la curcumina en la actualidad se considera un poderoso aliado en el combate de enfermedades.

Las formulaciones innovadoras de curcumina, como los vasos sanguíneos artificiales en 3D y las nanomicelas de dendrímeros, junto con las nanopartículas de  $\beta$ -ciclodextrina-curcumina y las micropartículas de curcumina, muestran un enfoque avanzado en mejorar la solubilidad, biodisponibilidad y eficacia terapéutica de la curcumina. Estas técnicas permiten una mejor estabilidad y absorción del compuesto, lo que es crucial para su uso efectivo en tratamientos oncológicos, antiinflamatorios y otros usos terapéuticos, destacando su potencial en la ingeniería de tejidos y en la administración controlada del fármaco. Además, la amplia gama de aplicaciones terapéuticas abarca desde el uso tópico en geles y cremas para la cicatrización de heridas y el tratamiento de afecciones dermatológicas, hasta formulaciones orales y parenterales para enfermedades sistémicas, subrayando la versatilidad de la curcumina en diversas presentaciones farmacéuticas.

### Hidrogeles en el tratamiento de heridas

Los hidrogeles pueden definirse como sistemas coloidales compuestos por uno o varios polímeros hidrófilos cuyas cadenas están entrecruzadas por uniones físicas o químicas formando una red tridimensional. Se caracterizan principalmente por su capacidad para captar fluidos acuosos del medio que los rodea hinchándose hasta el equilibrio, estos son capaces de ofrecer una estructura mecánica resistente para ingresar moléculas activas que favorezcan la cicatrización de heridas<sup>[34]</sup>. Así mismo, un hidrogel constituye un entrecruzado tridimensional a partir de cadenas flexibles de polímeros que absorben cantidades considerables de agua. Los polímeros que forman estos materiales son hidrófilos, es decir, tienen afinidad por el agua, pero no se disuelven en ella. Son blandos

y elásticos, lo que les confiere una buena adaptabilidad. Cuando entran en contacto con el agua, se expanden notablemente, incrementando su volumen, pero conservan su forma hasta alcanzar un estado de equilibrio termodinámico<sup>[35]</sup>.

**TABLA 2. Presentaciones farmacéuticas con curcumina como principio activo.**

| Presentación   | Descripción   | Aplicación   | Ref. |
|--|---|--|------|
| Vasos sanguíneos artificiales 3D                                       | Integración de nanopartículas estatinas/curcumina.  | En vasos sanguíneos artificiales (ABV) utilizando tecnología de impresión tridimensional.  | [25] |
| Nanomicelas de dendrones de fósforo.                                   | Plataforma de nanomedicina basada en dos nanomicelas de dendrones de fósforo anfílico (C11G3) modificados con sal de dimetil-fosfonato de sodio (TBP) que contienen tiramina encapsulados con curcumina (Cur), un fármaco antioxidante.   | Terapia combinada antiinflamatoria y antioxidante de enfermedades inflamatorias.   | [26] |
| Nanopartículas de $\beta$ -ciclodextrina-curcumina                     | Vehículo de administración de fármacos de $\beta$ -ciclodextrina ( $\beta$ -CD) dirigido al receptor de folato para mejorar la bio-disponibilidad, la bioseguridad y la capacidad de carga de fármacos de la curcumina.   | Terapia contra tumores cancerígenos a través de la orientación activa y la liberación controlable.   | [27] |
| Ginsenósido 20(S)-rg3 y curcumina                                      | Tratamiento conjunto con ginsenósido 20(S)-Rg3 y curcumina en células de cáncer de mama MDA-MB-231 con y sin radioterapia.  | Tratamiento para el cáncer de mama.  | [28] |
| Obleas liofilizadas-Curcumina  | Fabricadas por reticulación de quitosano con beta glicerofosfato bajo agitación magnética. Se prepararon obleas compuestas mediante la adición de hialuronato de sodio.   | Eficaz para la cicatrización de heridas, con propiedades anti-inflamatorias.   | [29] |
| Modulador de TGF- $\beta$ (tanto al alza como a la baja).              | Diferentes sistemas según la vía, dieta, intraperitoneal, oral, intranasal, evaluados en pruebas <i>in vitro</i> / <i>in vivo</i>   | Mejorar la fibrosis, los trastornos neurológicos, las enfermedades hepáticas, la diabetes y el asma. Además, de suprimir la proliferación de células tumorales e invadir células cancerosas. | [21] |
| Crema con curcumina  | Sistemas de aplicaciones en crema cargadas de curcumina.  | Utilizada en tratamientos dermatológicos como antiinflamatorio efectos saludables en quemaduras, heridas, cicatrices quirúrgicas, piel dañada por la luz y psoriasis.                        | [30] |
| Curcumina fitosomal  | El fitosoma, conocido como sistema de suministro de fitolípidos, es una tecnología patentada para conjugar fitoquímicos con fosfolípidos como la fosfatidilcolina (PC), con el objetivo de producir complejos moleculares compatibles con los lípidos que pueden mejorar la absorción y la biodisponibilidad de la carga fitoquímica. | Tratamiento de diversas enfermedades humanas como el cáncer, la osteoartritis, la diabetes y las enfermedades inflamatorias  | [31] |
| Vesículas inmovilizadas de hialuronato de sodio cargadas con curcumina | Nanovesículas altamente biocompatibles utilizando hialuronato de sodio, denominadas hialurosomas cargadas con curcumina, en alta concentración.   | Administración y rápida deposición del fármaco en toda la piel, los hialurosomas aparecen como nanoportadores prometedores para aplicaciones cosméticas y farmacéuticas.                     | [32] |
| Nanopartículas encapsuladas en curcumina                               | Curcumina encapsulada en un vehículo de nanopartículas de hidrogel de silano (curc-np) para superar su escasa solubilidad.  | Representan un nuevo adyuvante tópico antimicrobiano y de cicatrización de heridas para heridas por quemaduras infectadas y otras lesiones cutáneas.   | [33] |

Diversos estudios sobre hidrogeles han demostrado que son materiales excelentes, viables y ecológicos para el campo biomédico debido a su biocompatibilidad y biodegradabilidad, por ejemplo, se reporta que hidrogeles preparados con polisacáridos y nanopartículas magnéticas poseen una amplia contribución en el campo de administración de fármacos dirigidos, regeneración de tejidos y terapia de hipertermia<sup>[35]</sup>. Por ejemplo, Kovacevic B, *et al.*<sup>[36]</sup> describen hidrogeles que incorporan ácidos biliares que ejercen propiedades antioxidantes, antiinflamatorias e inmunosupresoras, y son efectivos para disminuir y mejorar la hipertensión, además que poseen propiedades anfóteras únicas, que permite generar polímeros, hidrogeles y/o polielectrolitos capaces de formar microcápsulas o nanocápsulas, que brindan una mayor estabilidad termodinámica, osmótica y estructural, y se encargan de la administración controlada a través de la orientación específica del tejido, la liberación dependiente del pH y guiada por la temperatura. Pourshahrestani S, *et al.*<sup>[37]</sup> en su análisis menciona la relevancia de la hemostasis y los procesos de cicatrización de heridas y que los avances más recientes en los sistemas de hidrogel diseñados a partir de polímeros naturales y sintéticos para aplicaciones hemostáticas, aprovechando sus excelentes propiedades mecánicas, biocompatibilidad, biodegradabilidad, efecto antibacteriano y fuertes propiedades de adhesión tisular.

Como se puede apreciar, la versatilidad que poseen los hidrogeles les permiten ser una base polimérica confiable para la dosificación de sustancias activas, en la Tabla 3 se registran aplicaciones de hidrogeles cargados de curcumina, dejando en claro que el desarrollo de estos materiales no se limitan al tratamiento de heridas en la piel, sino que su aplicación tiene alcances en el tratamiento de heridas de otras regiones del cuerpo y de otros padecimientos, como por ejemplo posterior a cirugías gástricas, enfermedades periodontales, cáncer, entre otros.

Cabe destacar que adicionalmente podemos encontrar que la celulosa, por su gran versatilidad en sus propiedades fisicoquímicas la coloca como un biopolímero del cual se pueden obtener derivados con amplias características favorables para la síntesis de hidrogeles.

## CONCLUSIONES

Las heridas crónicas, como el pie diabético, son un problema de salud complejo que va más allá de la piel. Estas lesiones pueden involucrar tejidos y tener diversas causas, como trastornos vasculares o enfermedades oncológicas. Debido a la complejidad de las heridas, se necesitan tratamientos novedosos y eficaces. Actualmente, existe una gran diversidad de biopolímeros que suelen ser usados en el tratamiento de heridas, aprovechando las características de materiales como el *Aloe vera*, colágeno, quitosano, alginato, ácido hialurónico y celulosa bacteriana por mencionar algunos. Para finalizar el objetivo de esta revisión era poner en contexto los avances en el desarrollo de hidrogeles combinados con curcumina para regeneración de tejidos de la piel, lo que nos lleva considerar que debido a sus numerosas actividades biológicas, su bajo nivel de toxicidad y los menores efectos adversos en comparación con fármacos, la curcumina se puede considerar como un agente activo seguro para el tratamiento de infecciones, inhibidor cancerígeno, entre otras, pero principalmente en el tratamiento de heridas con efecto favorable en la regeneración tisular y no solo de la piel, si no de otras regiones del cuerpo. Así mismo, en la actualidad existe un crecimiento en el desarrollo farmacéutico y en el área de biomateriales para el tratamiento de heridas con diversos activos, pero en particular ha crecido el uso de hidrogeles que por sus características de biocompatibilidad permiten mejorar el proceso de curación, además de representar un medio de liberación controlada de fármacos, abriendo la posibilidad que se desarrollen más de estos con polímeros combinados con curcumina específicamente para el tratamiento de los diversos tipos de heridas en el cuerpo y no solo de la piel. En particular, se encontró que los hidrogeles con curcumina, diseñados para tratar heridas crónicas cutáneas, podrían tener aplicaciones más amplias en otras regiones del cuerpo.

**TABLA 3. Aplicaciones de curcumina en hidrogeles para el tratamiento de enfermedades.**

| Autor                                   | Sistema  | Descripción   | Aplicación   |
|---|--|---|--|
| Zhu <i>et al.</i> 2024<br>[38]          | Micropartículas de gelatina de pescado   | Micropartículas de hidrogel de gelatina de pescado de metacrilato (FGMA) (FGMPs@Cur) que encapsulan Cur mediante tecnología de electrospray microfluídico.  | Tratamiento integral posoperatorio del cáncer gástrico.                            |
| Veerapandian <i>et al.</i> 2024<br>[39] | Hidrogel reticulado de levano-quitosano  | Material polimérico de red 3D, hidrogel reticulado de levano-quitosano (OLC) oxidado cargado con oleoresina de cúrcuma.   | Material de apósito para heridas.  |
| Lan <i>et al.</i> 2023<br>[40]          | Vesículas extracelulares derivadas de PDLSC cebadas con curcumina (Cur-PDLSC-EV) | Cultivo celular de células madre del ligamento periodontal (PDLSC) pretratadas con curcumina mediante ultra-centrifugación.   | Prevención y tratamiento de enfermedades periodontales.                            |
| Tomić <i>et al.</i> 2023<br>[41]        | Andamios de Hidrogel   | Andamios de hidrogel a base Alginato de sodio, gelatina, HEMA, GO, curcumina.   | Tratamiento dérmico, sistemas de administración de fármacos, antimicrobianos.      |
| Nawaz <i>et al.</i> 2022<br>[42]        | Hidrogel con aceites esenciales  | Curcumina 2% p/p en hidrogel que contiene aceite de eucalipto, <i>Aloe vera</i> y clavo, utilizando carboximetilcelulosa (CMC) como agente gelificante.   | Potencial opción efectiva contra infecciones de herida.                            |
| Bashash <i>et al.</i> 2022<br>[43]      | Niosomas de curcumina  | Hidrogeles de gelatina bovina y clara de huevo, vehículos de encapsulación y posterior liberación de niosomas a base de estearato de sacarosa cargados con curcumina.   | Sistema de administración controlada para la curcumina.                            |
| Islam <i>et al.</i> 2022<br>[44]        | Celulosa modificada con pectina/ mucina  | Incorporación de pectina (Pec) y mucina (Muc) en una red de hidrogel de celulosa pura preparada en un sistema solvente de urea/NaOH y reticulada con epíclorhidrina para crear hidrogeles superabsorbentes a base de celulosa adicionados con curcumina.              | Sistemas de administración controlada de fármacos y otras aplicaciones biomédicas. |
| Heidarifard <i>et al.</i> 2021<br>[45]  | Hidrogel Alginato-nanoemulsión de curcumina                                      | Nanoemulsiones curcumina en aceite de coco preparadas por desplazamiento de solventes, las nano-emulsiones obtenidas se convirtieron en hidrogeles a base de alginato de sodio por gelificación iónica.   | Absorción, encapsulación y liberación controlada de curcumina.                     |
| HaqAsif <i>et al.</i> 2021<br>[46]      | Hidrogel a base de goma guar   | Hidrogel de goma guar injertada con ácido acrílico (GG-g-PAA) usando de iniciador redox. persulfato de amonio. Se mejoró la estabilidad estructural del copolímero injertado utilizando N, N-metilenbisacrilamida como reticulante con carga simultánea de curcumina. | Administración de fármacos anti-cancerígenos naturales (curcumina).                |
| Bhubhanil <i>et al.</i> 2021<br>[47]    | Hidrogel de nanopartículas de plata- goma guar/curcumina                         | La curcumina se utiliza como agente de unión a la superficie para estabilizar las nanopartículas de plata (Cur-AgNP) que luego se combinan en hidrogeles de goma guar (GG/Cur-AgNP).  | Materiales para vendajes de heridas con alta capacidad antibacteriana.             |
| Qi <i>et al.</i> 2020<br>[48]           | Hidrogel termosensible de guanidina-quitosano                                    | El complejo de curcumina/HP-β-CD se preparó mediante el método de liofilización en una proporción molar de 1:2 de HP-β-CD y moléculas de curcumina.   | Antidepresivo de curcumina de administración nasal.                                |
| Abo El-Ela <i>et al.</i> 2020<br>[49]   | Hidrogel niosoma de curcumina-alginato de sodio/quitosano                        | Hidrogel de niosoma de curcumina sensible al pH in situ y nanopartículas de alginato de sodio y quitosano cargadas con doxiciclina.   | Tratamiento eficaz de la infección por brucelosis.                                 |
| Momin <i>et al.</i> 2016<br>[50]        | Esponja de hidrogel biodegradable  | Hidrogel superporoso biodegradable de quitosano y alginato incorporado con curcumina y miel.  | Cicatrización rápida y eficaz de heridas.  |

## DECLARACIÓN ÉTICA

Este artículo se fundamenta en la investigación documental, que consiste en la recopilación y análisis de información proveniente de diversas fuentes, sin realizar ningún tipo de experimentación con seres vivos

## CONFLICTO DE INTERESES

Los autores no presentan ningún conflicto de intereses que pueda afectar a la objetividad o la calidad de este trabajo ni en competencia.

## AGRADECIMIENTOS

La búsqueda fuentes científicas fue basada en la plataforma de OMICsearch perteneciente a la biblioteca virtual del Instituto Nacional de Medicina Genómica.

## CONTRIBUCIÓN DE LOS AUTORES

M. P. R. curación de datos, investigación, recursos, visualización, escritura, revisión y edición de manuscrito; M. V. F. M. conceptualización, adquisición de fondos, administración del proyecto, supervisión, escritura, revisión y edición del manuscrito; A. G. R. análisis formal, metodología, validación y revisión y edición de manuscrito.

## REFERENCIAS

- [1] E. Rezvani Ghomi, E. Khalili, S. Nouri Khorasani, R. Esmaeely Neisiany, S. Ramakrishna, "Wound dressings: Current advances and future directions," *J. Appl. Polym. Sci.*, vol. 136, 2019, art. no. 47738, doi: <https://doi.org/10.1002/app.47738>
- [2] T. H. Park, S. Lee, R. Amatya, P. Maharjan, et al., "Development and characterization of a superabsorbing hydrogel film containing *Ulmus davidiana* var. *Japonica* root bark and pullulan for skin wound healing," *Saudi Pharm. J.*, vol. 28, no. 7, pp. 791-802, 2020, doi: <https://doi.org/10.1016/j.jsps.2020.05.007>
- [3] E. Esteva, "El tratamiento de las heridas. Tipos de apósitos y antisépticos," *OFFARM*, vol. 25, no. 8, pp. 54-60, 2006.
- [4] C. C. Becerra G., M. P. García A., Y. D. Reyes M., M. G. Huertas, "Biopelículas bacterianas en heridas crónicas," *Rev. Salud Bosque*, vol. 9, no. 1, pp. 47-61, 2019, doi: <https://doi.org/10.18270/rsb.v9i1.2643>
- [5] G. Vela-Anaya, E. M. Stegensek-Mejía, and C. Leija-Hernández, "Características epidemiológicas y costos de la atención de las heridas en unidades médicas de la Secretaría de Salud," *Rev. Enferm. Inst. Mex. Seguro Soc.*, vol. 26, no. 2, pp. 105-114, 2018. [En línea]. Disponible en: <https://www.medicographic.com/pdfs/enfermeriaimss/eim-2018/eim182g.pdf>
- [6] S. Bashir, M. Hina, J. Iqbal, A. H. Rajpar, et al., "Fundamental concepts of hydrogels: Synthesis, properties, and their applications," *Polymers*, vol. 12, no. 11, 2020, art. no. 2702, doi: <https://doi.org/10.3390/polym12112702>
- [7] N. Van Long, B. T. Ha, A. V. Tuan, H. Van Luong, et al., "Phytosomal nanoparticles preparation of curcuminoids to enhance cellular uptake of curcuminoids on breast cancer cell line MCF-7," *Pharmacogn. J.*, vol. 11, no. 5, pp. 1037-1045, 2019, doi: <http://dx.doi.org/10.5530/pj.2019.11.163>
- [8] B. Higashida, *Ciencias de la Salud*, México: Mc Graw Hill, 2013.
- [9] R. Falabella Falabella, J. V. Chaparro, M. I. Barona Cabal, *Dermatología: Fundamentos de medicina*, 8ª ed. (8a edición). Medellín, Colombia: Fondo Editorial CIB, 2017.
- [10] M. I. Chaves-Rodríguez, L. A. Calvo-Castro, R. Alva-rado-Meza, O. Madrigal-Monge, A. Ulloa-Fernández, C. Centeno-Cerdas, "Sustitutos e injertos de piel desarrollados por ingeniería de tejidos Skin grafts and substitutes developed by Tissue Engineering," *Rev. Tecnol. Marcha*, vol. 28, no. 5, pp. 46-57, 2014. doi: <http://dx.doi.org/10.18845/tm.v28i5.2219>
- [11] M. Bahadoran, A. Shamloo, Y. D. Nokoorian, "Development of a polyvinyl alcohol/sodium alginate hydrogel-based scaffold incorporating bFGF-encapsulated microspheres for accelerated wound healing," *Sci. Rep.*, vol. 10, no. 1, 2020, art. no. 7342, doi: <https://doi.org/10.1038/s41598-020-64480-9>
- [12] S. Alven, V. Khwaza, O. O. Oyedeji, B. A. Aderibigbe, "Polymer-based scaffolds loaded with aloe vera extract for the treatment of wounds," *Pharmaceutics*, vol. 13, no. 7, 2021, art. no. 961, doi: <https://doi.org/10.3390/pharmaceutics13070961>
- [13] J. Ledesma-García, G. Orozco, R. Antaño, L. A. Godínez, "Preparation and study of cellulose acetate membranes modified with linear polymers covalently bonded to starburst polyamidoamine dendrimers," *J. Appl. Polym. Sci.*, vol. 110, no. 5, pp. 2898-2906, 2008, doi: <https://doi.org/10.1002/app.28833>

- [14] R. Naomi, H. Bahari, P. M. Ridzuan, F. Othman, "Natural-based biomaterial for skin wound healing (Gelatin vs. collagen): Expert review," *Polymers*, vol. 13, no. 14, 2021, art. no. 2319, doi: <https://doi.org/10.3390/polym13142319>
- [15] M. A. Matica, F. L. Aachmann, A. Tøndervik, H. Sletta, and V. Ostafe, "Chitosan as a wound dressing starting material: Antimicrobial properties and mode of action," *Int. J. Mol. Sci.*, vol. 20, no. 23, art. no. 5889, 2019, doi: <https://doi.org/10.3390/ijms20235889>
- [16] C. Cinthura, V. V. Priya, R. Gayathri, "A study on the effect of hyaluronic acid on tissue repair proteins," *Drug Invent. Today*, vol. 12, no. 10, pp. 2212-2216, 2019.
- [17] P. Olczyk, E. Mencner, K. Komosińska-Vassev, "Diverse Roles of Heparan Sulfate and Heparin in Wound Repair," *Biomed. Res. Int.*, vol. 2015, 2015, art. no. 549417, doi: <https://doi.org/10.1155/2015/549417>
- [18] W. Czaja, A. Krystynowicz, S. Bielecki, R. M. Brown, "Microbial cellulose - The natural power to heal wounds," *Biomaterials*, vol. 27, no. 2, pp. 145-151, 2006, doi: <https://doi.org/10.1016/j.biomaterials.2005.07.035>
- [19] J. Yin, L. Wei, N. Wang, X. Li, M. Miao, "Efficacy and safety of adjuvant curcumin therapy in ulcerative colitis: A systematic review and meta-analysis," *J. Ethnopharmacol.*, vol. 289, 2022, art. no. 115041, doi: <https://doi.org/10.1016/j.jep.2022.115041>
- [20] Y. Wang, Y. Wang, N. Cai, T. Xu, F. He, "Anti-inflammatory effects of curcumin in acute lung injury: In vivo and in vitro experimental model studies," *Int. Immunopharmacol.*, vol. 96, 2021, art. no. 107600, doi: <https://doi.org/10.1016/j.intimp.2021.107600>
- [21] M. Ashrafizadeh, A. Zarrabi, K. Hushmandi, V. Zarrin, et al., "Toward Regulatory Effects of Curcumin on Transforming Growth Factor-Beta Across Different Diseases: A Review," *Front. Pharmacol.*, vol. 11, 2020, art. no. 585413, doi: <https://doi.org/10.3389/fphar.2020.585413>
- [22] R. L. Thangapazham, S. Sharad, R. K. Maheshwari, "Phytochemicals in Wound Healing," *Adv. Wound Care (New Rochelle)*, vol. 5, no. 5, pp. 230-241, 2016, doi: <https://doi.org/10.1089/wound.2013.0505>
- [23] K. Morshedi, S. Borran, M. S. Ebrahimi, M. J. Masoud Khooy, et al., "Therapeutic effect of curcumin in gastrointestinal cancers: A comprehensive review," vol. 35, no. 9, pp. 4834-4897, doi: <https://doi.org/10.1002/ptr.7119>
- [24] B. Saifi, S. M. Haftcheshmeh, M. Feligioni, E. Izadpanah, et al., "An overview of the therapeutic effects of curcumin in reproductive disorders with a focus on the antiinflammatory and immunomodulatory activities," *Phytother. Res.*, vol. 36, no. 2, pp. 808-823, 2022, doi: <https://doi.org/10.1002/ptr.7360>
- [25] E. J. Lee, J. Choi, H. J. Lim, D. Yoon, et al., "3D-bioprinted cell-laden blood vessel with dual drug delivery nanoparticles for advancing vascular regeneration," *Int. J. Bioprint.*, vol. 10, no. 2, 2024, art. no. 1857, doi: <https://doi.org/10.36922/ijb.1857>
- [26] J. Li, L. Chen, C. Li, Y. Fan, et al., "Phosphorus dendron nanomicelles as a platform for combination anti-inflammatory and antioxidative therapy of acute lung injury," *Theranostics*, vol. 12, no. 8, pp. 3407-3419, 2022, doi: <https://doi.org/10.7150/thno.70701>
- [27] W. Hong, F. Guo, N. Yu, S. Ying, et al., "A novel folic acid receptor-targeted drug delivery system based on curcumin-loaded  $\beta$ -cyclodextrin nanoparticles for cancer treatment," *Drug Des. Devel Ther.*, vol. 15, pp. 2843-2855, 2021, doi: <https://doi.org/10.2147/dddt.s320119>
- [28] V. Changizi, V. Gharekhani, E. Motavaselil, "Co-treatment with ginsenoside 20(S)-rg3 and curcumin increases radiosensitivity of mda-mb-231 cancer cell line," *Iran J. Med. Sci.*, vol. 46, no. 4, pp. 291-297, 2021, doi: <https://doi.org/10.30476/ijms.2020.83977.1334>
- [29] I. M. Adel, M. F. ElMeligy, A. F. A. Abdelkhalik, N. A. Elkasabgy, "Design and characterization of highly porous curcumin loaded freeze-dried wafers for wound healing," *Eur. J. Pharm. Sci.*, vol. 164, 2021, art. no. 105888, doi: <https://doi.org/10.1016/j.ejps.2021.105888>
- [30] M. Heng, "Topical Curcumin: A Review of Mechanisms and uses in Dermatology," *Int. J. Dermatol. Clin. Res.*, vol. 3, no. 1, pp. 010-017, 2017, doi: <https://dx.doi.org/10.17352/2455-8605.000020>
- [31] H. Mirzaei, A. Shakeri, B. Rashidi, A. Jalili, Z. Banikazemi, A. Sahebkar, "Phytosomal curcumin: A review of pharmacokinetic, experimental and clinical studies," *Biomed. Pharmacother.*, vol. 85, pp. 102-112, doi: <https://doi.org/10.1016/j.biopha.2016.11.098>
- [32] M. L. Manca, I. Castangia, M. Zaru, A. Nácher, et al., "Development of curcumin loaded sodium hyaluronate immobilized vesicles (hyalurosomes) and their potential on skin inflammation and wound restoring," *Biomaterials*, vol. 71, pp. 100-109, 2015, doi: <https://doi.org/10.1016/j.biomaterials.2015.08.034>
- [33] A. E. Krausz, B. L. Adler, V. Cabral, M. Navati, et al., "Curcumin-encapsulated nanoparticles as innovative antimicrobial and wound healing agent," *Nanomedicine*, vol. 11, no. 1, pp. 195-206, 2015, doi: <https://doi.org/10.1016/j.nano.2014.09.004>
- [34] R. D. F. Soares, N. G. N. Campos, G. P. Ribeiro, B. C. C. Salles, et al., "Development of a chitosan hydrogel containing flavonoids extracted from *Passiflora edulis* leaves and the evaluation of its antioxidant and wound healing properties for the treatment of skin lesions in diabetic mice," *J. Biomed. Mater. Res. A*, vol. 108, no. 3, pp. 654-662, 2020, doi: <https://doi.org/10.1002/jbm.a.36845>
- [35] E. H. Fragal, V. H. Fragal, E. P. Silva, A. T. Paulino, et al., "Magnetic-responsive polysaccharide hydrogels as smart biomaterials: Synthesis, properties, and biomedical applications," *Carbohydr. Polym.*, vol. 292, 2022, art. no. 119665, doi: <https://doi.org/10.1016/j.carbpol.2022.119665>
- [36] B. Kovacevic, M. Jones, C. Ionescu, D. Walker, et al., "The emerging role of bile acids as critical components in nanotechnology and bioengineering: Pharmacology, formulation optimizers and hydrogel-biomaterial applications," *Biomaterials*, vol. 283, 2022, art. no. 121459, doi: <https://doi.org/10.1016/j.biomaterials.2022.121459>
- [37] S. Pourshahrestani, E. Zeimaran, N. A. Kadri, N. Mutlu, A. R. Boccaccini, "Polymeric Hydrogel Systems as Emerging Biomaterial Platforms to Enable Hemostasis and Wound Healing," *Adv. Healthc. Mater.*, vol. 9, no. 20, 2020, art. no. e2000905, doi: <https://doi.org/10.1002/adhm.202000905>
- [38] T. Zhu, D. Liang, Q. Zhang, W. Sun, X. Shen, "Curcumin-encapsulated fish gelatin-based microparticles from microfluidic electrospray for postopera-

- tive gastric cancer treatment,” *Int. J. Biol. Macromol.*, vol. 254, 2024, art. no.127763, doi: <https://doi.org/10.1016/j.ijbiomac.2023.127763>
- [39] B. Veerapandian, T. K. R. Selvaraj, S. R. Shanmugam, K. K. Sarwareddy, K. P. Mani, P. Venkatachalam, “In-vitro drug release and stability assessment of tailored levan-chitosan biocomposite hydrogel,” *Iran. Polym. J.*, vol. 33, no. 1, pp. 11-23, 2024, doi: <https://doi.org/10.1007/s13726-023-01229-x>
- [40] Q. Lan, J. Cao, X. Bi, X. Xiao, D. Li, Y. Ai, “Curcumin-primed periodontal ligament stem cells-derived extracellular vesicles improve osteogenic ability through the Wnt/ $\beta$ -catenin pathway,” *Front. Cell Dev. Biol.*, vol. 11, 2023, art. no. 1225449, doi: <https://doi.org/10.3389/fcell.2023.1225449>
- [41] S. L. Tomić, M. M. Babić Radić, J. S. Vuković, V. V. Filipović, J. Nikodinovic-Runic, M. Vukomanović, “Alginate-Based Hydrogels and Scaffolds for Biomedical Applications,” *Mar. Drugs.*, vol. 21, no. 3, 2023, art. no. 177, doi: <https://doi.org/10.3390/md21030177>
- [42] A. Nawaz, A. Farid, M. Safdar, M. S. Latif, et al., “Formulation Development and Ex-Vivo Permeability of Curcumin Hydrogels under the Influence of Natural Chemical Enhancers,” *Gels*, vol. 8, no. 6, 2022, art. no. 384, doi: <https://doi.org/10.3390/gels8060384>
- [43] M. Bashash, M. Varidi, J. Varshosaz, “Composite Hydrogel-Embedded Sucrose Stearate Niosomes: Unique Curcumin Delivery System,” *Food Bioproc. Tech.*, vol. 15, no. 9, pp. 2020-2034, 2022, doi: <https://doi.org/10.1007/s11947-022-02857-6>
- [44] F. Islam, S. Y. Wong, X. Li, M. T. Arafat, “Pectin and mucin modified cellulose-based superabsorbent hydrogel for controlled curcumin release,” *Cellulose*, vol. 29, no. 9, pp. 5207-5222, 2022, doi: <http://dx.doi.org/10.1007/s10570-022-04600-y>
- [45] M. Heidarifard, E. Taghavi, N. Anarjan, “Preparation of Nano-Emulsion-Based Hydrogels Conjugated Curcumin as Model Functional Lipid Bioactive Compound,” *J. Am. Oil Chem. Soc.*, vol. 98, no. 6, pp. 697-709, 2021, doi: <https://doi.org/10.1002/aocs.12473>
- [46] A. HaqAsif, R. R. Karnakar, N. Sreeharsha, et al., “pH and Salt Responsive Hydrogel based on Guar Gum as a Renewable Material for Delivery of Curcumin: A Natural Anti-Cancer Drug,” *J. Polym. Environ.*, vol. 29, no. 6, pp. 1978-1989, 2021, doi: <https://doi.org/10.1007/s10924-020-01934-1>
- [47] S. Bhubhanil, C. Talodthaisong, M. Khongkew, K. Namdee, et al., “Enhanced wound healing properties of guar gum/curcumin-stabilized silver nanoparticle hydrogels,” *Sci. Rep.*, vol. 11, no. 1, 2021, art. no. 21836, doi: <https://doi.org/10.1038/s41598-021-01262-x>
- [48] X. J. Qi, X. Y. Liu, L. M. Y. Tang, P. F. Li, F. Qiu, A. H. Yang, “Anti-depressant effect of curcumin-loaded guanidine-chitosan thermo-sensitive hydrogel by nasal delivery,” *Pharm. Dev. Technol.*, vol. 25, no. 3, pp. 316-325, 2020, doi: <https://doi.org/10.1080/10837450.2019.1686524>
- [49] F. I. Abo El-Ela, K. H. Hussein, H. A. El-Banna, A. Gamal, et al., “Treatment of Brucellosis in Guinea Pigs via a Combination of Engineered Novel pH-Responsive Curcumin Niosome Hydrogel and Doxycycline-Loaded Chitosan-Sodium Alginate Nanoparticles: an In Vitro and In Vivo Study,” *AAPS PharmSciTech*, vol. 21, no. 8, 2020, art. no. 325, doi: <https://doi.org/10.1208/s12249-020-01833-7>
- [50] M. Momin, S. Kurhade, P. Khanekar, S. Mhatre, “Novel biodegradable hydrogel sponge containing curcumin and honey for wound healing,” *J. Wound Care*, vol. 25, no. 6, pp. 364-372, 2016, doi: <https://doi.org/10.12968/jowc.2016.25.6.364>

<https://dx.doi.org/10.17488/RMIB.45.3.7>

E-LOCATION ID: 1447

## Development of a Frequent Exchange Coordinate Algorithm for Detection of Precordial Electrode Exchange during ECG based on Error and Correlation Parameters

### Desarrollo de un Algoritmo de Coordenadas de Intercambio Frecuente para Detección del Intercambio de Electrodo Precordiales ECG basado en Parámetros de Error y Correlación

Edward Carello Figueroa Tejada <sup>1</sup>, Carlos Esteban Mamani Huisa <sup>1</sup>, Erasmo Sullá Espinoza <sup>1</sup>, Jorge Rendulich <sup>1</sup>

<sup>1</sup>Universidad Nacional de San Agustín de Arequipa, Arequipa - Perú

#### ABSTRACT

In order to develop a method for detecting precordial electrode exchange, a frequent exchange coordinate (FEC) algorithm was implemented, that identified the minimum correlation points necessary to detect a specific electrode exchange, and its performance was tested with error estimators (mean square error and percent mean square difference). Validation of the algorithm was performed using the k-fold cross-validation technique on the PTB, Chapman University and Shaoxing Hospital, PTB XL, and Georgia 12-lead ECG Challenge databases. The results indicate averages of Se= 99.16 % and Sp= 99.38 % (MSE), Se= 95.38 % and Sp= 99.47 % (PRD), Se= 98.44 % and Sp= 99.49 % (Pearson), Se= 98.45 % and Sp= 99.48 % (modified Pearson), Se= 95.39 % and Sp= 99.81 % (Bray Curtis), Se= 80.00 % and Sp= 97.84 % (correlation sign). MSE presents a significant improvement in execution time (61.49 $\mu$ s N=1000), representing, on average, 44.99 % of the execution time for Pearson correlation. The frequent exchange coordinates algorithm was then validated using signal analysis with the mean square error (MSE), representing a good alternative to detect electrode exchange in real time, easy to implement, and low computational cost.

**KEYWORDS:** 12-lead ECG, correlation, error estimators, electrode exchange



## RESUMEN

Con objetivo de desarrollar un método de detección de intercambio de electrodos precordiales, se implementó un algoritmo de coordenadas de intercambio frecuentes (FEC) que identifica lo mínimos puntos de correlación necesarios para detectar un intercambio de electrodos específico y a su vez se probó su desempeño con estimadores de error (error cuadrático medio y diferencia cuadrática media porcentual). La validación del algoritmo se hizo mediante la técnica *k-fold cross-validation* en las bases de datos PTB, *Chapman University and Shaoxing Hospital*, PTB XL y Georgia 12-lead ECG Challenge. Los resultados indican promedios de Se= 99,16 % y Sp= 99,38 % (MSE), Se= 95,38 % y Sp= 99,47 % (PRD), Se= 98,44 % y Sp= 99,49 % (Pearson), Se= 98,45 % y Sp= 99,48 % (Pearson modificado), Se= 95,39 % y Sp= 99,81 % (Bray Curtis), Se= 80,00 % y Sp= 97,84 % (correlación signo). MSE presenta una mejora significativa en el tiempo de ejecución (61,49 $\mu$ s N=1000), representando en promedio el 44.99 % del tiempo de ejecución para correlación de Pearson. Se valida entonces el algoritmo de coordenadas de intercambio frecuente con análisis de señales con error cuadrático medio (MSE), representando una buena alternativa para detectar el intercambio de electrodos en tiempo real, de fácil implementación y bajo costo computacional.

**PALABRAS CLAVE:** ECG-12 derivaciones, correlación, estimadores de error, intercambio de electrodos

### Corresponding author

TO: Edward Carello Figueroa Tejada

INSTITUTION: UNIVERSIDAD NACIONAL DE SAN AGUSTÍN DE AREQUIPA.

ADDRESS: NICOLÁS DE PIEROLA 808, MARIANO MELGAR, AREQUIPA, PERÚ.

CORREO ELECTRÓNICO: efigueroat@unsa.edu.pe

### Received:

22 June 2024

### Accepted:

23 October 2024

## INTRODUCTION

The involuntary exchange of electrodes during electrocardiogram (ECG) testing is one of the most frequent technical errors in primary care health centers<sup>[1]</sup>, producing erroneous diagnoses in up to 24 % of cases<sup>[2][3]</sup>, some of which are severe medical conditions, such as acute ST-segment elevation myocardial infarction (STEMI), with an incidence of 11 %<sup>[3]</sup>. These exchanges occur more frequently with real-time biomedical devices, such as those intended for use in primary care health centers in remote areas using telemedicine, with reports of reversals in up to 50 % of cases caused mainly by medical personnel not specialized in cardiology<sup>[2]</sup>.

Early electrode exchange detection algorithms used alterations in the P- QRS -T wave morphology of the electrocardiogram signal<sup>[4]</sup>, signal reconstruction, and correlation<sup>[5][6]</sup> with low accuracy for specific detections. The following methods are based on the use of Machine Learning: Decision Trees<sup>[4][7][8][9][10]</sup>, Artificial Neural Networks<sup>[6][11][12]</sup>, Support Vector Machines<sup>[7][9][13]</sup>, and amplitude thresholding<sup>[14]</sup>, techniques of variable accuracy in terms of sensitivity and specificity, which, although they can reach high values, have the drawback of requiring high processing power and a high waiting time<sup>[15][16]</sup>, which complicates their implementation in real-time embedded devices. Subsequently, Jekova<sup>[17]</sup> developed a method based on Pearson correlation coefficients distributed in an ordered manner in correlation matrices, achieving Se= 87 % - 97.8 % and Sp = 91 %, an improvement in the accuracy and processing of electrode detection algorithms.

The current research team intends to implement a method of automatic detection of electrode exchange in biomedical devices in real time, as part of the Think Health project, based on an edge computing model. This project, in turn, is part of the Biomedical Engineering at the “Universidad Nacional de San Agustín de Arequipa”<sup>[18][19][20][21][22]</sup><sup>[23]</sup>. However, the current detection method is computationally expensive<sup>[24]</sup>.

Some methods that correlate or quantify the morphological similarity between biological signals are the Bray-Curtis similarity (mBC) and signed correlation coefficient (SCC), with fewer operations during processing compared with the traditional Pearson correlation<sup>[25]</sup>. The study of<sup>[26]</sup> represented ECG precordial signals as a displacement of precordial V1, so it can be deduced that the precordial signs differ little. With this in mind, it is possible to compare this difference using error parameters. These error estimators, such as the mean squared error (MSE) or root mean square difference (PRD), have been widely used as performance parameters to determine filter quality<sup>[27]</sup>, validate preprocessing techniques<sup>[28]</sup>, and evaluators of ECG signal acquisition<sup>[29]</sup>; however, they may have potential in this detection algorithm.

This paper proposes a new precordial electrode exchange detection method based on error estimators (MSE and PRD) and improves the algorithm based on correlation coefficients using signal correlation methods with lower computational complexity (Bray Curtis, Pearson Correlation, Modified Pearson Correlation, and Signed Correlation). This research determines the most suitable electrode exchange detection algorithm for implementation in embedded biomedical systems, such as the Think Health project.

## Databases

The databases used in this article are PTB (Physikalisch Technische Bundesanstalt)<sup>[30][31]</sup>, with 549 conventional 12-lead and 3-lead Frank records from 290 subjects; the extended version of PTB: PTB XL, with 21837 clinical ECG

records belonging to 18885 patients<sup>[32]</sup>; Georgia 12-Lead ECG Challenge Database (G12EC) from Emory University, Atlanta,<sup>[33]</sup> with 10344 records representing a demographic group from the southeastern United States; and the database created by Chapman University and Shaoxing People's Hospital (CUSPH),<sup>[34]</sup> with records from 10646 patients; whose main characteristics are summarized in Table 1.

TABLE 1. Databases used.

| Dataset | Records | Duration | Leads                           | Sampling |
|---------|---------|----------|---------------------------------|----------|
| PTB     | 549     | 32–120 s | I, II, II, aVR, aVL, aVF, V1–V6 | 1000 Hz  |
| PTB-XL  | 21837   | 10s      | I, II, II, aVR, aVL, aVF, V1–V6 | 500 Hz   |
| G12EC   | 10344   | 10s      | I, II, II, aVR, aVL, aVF, V1–V6 | 500 Hz   |
| CUSPH   | 10 646  | 10s      | I, II, II, aVR, aVL, aVF, V1–V6 | 500 Hz   |

These databases were chosen because they are the only databases with 12-lead digital signals. The pathological signals present in some recordings make them ideal for testing detection algorithms, whereas databases such as PTB and PTB-XL have unmodified signals with different types of noise and artifacts and a realistic distribution of data quality in clinical practice and in the face of changes in environmental conditions or various imperfections in the input data<sup>[32]</sup>.

## MATERIALS AND METHODS

### Precordial electrode exchange detection

The precordial electrode detection algorithm is based on the correlation between nearby precordial leads with a more significant similarity between the signals of adjacent electrodes<sup>[17]</sup>. The coefficients in a correlation matrix give the maximum correlation (with value 1) on the diagonal for a signal with itself and a descending numerical sequence of the other correlation coefficients, as shown in Figure 1.

|    | V1       |   | V2       |   | V3       |   | V4       |   | V5       |   | V6       |
|----|----------|---|----------|---|----------|---|----------|---|----------|---|----------|
| V1 | $a_{11}$ | > | $a_{12}$ | > | $a_{13}$ | > | $a_{14}$ | > | $a_{15}$ | > | $a_{16}$ |
| V2 | $a_{21}$ | < | $a_{22}$ | > | $a_{23}$ | > | $a_{24}$ | > | $a_{25}$ | > | $a_{26}$ |
| V3 | $a_{31}$ | < | $a_{32}$ | < | $a_{33}$ | > | $a_{34}$ | > | $a_{35}$ | > | $a_{36}$ |
| V4 | $a_{41}$ | < | $a_{42}$ | < | $a_{43}$ | < | $a_{44}$ | > | $a_{45}$ | > | $a_{46}$ |
| V5 | $a_{51}$ | < | $a_{52}$ | < | $a_{53}$ | < | $a_{54}$ | < | $a_{55}$ | > | $a_{56}$ |
| V6 | $a_{61}$ | < | $a_{62}$ | < | $a_{63}$ | < | $a_{64}$ | < | $a_{65}$ | < | $a_{66}$ |

FIGURE 1. Correlation coefficient matrix. Blue squares: Coefficients of maximum value (1) in signals correlated with themselves ( $a_{m,m}$ ). Light blue squares: The coefficients are ordered in descending order. Gray boxes: Comparison of adjacent correlation coefficients.

This article proposes new matrix based on the calculation of error coefficients by measuring the difference between adjacent leads. This may allow the creation of a matrix of error coefficients with characteristics opposite to those of the correlation matrix presented in Figure 1, having on the diagonal the comparison of a signal with itself, with difference 0, and an ascending numerical sequence as the other precordial leads are compared, as shown in Figure 2.

|    | V1       |   | V2       |   | V3       |   | V4       |   | V5       |   | V6       |
|----|----------|---|----------|---|----------|---|----------|---|----------|---|----------|
| V1 | $a_{11}$ | < | $a_{12}$ | < | $a_{13}$ | < | $a_{14}$ | < | $a_{15}$ | < | $a_{16}$ |
| V2 | $a_{21}$ | > | $a_{22}$ | < | $a_{23}$ | < | $a_{24}$ | < | $a_{25}$ | < | $a_{26}$ |
| V3 | $a_{31}$ | > | $a_{32}$ | > | $a_{33}$ | < | $a_{34}$ | < | $a_{35}$ | < | $a_{36}$ |
| V4 | $a_{41}$ | > | $a_{42}$ | > | $a_{43}$ | > | $a_{44}$ | < | $a_{45}$ | < | $a_{46}$ |
| V5 | $a_{51}$ | > | $a_{52}$ | > | $a_{53}$ | > | $a_{54}$ | > | $a_{55}$ | < | $a_{56}$ |
| V6 | $a_{61}$ | > | $a_{62}$ | > | $a_{63}$ | > | $a_{64}$ | > | $a_{65}$ | > | $a_{66}$ |

**FIGURE 2. Matrix based on error estimators. Blue boxes: Coefficients of minimum value (0), error of signal with itself. Light blue boxes: Coefficients ordered in ascending order. Gray boxes: Comparison of adjacent correlation coefficients.**

To find the minimum number of coefficients needed to detect a specific electrode exchange, Frequent Exchange Coordinates (FECs) were established. These FECs can detect specific electrode exchanges without using the full correlation matrix or error matrix, thus minimizing the number of correlation or error estimation coefficients used during testing.

The FECs are determined through the change in the comparisons of a standard correlation matrix or error matrix and can be represented in a 6x5 matrix, as shown in Figure 3; this matrix is obtained from the comparisons between the coefficients in Figures 1 and 2. In Figure 3,  $r(XY)$  represents the comparison (higher or lower) of the correlation or error coefficients between  $V(X, Y)$  and  $V(X, Y+1)$ . The coordinates found are presented in the results with a value of 1 if there is a reverse of the comparison between the pairs of coefficients and 0 if there is no change in contrast in most cases.

| $V_{x1} - V_{x2}$ | $V_{x2} - V_{x3}$ | $V_{x3} - V_{x4}$ | $V_{x4} - V_{x5}$ | $V_{x5} - V_{x6}$ |
|-------------------|-------------------|-------------------|-------------------|-------------------|
| $r_{11}$          | $r_{12}$          | $r_{13}$          | $r_{14}$          | $r_{15}$          |
| $r_{21}$          | $r_{22}$          | $r_{23}$          | $r_{24}$          | $r_{25}$          |
| $r_{31}$          | $r_{32}$          | $r_{33}$          | $r_{34}$          | $r_{35}$          |
| $r_{41}$          | $r_{42}$          | $r_{43}$          | $r_{44}$          | $r_{45}$          |
| $r_{51}$          | $r_{52}$          | $r_{53}$          | $r_{54}$          | $r_{55}$          |
| $r_{61}$          | $r_{62}$          | $r_{63}$          | $r_{64}$          | $r_{65}$          |

**FIGURE 3. Matrix for comparing correlation coefficients or error estimators.**

## Electrode exchange detection algorithm

Based on the behavior of the precordial signals described above, the algorithm summarized in Figure 4.

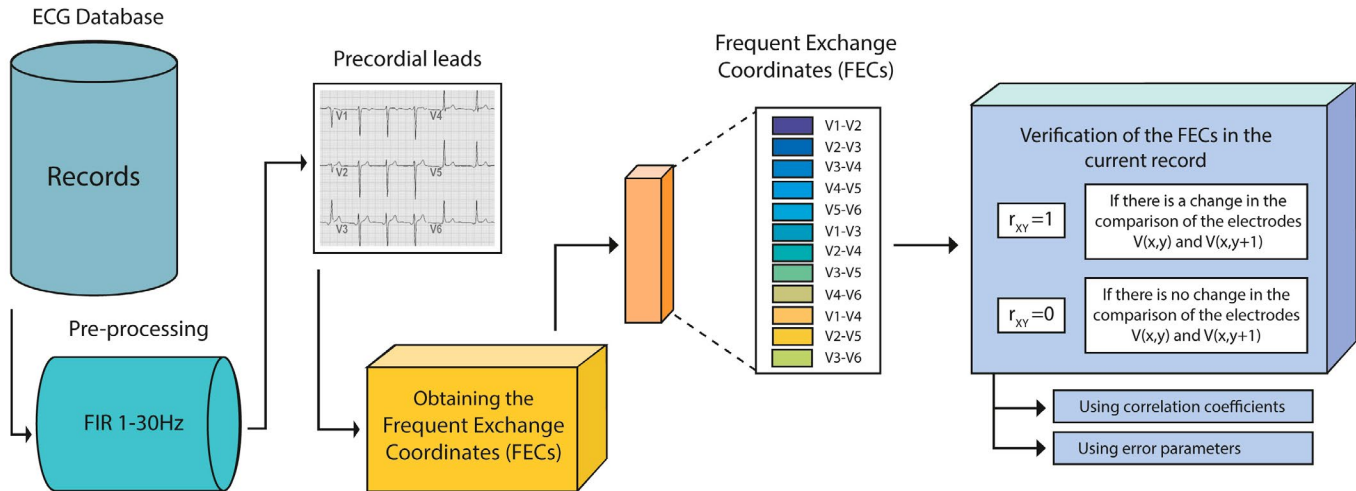


FIGURE 4. Summary of the Electrode Exchange Detection Algorithm.

The algorithm begins by preprocessing the signal in its input records using a 1Hz - 30Hz FIR filter. The FIR filter designed in MATLAB uses the syntax  $b = \text{fir1}(n, [Wn1 \ Wn2])$ . This method uses a least squares approximation to calculate the filter coefficients and then smooths the signal using a window. This filter creates a row vector  $b$  containing the Hamming window filter coefficients of order  $n$ . Then, vector  $[Wn1 \ Wn2]$  contains two elements containing the pass-band edge frequencies, which, in turn, respond to the Nyquist frequency, half the sampling frequency.

The choice of the 1-30 Hz band was based on the work done by Jekova<sup>[17]</sup>, who obtained good performance when preprocessing the signal for precordial signal correlation algorithms. In addition, preliminary tests showed that the noise in the signals and artifacts present in the evaluated databases evaluated were attenuated with this range of filters.

Likewise, another future objective of this work is to implement this algorithm in embedded systems for which the finite impulse digital filter (FIR) is an ideal candidate in this type of systems, presenting implementation advantages over other types of digital filters, such as the IIR infinite impulse response filter for real-time ECG signal processing applications, as described by Bui and Byun<sup>[35]</sup>.

For the evaluation of this specific algorithm, 2 s of the 10 available samples in each record were taken for the PTB-XL, G12EC, and CUSPH databases, which have a sampling frequency of 500 Hz, and only 1 s in the PTB database with a sampling frequency of 1000 Hz, with the objective of having an equal number of samples to evaluate in each record; likewise, the full wave signal around the R peak was considered for this analysis. In the future, the application of this algorithm in an embedded system could take action at the time of starting to use the 12-lead ECG or continuously, remembering that this will only be an emergency system in case of a possible error in the placement of electrodes, and the filters applied here will not influence the signal recorded for diagnosis by health personnel.

Then, the verification of the frequent exchange coordinates (FECs) was performed in 2 approaches: correlation coefficients and error parameters, to determine the type of comparison with the best results.

In this test, the effectiveness of using the difference between the precordial lead signals was determined using error parameters, such as the mean square error (MSE) presented in equation 1 and, the percent root mean square error (PRD), presented, in equation 2:

Mean Squared Error (MSE)

$$MSE = \frac{1}{N} \sum_{i=1}^N (x_i - y_i)^2 \quad (1)$$

Percent Root Mean Square Difference (PRD)

$$PRD = \sqrt{\frac{\sum_{i=1}^N (x_{[i]} - y_{[i]})^2}{\sum_{i=1}^N (x_{[i]})^2}} \times 100 \quad (2)$$

These methods are compared to the conventional Pearson correlation presented in equation 3:

$$\rho = \frac{\sum_{i=1}^N (x_i - \bar{x}) - (y_i - \bar{y})}{\sqrt{\sum_{i=1}^N (x_i - \bar{x})^2} \sqrt{\sum_{i=1}^N (y_i - \bar{y})^2}} \quad (3)$$

To improve the signal correlation method in terms of computational cost, a modified Pearson correlation method, (Equation 4) was used. Gembris *et al.* reported that this formula reduces the redundancy produced by pairwise correlations<sup>[36]</sup>. At the same time, the performance of other signal similarity assessment methods will be tested, such as the Bray-Curtis similarity coefficient (Equation 5) and the signed correlation coefficient (Equation 6) mentioned by Lian, Muessig, and Lang, because of their low computational requirements and sensitivity to amplitude difference<sup>[25]</sup>:

Modified Pearson Correlation

$$m\rho = \frac{T \sum_{i=1}^T (x_i y_i) - \sum_{i=1}^T x_i \cdot \sum_{i=1}^T y_i}{\sqrt{\sum_{i=1}^T x_i^2 - (\sum_{i=1}^T x_i)^2} \cdot \sqrt{\sum_{i=1}^T y_i^2 - (\sum_{i=1}^T y_i)^2}} \quad (4)$$

Bray-Curtis similarity coefficient (mBC)

$$mBC = 1 - \frac{\sum_{i=1}^N |x_i - y_i|}{\sum_{i=1}^N |x_i| + |y_i|} \quad (5)$$

Correlation coefficient with sign (SCC)

$$SCC = \frac{\sum_{i=1}^N sgn(x_i)sgn(y_i)}{N} \quad (6)$$

To further reduce the computational complexity and based on the symmetric property of the Pearson Correlation coefficient ( $\text{corr}(x,y) = \text{corr}(y,x)$ )<sup>[36]</sup>, reducing the number of coefficients from  $N^2=36$  elements to  $N(N-1)/2=15$ , which corresponds to the upper triangle above the main diagonal part of the correlation matrix (Figure 5).

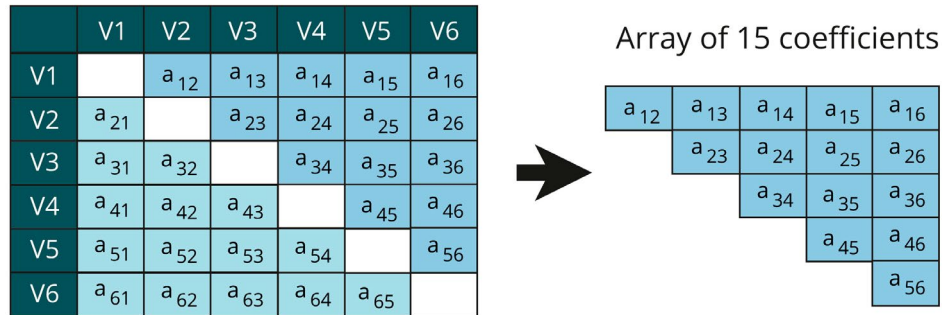


FIGURE 5. Simplification of the coefficients in the correlation matrix.

The above-mentioned calculations for verifying frequent exchange coordinates were performed by simulating electrode exchanges in a training group. Finally, these FECs were tested in test groups (The determination of the training and test groups will be mentioned later).

### Electrode exchange simulations

Simulations of precordial electrode exchange were performed to determine the frequent exchange points and to verify the sensitivity and specificity of the algorithm for detecting these simulated changes.

The simulation was performed by changing the data matrices of each lead in Matlab R2020a program. The electrode exchange simulation was performed assuming that the database records had no previous electrode exchanges.

Exchanges can be classified into hops; when the exchange is between 2 adjacent electrodes, it is a one-hop exchange; if the distance between the exchanged electrodes is two, it is a two-hop exchange, and for a distance of 3, it is a 3 hop exchange. In these cases, 12 simulated exchange shapes were obtained.

The precordial electrode exchange simulation results are presented in Table 2.

TABLE 2. Simulated exchanges in precordial electrodes.

| Hop   | Simulated swap | Hop   | Simulated swap | Hop   | Simulated swap |
|-------|----------------|-------|----------------|-------|----------------|
| 1 hop | V1-V2          | 2 hop | V1-V3          | 3 hop | V1-V4          |
|       | V2-V3          |       | V2-V4          |       | V2-V5          |
|       | V3-V4          |       | V3-V5          |       | V3-V6          |
|       | V4-V5          |       | V4-V6          |       |                |
|       | V5-V6          |       |                |       |                |

## Validation of the proposed method in databases

The validation of the algorithms using each error and correlation method was performed using the block diagram presented in Figure 6.

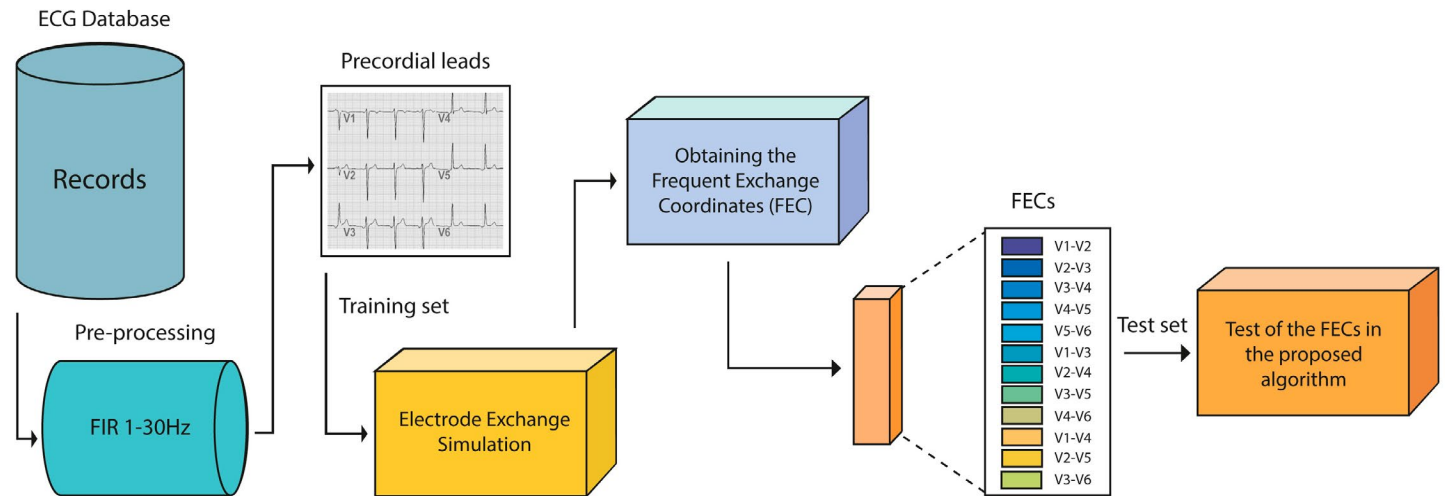


FIGURE 6. Validation of algorithms in databases.

Validation was performed using the k-fold cross-validation technique (Figure 7); the records of each database were randomly separated into eight groups of an equal number of data. In the first cycle, group 1 took the role of the test set, and the rest of the training set. Specific exchange points for 1, 2, and 3 hop electrode exchanges will be determined throughout training and tested in the test group. In the next cycle, group 2 is the test set, and the other records are the training set. The k-fold cross-validation method assumes that the test set iterates with the 8 groups created.

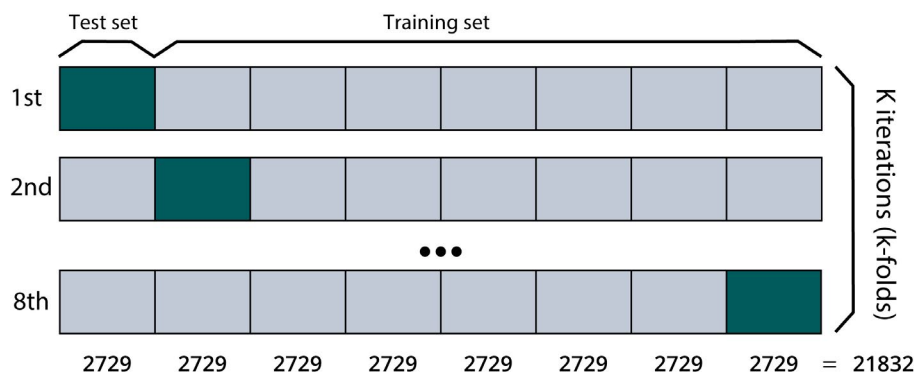


FIGURE 7. k-fold cross validation(k=8) in PTB-XL database.

As mentioned above, to validate the method with K fold cross validation, 8 groups are separated from the total number of records in each database and placed in the Records column of Table 3, this table in turn presents the size of each group and the dynamic training and test sets. As can be seen, the number of records was less than the total number of records in the database because the total group size evaluated was required to be a multiple of  $k = 8$ .



TABLE 3. Group sizes for k-fold cross validation.

| Dataset | Records | k | Group size | Training set | Test set |
|---------|---------|---|------------|--------------|----------|
| PTB     | 549     | 8 | 68         | 476          | 68       |
| PTB-XL  | 21832   | 8 | 2729       | 19103        | 2729     |
| G12EC   | 10344   | 8 | 1293       | 9051         | 1293     |
| CUSPH   | 10640   | 8 | 1330       | 9310         | 1330     |
| PTB     | 549     | 8 | 68         | 476          | 68       |

This process is performed iteratively to obtain the mean values of Sensitivity (Equation 7) and Specificity (Equation 8) for each database. These performance metrics were obtained from the confusion matrix shown in Figure 8.

|                  |                          | Identified exchange |                     |
|------------------|--------------------------|---------------------|---------------------|
|                  |                          | Positive (EP)       | Negative (EN)       |
| Actual condition | Total population<br>=P+N |                     |                     |
|                  | Positive (P)             | True positive (TP)  | False negative (FN) |
|                  | Negative (N)             | False positive (FP) | True negative (TN)  |

FIGURE 8. Confusion Matrix.

Where:

- TP is the number of positive exchanges correctly classified as positive by the model.
- TN is the number of negative exchanges correctly classified as negative by the model.
- FN is the number of positive exchanges incorrectly classified as negative.
- FP is the number of negative exchanges incorrectly classified as positive.

$$Se(\%) = \frac{TP}{TP + FN} * 100 \quad (7)$$

$$Sp(\%) = \frac{TN}{TN + FP} * 100 \quad (8)$$

where TP = true positive, TN = true negative, FN = false negative, and FP = false positive.

The FECs obtained during training in a more extensive database (PTB XL) were used to ensure that coordinates were valid in any database. Finally, these FECs from the more extensive database were tested on the other databases.

### Determination of processing time

Additional tests were performed to determine processing time for each method (Table 4). The `cputime` function available in matlab was used in sets of  $N$  samples taken at random in each database ( $N=250$ ,  $N=500$ ,  $N=1000$ ,  $N=2000$ ,  $N=3000$ ,  $N=4000$ ,  $N=5000$ ). This function determines the time required by the central processing unit (CPU) to process program instructions. All formative and direct experiments were performed using Matlab R2020a software on a PC with a Windows 10 operating system, 2.4-GHz Intel Core i5 processor, and 4.096-GHz RAM.

TABLE 4. Execution times to find.

| Method               | Abbreviation |
|----------------------|--------------|
| Mean squared error   | $T_{MSE}$    |
| PRD                  | $T_{PRD}$    |
| Conventional Pearson | $T_p$        |
| Modified Pearson     | $T_{mp}$     |
| Bray Curtis          | $T_{mBC}$    |
| Signed correlation   | $T_{SCC}$    |

## RESULTS AND DISCUSSION

### Sensitivities and specificity of the algorithm

The methodology described above was used to obtain the average sensitivity and specificity of each database. The Frequent Exchange Coordinates algorithm was tested using correlation ( $p$ ,  $mp$ ,  $mBC$ ,  $SCC$ ) and error parameters ( $MSE$  and  $PRD$ ). The average  $Se$  and  $Sp$  values are listed in Table 5. As can be seen, on average, the correlation methods were slightly more accurate in diagnosing electrode exchanges, with the Pearson and modified Pearson correlations being more accurate.

TABLE 5. Average  $Se$  and  $Sp$  values of the algorithm with own FECs.

| Database   | PTB     |         | PTB XL  |         | G12EC   |         | CUSPH   |         | Mean    |         |
|------------|---------|---------|---------|---------|---------|---------|---------|---------|---------|---------|
|            | Se (%)  | Sp (%)  | Se (%)  | Sp (%)  | Se (%)  | Sp (%)  | Se (%)  | Sp (%)  | Se (%)  | Sp (%)  |
| <b>MSE</b> | 96.29 % | 97.52 % | 99.96 % | 98.26 % | 98.23 % | 99.93 % | 99.96 % | 98.91 % | 98.61 % | 98.66 % |
| <b>PRD</b> | 96.26 % | 97.57 % | 99.95 % | 98.96 % | 94.62 % | 99.74 % | 93.89 % | 99.62 % | 96.18 % | 98.97 % |
| <b>p</b>   | 99.52 % | 99.60 % | 98.99 % | 99.01 % | 98.93 % | 98.41 % | 99.29 % | 98.89 % | 99.18 % | 98.98 % |
| <b>mp</b>  | 99.52 % | 96.72 % | 99.00 % | 98.96 % | 98.93 % | 98.37 % | 99.29 % | 98.88 % | 99.19 % | 98.23 % |
| <b>mBC</b> | 93.13 % | 95.94 % | 97.93 % | 99.99 % | 97.00 % | 97.49 % | 98.67 % | 99.98 % | 96.68 % | 98.35 % |
| <b>SCC</b> | 75.09 % | 96.76 % | 90.99 % | 94.81 % | 92.25 % | 96.29 % | 97.28 % | 96.81 % | 88.90 % | 96.17 % |

Table 6 shows the Frequent Exchange Coordinates (FEC) obtained from the training database of the more extensive database (PTB-XL). This table displays the highest percentage of exchange in the coordinates of the FEC columns (with exchange) and the percentage of exchange in coordinates that usually remain unchanged in the FEC (without exchange). For example, in the simulated exchange between V1 and V2, the coordinates r31 and r41 change in 99.23 % and 99.89 % of cases, respectively. For the same simulation, V1 and V2, the coordinates r42 and r53 were unchanged in 99.82 % and 99.94 % of the cases, respectively. Using the proposed algorithm, these FECs (r31 r41 r42 r53) can be coded as 1 if there is an exchange and 0 if there is no exchange. The proposed coding scheme is presented in Table 6.

**TABLE 6. Average Se and Sp in the PTB-XL database.**

| Swap |       | FEC (With exchange) |       |        |       |        |       | FEC (Without exchange) |       |        |       |
|------|-------|---------------------|-------|--------|-------|--------|-------|------------------------|-------|--------|-------|
| N    | Leads | Coord.              | %     | Coord. | %     | Coord. | %     | Coord.                 | %     | Coord. | %     |
| 1    | V1-V2 | r31                 | 99.23 | r41    | 99.89 | -      | -     | r42                    | 99.82 | r53    | 99.94 |
| 2    | V2-V3 | r42                 | 99.7  | r52    | 99.47 | -      | -     | r41                    | 99.94 | r53    | 99.98 |
| 3    | V3-V4 | r53                 | 99.78 | r63    | 99.41 | -      | -     | r52                    | 99.97 | r64    | 99.96 |
| 4    | V4-V5 | r34                 | 99.43 | r64    | 99.63 | -      | -     | r35                    | 99.99 | r23    | 99.99 |
| 5    | V5-V6 | r35                 | 98.12 | r45    | 97.7  | -      | -     | r34                    | 99.98 | -      | -     |
| 6    | V1-V3 | r41                 | 99.73 | r42    | 98.89 | -      | -     | r53                    | 99.98 | -      | -     |
| 7    | V2-V4 | r63                 | 99.46 | r52    | 99.63 | -      | -     | r14                    | 99.99 | r51    | 99.98 |
| 8    | V3-V5 | r64                 | 99.41 | r63    | 99.34 | r35    | 98.57 | r12                    | 99.99 | -      | -     |
| 9    | V4-V6 | r34                 | 99.43 | r35    | 99.43 | -      | -     | r23                    | 99.99 | -      | -     |
| 10   | V1-V4 | r51                 | 99.92 | r12    | 99.73 | r53    | 99.73 | r31                    | 99.99 | -      | -     |
| 11   | V2-V5 | r23                 | 99.74 | r62    | 99.82 | r64    | 99.64 | r15                    | 99.99 | r52    | 99.99 |
| 12   | V3-V6 | r25                 | 99.6  | r64    | 99.44 | r23    | 98.94 | r12                    | 99.99 | r63    | 99.99 |

As can be seen, it is only necessary to verify the code of the FEC specific to detect electrode exchange. That is, obtaining correlation or error coefficients to find the FECs and determine whether an exchange occurred at those points significantly minimizes computational cost. The frequent exchange coordinates listed in Table 7 were tested in the PTB, G12EC, and CUSPH databases.

**TABLE 7. Frequent Exchange Coordinates codes for each hop.**

| N  | Swap  | FEC                 | Code |
|----|-------|---------------------|------|
| 1  | V1-V2 | r31 r41 r42 r53     | 1100 |
| 2  | V2-V3 | r41 r42 r52 r53     | 110  |
| 3  | V3-V4 | r52 r53 r63 r64     | 110  |
| 4  | V4-V5 | r23 r34 r35 r64     | 101  |
| 5  | V5-V6 | r34 r35 r45         | 11   |
| 6  | V1-V3 | r41 r42 r53         | 110  |
| 7  | V2-V4 | r14 r51 r52 r63     | 11   |
| 8  | V3-V5 | r12 r35 r63 r64     | 111  |
| 9  | V4-V6 | r23 r34 r35         | 11   |
| 10 | V1-V4 | r12 r51 r53 r64     | 1110 |
| 11 | V2-V5 | r15 r23 r52 r62 r64 | 1011 |
| 12 | V3-V6 | r12 r23 r25 r63 r64 | 1101 |

The Sensitivities and Specificities of each exchange were then averaged and presented in Table 8.

**TABLE 8. Average Se and Sp values in the test databases.**

| Set      | Training set |         | Test set 1 |         | Test set 2 |         | Test set 3 |         | Mean    |         |
|----------|--------------|---------|------------|---------|------------|---------|------------|---------|---------|---------|
| Database | PTB XL       |         | PTB        |         | G12EC      |         | CUSPH      |         |         |         |
| Method   | Se(%)        | Sp(%)   | Se(%)      | Sp(%)   | Se(%)      | Sp(%)   | Se(%)      | Sp(%)   | Se(%)   | Sp(%)   |
| MSE      | 99.96 %      | 98.26 % | 97.22 %    | 99.69 % | 99.67 %    | 99.87 % | 99.77 %    | 99.68 % | 99.16 % | 99.38 % |
| PRD      | 99.95 %      | 98.96 % | 93.23 %    | 99.61 % | 94.45 %    | 99.45 % | 93.89 %    | 99.86 % | 95.38 % | 99.47 % |
| p        | 98.99 %      | 99.01 % | 99.11 %    | 99.66 % | 97.96 %    | 99.56 % | 97.68 %    | 99.74 % | 98.44 % | 99.49 % |
| mp       | 99.01 %      | 98.96 % | 99.11 %    | 99.66 % | 97.95 %    | 99.56 % | 97.74 %    | 99.74 % | 98.45 % | 99.48 % |
| mBC      | 97.93 %      | 99.99 % | 92.05 %    | 99.45 % | 97.12 %    | 99.94 % | 94.45 %    | 99.86 % | 95.39 % | 99.81 % |
| SCC      | 90.99 %      | 94.81 % | 60.69 %    | 98.78 % | 83.36 %    | 98.76 % | 84.96 %    | 99.01 % | 80.00 % | 97.84 % |

Sensitivity is excellent, with values above 95 % and specificity greater than 99 %. However, the correlation by SCC is somewhat lower.

### Determination of algorithm processing time

Table 9 presents the average processing time of the frequent exchange coordinate algorithm for each method (MSE, PRD, p, mp, mp, mBC, SCC) on a set of N samples (N=250, N=500, N=1000, N=2000, N=3000, N=4000, N=5000) taken at random in each database. The processing time was determined using the CPU time function (cputime).

The MSE and SCC methods had the shortest processing times in all databases, with an average of 61.49us (MSE) and 68.51us (SCC) for N = 1000. In contrast, the Pearson and modified Pearson correlation methods had average processing times of 231.10 and 141.39 US for K = 1000. Comparing the MSE processing method with the Pearson evaluation method for all values of N, the average processing time with the MSE method represented 44.99 % of the processing time with the Pearson evaluation.

### Discussion

The detection of electrode exchange using the error estimators presented an average accuracy of Se= 99.16 % and Sp=99.38 % for the MSE, compared to the correlation methods whose maximum was Se= 98.45 % and Sp=99.48 % = for mp. This accuracy is comparable to the previous correlation method <sup>[17]</sup>, with Se=. 93.8%-99.8% and Sp = 98.9 %, as well as methods based on Machine Learning: Decision Trees <sup>[4][8][9][10]</sup>: Se = 17.9 % - 99.3 % Sp= 86.6 % - 100 %, Neural Networks <sup>[6][11][12]</sup>: Se = 44.5 % - 99.9 % Sp= 99 %, SVM <sup>[9][13]</sup>: Se = 56.5 % - 93.7 % Sp = 86.6 % - 99.9 % and Amplitude Thresholds <sup>[14]</sup>: Se = 20 % - 90 % and Sp = 99.8 %.

Average processing times of 61.49μs for MSE (N=1000) and 89.78μs for PRD were obtained, thus achieving a reduction of up to 73.39 % compared with the conventional Pearson correlation method with 231.10μs <sup>[17]</sup>. These results allow us to deduce that this detection method can also be applied to the analysis of peripheral electrodes. Although the shortest processing times correspond to SCC and MSE, SCC is not highly accurate and is not recommended for

use in this algorithm. On the other hand, MSE has a shorter processing time and adequate accuracy, with SE = 99.16 % and SP = 99.38 %, making it ideal for use in the Frequent Exchange Coordinate algorithm.

**TABLE 9. Processing time for each method and test database.**

| Database | N    | TMSE(us) | TPRD(us) | Tp(us) | Tmp(us) | TmBC(us) | TSCC(us) |
|----------|------|----------|----------|--------|---------|----------|----------|
| PTB      | 250  | 0.12     | 0.14     | 0.24   | 0.22    | 0.25     | 56.76    |
|          | 500  | 66.44    | 85.74    | 145.95 | 160.53  | 79.67    | 65.56    |
|          | 1000 | 77.08    | 106.84   | 177.22 | 250.47  | 107.03   | 84.06    |
|          | 2000 | 108.11   | 167.86   | 264.23 | 436.56  | 169.69   | 122.7    |
|          | 3000 | 161.65   | 241.82   | 331.53 | 653.49  | 250.25   | 171.18   |
|          | 4000 | 191.82   | 305.48   | 401.93 | 838.4   | 316.09   | 212.12   |
|          | 5000 | 226.93   | 371.71   | 480.14 | 1062.56 | 381.75   | 249.56   |
| G12EC    | 250  | 0.04     | 0.06     | 0.1    | 0.33    | 0.06     | 38.76    |
|          | 500  | 42.13    | 60.18    | 99.63  | 134.3   | 58.36    | 47.2     |
|          | 1000 | 48.66    | 72.59    | 115.38 | 217.33  | 70.91    | 54.75    |
|          | 2000 | 55.92    | 86.58    | 129.84 | 398.19  | 85.71    | 63.31    |
|          | 3000 | 70.27    | 114.22   | 164.34 | 601.81  | 114.1    | 81.53    |
|          | 4000 | 86.24    | 143.24   | 197.9  | 783.24  | 143.41   | 99.52    |
|          | 5000 | 106.93   | 185.64   | 236.25 | 992.74  | 185.66   | 122.43   |
| CUSPH    | 250  | 0.02     | 0.03     | 0.05   | 0.1     | 0.03     | 64.3     |
|          | 500  | 45.16    | 62.54    | 101.91 | 139.75  | 63.01    | 49.61    |
|          | 1000 | 58.73    | 89.92    | 131.59 | 225.5   | 88.66    | 66.73    |
|          | 2000 | 88.77    | 145      | 200.39 | 400.96  | 147.04   | 103.26   |
|          | 3000 | 139.08   | 233.47   | 280.31 | 656.81  | 245.93   | 153.69   |
|          | 4000 | 175.75   | 297.91   | 355.53 | 852.62  | 314.32   | 194.85   |
|          | 5000 | 221.48   | 379.4    | 444.28 | 1058.54 | 396      | 245.16   |

The use of coefficient reduction for pairwise comparisons performed by Gembris *et al.* [36] is validated and recommended, finding that only  $N(N-1)/2=15$  correlation or error coefficients need to be obtained compared to the 36 coefficients described in the work of Jekova [17] to detect electrode inversions effectively. However, its method is not applicable when using the PRD error estimator because it excludes symmetric coefficients. In turn, the developed algorithms are effective for both standard and pathological or noisy signals; this is demonstrated when used in databases with these characteristics, such as G12EC, which has high accuracy values ranging from 94.45% to 99.67 % using the error estimators.

## CONCLUSIONS

This article presents a novel method for automatically detecting precordial electrode exchange by replacing correlation coefficients with error estimators. This strategy significantly improves the algorithm execution time and

dramatically reduces the amount of data processing, thereby reducing the computational cost while achieving test accuracy comparable to correlation-based algorithms. The experimental results demonstrated that the most efficient method in terms of execution time, memory, and accuracy was the MSE method, with an average processing time of 61.49 $\mu$ s for the MSE (N=1000), which is a reduction of 56.51% compared to the conventional Pearson correlation method; in terms of accuracy, this method obtained Se= 99.16% and Sp=99.38 comparable to high computational cost methods such as those based on Machine Learning previously mentioned and with results superior to correlation methods [17] with Se=. 93.8%-99.8% and Sp= 98.9%.

Algorithms based on correlation and error estimators, such as Bray-Curtis, modified Pearson, MSE, and PRD, are accurate methods for electrode exchange detection with high sensitivity and specificity. Among these, MSE has the shortest processing time, making it ideal for use in the Frequent Exchange Coordinates (FEC) algorithm. In turn, FEC coordinates increase the specificity of the algorithm, which is an advantage for algorithms intended for use in embedded systems because it reduces the percentage of false alarms. In other words, the use of the MSE-based FEC algorithm is an accurate and easy method to implement in any embedded system because it, is only necessary to find the coefficients of the codes presented in Table 7. However, it should be considered that it is possible that some diseases may alter electrical signals and therefore the correlation or difference between these signals. However, although this topic is beyond the scope of this research, it can be further explored in future work.

For all these reasons, MSE was determined to be the most suitable method for implementation in the Think Health Project biomedical kit.

## ACKNOWLEDGMENTS

This work is part of the research project "Think Health - Development of a kit of Biomedical Instruments for basic health care centers and to assist in the study of chronic and congenital diseases" financed by the "Universidad Nacional de San Agustín de Arequipa" through contract number IBA-IB-44-2020-UNSA.

## CONFLICTS OF INTEREST

The authors declare no conflicts of interest.

## AUTHOR CONTRIBUTIONS

E. C. F. T. conceptualization, formal analysis, investigation, methodology, validation, and writing- review and editing; C. E. M. H. conceptualization, data curation, formal analysis, validation; E. S. E. project administration, supervision, validation; J. R. funding acquisition, project administration, and supervision.

## REFERENCES

- [1] D. M. F. Palhares, M. S. Marcolino, T. M. M. Santos, J. L. P. da Silva, et al., "Normal limits of the electrocardiogram derived from a large database of Brazilian primary care patients," *BMC Cardiovasc. Disord.*, vol. 17, 2017, art. no. 152, doi: <https://doi.org/10.1186/s12872-017-0572-8>
- [2] A. Hadjiantoni, K. Oak, S. Mengi, J. Konya, T. Ungvari, "Is the Correct Anatomical Placement of the Electrocardiogram Electrodes Essential to Diagnosis in the Clinical Setting: a Systematic Review," *Cardiol. Cardiovasc. Med.*, vol. 5, no. 2, pp. 182-200, 2021, doi: <https://www.doi.org/10.26502/fccm.92920192>
- [3] R. R. Bond, D. D. Finlay, C. D. Nugent, C. Breen, D. Guldenring, and M. J. Daly, "The effects of electrode misplacement on clinicians' interpretation of the standard 12-lead electrocardiogram," *Eur. J. Intern. Med.*, vol. 23, no. 7, pp. 610-615, 2012, doi: <https://doi.org/10.1016/j.ejim.2012.03.011>
- [4] C. Han, R. E. Gregg, and S. Babaeizadeh, "Automatic detection of ECG lead wire interchange for conventional and Mason-Likar lead systems," in *Computing in Cardiology 2014*, Cambridge, MA, USA, 2014, pp. 145-148.

- 127 **Edward Carello Figueroa Tejada** *et al.* Development of a Frequent Exchange Coordinate Algorithm for Detection of Precordial Electrode Exchange during ECG based on Error and Correlation Parameters
- [5] H. Xia, G. A. Garcia, and X. Zhao, "Automatic detection of ECG electrode misplacement: a tale of two algorithms," *Physiol. Meas.*, vol. 33, 2012, art. no. 1549, doi: <https://doi.org/10.1088/0967-3334/33/9/1549>
- [6] J. A. Kors and G. van Herpen, "Accurate automatic detection of electrode interchange in the electrocardiogram," *The Am. J. Cardiol.*, vol. 88, no. 4, pp. 396-399, 2001, doi: [https://doi.org/10.1016/S0002-9149\(01\)01686-1](https://doi.org/10.1016/S0002-9149(01)01686-1)
- [7] K. Rjoob, R. Bond, D. Finlay, V. McGilligan, et al., "Machine learning techniques for detecting electrode misplacement and interchanges when recording ECGs: a systematic review and meta analysis," *J. Electrocardiol.*, vol. 62, pp. 116-123, 2020, doi: <https://doi.org/10.1016/j.jelectrocard.2020.08.013>
- [8] J. Kors and G. van Herpen, "A novel method to detect electrocardiographic electrode interchanges," *Journal of Electrocardiology*, vol. 33, pp. 209-210, 2000, doi: <https://doi.org/10.1054/jelc.2000.20352>
- [9] K. Rjoob, R. Bond, D. Finlay, V. McGilligan, et al., "Data driven feature selection and machine learning to detect misplaced V1 and V2 chest electrodes when recording the 12-lead electrocardiogram," *J. Electrocardiol.*, vol. 57, pp. 39-43, 2019, doi: <https://doi.org/10.1016/j.jelectrocard.2019.08.017>
- [10] R. E. Gregg, E. W. Hancock, and S. Babaeizadeh, "Detecting ECG limb lead wire interchanges involving the right leg lead-wire," in *Computing in Cardiology 2017*, Rennes, France, 2017, doi: <https://doi.org/10.22489/CinC.2017.014-061>
- [11] B. Hedeń, M. Ohlsson, L. Edenbrandt, R. Rittner, O. Pahlm, and C. Peterson, "Artificial neural networks for recognition of electrocardiographic lead reversal," *Am. J. Cardiol.*, vol. 75, no. 14, pp. 929-933, 1995, doi: [https://doi.org/10.1016/S0002-9149\(95\)80689-4](https://doi.org/10.1016/S0002-9149(95)80689-4)
- [12] B. Hedeń, M. Ohlsson, H. Holst, M. Mjńman, et al., "Detection of frequently overlooked electrocardiographic lead reversals using artificial neural networks," *Am. J. Cardiol.*, vol. 78, no. 5, pp. 600-604, 1996, doi: [https://doi.org/10.1016/S0002-9149\(96\)00377-3](https://doi.org/10.1016/S0002-9149(96)00377-3)
- [13] K. Rjoob, R. Bond, D. Finlay, V. McGilligan, S. J. Leslie, A. Iftikhar, and A. Peace, "Machine learning improves the detection of misplaced v1 and v2 electrodes during 12-lead electrocardiogram acquisition," in *2019 Computing in Cardiology (CinC)*, Singapore, Singapore, 2019, pp. 1-4, doi: <https://doi.org/10.22489/CinC.2019.035>
- [14] J. de Bie, D. W. Mortara, and T. F. Clark, "The development and validation of an early warning system to prevent the acquisition of 12-lead resting ECGs with interchanged electrode positions," *J. Electrocardiol.*, vol. 47, no. 6, pp. 794-797, 2014, doi: <https://doi.org/10.1016/j.jelectrocard.2014.08.015>
- [15] G. Zhu, D. Liu, Y. Du, C. You, J. Zhang, and K. Huang, "Toward an intelligent edge: Wireless communication meets machine learning," *IEEE Commun. Mag.*, vol. 58, no. 1, pp. 19-25, 2020, doi: <https://doi.org/10.1109/MCOM.001.1900103>
- [16] Khanzode, K. C. A., Sarode, R. D., "Advantages and Disadvantages of Artificial Intelligence and Machine Learning: A Literature Review," *Int. J. Libr. Inf. Sci.*, vol. 9, no. 1, 30-36, 2020, doi: <https://doi.org/10.17605/OSF.IO/GV5T4>
- [17] I. Jekova, V. Krasteva, R. Leber, R. Schmid, et al., "Interlead correlation analysis for automated detection of cable reversals in 12/16-lead ECG," *Comput. Methods Programs Biomed.*, vol. 134, pp. 31-41, 2016, doi: <https://doi.org/10.1016/j.cmpb.2016.06.003>
- [18] A. Medina, N. Lopez, J. Galdos, E. Supo, J. Rendulich, and E. Sulla, "Continuous Blood Pressure Estimation in Wearable Devices Using Photoplethysmography: A Review," *Int. J. Emerging Technol. Adv. Eng.*, vol. 12, no. 10, 104-113, 2022, doi: [https://doi.org/10.46338/ijetae1022\\_12](https://doi.org/10.46338/ijetae1022_12)
- [19] J. R. Huamani Talavera, E. A. S. Mendoza, N. M. Dávila, and E. Supo, "Implementation of a real-time 60 Hz interference cancellation algorithm for ECG signals based on ARM cortex M4 and ADS1298," in *2017 IEEE XXIV International Conference on Electronics, Electrical Engineering and Computing (INTERCON)*, Cusco, Perú, 2017, pp. 1-4, doi: <https://doi.org/10.1109/INTERCON.2017.8079725>
- [20] T. R. Sulla, S. J. Talavera, C. E. Supo, and A. A. Montoya, "Non invasive glucose monitor based on electric bioimpedance using AFE4300," in *2019 IEEE XXVI International Conference on Electronics, Electrical Engineering and Computing (INTERCON)*, Lima, Perú, 2019, pp. 1-3, doi: <https://doi.org/10.1109/INTERCON.2019.8853561>
- [21] J. R. Beingolea, M. A. Zea Vargas, R. Huallpa, X. Vilca, R. Bolivar, and J. Rendulich, "Assistive Devices: Technology Development for the Visually Impaired," *Designs*, vol. 5, no. 4, 2021, art. no. 75, doi: <https://doi.org/10.3390/designs5040075>
- [22] J. R. Beingolea, H. A. Rodrigues, M. Zegarra, E. Sulla Espinoza, R. Torres Silva, and J. Rendulich, "Designing a Multiaxial Extensometric Force Platform: A Manufacturing Experience," *Electronics*, vol. 10, no. 16, 2021, art. no. 1907, doi: <https://doi.org/10.3390/electronics10161907>
- [23] M. Huisa C., T. E. Figueroa, E. Supo, J. Rendulich, and E. Sulla Espinoza, "PCG heart sounds quality classification using neural networks and Smote Tomek Links for the Think Health project," in *1st International Conference on Computational Intelligence and Innovative Technologies (ICCIIT)*, Pune, India, 2022, pp. 803-811, do: [https://doi.org/10.1007/978-981-19-7615-5\\_65](https://doi.org/10.1007/978-981-19-7615-5_65)
- [24] T. Eslami and F. Saeed, "Fast GPU PCC: A GPU-based technique to compute pairwise Pearson's correlation coefficients for time series data FMRI study," *High-Throughput*, vol. 7, no. 2, 2018, art. no. 11, doi: <https://doi.org/10.3390/ht7020011>
- [25] J. Lian, G. Garner, D. Muessig, and V. Lang, "A simple method to quantify the morphological similarity between signals," *Signal Process.*, vol. 90, no. 2, pp. 684-688, 2010, doi: <https://doi.org/10.1016/j.sigpro.2009.07.010>
- [26] M. J. Mc Loughlin, "New Electrocardiographic Methods Based on the Standard 12-Leads Ecg: Bipolar Precordial Leads," 2022, ssnr.4250757, doi: <http://dx.doi.org/10.2139/ssrn.4250757>
- [27] T. N. Nguyen, T. H. Nguyen, and V. T. Ngo, "Artifact elimination in ECG signal using wavelet transform," *Telkomnika*, vol. 18, no. 2, pp. 936-944, 2020, doi: <https://doi.org/10.12928/TELKOMNIKA.v18i2.14403>
- [28] V. Gupta, M. Mittal, and V. Mittal, "Performance evaluation of various pre-processing techniques for R peak detection in ECG signal," *IETE J. Res.*, vol. 68, no. 5, pp. 3267-3282, 2020, doi: <https://doi.org/10.1080/03772063.2020.1756473>

- [29] S. Banerjee and G. S. Kumar, "Quality guaranteed ECG signal compression using tunable-q wavelet transform and möbius transform based AFD," *IEEE Trans. Instrum. Meas.*, vol. 70, pp. 1-11, 2021, doi: <https://doi.org/10.1109/TIM.2021.3122119>
- [30] A. L. Goldberger, L. A. Amaral, L. Glass, J. M. Hausdorff, et al., "PhysioBank, PhysioToolkit, and PhysioNet: Components of a new research resource for complex physiologic signals," *Circulation*, vol. 101, no. 23, pp. e215-e220, 2000, doi: <https://doi.org/10.1109/TIM.2021.3122119>
- [31] R. Boussejot, D. Kreiseler, and A. Schnabel, "Nutzung der EKG Signaldatenbank CARDIODAT der PTB über das Internet," *J. Biomed. Eng.*, vol. 40, suppl. 1, 317, 1995, doi: <https://doi.org/10.1515/bmte.1995.40.s1.317>
- [32] P. Wagner, N. Strodthoff, R. Boussejot, W. Samek, and T. Schaeffter, PTB-XL, a large publicly available electrocardiography dataset (version 1.0.1), *PhysioNet*. Accessed: 2024. [Online]. Available: <https://doi.org/10.13026/x4td-x982>
- [33] M. A. Reyna, E. A. Perez Alday, A. Gu, C. Liu, et al., "Classification of 12-lead ECGs: the physionet/computing in cardiology challenge 2020," in *2020 Computing in Cardiology, Rimini, Italy, 2020*, pp. 1-4. doi: <https://doi.org/10.22489/CinC.2020.236>
- [34] J. Zheng, J. Zhang, S. A. Danioko, H. Yao, H. Guo, C. Rakovski, "A 12-lead electrocardiogram database for arrhythmia research covering more than 10,000 patients," *Sci. Data*, vol. 7, 2020, art. no. 48, doi: <https://doi.org/10.1038/s41597-020-0386-x>
- [35] N.-T. Bui, G.-s. Byun, "The comparison features of ECG signal with different sampling frequencies and filter methods for real-time measurement," *Symmetry*, vol. 13, no. 8, 2021, art. no. 1461, doi: <https://doi.org/10.3390/sym13081461>
- [36] D. Gembris, M. Neeb, M. Gipp, A. Kugel, and R. Männer, "Correlation analysis on GPU systems using NVIDIA's CUDA," *J. Real Time Image Proc.*, vol. 6, no. 4, pp. 275-280, 2011, doi: <https://doi.org/10.1007/s11554-010-0162-9>